Strathclyde Institute of Pharmacy & Biomedical Sciences

Development of Adverse Outcome Pathways Framework for the Identification of Novel Mechanistic and Clinical Insights into the Cardiotoxic Actions of Thiazolidinediones

Abdullah B. Al-Sultan

A thesis submitted in fulfilment of the requirements for the degree of Doctor of Philosophy

Strathclyde Institute of Pharmacy and Biomedical Sciences, University of Strathclyde, Glasgow G4 0RE

May 2024

University of Strathclyde Glasgow

Royal Charter since 1964

Useful Learning since 1796

Declaration of Authenticity and Author's Rights

This thesis is the result of the author's original research. It has been composed by the author and has not been previously submitted for examination which has led to the award of a degree. The copyright of this thesis belongs to the author under the terms of the United Kingdom Copyright Acts as qualified by University of Strathclyde Regulation 3.50. Due acknowledgment must always be made of the use of any material contained in, or derived from, this thesis.

Signed: 

Date: 1 May 2024

Acknowledgements

First and foremost, I would like to express my sincere gratitude to my parents, Khulood Alomar and Bader Al-Sultan. Their unwavering love, support, and encouragement throughout my academic journey have been instrumental in bringing me to this point. I am incredibly grateful for their belief in me and sacrifices to provide me with this educational opportunity. Moreover, I extend my deepest appreciation to Kuwait University for awarding me a scholarship that allowed me to pursue this research, to further my education, and to contribute to the field of clinical toxicology, for which I am sincerely thankful.

I extend my heartfelt gratitude to my supervisor, Dr Nicholas Rattray, for his invaluable support, guidance, and mentorship throughout my doctoral journey. His expertise in clinical metabolomics proved instrumental in shaping my research and academic growth. His constant encouragement and insightful feedback further fuelled my progress. I am deeply appreciative of his patience, dedication, and constructive feedback, which have played a pivotal role in helping me navigate the challenges and complexities of my doctoral studies. I am deeply grateful to my second supervisor, Dr Ibrahim Khadra, for his well-rounded support throughout my PhD studies. His proficiency in toxicological studies was indispensable in guiding the trajectory and upholding the academic rigour of my research. Dr Khadra's guidance extended beyond academia, providing me with invaluable support in navigating administrative hurdles that arose during my doctoral journey. His willingness to listen and offer advice created a truly supportive environment for which I am incredibly thankful.

Finally, I am incredibly grateful to Dr Zahra Rattray for her continuous support and to my incredible group members for their contributions.Throughout this journey, their camaraderie and infectious enthusiasm made all the difference. A special thank you goes to my friend, Domenica Berardi, with whom I spent the most time in the laboratory and office. Berardi's presence was a constant source of support and laughter, and I cherish the memories and friendships we have formed. My deepest appreciation also goes to my wonderful friends, Abdullah Aldasem, Zainab Bosakhar, Rand Abdulrahman, Karim Daramy, Jene, Gillian, and Lisa, whose endless support and unfailing presence were invaluable. I am truly grateful for the friendships I have formed with all of you, and I look forward to seeing what the future holds for each of you.

Dissemination of Research

1. External Engagement and Collaborative Initiatives

- Completed the EASD Scientists Training Course 2022: “Proteomics in Diabetes Research” at the German Diabetes Center (DDZ) in Düsseldorf, Germany.
- Collaborated with Aberdeen University on the research project “Colorectal Cancer Detection at Low Magnetic Fields.” Contributed by performing in-depth proteomics analysis, utilising bioinformatics tools and R-coding to identify potential biomarkers associated with colorectal cancer. This involved processing and interpreting large datasets to extract meaningful insights crucial for advancing cancer-detection methodologies (paper in draft).
- Collaborated with Dr. Margaret and her PhD student Zainab Bosakhar from the University of Strathclyde on a research project investigating chronic hypertension induced by angiotensin II in rats and participated in in-depth proteomic analysis to profile the changes in the cardiac tissue proteome following angiotensin II treatment. This analysis aimed to elucidate the mechanisms by which angiotensin II contributes to hypertension development (paper in draft).
- Collaborated with Dr. Domenica Berardi, a PhD graduate from the Rattray Group at the University of Strathclyde, on a project titled “Integration of Mass-Spectrometry-Based Global Metabolomics and Proteomics Analysis to Characterize Different Senescence-Induced Molecular Sub-Phenotypes.” Played a crucial role in performing proteomics analysis to identify and characterize these sub-phenotypes. The project has been submitted for publication, reflecting contributions to advancing understanding in senescence-induced molecular biology (paper in draft).

2. Conferences List/ Participation

A. Poster Presentation

- Abdullah AlSultan, Ibrahim Khadra, Zahra Rattray, Nicholas J. W. Rattray. Integration of Metabolomics and Proteomics Data: New Molecular Insights into Pioglitazone-Induced Cardiotoxicity in AC16 Cells. Poster presented at 19th

World Congress of Basic & Clinical Pharmacology; July 2023; Glasgow, Scotland.

- Abdullah AlSultan, Ibrahim Khadra, Zahra Rattray, Nicholas J. W. Rattray. Integration of Metabolomics and Proteomics Data: New Molecular Insights into Pioglitazone-Induced Cardiotoxicity in AC16 Cells. Poster presented at Scottish Metabolomics Network Annual Symposium; November 2022; Aberdeen, Scotland.
- Abdullah AlSultan, Ibrahim Khadra, Zahra Rattray, Nicholas J. W. Rattray. Metabolomics Based Cardiotoxicity Evaluation of Pioglitazone Exposure in Human Derived Cardiomyocyte. Poster presented at 18th International Conference of the Metabolomics Society; June 2022; Valencia, Spain.

B. Oral Presentation

- Abdullah AlSultan. Cardiotoxicity Evaluation of Pioglitazone Exposure in Human Derived Cardiomyocytes Using LC–MS-Based Metabolomics. Scottish Metabolomics Network Virtual Symposium; November 2021.

C. Other Conferences" Attendee Only"

- Pharmacology 2021, British Pharmacological Society Online Conference 2021
- The 10th MENATOX Clinical Toxicology Conference 2021
- Pharmacology 2020, British Pharmacological Society Online Conference 2020

3. Publications

- Al Sultan A, Rattray Z, Rattray NJ. Cytotoxicity and toxicoproteomics analysis of thiazolidinedione exposure in human-derived cardiomyocytes. Journal of Applied Toxicology. 2024 Apr 2. https://doi.org/10.1002/jat.4613
- Al Sultan A, Rattray Z, Rattray NJ. Toxicometabolomics-Based Cardiotoxicity Evaluation of Thiazolidinedione Exposure in Human-Derived Cardiomyocytes. Metabolomics. 2024 Feb 23;20(2):24. https://doi.org/10.1007/s11306-024-02097-z
- Al Sultan A, Rattray Z, Rattray NJ. Integrative Analysis of Toxicometabolomics and Toxicoproteomics Data: New Molecular Insights into Thiazolidinedione-Induced Cardiotoxicity. (Under Review)

- Al Sultan A, Rattray Z, Rattray NJ. A Holistic View of Type II Diabetes Mellitus Research in the Omics Era. (Drafted for submission)
- Berardi D, Farrell G, Alsultan A, McCulloch A, Rattray Z, Rattray NJ. Integration of Mass-Spectrometry-Based Global Metabolomics and Proteomics Analysis to Characterise Different Senescence-Induced Molecular Sub-Phenotypes. bioRxiv. 2022 Nov 30:2022-11.

General Abstract

Type 2 diabetes mellitus (T2DM) represents a burgeoning global pandemic that has currently afflicted nearly half a billion individuals. With the uncertainties surrounding the underlying pathoetiogenesis and course of T2DM, lifelong medication adherence remains the central cornerstone of comprehensive disease management. Thiazolidinediones (TZDs), represented by pioglitazone and rosiglitazone, are a class of cost-effective oral anti-diabetic agents that pose a marginal hypoglycaemia risk. While TZDs initially demonstrated efficacy in maintaining glycaemic control, safety concerns, particularly regarding their cardiotoxicity, have restricted their clinical usefulness. The uncharacterised mechanisms underlying TZD-induced cardiotoxicity continue to fuel debate, limiting the broader application of TZDs as a treatment option. Capitalising on the increasing potential of omics technologies, this project integrated an adverse outcome pathway framework that combined traditional *in vitro* toxicity testing with multi-omics approaches to illuminate the mechanisms underlying the cardiotoxicity debate surrounding TZD use. *In vitro* cytotoxicity testing of TZDs against AC16 human adult cardiomyocytes and primary human cardiac fibroblasts revealed a novel crosstalk between TZDs and mitochondrial dysfunction, manifested by perturbations in mitochondrial energetics and the induction of oxidative stress independent of PPAR-γ activation, highlighting two potential key mechanisms by which TZDs exert their cytotoxic actions on cardiac cells. Accordingly, to gain a more comprehensive understanding of the metabolic changes induced by TZDs, an untargeted liquid chromatography–mass spectrometry (LC–MS)-based toxicometabolomics pipeline was used, with AC16 cells as a model system. The toxicometabolomics analysis revealed a significant modulation in carnitine content after the acute administration of either TZD agent, reflecting the potential disruption of the mitochondrial carnitine shuttle. Furthermore, perturbations were observed in purine metabolism and amino acid fingerprints, strongly conveying aberrations in the cardiac energetics associated with TZD use. The analysis of our findings also highlighted alterations in polyamine (spermine and spermidine) and amino acid (L-tyrosine and valine) metabolisms, which are known modulators of cardiac hypertrophy, suggesting a potential link to TZD cardiotoxicity that necessitates further research. To further complement the metabolic changes found at the most downstream molecular level, an LC–MS-based toxicoproteomics pipeline on AC16 cells was conducted. Our

toxicoproteomics analysis revealed a mitochondrial dysfunction accompanying TZD exposure that primarily stemmed from impaired oxidative phosphorylation, with distinct signalling mechanisms observed for both agents. Furthermore, our analysis revealed additional mechanistic aspects of cardiotoxicity, showing drug specificity. The downregulation of various proteins involved in the protein machinery and protein processing in the endoplasmic reticulum was observed in rosiglitazone-treated cells, implicating proteostasis in rosiglitazone cardiotoxicity. Regarding pioglitazone, the findings suggest the potential activation of the interplay between the complement and coagulation systems and the disruption of the cytoskeletal architecture, which was primarily mediated by the integrin-signalling pathways responsible for pioglitazone-induced myocardial contractile failure. Finally, to move beyond association and establish causality in the observed effects, a multi-omics approach that integrated toxicoproteomics and toxicometabolomics data was implemented. A network analysis of proteometabolomic data revealed a distinct fingerprint of disrupted biochemical pathways, which were primarily related to energy metabolism. In addition, the study identified a marked disruption in the glutathione system, indicating an imbalanced redox state triggered by TZD exposure. In conclusion, the combined findings from our framework illuminate novel molecular mechanisms, potentially offering a resolution to the decades-long controversy surrounding the cardiotoxicity of TZDs. This research showcases the transformative power of combining traditional and omics-based methods that enables the re-evaluation of long-neglected medications and signals a new era of safer medications and improved patient compliance.

Table of Contents

List of Tables

List of Figures

Figures 1.3–1.9, 1.11, 1.12, 1.16–1.18, 1.21, 1.22, 2.1, 2.2, 3.1, 3.3, and 4.1, 4.2 and 4.6 in this thesis were created with BioRender.com.

List of Abbreviations

2D-DIGE	2D differential gel electrophoresis
AAAs	Aromatic amino acids
ADA	American Diabetes Association
ADOPT	A Diabetes Outcome Progression Trial
ADP	Adenosine diphosphate
ADRs	Adverse drug reactions
AMP	Adenosine monophosphate
ANOVA	A non-repeated one-way analysis of variance
ANTs	Adenine nucleotide translocators
AOP	Adverse outcome pathway
aSC	Adult stem cell
ASCVD	Atherosclerotic cardiovascular disease
ATAC-Seq	Assay for transposase-accessible chromatin with sequencing
ATP	Adenosine triphosphate
AUC	Area under the curve
BCAAs	Branched-chain amino acids
BER	Balanced error rate
BP	Biological process
BS-Seq	Bisulfite sequencing
cAMP	Cyclic adenosine monophosphate
CC	Cellular component
CDC	Centers for Disease Control and Prevention
CEs	Cholesterol esters
ChEBI	Chemical Entities of Biological Interest
ChIA-PET	Chromatin interaction analysis with paired-end tag sequencing
CI	Confidence interval
CKD	Chronic kidney disease
CVD	Cardiovascular disease

DDA	Data-dependent acquisition
DEFs	Differential expressed features
DEGs	Differential expressed genes
DEPs	Differential expressed proteins
DIABLO	Data Integration Analysis for Biomarker Discovery using Latent cOmponents
DMEM	Dulbecco's Modified Eagle's Medium
DMSO	Dimethylsulfoxide
DNase-seq	DNase I hypersensitive sites sequencing
DO	Disease ontology
DPP-4	Dipeptidyl peptidase 4
DRP1	Dynamin-related protein 1
DSPC	Debiased sparse partial correlation
ECM	Extracellular matrix
eNOS	Endothelial nitric oxide synthase
ER	Endoplasmic reticulum
ESCs	Embryonic stem cells
EWASs	Epigenome-wide association studies
FAs	Focal adhesions
FBS	Foetal bovine serum
FC	Fold change
FDA	Food and Drug Administration
FDR	False discovery rate
FH	Fumarate hydratase
FPG	Fasting plasma glucose
GC–MS	Gas chromatography–mass spectrometry
GFR	Glomerular filtration rate
GIP	Glucose-dependent insulinotropic polypeptide
GLP-1	Glucagon-like peptide-1
GLUD	Glutamate dehydrogenase
GLUT2	Glucose transporter 2

GO	Gene ontology
GPX4	Glutathione peroxidase-4
GSH	Glutathione
GSSG	Glutathione disulfide
H_2DCFDA	2′,7′-Dichlorofluorescein diacetate
HbA1c	Glycated haemoglobin test
HCFs	Human cardiac fibroblasts
HDL	High-density lipoprotein
HF	Heart failure
HMDB	Human Metabolome Database
HNF	Hepatocyte nuclear factor
HPLC	High-performance liquid chromatography
HR	Hazard ratio
HTS	High-throughput screens
IC_{50}	Half maximal inhibitory concentration
IDF	International Diabetes Federation
iPSC	Induced pluripotent stem cells
IR	Insulin resistance
IRIS	Insulin Resistance Intervention After Stroke trial
IRS	Insulin receptor substrate
ISO	Isoproterenol
iTRAQ	Isobaric tag for absolute and relative quantitation
KEGG	Kyoto Encyclopedia of Genes and Genomes
LC–MS	Liquid chromatography–mass spectrometry
LDCVs	Large dense-core vesicles
LFQ	Label free quantitation
LPS	Lipopolysaccharides
LPs	Lysophospholipids
MF	Molecular function
MI	Myocardial infraction
MIE	Molecular initiating event

miRNA	MircoRNA
MLKL	Mixed-lineage kinase domain-like pseudokinase
MMP	Mitochondrial membrane potential
MODY	Maturity-onset diabetes of the young
mRNA	messenger ribonucleic acid
MS	Mass spectrometry
MSEA	Metabolite set enrichment analysis
MT-CO1	Mitochondrially encoded cytochrome c oxidase I
mTOR	Mammalian target of the rapamycin
NADPH	Nicotinamide adenine dinucleotide phosphate
NASH	Non-alcoholic steatohepatitis
NDM	Neonatal diabetes mellitus
NGS	Next-generation sequencing
NHS	National Health Service
NMR	Nuclear magnetic resonance spectroscopy
NPSA	National Patient Safety Agency
NRC	National Research Council
NYHA	New York Heart Association
OPLS-DA	Orthogonal partial least squares-discriminant analysis
OXPHOS	Oxidative phosphorylation
PBS	Phosphate-buffered saline
PC-PLs	Phosphatidylcholine-plasmalogens
PCA	Principal component analysis
PD	Proteome Discoverer
PDE-3B	Phosphodiesterase-3B
PEs	Phosphatidylethanolamines
PGAM5	Phosphoglycerate mutase family member 5
PGZ	Pioglitazone
PI3K	Phosphatidylinositol 3-kinase
PKB	Protein kinase B

PP-1	Protein phosphatase-1
PPAR-α	Peroxisome proliferator-activated receptor-alpha
PPAR-γ	Peroxisome proliferator-activated receptor-gamma
PPI	Protein-protein interaction
PROactive	PROspective pioglitAzone Clinical Trial In macroVascular Events
PTB	Phosphotyrosine-binding domain
QC	Quality control
qRT-PCR	Quantitative real-time reverse-transcription polymerase chain reaction
RCT	Randomised controlled trial
RECORD	Rosiglitazone Evaluated for Cardiac Outcomes and Regulation of Glycaemia in Diabetes
RF	Random forest
RIPK1	Receptor-interacting protein kinases 1
RLU	Relative luminescence unit
ROS	Reactive oxygen species
ROSI	Rosiglitazone
RR	Relative risk
RTKs	Receptor-tyrosine kinases
SD	Standard deviation
SFA	Saturated fatty acid
SGLT2	Sodium-glucose cotransporter 2
SILAC	Stable isotope labeling by/with amino acids in cell culture
SLC2A2	Solute carrier family 2, member 2
SMs	Sphingomyelins
SNAP	Soluble N-ethylmaleimide-sensitive factor attachment protein
SNAP-25	Synaptosomal protein of 25 kDa
SNAREs	Soluble N-ethylmaleimide-sensitive factor attachment receptor proteins

SNPs	Single-nucleotide polymorphisms
SNVs	Single-nucleotide variations
sPLS-DA	Sparse partial least squares discriminant analysis
STRING	Search Tool for the Retrieval of Interacting Genes/Proteins
SV40	Simian vacuolating virus 40
t-SNE	t-distributed stochastic neighbor embedding
T1DM	Type 1 diabetes mellitus
T2DM	Type 2 diabetes mellitus
TAGs	Triacylglycerols
TCA	Citric acid cycle
TFs	Transcription factors
TMT	Tandem mass tag
TNDM	Transient neonatal diabetes mellitus
TNF	Tumour necrosis factor
TOM	Topology overlap matrix
TPDM	Permanent neonatal diabetes mellitus
TZDs	Thiazolidinediones
UK	United Kingdom
UKPDS	United Kingdom Prospective Diabetes Study
UQCRC1	Ubiquinol-cytochrome c reductase core protein 1
US	United States
VAMP2	Vesicle-associated membrane protein
VAT	Visceral adipose tissue
VIP	Variable importance in the projection
WES	Whole-exome sequencing
WGCNA	Weighted correlation network analysis
WGS	Whole-genome sequencing
WHO	World Health Organization
wKDA	Weighted key driver analysis
α-MHC	α-Myosin heavy chain

Chapter 1. Diabetes Mellitus: A Panoramic View on Its Pathogenesis and Pharmacological Modalities

1.1 Aetiologic Classification and Epidemiology of Diabetes Mellitus

The term 'diabetes mellitus' represents a spectrum of chronic, progressive metabolic disorders chiefly characterised by elevated levels of blood glucose (hyperglycaemia) (ADA, 2023; Lankatillake et al, 2019). Diabetes mellitus is complex in aetiology and incompletely understood; however, the consensus is that a relative or absolute deficiency in insulin secretion, accompanied by varying degrees of peripheral resistance to insulin actions, are the significant contributors to the imbalance in glucose homeostasis that manifests disease pathology (Chetan et al, 2019; Lankatillake et al, 2019). The most common aetiologic classification of diabetes includes type 1 diabetes mellitus (T1DM), type 2 diabetes mellitus (T2DM), and gestational diabetes mellitus (ADA, 2023; Egan & Dinneen, 2019).

1.1.1 Epidemiology of T1DM

T1DM is the most common endocrine disorder of childhood and adolescence, accounting for almost all diabetes diagnoses before age 10 in the United States (US) (Tönnies et al, 2023). Nevertheless, it may present at any age, as 25% of cases are diagnosed in adults (Martin et al, 2020). The age of onset of T1DM in childhood has a bimodal distribution with two peaks: one at pre-school age, and another onset at puberty **(Figure 1.1)** (Pedrosa et al, 2023). In the United Kingdom (UK), T1DM affects 400,000 individuals, including almost 29,000 children (Ng & Soni, 2023).

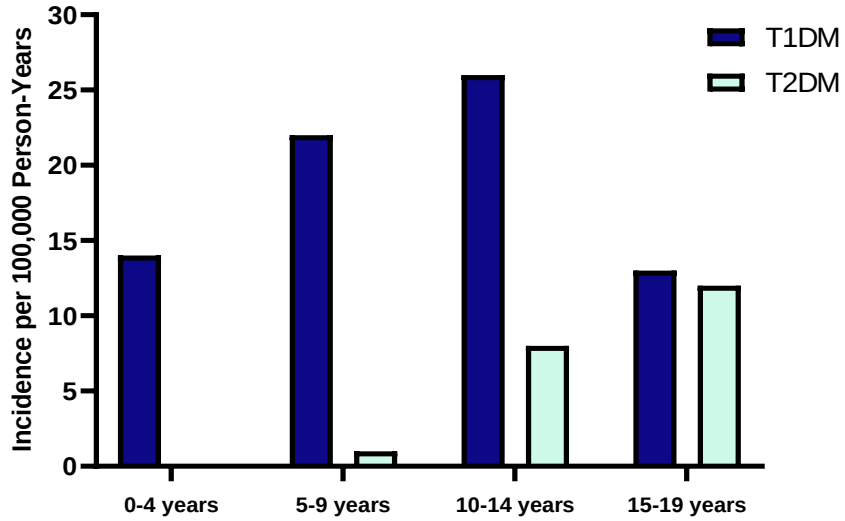

Figure 1.1 Incidence of T1DM and T2DM in youth by age group. T1DM: type 1 diabetes mellitus; T2DM: type 2 diabetes mellitus. Adopted from (Pedrosa et al, 2023).

1.1.2 Epidemiology of T2DM

T2DM is the most prevalent form of diabetes mellitus, accounting for more than 90% of all cases in adults (ADA, 2023; Forouhi & Wareham, 2022). The prevalence of T2DM is increasing at a tremendous rate and is thus a pandemic concern (ADA, 2023; Forouhi & Wareham, 2022). As of 2021, according to the International Diabetes Federation (IDF), roughly 537 million adults have been diagnosed with diabetes globally, and this number is projected to reach 783 million adults by 2045 **(Figure 1.2)** (Forouhi & Wareham, 2022). In the US, in 2022, the Centers for Disease Control and Prevention (CDC) reported that diabetes mellitus affects more than 37 million Americans (1 in 10), the considerable majority of whom were diagnosed with T2DM (90–95%) (Herman et al, 2023).

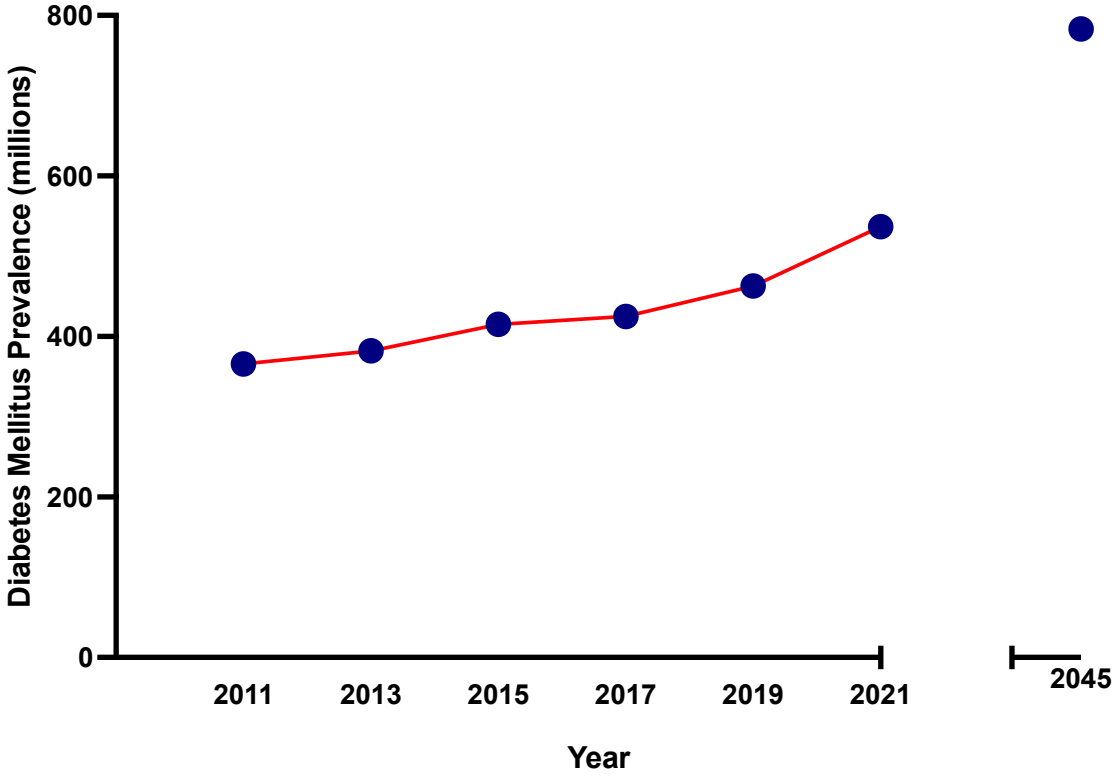

Figure 1.2 Estimates and projections of global diabetes prevalence in the adult population. Adopted from (Forouhi & Wareham, 2022).

Furthermore, in 2021, in the Middle East and North Africa region, the prevalence of adult diabetes was found to be 16.2% (73 million adults aged between 20 and 79), reflecting the highest estimated prevalence compared to other IDF regions (Bodhini & Mohan, 2022). Additionally, the region is estimated to experience the second-highest increase (86%) in the total number of diabetic subjects to 136 million by 2045 (Bodhini & Mohan, 2022).

In the UK, in 2019, more than 4.9 million individuals were diagnosed with diabetes (Whicher et al, 2020). A National Health Service (NHS) report revealed that one in 15 people in the UK has diabetes, including one million people who have T2DM but have been underdiagnosed (Whicher et al, 2020). Since 1996, the prevalence of diabetes in the UK has more than doubled, and if this trend continues, it is projected that more than 5.5 million people will have diabetes by 2030 (Penn et al, 2018; Whicher et al, 2020). Most cases in the UK were diagnoses of T2DM, and the same NHS report (2019) indicated that a further 13.6 million people are at high risk of developing T2DM (Whicher et al, 2020).

1.1.3 Gestational Diabetes Mellitus

Additional forms of diabetes mellitus include gestational diabetes mellitus, which can be defined as an impairment in glucose tolerance initially recognised in the second or third trimester of pregnancy (Egan & Dinneen, 2019). The prevalence of gestational diabetes mellitus varies globally and among different racial and ethnic groups (Deputy et al, 2018). This variation can be partially attributed to the various criteria and screening programmes adopted worldwide (ADA, 2023). In the US, the prevalence of gestational diabetes mellitus in pregnant women is about 8.3%, with a higher prevalence in African American women than in white women (Prevention, 2023). In addition, pregnant women aged 40 years and above are at approximately six times higher risk for developing gestational diabetes mellitus compared to women aged 20 or under (Prevention, 2023). Women diagnosed with this form of diabetes are at an increased risk of getting type T2DM after pregnancy (Deputy et al, 2018).

1.1.4 Other Specific Types of Diabetes

Other uncommon types of diabetes can be induced by genetic defects, pancreatic disorders, endocrinopathies, infections, and chemicals (e.g., drugs) (ADA, 2023). The American Diabetes Association (ADA) has classified these forms of diabetes as ‘other specific types of diabetes’ (ADA, 2023).

1.1.4.1 Genetic Defects

The clinical phenotype of monogenic defects that give rise to impairment in β-cell function includes maturity-onset diabetes of the young (MODY) and transient or permanent neonatal diabetes mellitus (NDM) (Urakami, 2019). Monogenic diabetes

accounts for less than 5% of all diabetic cases, with the majority being diagnosed with MODY (Bonnefond et al, 2023; Urakami, 2019).

MODY represents a heterozygous monogenic form of diabetes with an autosomal dominant inheritance and early onset age (before age 25 years) (Bonnefond et al, 2023; Urakami, 2019). MODY is primarily characterised by a defect in insulin secretion, with minimal or no effects on insulin action (Urakami, 2019). In the UK, the prevalence of MODY is roughly 68 to 108 cases per million (Whicher et al, 2020). To date, several genetic mutations have been identified including hepatocyte nuclear factor (HNF) 4α (*HNF4α*), *HNF1α*, *HNF1β*, and glucokinase (*GCK*), each leading to a different type of MODY (Urakami, 2019). The most common subtypes of MODY listed by ADA classification of diabetes include HNF1α-MODY (MODY 3), GCK-MODY (MODY2), and HNF4α-MODY (MODY1) (ADA, 2023).

NDM is another rare form of monogenic diabetes that occurs mostly within the first month of life (<six months of age) (Lemelman et al, 2018). NDM is sub-classified into transient neonatal diabetes mellitus (TNDM) and permanent neonatal diabetes mellitus (PNDM) (Lemelman et al, 2018). The incidence is infrequent, accounting for 1:20,000-500,000 live births (Mancioppi et al, 2023). TNDM often results from genetic mutations in chromosome 6q24 (Lemelman et al, 2018). PNDM is due to mutations in potassium channels in pancreatic β-cells that lead to defects in insulin secretion (Lemelman et al, 2018).

1.1.4.2 Diseases of the Exocrine Pancreas

Any pathological condition that damages the pancreas can lead to diabetes (Egan & Dinneen, 2019). Diabetes initiated by diseases of the exocrine pancreas has been termed “type 3c DM” or pancreoprivic diabetes (Conlon & Duggan, 2017). The most common diseases are cystic fibrosis, acute and chronic pancreatitis, hemochromatosis, and pancreatic carcinoma (Conlon & Duggan, 2017). Current research suggests that the prevalence of type 3c diabetes mellitus is approximately 8%, with chronic pancreatitis being the primary underlying cause. (Conlon & Duggan, 2017; Śliwińska-Mossoń et al, 2023).

1.1.4.3 Endocrinopathies

Physiologically, counterregulatory hormones, such as cortisol, glucagon, growth hormone, and epinephrine, induce insulin resistance in the liver and peripheral tissues and antagonise insulin action in response to hypoglycaemia (Okura et al, 2020). However, overproduction of these hormones may precipitate or worsen overt diabetes (Okura et al, 2020). Examples of endocrine disorders that can lead to impairment in glucose homeostasis include Cushing's syndrome, glucagonomas, somatostatinomas, acromegaly, and hyperthyroidism (Okura et al, 2020).

1.1.4.4 Viral Infections

Viral infections have been reported to cause diabetes mellitus (Korkmaz & Ermiş, 2019). The etiopathogenesis could be either through inducing autoimmune damage or direct destruction to β-cell mass (Korkmaz & Ermiş, 2019). Congenital rubella in infants is a well-recognised infection that has been found to develop into autoimmune T1DM in 20% of cases when they become young adults (Korkmaz & Ermiş, 2019).

1.1.4.5 Drug-Induced Diabetes

A variety of medications can alter glucose homeostasis by increasing hepatic gluconeogenesis, inducing insulin resistance, and/or decreasing insulin release, resulting in impairment in glucose tolerance or development of diabetes mellitus in susceptible individuals (Yi & Kang, 2017). Common pharmaceutical classes that can elevate plasma glucose levels include fluoroquinolones, thiazide diuretics, beta-blockers, second-generation antipsychotics, corticosteroids, etc (Yi & Kang, 2017).

1.2 Clinical Diagnosis of Diabetes Mellitus

Recent ADA guidelines have recommended four available tests for the clinical diagnosis of diabetes: fasting plasma glucose (FPG), 2-h plasma glucose (2-h PG) during a 75-g oral glucose tolerance test (OGTT), random glucose test, and glycated haemoglobin test (HbA1c) (ADA, 2023). All these tests are equally appropriate and can be used to screen and diagnose diabetes, and to identify individuals with glucose levels that are higher than normal, but not enough to be classified as diabetic (prediabetes) (ADA, 2023). The diagnostic criteria for diabetes and prediabetes are shown in **Table 1.1.**

Table 1.1 The diagnostic criteria for diabetes and prediabetes* (ADA, 2023).

Measure	Normal	Prediabetes	Diabetes
FPG	≤99 mg/dL	100–125 mg/dL	≥126 mg/dL
OGTT	≤139 mg/dL	140–199 mg/dL	≥200 mg/dL
Random Plasma Glucose			≥200 mg/dL
HbA1c	≤5.6%	5.7–6.4%	≥6.5 %

*In the absence of unequivocal hyperglycaemia, diagnosis requires two abnormal test results from the same sample or in two separate test samples.
Abbreviations: FPG: fasting plasma glucose; OGTT: oral glucose tolerance test

1.3 Health and Economic Burden of T2DM

Patients with T2DM are at high risk of developing severe long-term complications, including macrovascular and microvascular complications **(Figure 1.3)** (ADA, 2023).

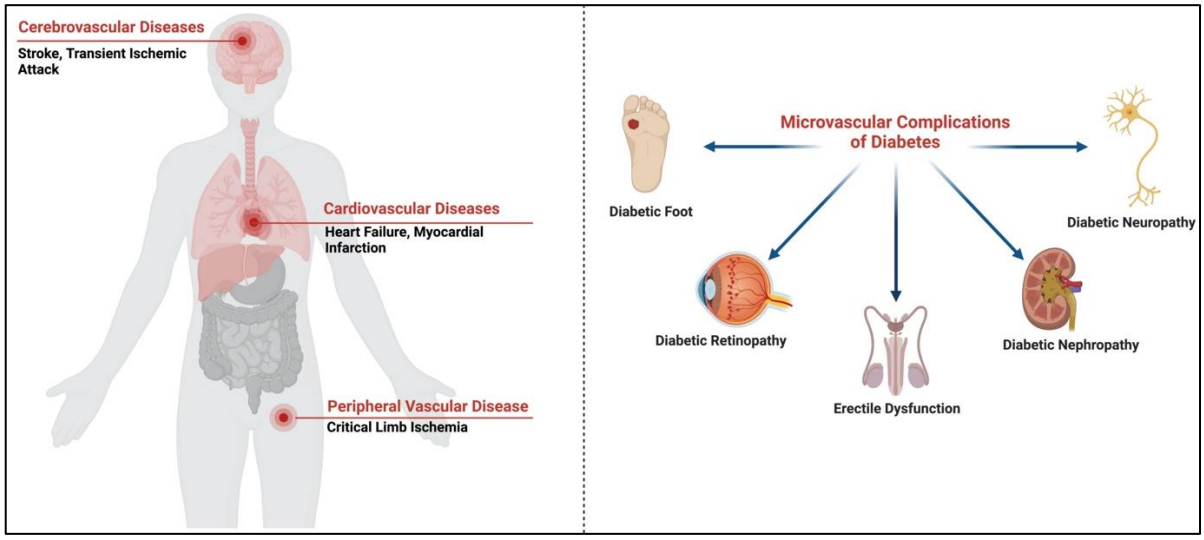

Figure 1.3 Macrovascular and microvascular complications of type 2 diabetes mellitus. Chronic diabetes can lead to a multitude of complications. Microvascular complications, affecting small blood vessels, include retinopathy (eye damage), nephropathy (kidney damage), and neuropathy (nerve damage). Neuropathy can further contribute to diabetic foot; it can also lead to erectile dysfunction. Macrovascular complications, affecting large blood vessels, encompass coronary artery disease (heart issues), peripheral artery disease (circulation problems in legs and feet), and stroke (brain damage). Adopted from (ADA, 2023).

Studies have shown that patients with chronic metabolic imbalances have a two-to-six times higher risk of developing macrovascular complications, including ischemic heart disease, cardiovascular disease (CVD) and peripheral vascular diseases, compared to the general population (ADA, 2023). Studies have reported that diabetic patients'

risk of developing myocardial infarction (MI) is equivalent to those who are non-diabetic with a previous history of MI (Viigimaa et al, 2020). Similar to coronary artery disease, diabetes is an independent risk factor for stroke and cerebrovascular diseases (Viigimaa et al, 2020). Diabetic patients have an increased risk of 150–400% for stroke compared to the general population (Viigimaa et al, 2020). Furthermore, the risk of vascular dementia and stroke-related deaths is elevated in diabetic patients (Viigimaa et al, 2020). Heart failure (HF), which is another leading cause of morbidity and mortality from CVD, has also been associated with diabetes mellitus (ADA, 2023; Viigimaa et al, 2020). Recent studies have shown a twofold increase in HF-related hospitalisation among patients with diabetes compared to those without diabetes (ADA, 2023; Viigimaa et al, 2020).

Microvascular complications refer to diseases of the small blood vessels associated with the thickening of the basement membranes, which include diabetic retinopathy, diabetic nephropathy, and diabetic neuropathy. Chronic kidney disease (CKD) attributed to diabetes affects 20–40% of diabetic patients (Park et al, 2019). It typically presents at the time of T2DM diagnosis and is likely to progress to end-stage renal disease, which requires dialysis or kidney transplantation (ADA, 2023). In fact, CKD attributed to diabetes is the leading cause of end-stage renal disease in the US (An et al, 2021; ADA, 2023; Park et al, 2019). Diabetic retinopathy is a progressive disease of the retinal microvasculature associated with persistent hyperglycaemia and other factors linked to diabetes, including hypertension (An et al, 2021). The risk of developing diabetic retinopathy is strongly related to the duration of diabetes and the level of diabetic control (An et al, 2021). Diabetic retinopathy is attributed to 4.8% of the 37 million cases of blindness worldwide and is considered the leading cause of blindness in patients aged 15–64 (Park et al, 2019). Diabetic neuropathy refers to a heterogeneous group of disorders characterised by nerve dysfunction that results in the loss of sensation, ulceration and ultimately amputation (Park et al, 2019). Approximately half of all diabetic patients develop diabetic neuropathy within 25 years of disease onset (Park et al, 2019). Similar to other microvascular complications, the risk of developing diabetic neuropathy is proportional to the duration and level of glycaemic control (Park et al, 2019). Depending on the clinical manifestations and the site at which the peripheral nervous system is affected, diabetic neuropathy may manifest in several ways, including distal symmetric polyneuropathy and autonomic

neuropathy (An et al, 2021). Diabetic polyneuropathy is the most prevalent form of neuropathy in developed countries (Sloan et al, 2022). According to a large community-based study in the UK, the prevalence of clinical neuropathy among 15,692 diabetic patients was 49% (Sloan et al, 2022). This high prevalence rate indicates substantial morbidity consequences, including diabetic foot ulceration, which carries a risk of progressing to limb amputation (Sloan et al, 2022). In fact, more than 80% of amputations following foot ulceration or injuries are due to diabetic neuropathy (Park et al, 2019). A total of 40–60 million diabetic patients are affected by diabetic foot and lower limb complications globally (Park et al, 2019).

Hence, diabetes mellitus is a global pandemic that poses a serious health and economic burden to all health care systems. The direct and indirect economic costs and related complications have a significant impact on national economics. In 2021, 6.7 million deaths were caused secondary to diabetes (Forouhi & Wareham, 2022). According to the ADA's 2023 guidelines, macrovascular complications account for almost half of all diabetes-related cases of mortality and cost approximately $37.3Bn in CVD-related spending annually (ADA, 2023). Furthermore, in the UK, the NHS spends approximately £10Bn annually on diabetes (Whicher et al, 2020). The number of items prescribed for diabetes increased from 35.5 million in 2009 to 57.7 million in 2019 (Whicher et al, 2020). In 2021, the International Diabetes Federation stated that the total direct health expenditure for diabetes alone cost at least $966Bn, labelling it the costliest chronic disease (Karugu et al, 2023).

1.4 Blood Glucose Homeostasis

Glucose is an essential metabolic fuel for various body tissues and organs, and therefore maintaining blood glucose homeostasis is of critical importance to ensure proper body function (Röder et al, 2016). This is accomplished by a complex network of biomolecular processes that involves various glucoregulatory hormones and neuropeptides released chiefly from the pancreas, brain, liver, intestine, and adipose and muscle tissues (Röder et al, 2016).

Within this network, the pancreas plays a central role in the regulation of blood glucose and maintenance of metabolic homeostasis (Bakhti et al, 2019; Röder et al, 2016). It is a unique gland that consists of both exocrine and endocrine functionality (Bakhti et

al, 2019; Röder et al, 2016). The exocrine pancreas constitutes 85% of the pancreatic mass and is made up of acinar cells that secrete digestive juice essential for digestion (Röder et al, 2016). By contrast, the endocrine gland of the pancreas takes the form of clumps of small secretory cells called islets of Langerhans, or simply islet cells (Bakhti et al, 2019; Röder et al, 2016). A human pancreas comprises 1–3 million pancreatic islets, which are complex micro-organs that work to synthesise and release hormones directly into the bloodstream (Bakhti et al, 2019; Röder et al, 2016). There are five major types of cells in the islets of Langerhans: glucagon-producing α-cells that account for 15–20% of the total endocrine cells; insulin and amylin-secreting β-cells, which represent almost 65–80% of the whole islet cells; somatostatin-secreting δ-cells, which make up 3–10% of the endocrine cells; pancreatic polypeptide-producing PP-cells, which constitute 3–5% of the islets of Langerhans; and ghrelin-releasing ε-cells (< 1% of the total cells) **(Figure 1.4)** (Alamri et al, 2016; Bakhti et al, 2019; Kumar & Singh, 2020; Röder et al, 2016).

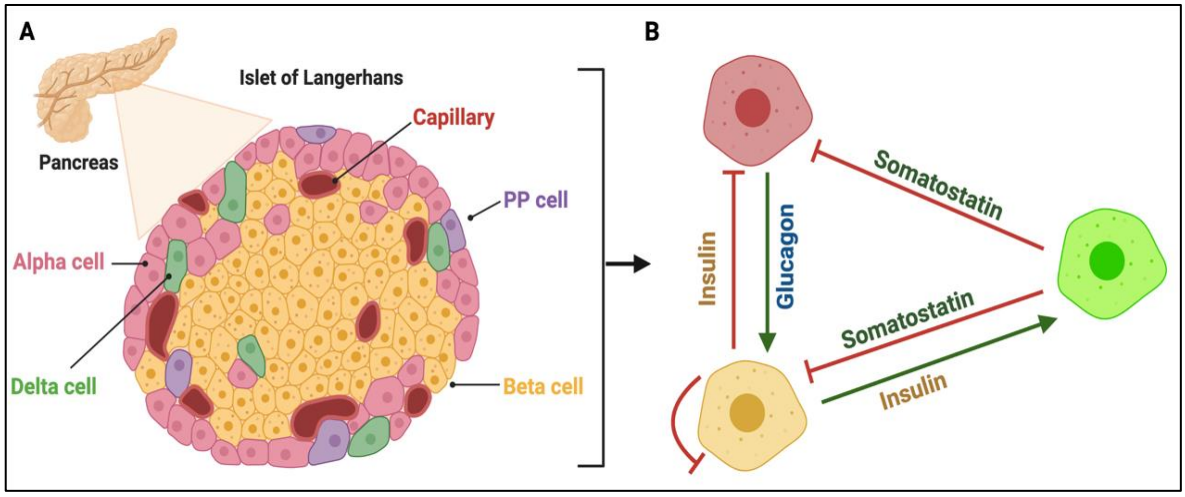

Figure 1.4 The pancreas anatomy 'islets of Langerhans'. Islets of Langerhans cell types (A). The potential interactions among the major islet cell types (B). Red flathead arrows indicate inhibitory action, while green arrows denote the activation effect. PP cell: pancreatic polypeptide-producing cell. Adopted from (Bakhti et al, 2019; Röder et al, 2016).

Each hormone has its own definite functions (Alamri et al, 2016; Bakhti et al, 2019; Kumar & Singh, 2020; Röder et al, 2016). Insulin is the primary hormone capable of lowering blood glucose levels, while glucagon acts primarily on raising these levels during the fasting state (Röder et al, 2016). Somatostatin inhibits the secretion of both insulin and glucagon from adjacent cells, and pancreatic polypeptide works to

self-regulate the secretion activity of the pancreas (Kumar & Singh, 2020). The role of ghrelin in pancreatic function remains not fully known. However, recent evidence has shown that ghrelin exerts inhibitory actions on pancreatic exocrine and endocrine secretions and has pleiotropic activity on energy metabolism (Alamri et al, 2016). Collectively, the human pancreas, through its endocrine system, particularly α and β-cells, works to achieve the homeostatic equilibrium between the rate of glucose appearance in the circulation and the metabolic clearance of glucose, through which fasting blood glucose levels is maintained between 79 and 99 mg/dL (Lankatillake et al, 2019).

1.5 Glucose Metabolism and the Insulin Secretion Signalling Pathway

Insulin is a small anabolic polypeptide hormone of 51 amino acids, arranged in two polypeptide chains, A (21-residue) and B (30-residue), held together by two disulphide bridges formed between cysteine residues A7–B7 and A20–B19 **(Figure 1.5)** (Lankatillake et al, 2019).

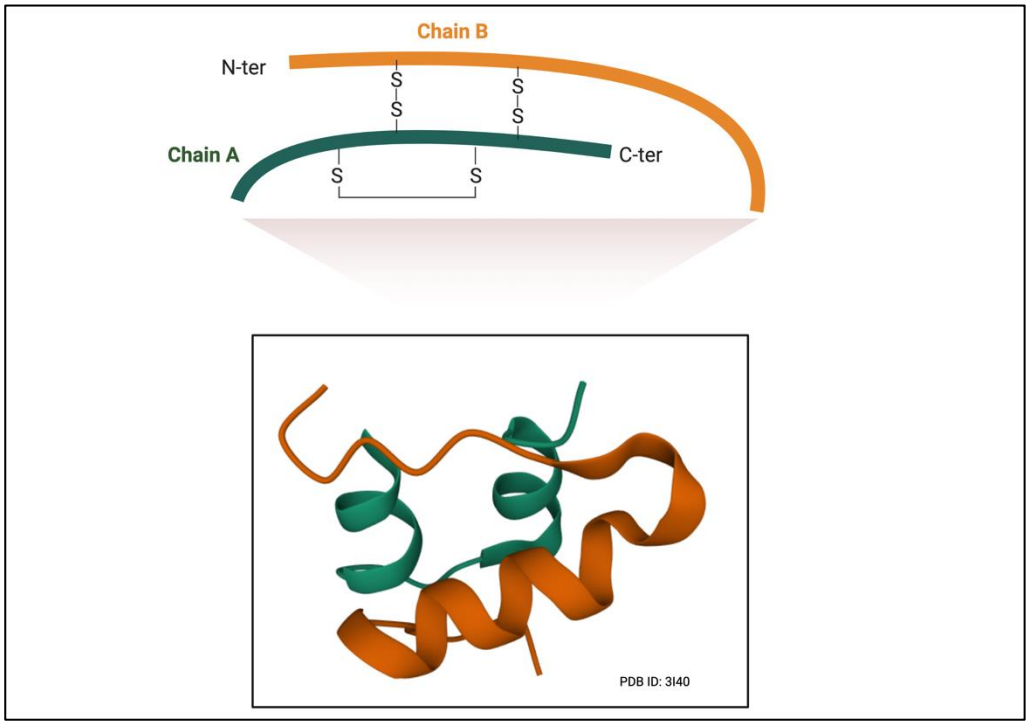

Figure 1.5 Schematic diagram of human insulin and its X-ray 3D structure (PDB ID: 3I40). The A-chain is illustrated in green and the B-chain in orange. The inter-and intra-chain disulphide bonds formed between cysteine residues are shown in black. Adopted from (PDB ID: 3I40; Timofeev et al, 2010).

Glucose is the most potent insulin secretagogue in the blood circulation (Lankatillake et al, 2019). The glucose-stimulated β-cell insulin release is a multistep molecular

process. When the exogenous glucose level is elevated, the circulating blood glucose enters β-cells through a facilitated transporter isoform expressed on the surface of β-cells called glucose transporter 2 (GLUT2), also known as solute carrier family 2, member 2 (SLC2A2) (Röder et al, 2016). Inside the cell, glucose undergoes glycolysis, resulting in increased production of adenosine triphosphate (ATP) molecules (Al-Daghri et al, 2016; Lankatillake et al, 2019; Skelin et al, 2010). Elevated ATP levels raise the ATP/Adenosine diphosphate (ADP) ratio, which consequently leads to the closure of ATP-sensitive potassium channels (Al-Daghri et al, 2016; Lankatillake et al, 2019; Skelin et al, 2010). When glucose levels are not high, the ATP levels are too low to maintain the ATP-sensitive potassium channel closure (Al-Daghri et al, 2016; Lankatillake et al, 2019; Skelin et al, 2010). The closure of these channels is a critical step in insulin secretion, as this closure causes subsequent depolarisation of the plasma membrane, which in turn results in activation of voltage-gated calcium channels and increased influx of extracellular calcium (Al-Daghri et al, 2016; Lankatillake et al, 2019; Skelin et al, 2010). This electrical activity, together with calcium influx, triggers the fusion of insulin-granule with the plasma membrane (exocytosis), leading to insulin release into the circulation (**Figure 1.6)** (Al-Daghri et al, 2016; Lankatillake et al, 2019; Skelin et al, 2010).

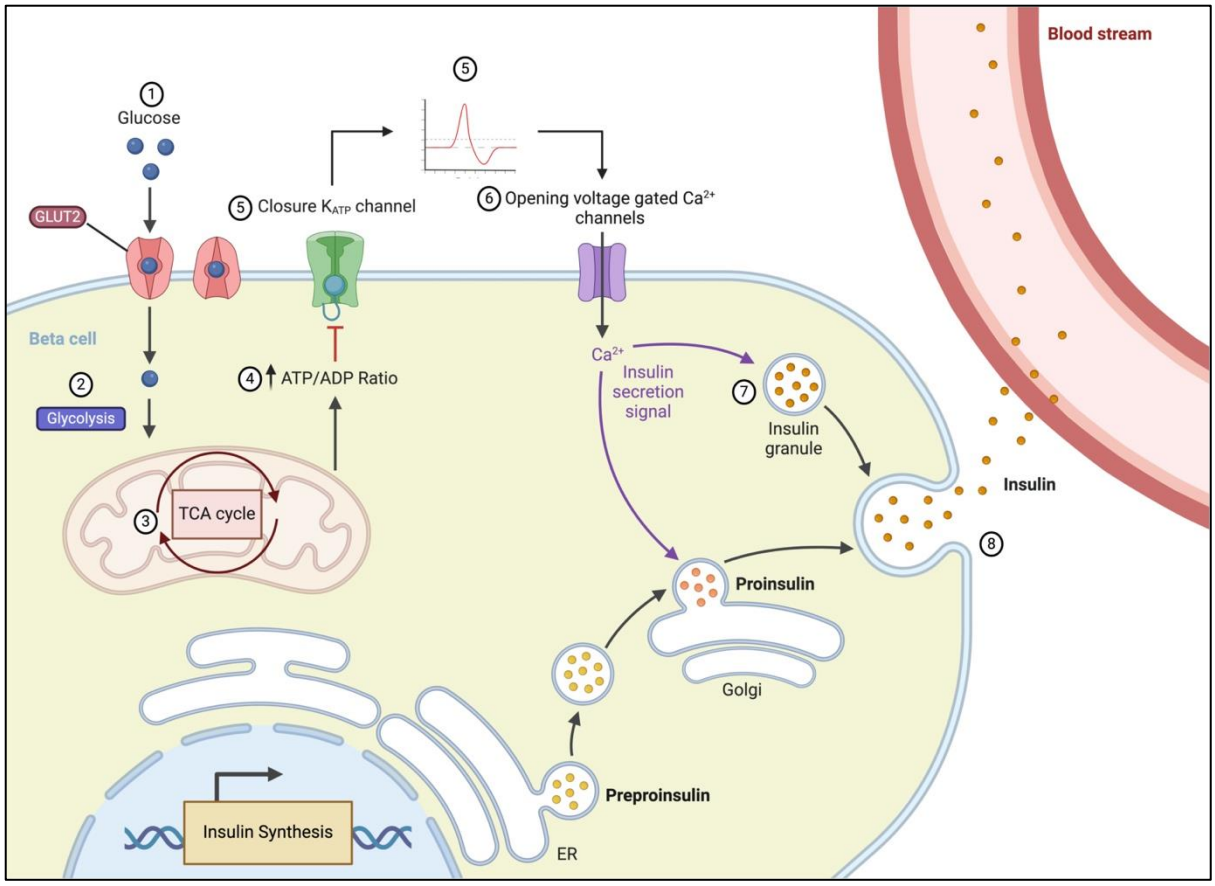

Figure 1.6 Signalling pathways involved in insulin secretion. When glucose levels are high, the GLUT2 transporter, expressed on the surface of β-cells, facilitates the entry of glucose into β-cells (1). Once inside the cell, glucose undergoes glycolysis (2), leading to increased production of ATP molecules (3) and subsequently a high ATP/ADP ratio (4). The elevated ATP/ ADP ratio causes the closure of ATP-sensitive potassium channels (5), which in turn causes membrane depolarisation (6) and results in the activation of voltage-sensitive calcium channels (7). Activation of the calcium channels increases calcium influx, which promotes exocytosis of secretory granules containing insulin (8). ATP: adenosine triphosphate; ADP: adenosine diphosphate; GLUT2: glucose transporter 2. Adopted from (Al-Daghri et al, 2016; Lankatillake et al, 2019; Skelin et al, 2010).

The exocytosis mechanism underlying insulin release is mediated by sophisticated extracellular machinery. Insulin is stored in large dense-core vesicles (LDCVs) that are recruited to the plasma membrane in response to meal congestion and high glucose levels (Röder et al, 2016). There are a number of key proteins that mediate the fusion process of secretory granules of insulin with the plasma membrane, including the vesicle-associated membrane protein (VAMP2)/synaptobrevin 2, the synaptosomal protein of 25 kDa (SNAP-25), and syntaxin-1, which collectively belong to the superfamily of the soluble N-ethylmaleimide-sensitive factor attachment protein (SNAP) receptor proteins (SNAREs) (Al-Daghri et al, 2016; Ramakrishnan et al, 2012). The Sec1/Munc-18 (SM)-family proteins are fundamental molecules involved

in the exocytosis process, which together with SNAREs form the so-called SNARE complex (Al-Daghri et al, 2016; Ramakrishnan et al, 2012). To enable exocytosis, the VAMP2 present in the vesicle's membrane binds to SNAP-25 and syntaxin-1, which are both integrated into the target cell membrane, hence allowing fusion to occur (Al-Daghri et al, 2016; Ramakrishnan et al, 2012).

To proceed with the fusion of the secretory granules of insulin with the plasma membrane, a calcium sensor is needed (Al-Daghri et al, 2016). In endocrine cells, synaptotagmins, the vesicle-bound calcium sensors, have been reported to be involved in calcium-dependent insulin-secretion (Gauthier & Wollheim, 2008; Röder et al, 2016). Synaptotagmins interact with SNAREs, following calcium binding, and form a complex that triggers the exocytosis process (Gauthier & Wollheim, 2008; Röder et al, 2016). Currently, the synaptotagmin gene family consists of 17 members (Syts 1-17), with only eight members (Syt-1, -2, -3, -5, -6, -7, -9, and -10) possessing calcium-binding affinities consistent with their potential role as calcium sensors (Gauthier & Wollheim, 2008; Röder et al, 2016).

1.6 Insulin Receptor and Mechanism of Signalling

Insulin exerts its cellular actions by binding to its specific receptor, leading to intracellular signalling cascade activation (De Meyts, 2016; Lankatillake et al, 2019). The insulin receptor belongs to the superfamily of receptor-tyrosine kinases (RTKs), which phosphorylate their substrates on tyrosine residues (De Meyts, 2016; Lankatillake et al, 2019). It comprises two extracellular α-subunits and two transmembrane β-subunits connected through disulphide bonds to form a functional receptor that exists as an α2β2 dimer/heterotetrameric complex (De Meyts, 2016; Lankatillake et al, 2019).

Binding of insulin to the ligand-binding site of the insulin receptor induces dimerisation and conformational changes in the insulin receptor (De Meyts, 2016; Lankatillake et al, 2019; Pelley, 2012). This results in the activation of the receptor tyrosine kinase domain, which leads to autophosphorylation of various tyrosine residues within the β-subunit, triggering the activation of signalling pathways that are responsible for both metabolic and mitogenic cellular responses **(Figure 1.7)** (De Meyts, 2016; Lankatillake et al, 2019; Pelley, 2012). The mitogenic actions of insulin are crucial even though it

is considered a mild growth factor (Draznin, 2011). Insulin promotes cell proliferation, cell division, and migration and inhibits cell death (apoptosis), collectively essential for cellular physiology (Draznin, 2011). Additionally, it modulates cellular responsiveness to other growth factors, including vascular endothelial growth factor, platelet-derived growth factor, and epidermal growth factor, promoting their actions (Draznin, 2011).

In the presence of ligand (e.g. insulin) bound to the extracellular domain of the insulin receptor, dimerisation and conformational changes in the insulin receptor take place (Pelley, 2012). These changes activate the tyrosine kinase domain of the insulin receptor, leading to autophosphorylation of specific tyrosine residues (Tyr-1146, Tyr-1150, and Tyr-1151) within the β-subunit (De Meyts, 2016; Lankatillake et al, 2019; Pelley, 2012). These phosphorylated residues act as a binding site and facilitate the recruitment of adaptor proteins containing Src-homology (SH2) domains and phosphotyrosine-binding domain (PTB) domains that are also phosphorylated, thus initiating insulin signalling responsible for both metabolic and mitogenic cellular responses by two main pathways (De Meyts, 2016; Pelley, 2012).

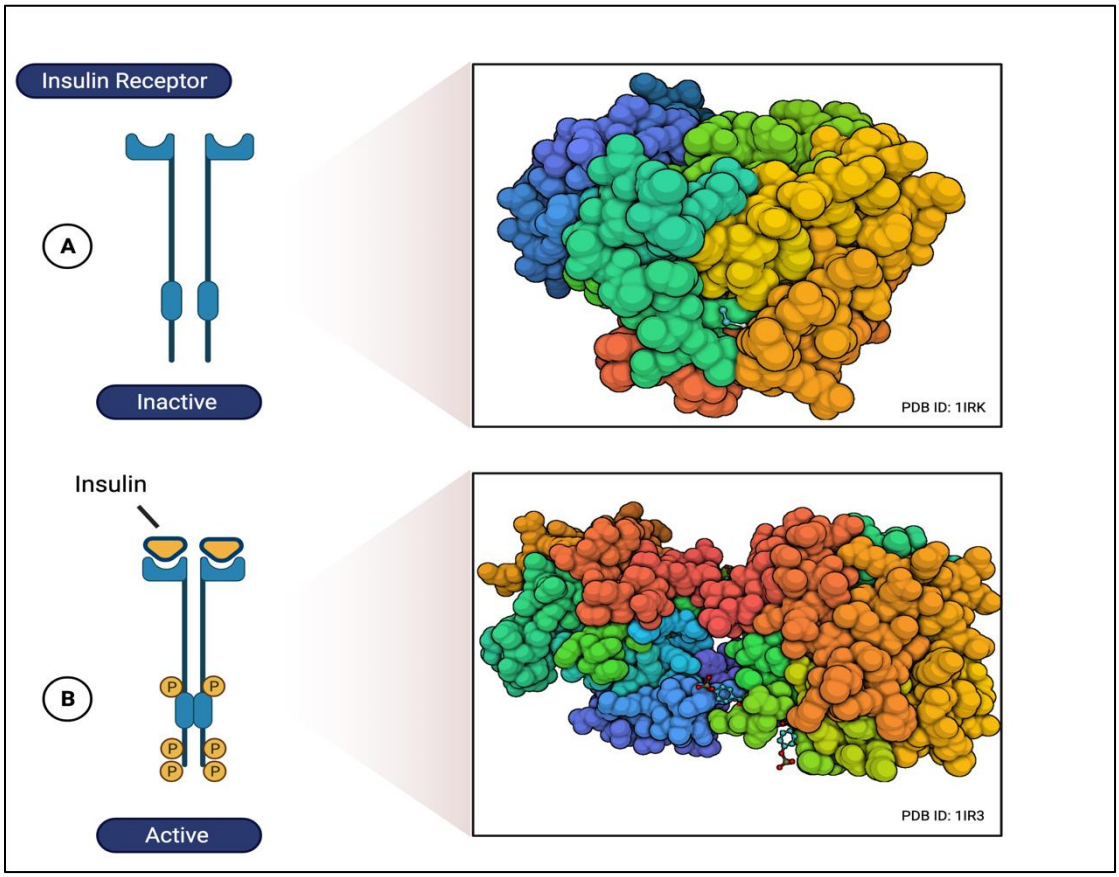

Figure 1.7 Schematic drawing along with the X-ray structures of the tyrosine kinase domain of the human insulin receptor. (A) represents the 3D crystal structure of the inactive insulin receptor tyrosine kinase domain (PDB ID: 1IRK). (B) illustrates the active form following insulin engagement (PDB ID: 1IR3). The representation of the crystal structure is showing the seven structural units or domains of the insulin receptor. Domains are coloured: large domains (L domains), L1 and L2, are coloured in orange and yellow, respectively, and separated by a cysteine-rich rod-like structure (labelled in green), termed as the cysteine-rich region. L2 is followed by three tandem fibronectin type III (FnIII) domains, FnIII-1, 2, and 3 domains coloured in pink, cyan, and light blue, respectively, collectively acting as structural spacers to arrange other domains in space. Following the FnIII domains is the tyrosine kinase domain (blue), the binding pocket of insulin. Adopted from (PDB ID: 1IRK; Hubbard et al, 1994) and (PDB ID: 1IR3; Hubbard, 1997).

The two main intracellular insulin receptor signal transduction networks are Ras-dependent and Ras-independent pathways (Boucher et al, 2014; De Meyts, 2016; Pelley, 2012; Świderska et al, 2018). Ras proteins belong to a large family of small molecular weight guanosine triphosphate (GTP) binding proteins that play a role in regulating insulin cellular signalling pathways (De Meyts, 2016; Pelley, 2012). Upon insulin binding and RTK activation, insulin receptor substrate (IRS) proteins, which are a family of large docking proteins, become activated as a result of autophosphorylation and are phosphorylated upon binding to the phosphotyrosine residue through a PTB domain (De Meyts, 2016; Pelley, 2012). The insulin receptor, unlike other RTK

receptors, does not directly bind to signalling proteins, but rather attaches to IRS or the adapter Shc (Src-homology (SH2) domain-containing) to form a complex that aid in the recruitment of signalling proteins that are critically involved in the insulin signalling network (De Meyts, 2016; Pelley, 2012).

Both Ras-dependent and Ras-independent pathways arise from the insulin receptor-IRS node (De Meyts, 2016; Pelley, 2012). The Ras-independent pathway, also known as the phosphatidylinositol 3-kinase (PI3K, a lipid kinase)/AKT (PKB or protein kinase B) pathway, is linked only through IRS and is responsible for the metabolic effects of insulin (Boucher et al, 2014; De Meyts, 2016; Pelley, 2012; Świderska et al, 2018). The Ras-dependent pathway arises from both IRS and Shc and is implicated in the regulation of cell proliferation, differentiation, and gene expression (Boucher et al, 2014; De Meyts, 2016; Pelley, 2012).

1.7 Insulin Actions

Insulin is a major anabolic hormone that promotes anabolism by channelling metabolism towards protein synthesis and carbohydrates and lipid storage (Lankatillake et al, 2019). Insulin exerts its metabolic actions in multiple body tissues and organs (Lankatillake et al, 2019). The main insulin action sites are the liver, muscles, and adipose tissue (Dimitriadis et al, 2011; Edgerton et al, 2017; Lankatillake et al, 2019). As previously mentioned, the primary sources of glucose to the human body include dietary intake of carbohydrates, breakdown of glycogen (glycogenolysis), which is the storage form of glucose in the liver and skeletal muscles into glucose, and through *de novo* synthesis of glucose from non-carbohydrate sources (gluconeogenesis) (Lankatillake et al, 2019).

Apart from carbohydrate intake and during short period fasting, the glucose level is replenished by the process of glycogenolysis (Edgerton et al, 2017). Even though glycogenolysis occurs in most tissues in the human body, the liver and kidneys are the only organs that express glucose-6-phosphatase, which is the enzyme needed for liberating glucose into the circulation (Lankatillake et al, 2019). However, after prolonged fasting, glycogen is depleted, and glucose is mainly produced by the liver through gluconeogenesis using non-hexose precursors (Lankatillake et al, 2019). Once glucose enters the cell, it is either stored in the form of glycogen or undergoes

glycolysis to yield pyruvate (Röder et al, 2016). The new pyruvate molecules can then be fed into the Krebs cycle if oxygen is present or reduced to lactate in the absence of oxygen (Röder et al, 2016).

At these stages of glucose production and metabolism, insulin exerts several metabolic actions to ensure glucose homeostasis (Röder et al, 2016). Since both glycogenolysis and gluconeogenesis occur mainly in the liver, insulin acts through direct and indirect mechanisms to limit hepatic glucose output (Edgerton et al, 2017). This includes direct inhibition of the glycogen phosphorylase enzyme, which catalyses the rate-limiting step in glycogenolysis and therefore suppresses the breakdown of glycogen into glucose (Edgerton et al, 2017). Furthermore, it suppresses gluconeogenesis through several pathways, including inhibiting gene expression of catalytic enzymes, glucose 6-phosphatase, and phosphoenolpyruvate carboxykinase, involved in the metabolic pathway of gluconeogenesis, limiting glucagon secretion, and changing autonomic neural input to the liver (Edgerton et al, 2017).

In terms of glucose utilisation, insulin improves glucose uptake into skeletal muscle and adipose tissues (Dimitriadis et al, 2011). Mechanistically, insulin stimulates the glucose transporter movement, GLUT4, from intracellular cytoplasmic vesicles onto the cell surface, thereby promoting glucose uptake by muscle and fat tissues (Dimitriadis et al, 2011). Moreover, insulin induces glucose disposal into cells by stimulating glycogen synthesis and increasing the rate of glycolysis in muscle and adipose tissue (Dimitriadis et al, 2011). The effects of insulin on glycogenesis are achieved by activating glycogen synthase and promoting glycogen synthesis in the liver, skeletal, and adipose tissue (Dimitriadis et al, 2011). Insulin increases the rate of glycolysis by potentiating the activity of hexokinase and 6-phosphofructokinase enzymes that are involved in the glycolytic pathway (Dimitriadis et al, 2011).

Besides insulin’s crucial role in carbohydrate metabolism, insulin also contributes considerably to lipid and protein metabolism (Lankatillake et al, 2019). In the feed state, once glucose levels are high, insulin promotes the synthesis and storage of triglycerides from glucose by providing glycerol 3-phosphate and nicotinamide adenine dinucleotide phosphate (NADPH) (Dimitriadis et al, 2011). Insulin stimulates a key enzyme presented on the vascular endothelial surface within muscle and adipose tissue called lipoprotein lipase, which hydrolyses circulating chylomicron

triglycerides in the bloodstream into fatty acids and glycerol (Dimitriadis et al, 2011). The liberated free fatty acids are then used as fuel for skeletal muscle or storage in adipose tissue (Dimitriadis et al, 2011). Noticeably, insulin actions on lipoprotein lipase enzyme are tissue-specific, through which it activates the adipose tissue lipoprotein lipase and inhibits the exact enzyme in skeletal muscle, causing the diversion of free fatty acids from skeletal muscle to adipose tissue (Dimitriadis et al, 2011). Another mechanism is the fact that insulin increases glucose uptake by adipose tissue in an insulin-dependent manner (Petersen & Shulman, 2018). This, in turn, increases glycolytic activity within fatty cells, resulting in elevated levels of glycerol-3-phosphate (Petersen & Shulman, 2018). The glycolytic end-product glycerol-3-phosphate will then act on the re-esterification of free fatty acids into triglycerides (Petersen & Shulman, 2018). Insulin effects on lipid metabolism are also extended to inhibit the lipolysis of storage triglycerides (Petersen & Shulman, 2018). Insulin inhibits lipolysis through phosphorylation and activation of phosphodiesterase-3B (PDE-3B) (Petersen & Shulman, 2018). PDE-3B catalyses the breakdown of cyclic adenosine monophosphate (cAMP) to its inactive form, which subsequently reduces PKA activation responsible for phosphorylating and activating the hormone-sensitive lipase, the key enzyme involved in the rate-limiting step in lipolysis (Petersen & Shulman, 2018). Insulin may also inhibit lipolysis via phosphorylation of protein phosphatase-1 (PP-1), which once triggered rapidly dephosphorylates and inactivates hormone-sensitive lipase, hence decreasing the rate of lipolysis (Petersen & Shulman, 2018).

In the case of protein metabolism, insulin also exerts anabolic effects on skeletal muscle (Vargas et al, 2020). Insulin stimulates the uptake of many amino acids into cells and increases the translation of messenger ribonucleic acid (mRNA) (Vargas et al, 2020). Also, insulin prevents the catabolism of proteins, which collectively leads to an increase in protein production (Dimitriadis et al, 2011; Vargas et al, 2020). Since insulin has an inhibitory action on gluconeogenesis, this effect contributes to preventing further utilisation of amino acids and thus conserves their availability for protein synthesis (Edgerton et al, 2017). Therefore, insulin promotes the synthesis and storage of proteins via direct and indirect actions (Dimitriadis et al, 2011; Vargas et al, 2020).

1.8 Insulin Resistance

Insulin resistance (IR) is generally defined as a decreased biological response to the normal concentration of endogenous and/or exogenous insulin (Boucher et al, 2014; Lankatillake et al, 2019). IR is a hallmark of T2DM; it may present for several years prior to the diagnosis of T2DM with the capability to progress during the course of the disease (Ciregia et al, 2017). In IR, there is a failure of insulin-sensitive cells to respond to normal concentrations of insulin, leading to an impairment in insulin biological actions (Boucher et al, 2014; Lankatillake et al, 2019). The primary defects in the effect of insulin mostly appear in skeletal muscle and adipose tissue, where a defect in GLUT4 translocation occurs, leading to a decrease in insulin-mediated glucose uptake (Chen et al, 2017). Consequently, and in response to IR, pancreatic β-cells increase their insulin production to maintain normoglycaemia, which further contributes to hyperinsulinemia (Chen et al, 2017). With chronic overstimulation of pancreatic β-cells as glucose levels rise, exhaustion and dysregulation results in β-cells, leading to a reduction in β-cell mass, insulin deficiency, and eventually glucose intolerance and diabetes (Boucher et al, 2014). The exact mechanism of IR is not entirely understood; nevertheless, numerous risk factors have been associated with its development (Lankatillake et al, 2019). Obesity, in the form of abdominal obesity and ectopic fat deposition (e.g., in muscles and the liver), has been highly implicated in the pathogenesis of IR (Boucher et al, 2014). It has been found that high levels of circulating free fatty acids initiate an inflammatory state and cause IR (Boucher et al, 2014; Ciregia et al, 2017). One explanation for the inflammatory state associated with obesity is that the secretory profile of adipocytokines, secretory proteins secreted by adipose tissue, changes during adipocyte lipolysis (Boucher et al, 2014; Ciregia et al, 2017). Numerous studies have reported increased production of adipocytokines, such as tumour necrosis factor (TNF)-α, or decreased release of protective adipocytokines, including adiponectin in obese patients, which collectively are thought to mediate the effects of obesity in the pathogenesis of insulin resistance (Boucher et al, 2014; Ciregia et al, 2017). Moreover, excess fat deposition in muscles or the liver, due to relative deficiency of adipose tissue storage space in the usual fat depot sites, reduces insulin sensitivity, and disrupts insulin signalling (Boucher et al, 2014; Chen et al, 2017; Ciregia et al, 2017). Circulating free fatty acids, in particular, high levels of palmitatic acid and arachidonic acid, in addition to adipocytokine tumour necrosis factor (TNF)-

α, may increase serine phosphorylation of IRS proteins, thereby reducing IRS1-associated PI3K activity, resulting in impairment in the regulation of GLUT4 and IR (**Figure 1.8)** (Boucher et al, 2014; Chen et al, 2017; Ciregia et al, 2017).

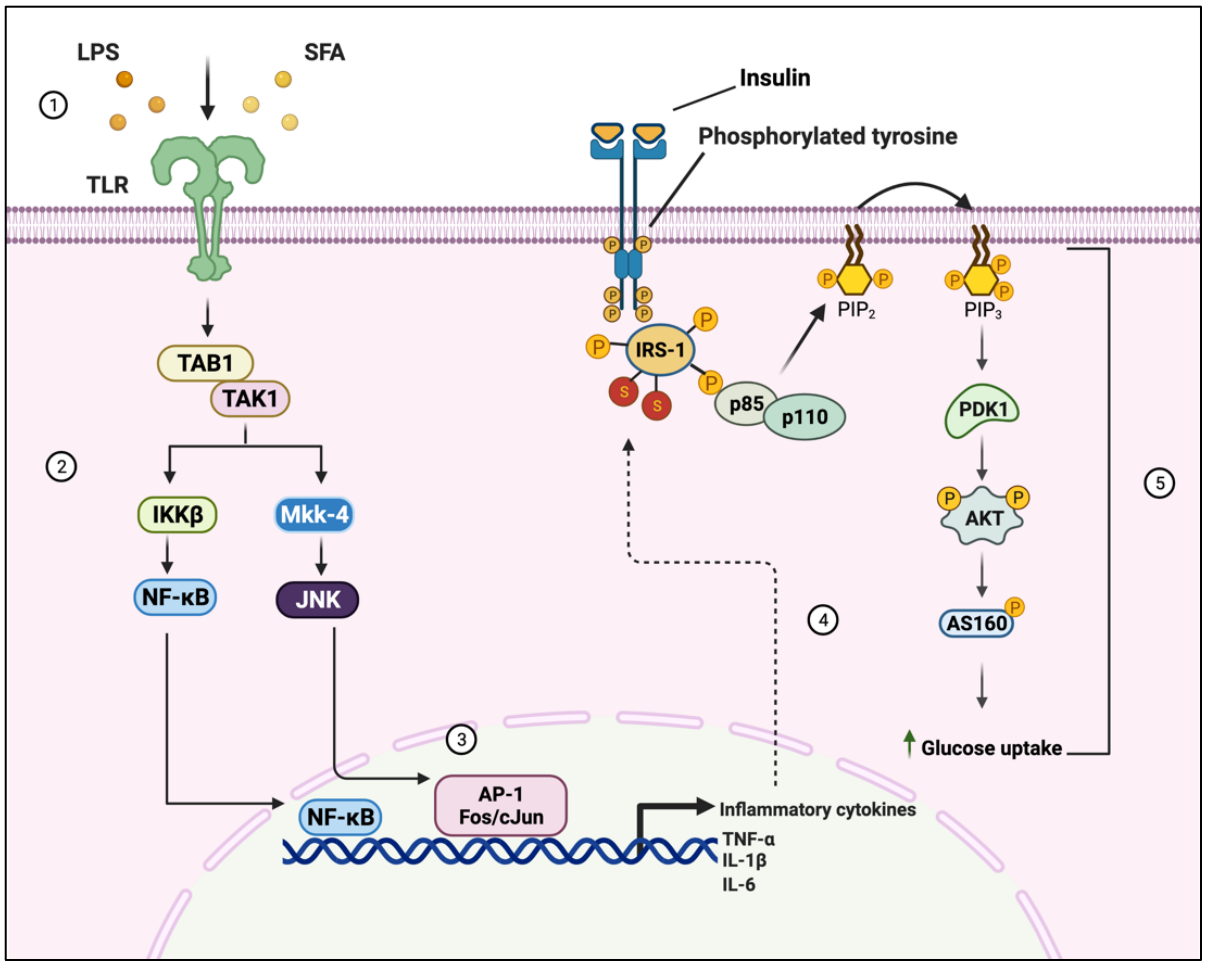

Figure 1.8 Fatty acids-induced insulin resistance. The activation of TLRs by its ligands (SFA or LPS) causes the assembly of TAK1 kinase with TAB1, TAK1-TAB1 complex (1), which promotes the activation of JNK and IKKβ (2). This subsequently activates transcriptional genes (e.g., NF-κB and AP-1), which are responsible for upregulating the transcription of inflammatory genes (TNF-α, IL-1β, IL-6) (3). These inflammatory genes increase serine phosphorylation of IRS proteins (4), thereby reducing IRS1-associated PI3K activity, resulting in impairment of the regulation of GLUT4 and IR (5). LPS: lipopolysaccharides; SFA: saturated fatty acid; TLR: toll-like receptors; TAK1: transforming growth factor β-activated kinase 1; TAB1: transforming growth factor β-activated protein kinase 1-binding protein 1-β; NF-κB: nuclear factor kappa B; JNK: c-JUN amino-terminal kinase; IKKβ: inhibitor of nuclear factor kappa B kinase subunit β; Ap-1: activator protein 1; IRS: insulin receptor substrate; TNF-α; tumour necrosis factor α; IL-1β: interleukin 1β; IL-6: interleukin 6; Akt: protein kinase B; PDK1: phosphoinositide-dependent protein kinase 1; PIP2: phosphatidylinositol-4,5-biphosphate; PI3K: phosphatidylinositol kinase 3; PIP3: phosphatidylinositol-3,4,5-triphosphate; PKC: protein kinase C. Adopted from (Boucher et al, 2014; Chen et al, 2017; Ciregia et al, 2017).

1.9 Pharmacological Therapies Used for T2DM

Within the last 20 years, the therapeutic management of T2DM has undergone some major revisions due to advancements in evidence-based diabetes care (Schernthaner et al, 2010; Syed et al, 2019). The ultimate aim in the management of diabetes is to maintain good glycaemic control that aids in preventing or delaying the onset and progression of diabetes-related complications (Syed et al, 2019). The cornerstones of diabetes management involve lifestyle interventions, concomitant with pharmacological treatments and self-monitoring of blood glucose (Chaudhury et al, 2017). Owing to the progressive nature of T2DM, a stepwise approach is predominantly adopted in clinical practice, through which diet regulation and exercise can be initially recommended (Chaudhury et al, 2017; Schernthaner et al, 2010; Syed et al, 2019). However, if blood glucose levels remain high and inadequately controlled even with the employment of these measures, anti-diabetic medications are warranted (Chaudhury et al, 2017; Schernthaner et al, 2010; Syed et al, 2019).

Currently, several medications are available for the management of T2DM. The major pharmacological classes include biguanides, sulfonylureas, meglitinides, thiazolidinediones (TZDs), dipeptidyl peptidase 4 inhibitors (DPP-4 inhibitors or gliptins), sodium-glucose cotransporter 2 (SGLT2) inhibitors, α-glucosidase inhibitors and glucagon-like peptide-1 receptor agonists (GLP-1 agonists) (Chaudhury et al, 2017). Anti-diabetic medications lower glucose levels through one or more of the following mechanisms: (i) increase insulin availability by promoting insulin secretion from pancreatic β-cells; (ii) improve glucose uptake in peripheral tissues; (iii) delay the absorption of carbohydrates; (iv) increase satiety and regulate gastric emptying; (v) induce glucosuria; (vi) decrease hepatic glucose production; and (vii) suppress glucagon production from pancreatic α-cells (Chaudhury et al, 2017; Schernthaner et al, 2010; Syed et al, 2019). The following subsections offer a brief overview of the major pharmacological classes used in the management of T2DM.

1.9.1 Insulin Sensitisers

Biguanides and TZDs are the two pharmacological classes that work primarily in enhancing insulin actions (Syed et al, 2019). These classes lower blood glucose levels by boosting insulin-sensitive cell response to insulin without promoting insulin

secretion from the pancreatic β-cells (Syed et al, 2019). A brief overview of each class is given below.

1.9.1.1 Biguanides

The only biguanide that is currently available and approved by the Food and Drug Administration (FDA) and the Medicines and Healthcare products Regulatory Agency (MHRA) is metformin (ADA, 2023). Metformin is the most commonly prescribed anti-diabetic medication and considered as the first-line agent in the management of T2DM (Zhou et al, 2018). Metformin is highly efficient in reducing both fast and postprandial glucose levels by exerting collective action on multiple target sites (Zhou et al, 2018). It suppresses the hepatic glucose output largely by inhibiting hepatic gluconeogenesis (Zhou et al, 2018). It also slows the intestinal absorption of glucose and improves insulin sensitivity by increasing glucose uptake and utilisation in both the hepatic and peripheral muscle tissues (Zhou et al, 2018). Its molecular mechanisms remain debatable, but evidence has shown that metformin activates adenosine monophosphate (AMP) activated protein kinase (AMPA-PK), leading to an increase in hepatic glucose uptake and suppression of hepatic gluconeogenesis via complex interactions with mitochondrial enzymes **(Figure 1.9)** (Chaudhury et al, 2017).

In addition, it sensitises peripheral tissues to insulin by activating the insulin receptor expression and tyrosine kinase activity (Chaudhury et al, 2017). Apart from its well-characterised anti-diabetic properties, metformin also lowers plasma very-low-density lipoprotein triglyceride (TG) levels by acting on the peroxisome proliferator-activated receptor alpha (PPAR-α) pathway, thereby preventing CVDs (Chaudhury et al, 2017). Potential CVD benefits were shown in the United Kingdom Prospective Diabetes Study (UKPDS) trial in which patients who were receiving metformin exhibited decreased risk of myocardial infarction and coronary death by 39% and 50%, respectively, compared to other therapies (Holman et al, 2008).

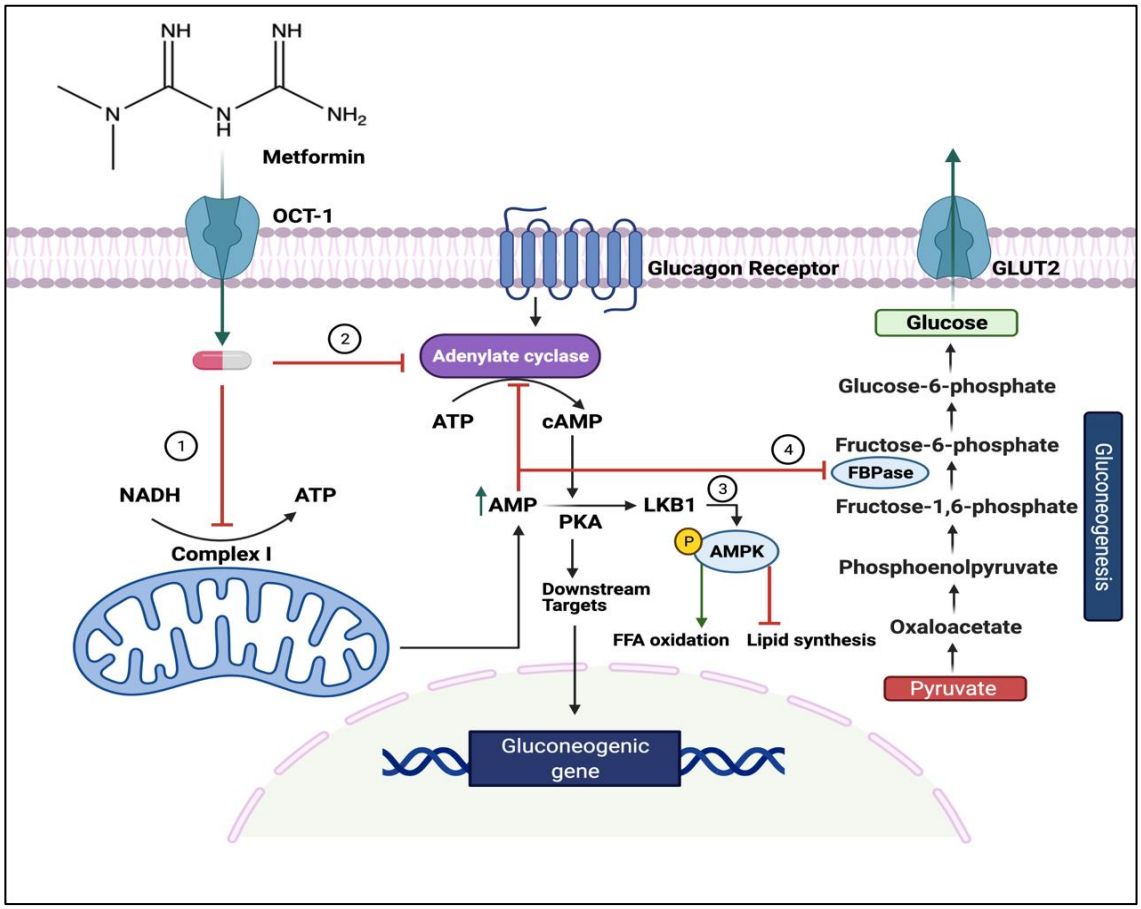

Figure 1.9 Potential molecular mechanisms of the blood glucose-lowering effect of metformin. Multiple pathways have been proposed under the inhibitory action of metformin on hepatic gluconeogenesis. Following the hepatic uptake of metformin through organic cation transporter 1 (OCT1), metformin inhibits mitochondrial complex 1, thereby reducing the ATP/AMP ratio and activating the AMP-activated protein kinase (AMPK) system (1). Based on *in-vivo* studies, metformin inhibits adenylate cyclase, reducing cyclic AMP levels and protein kinase A (PKA) activity, antagonising the glucagon on hepatocytes (2). Another potential mechanism is through the serine-threonine liver kinase B1 (LKB1)-dependent activation of the AMPK pathway, which is believed to exert indirect action on hepatic insulin sensitivity via its effects on lipid metabolism (3). Metformin reduces hepatic glucose output by lowering the level of fructose 1,6-bisphosphatase (FBPase), a key enzyme involved in hepatic gluconeogenesis (4). ATP: adenosine triphosphate; AMP: adenosine monophosphate; MAPK: AMP-activated protein kinase; GLUT2: glucose transporter 2. Adopted from (Chaudhury et al, 2017).

1.9.1.2 Thiazolidinediones

Pioglitazone and rosiglitazone are the only two drugs under the TZD class that are accessible in the market (**Figure 1.10)** (Syed et al, 2019). They constitute potent and selective ligands of PPAR-γ that modulate the expression of the genes involved in lipid and glucose metabolism, insulin signalling pathway and adipocyte tissue differentiation (**Figure 1.11)** (Syed et al, 2019). This ligand-receptor activation leads

to an augmentation in glucose uptake in the adipose and skeletal tissues, as well as a depletion in plasma fatty acids, which collectively result in the decrease of the HbA1c level (Chaudhury et al, 2017). Regarding the beneficial effects of TZDs on lipid metabolism, a review of six randomised trials revealed an increase in high-density lipoprotein (HDL) cholesterol levels by 10% with both drugs and a decrease in TG levels at a greater extent following pioglitazone administration rather than rosiglitazone (Yki-Järvinen, 2004). Additionally, a meta-analysis comprising 19 trials of pioglitazone for the management of T2DM noted a reduction in atherosclerotic cardiovascular events in the pioglitazone group, suggesting the potential CVD benefits of pioglitazone usage (Lincoff et al, 2007). Moreover, in patients with T2DM and biopsy-proven non-alcoholic steatohepatitis (NASH), pioglitazone shows a beneficial impact on liver histology; it improves fibrosis, inflammation and steatosis (ADA, 2023).

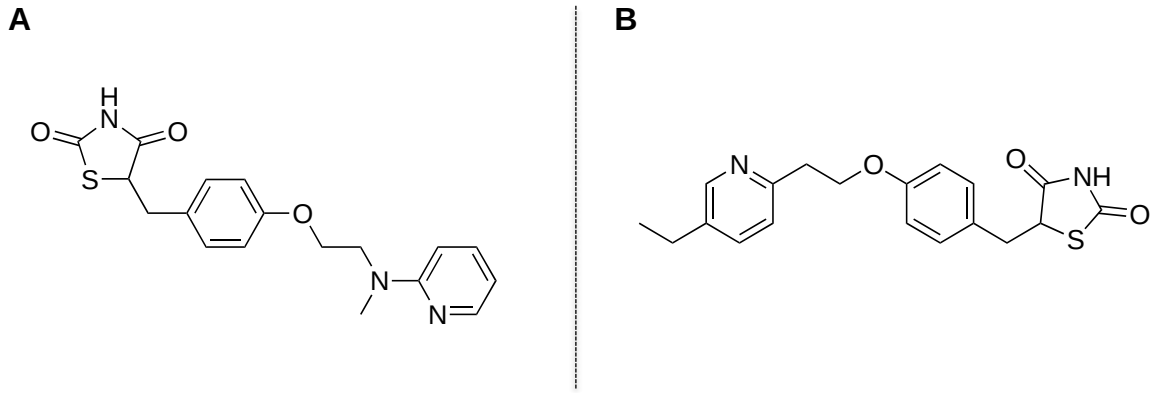

Figure 1.10 Chemical structures of thiazolidinedione agents: rosiglitazone (A) and pioglitazone (B).

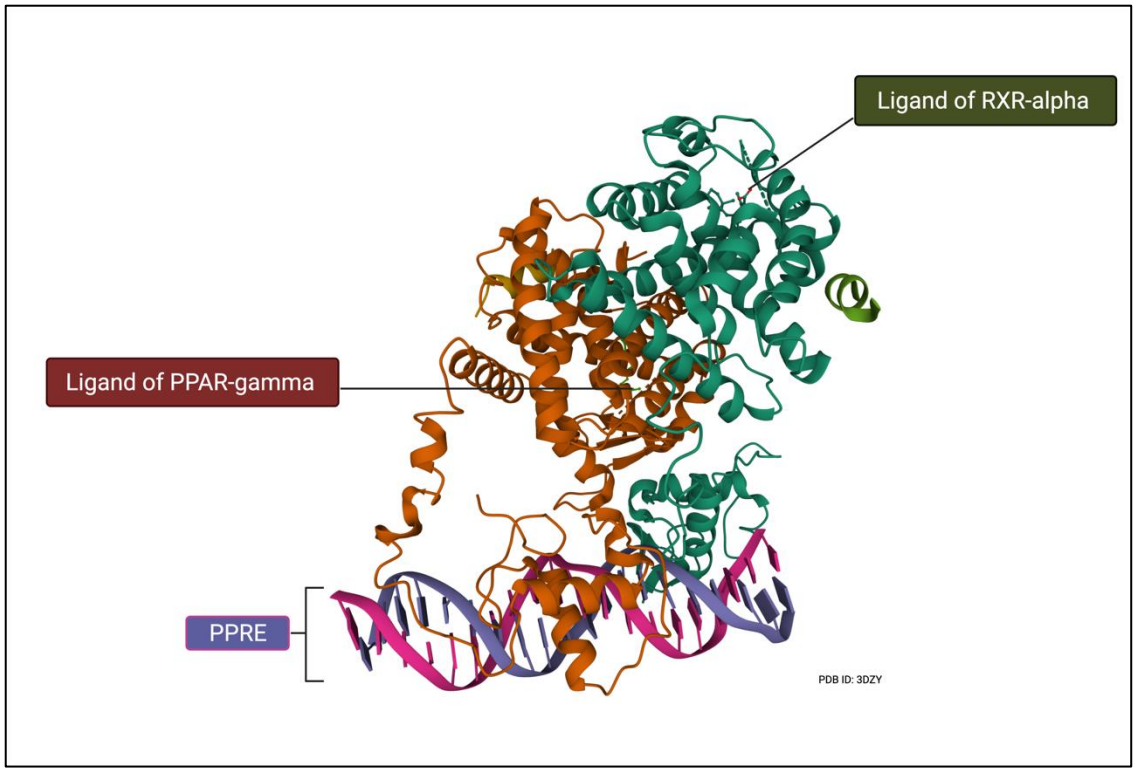

Figure 1.11 X-ray 3D structure of the PPAR-γ–RXR-α complex on PPRE (PDB ID: 3DZY). Upon binding of activating ligands (TZDs) to PPAR-γ receptor, an obligate heterodimerisation between PPAR-γ and human retinoid X receptor-alpha (RXR-α) is formed. This complex recognises and binds to a specific DNA consensus sequence, termed PPRE, located at the promoter regions of several genes involved in glucose and lipid metabolism. The PPAR-γ receptor is represented in orange and RXR-α in green. The ligands of PPAR-γ and RXR-α receptors–rosliglitazone and 9-cis-retinoic acid–are indicated with brown and green labels, respectively. PPAR-γ: human peroxisome proliferator-activated receptor-gamma; PPRE: peroxisome proliferator response element; TZDs: thiazolidinediones. Adopted from (PDB ID: 3DZY; Chandra et al, 2008).

1.9.2 Insulin Secretagogues

Sulfonylureas and meglitinides are two pharmacological classes that are classified as insulin secretagogues because they primarily lower glucose levels by promoting insulin release from the pancreatic β-cells (Schernthaner et al, 2010; Syed et al, 2019).

1.9.2.1 Sulfonylureas

Sulfonylureas induce insulin secretion by blocking the ATP-dependent potassium channels, leading to membrane depolarisation and calcium influx that cause insulin release from secretory granules in a non-glucose dependent manner (**Figure 1.12)** (Schernthaner et al, 2010; Syed et al, 2019).

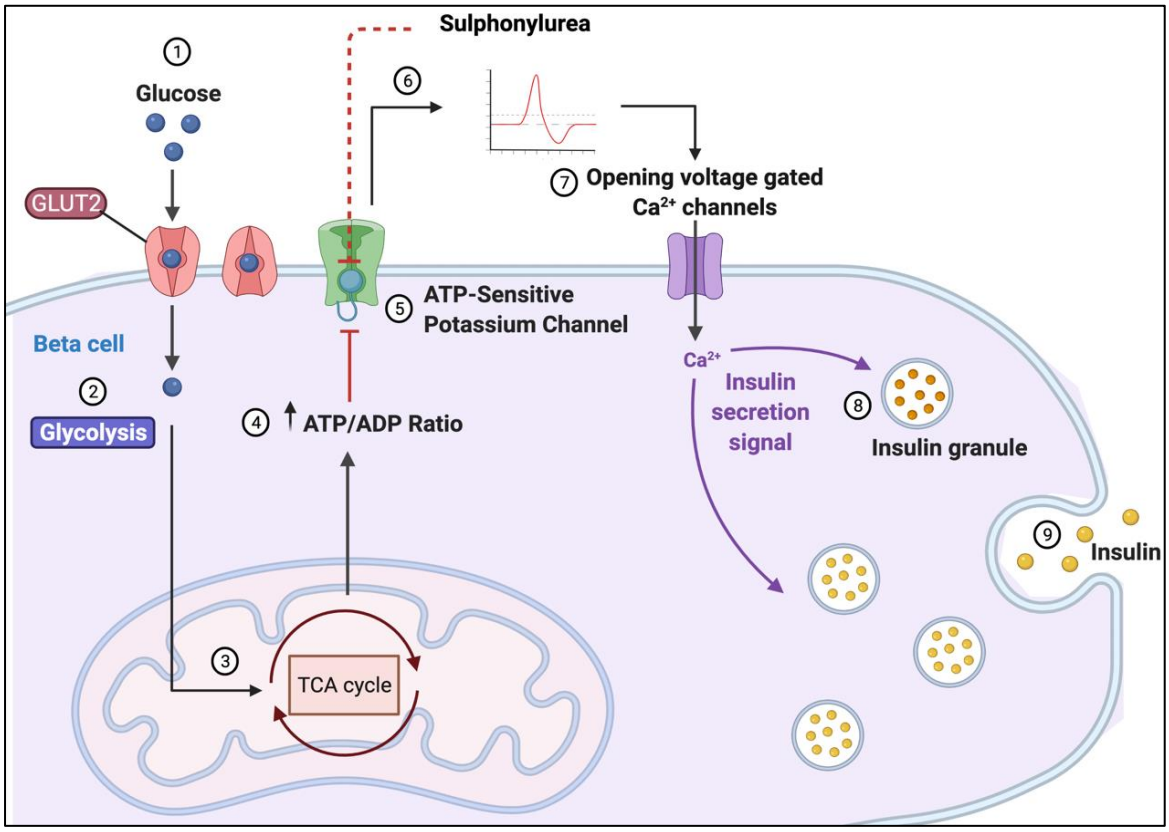

Figure 1.12 Sulfonylurea's mechanism of action. Upon its entrance into cells via the GLUT2 transporter (1), glucose undergoes glycolysis (2), leading to increased production of ATP molecules (3) and subsequently a high ATP/ADP ratio (4). The binding of sulfonylurea to the sulfonylurea subunit of the ATP-sensitive K^+ channel reduces the efflux of K^+ ions across the cell membrane and leads to the closure of the channel (5). This, in turn, causes membrane depolarisation (6) and triggers the opening of voltage-sensitive calcium channels (7). Increased calcium influx causes the release of preformed insulin from insulin-containing secretory granules (8) into the blood circulation (9). ATP: adenosine triphosphate; ADP: adenosine diphosphate; GLUT2: glucose transporter 2. Adopted from (Schernthaner et al, 2010; Syed et al, 2019).

Sulfonylureas also cause a reduction in hepatic glucose output and improve insulin sensitivity at peripheral target sites (Schernthaner et al, 2010; Syed et al, 2019). Sulfonylureas are generally divided into first-and second-generation agents (Chaudhury et al, 2017). The first-generation agents include chlorpropamide, tolazamide and tolbutamide, while the second-generation agents are glipizide,

glimepiride and glyburide (Chaudhury et al, 2017). Both generations are equally effective when administered at equivalent doses. Nevertheless, second-generation sulfonylureas are more commonly used than first-generation, as they are more potent than first-generation agents, and subsequently lower doses are needed to meet glycaemic control (**Figure 1.13)** (Chaudhury et al, 2017).

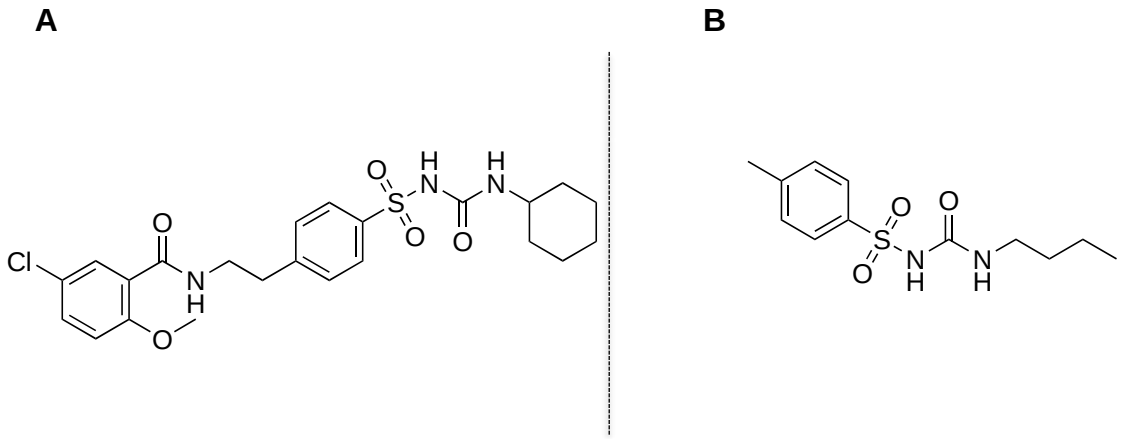

Figure 1.13 Chemical structures of second-and first-generation sulfonylureas: glyburide (A) and tolbutamide (B).

1.9.2.2 Meglitinides

Meglitinides, also known as non-sulfonylurea secretagogues, act in a similar manner to sulfonylureas, but with shorter duration of activity and more rapid onset of action (Schernthaner et al, 2010; Syed et al, 2019). Two agents that are currently available, namely, repaglinide and nateglinide, are shown to be primarily effective in reducing postprandial glucose levels (**Figure 1.14)** (Schernthaner et al, 2010; Syed et al, 2019).

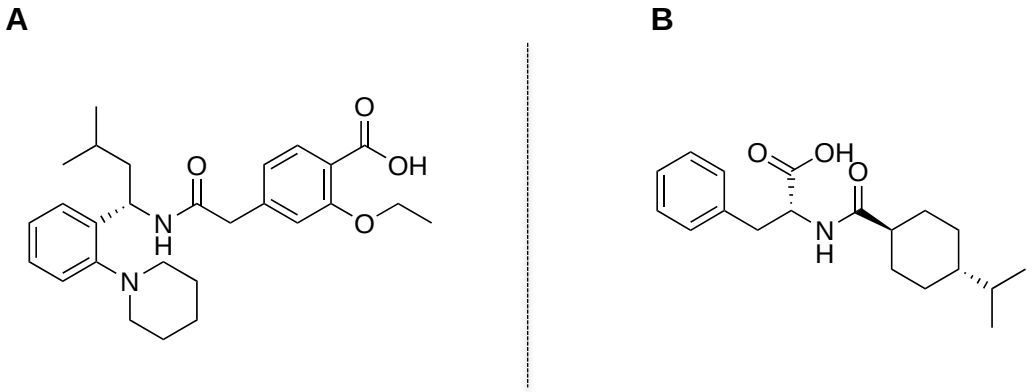

Figure 1.14 Chemical structures of meglitinides: repaglinide (A) and nateglinide (B).

1.9.3 Incretin Mimetics

Glucagon-like peptide 1 (GLP-1)-based therapies (e.g., GLP-1 receptor agonists, DPP-4 inhibitors) affect blood glucose levels mainly by targeting the incretin system (Lankatillake et al, 2019). This is achieved through the restoration of GLP-1 and glucose-dependent insulinotropic polypeptide (GIP) activities that are responsible for mediating several effects, including potentiating glucose-mediated insulin secretion, delaying gastric emptying and reduction of postprandial glucagon release (Lankatillake et al, 2019).

1.9.3.1 DPP-4 Inhibitors

DPP-4 inhibitors, including sitagliptin, saxagliptin, vildagliptin, linagliptin, teneligliptin and alogliptin, constitute an anti-diabetic class that is often used as an add-on treatment for adults with T2DM (**Figure 1.15)** (ADA, 2023).

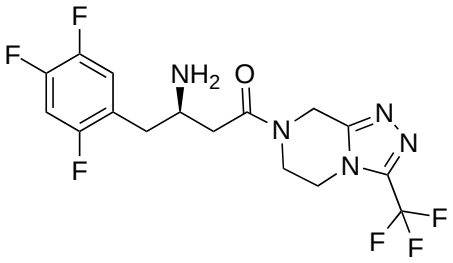

Figure 1.15 Chemical structure of sitagliptin.

They exert a blood glucose level-lowering effect chiefly on postprandial levels and act by inhibiting DPP-4, the enzyme responsible for degrading the hormone incretin, such as GLP-1 and GIP (Syed et al, 2019).Consequently, incretin levels are increased, which increases insulin secretion, limits glucagon release, decreases gastric emptying and promotes satiety (**Figure 1.16)** (Syed et al, 2019). Apart from their anti-diabetic characteristics, DPP-4 inhibitors have no additional benefits on CVD mortality, all-cause mortality or chronic kidney disease progression (ADA, 2023).

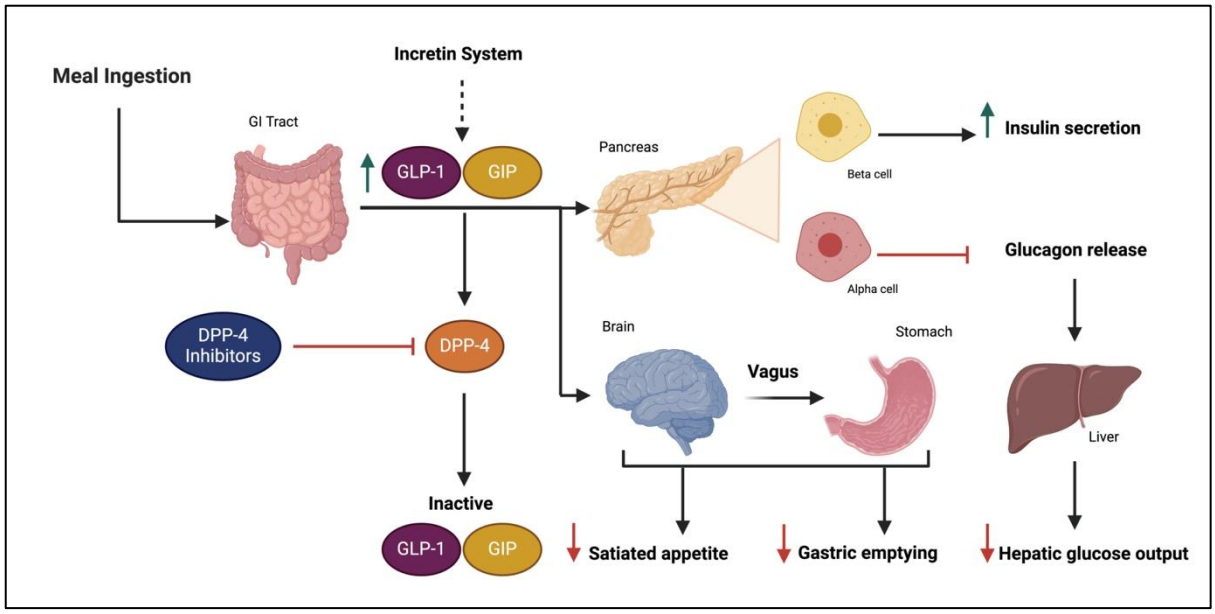

Figure 1.16 Mechanism of action of incretin mimetics and DPP-4 inhibitors. Under normal physiological conditions, incretin peptide hormones GLP-1 and GIP are released from enteroendocrine cells into the circulation in response to food ingestion. These hormones are rapidly inactivated by the DPP-4 enzyme. The administration of DPP-4 (e.g., sitagliptin) inhibits the breakdown of incretin peptide hormones and therefore prolongs the incretin effects in diabetic patients. GLP-1 and GIP hormones exert multiple actions to maintain glucose homeostasis. They increase insulin release from pancreatic β-cells and limit glucagon release, thereby decreasing hepatic glucose production, prolonging gastric emptying, and promoting satiety. GIP: Glucose-dependent insulinotropic polypeptide; GLP-1: glucagon-like peptide-1; DPP-4: dipeptidyl peptidase-4. Adopted from (ADA, 2023).

1.9.3.2 GLP-1 Agonists

GLP-1 agonists albiglutide, dulaglutide, exenatide, liraglutide, semaglutide and lixisenatide are analogues of human GLP-1 hormones (**Figure 1.17)** (Chaudhury et al, 2017). They bring about glucose-dependent insulin release, suppress postprandial glucagon release, slow gastric emptying and boost β-cell growth/replication, as shown in **Figure 1.16** (Chaudhury et al, 2017). Given GLP-1 agonists' effects on gastric emptying, they have a beneficial impact on weight loss (ADA, 2023). Therefore, their use is highly recommended to patients diagnosed with T2DM, along with obesity and metabolic dysfunction (ADA, 2023).

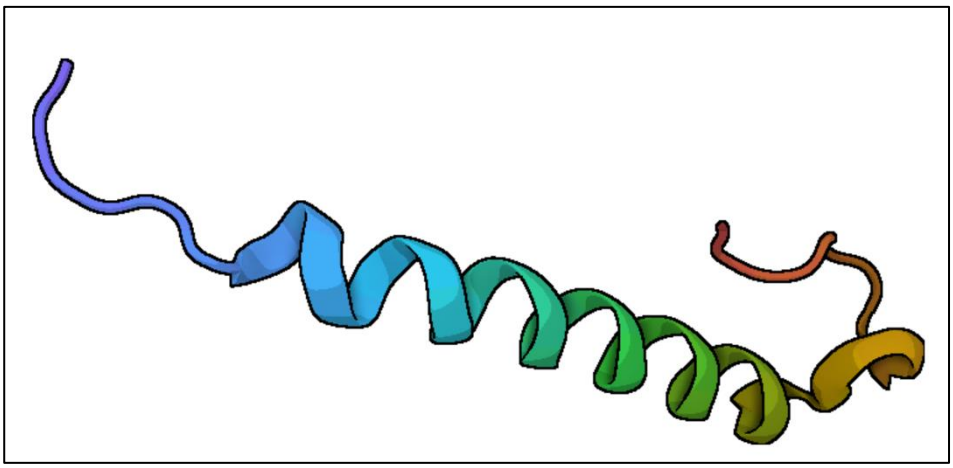

Figure 1.17 Nuclear magnetic resonance solution structure of exenatide (PDB ID: 1JRJ). Adopted from (PDB ID: 1JRJ; (Neidigh et al, 2001).

Furthermore, a reduction in CVD outcomes was observed in patients with T2DM and CVD who were treated with one of the following medications, i.e., liraglutide, semaglutide once weekly, dulaglutide and albiglutide, compared with the placebo group (Buse, 2016; Marso et al, 2016). Nevertheless, these favourable CVD outcomes were not reported in T2DM patients who experienced overt CVD and were administered oral semaglutide, extended-release exenatide or lixisenatide (Holman et al, 2017; Pfeffer MA et al, 2015). These differences in CVD outcomes among GLP-1 agonist agents could be attributed to the variation in the intrinsic characteristics of each agent (e.g., pharmacokinetics profile), the differences in the patients' demographics or the disparity in the study design.

GLP-1 agonists (liraglutide) have also shown their efficacy in improving renal events in diabetic kidney disease (Mann et al, 2017). In a liraglutide phase 3 trial, liraglutide lowered the incidence of new-onset macroalbuminuria and delayed the decline of glomerular filtration rate (GFR) in diabetic patients (Mann et al, 2017). Thus, it offers another potentially favourable outcome, in addition to its glycaemic, CVD and weight loss benefits.

1.9.4 SGLT2 Inhibitors

SGLT2 inhibitors represented by canagliflozin, dapagliflozin, empagliflozin and ertugliflozin are new glucosuric agents that have been recently approved for

monotherapy or in combination with other anti-diabetic agents in the management of T2DM (Syed et al, 2019). SGLT2 inhibitors block the sodium-glucose cotransporter 2 in the proximal renal tubules, the leading site of filtered glucose reabsorption, thereby reducing the reabsorption of filtered glucose and increasing the urinary excretion of glucose (**Figure 1.18)** (Chaudhury et al, 2017). Due to their glucose-independent mechanism, these medications can preserve their effectiveness at later stages of T2DM when the pancreatic β-cells are extremely exhausted (Syed et al, 2019).

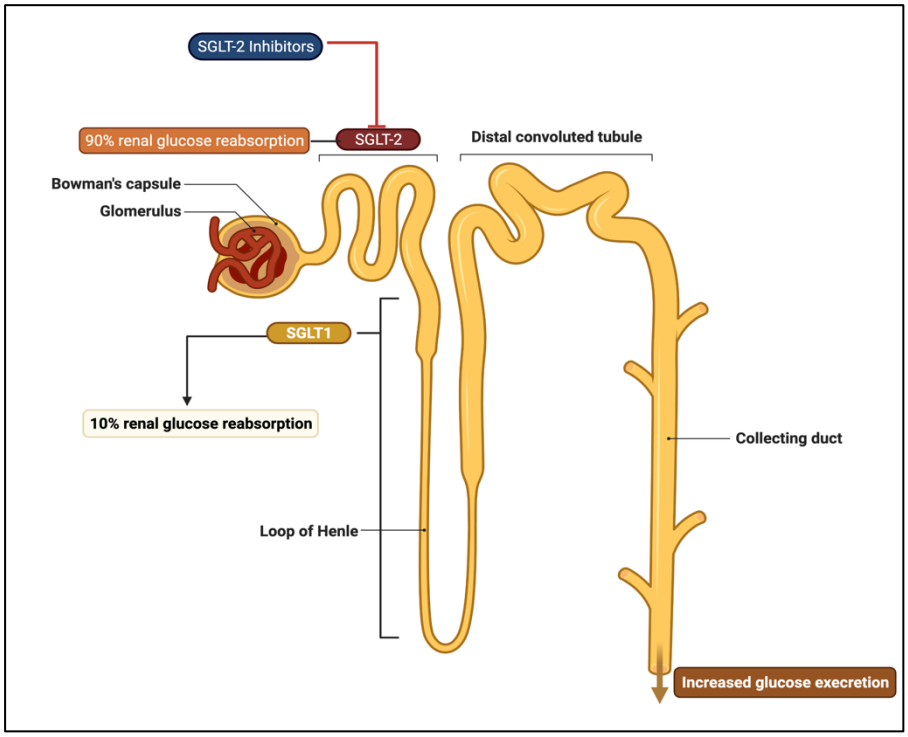

Figure 1.18 The primary mechanism of action of SGLT2 inhibitors. SGLT2, found in the proximal straight tubule of the nephron, is responsible for 90% of renal glucose reabsorption. Thereby, inhibition of SGLT2 with SGLT2 inhibitors (e.g., dapagliflozin) reduces glucose reabsorption and lowers the renal threshold for glucose. This, in turn, results in increased urinary excretion of glucose and consequently lowers plasma glucose levels. SGLT2: sodium-glucose cotransporter 2. Adopted from (Syed et al, 2019).

Previous studies have demonstrated the additional benefits of SGLT2 inhibitor usage, including weight loss and blood pressure reduction (ADA, 2023). Moreover, recent clinical trials have reported significant positive cardiovascular outcomes associated with SGLT2 inhibitors (Guthrie, 2018; Zinman et al, 2016). These include a decrease in atherosclerotic CVD (ASCVD) morbidity and mortality in patients with T2DM and established CVD (Guthrie, 2018; Zinman et al, 2016). Moreover, a reduction in HF hospitalisation has been observed with the use of SGLT2 inhibitors in people with and without prevalent HF or overt CVD at baseline (Zelniker et al, 2019). In addition to its

CVD beneficial effects, a meta-analysis of three major CVD outcome trials demonstrated kidney-related benefits in patients receiving SGLT2 inhibitors (Zelniker et al, 2019). In these trials, the results showed a reduction in the risk of end-stage kidney disease and worsening of kidney function in patients with overt ASCVD or with multiple risk factors for CVD (Zelniker et al, 2019).

1.9.5 α-Glucosidase Inhibitors

The α-glucosidase inhibitors (acarbose, miglitol, voglibose) are oral hypoglycaemic agents that exert their actions by reversibly inhibiting α-glucosidase enzymes in the brush border of the small intestine mucosa (**Figure 1.19)** (Schernthaner et al, 2010; Syed et al, 2019). These enzymes are responsible for the breakdown of complex polysaccharide carbohydrates into monosaccharides, subsequently slowing the absorption of carbohydrates and reducing the postprandial glucose levels (Schernthaner et al, 2010; Syed et al, 2019).

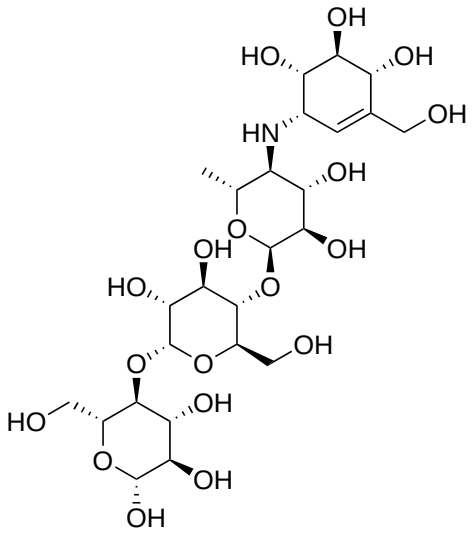

Figure 1.19 Chemical structure of acarbose.

1.9.6 Miscellaneous Hypoglycaemics

Bile acid sequestrants comprise another pharmacological class used for T2DM management (ADA, 2023). Colesevelam, primarily used for cholesterol management, is the only bile acid sequestrant agent approved by the FDA for use in T2DM (ADA, 2023). The hypoglycaemic property of colesevelam remains unknown, and it is only

approved as an adjunctive therapy, alongside lifestyle interventions and insulin or oral agents to improve glycaemic control (Chaudhury et al, 2017). Bromocriptine, a central-acting dopamine agonist, is also approved for T2DM treatment (ADA, 2023). Its mechanism of action is not yet clearly understood, but evidence has shown that improvement in insulin sensitivity sets in following a morning administration of bromocriptine (Chaudhury et al, 2017).

1.10 Drawbacks of Current Anti-Diabetic Agents

Despite the broad range of clinical benefits have been achieved by anti-diabetic drug design in the past decades, a number of drawbacks that may limit their use still exist. The most critical limitations associated with their usage are cost and drug toxicity (ADA, 2023; Schernthaner et al, 2010).

1.10.1 Cost of Anti-Diabetic Agents

According to the ADA 2023, the pharmacological classes GLP-1 agonists, DPP-4 inhibitors, SGLT-2 inhibitors and insulin analogues are classified as high-cost medications (ADA, 2023). Given that T2DM is progressive in nature, most patients need combination therapies with two or more anti-diabetic agents, especially with the classes mentioned above, for their additional benefits in bringing about positive glycaemic, metabolic and CVD outcomes (e.g., GLP-1 agonists). This poses a substantial economic burden on patients and healthcare systems.

1.10.2 Safety Concerns

Another concern that is corollary to the use of anti-diabetic agents is the range of adverse side-effects. Recently, the pharmacological classes used for T2DM have been expanded. As each class exerts a unique mechanism of action, diversity in toxicological profiles could consequently be induced by these anti-diabetic drugs that typically require follow-up assessment and treatment.

The following subsections set forth some adverse effects caused by anti-diabetic agents.

1.10.2.1 Gastrointestinal Side Effects

Metformin is one of the most tolerable anti-diabetic medications with a favourable safety profile (Zhou et al, 2018). Nevertheless, it may cause gastrointestinal (GI) disturbances, such as nausea and diarrhoea, in almost 28% of patients after initiation (Zhou et al, 2018). Other pharmacological classes that can cause GI side effects, which are mainly nausea and vomiting, include GLP-1 agonist agents (e.g., exenatide), bile acid sequestrants (e.g., colesevelam) and α-glucosidase inhibitors (e.g., acarbose, miglitol) (Schernthaner et al, 2010).

1.10.2.2 Skeletal Fracture Risk

TZDs (pioglitazone and rosiglitazone) decrease bone density and increase bone fracture risk more often in women (Yki-Järvinen, 2004). In the Diabetes Outcome Progression Trial (ADOPT), 4,351 participants (2,511 men and 1,840 women) were randomly allocated to three treatment groups (metformin, glyburide, and rosiglitazone), and the time to first skeletal fracture was assessed (Kahn et al, 2006). During the trial, 200 participants, divided into 89 men and 111 women, reported bone fractures: 93 patients were treated with rosiglitazone, 49 were assigned to the glyburide group, and 59 patients were exposed to metformin (Kahn et al, 2006). Thus, the fracture rate per 100 patient years in women was 2.7 for rosiglitazone, 1.5 for metformin, and 1.3 for glyburide, respectively (Kahn et al, 2006). In men, the fracture rates did not show any difference following the drugs' administration (1.2, 1.0, and 1.1, respectively) (Kahn et al, 2006). Similar to TZDs, the incidence of bone fractures was found to be high in patients on canagliflozin (Watts et al, 2016). In a randomised phase 3 study involving patients with T2DM, the bone fracture per 100 patient years was 1.4 for 100 mg and 1.5 for 300 mg canagliflozin, respectively, compared to 1.1 per 100 patient years in the placebo group (Watts et al, 2016).

1.10.2.3 Acute Pancreatitis

There have been post-marketing cases of acute pancreatitis in patients using incretin mimetics, such as exenatide and sitagliptin (Singh et al, 2013). To date, there are conflicting data regarding the association between incretin-based therapies and pancreatitis (Li et al, 2014; Singh et al, 2013). In a population-based matched case-control study using an extensive database in the US, 1269 hospitalised acute

pancreatitis cases were identified and matched with 1269 control subjects (Singh et al, 2013). The results showed an increased risk of hospitalisation due to acute pancreatitis in exenatide and sitagliptin patients (odds ratio [OR]: 2.07, 95% CI: 1.36-3.13) in comparison with non-users (Singh et al, 2013). In a systematic review and meta-analysis of 60 studies consisting of 55 randomised trials and five observational studies (total n = 353, 639), acute pancreatitis associated with the use of incretin-based therapy was investigated (Li et al, 2014). The findings revealed comparable results in the risk of pancreatitis in patients taking GLP-1-based treatments compared with metformin and glibenclamide (Li et al, 2014). Therefore, collectively, the risk of pancreatitis appears to be low, nevertheless not definitive, and further studies are needed to definitively establish the risk level.

1.10.2.4 Cancer

There is also concern about the increased risk of bladder cancer in patients undergoing pioglitazone therapy (Schernthaner et al, 2010; Yki-Järvinen, 2004). Data on the association between pioglitazone and bladder cancer are contradictory and uncertain, yet the use of pioglitazone is contraindicated in patients with active bladder cancer (ADA, 2023). Furthermore, based on *in-vivo* studies, the FDA has issued a black box warning regarding the increased risk of thyroid C-cell tumours in patients receiving GLP-1 agonists (Elashoff et al, 2011). To date, it remains unknown if this adverse effect also afflicts humans, so clinical studies are warranted for further investigation.

1.10.2.5 Fluid Retention/ Heart Failure

It is well recognised that all TZD medications have the potential of causing peripheral oedema and further worsening of HF (Spiller & Sawyer, 2006; Syed et al, 2019; Yki-Järvinen, 2004). Nonetheless, this adverse effect does not appear to affect HF mortality rates (Schernthaner et al, 2010). Furthermore, safety studies on saxagliptin have shown increased risk of HF hospitalisation in patients with pre-existing HF or renal impairment and during the first year of treatment compared to the placebo (ADA, 2023). As a result, ADA has spoken out against the use of saxagliptin in patients with HF (ADA, 2023).

1.10.2.6 Hypoglycaemia and Weight Changes

Iatrogenic hypoglycaemia is a serious adverse effect that is associated with insulin and insulin secretagogue medication usage (Wang et al, 2007). Various guidelines have recommended strict glycaemic control (HbA1c < 7%) as an approach to prevent the progression of T2DM regardless of the agents used and the patient's history of CVD (Kirkman et al, 2018). Subsequently, poor outcomes have been associated with tight control, including increased rate of all-cause and CVD-caused mortality, as well as severe hypoglycaemic events, in comparison with the conventional group (HbA1c = 7.5%) (Group, 2008). Although the exact cause of mortality is unknown, iatrogenic hypoglycaemia could be a possible explanation for those consequences, as it has been clinically proven to be associated with autonomic and neuroglycopenic complications that require urgent treatment (Bonaventura et al, 2015).

The effect of an anti-diabetic on body weight varies depending on the pharmacological class (Chaudhury et al, 2017). Weight loss is a favourable side effect induced by new anti-diabetic classes used for T2DM, as the majority of T2DM-diagnosed patients suffer from overweightness or obesity (Lankatillake et al, 2019). **Table 1.2** summarises the effects of each pharmacological class on body weight with their risk of hypoglycaemia.

Table 1.2 Hypoglycaemic risk and weight changes associated with anti-diabetic classes (ADA, 2023)**.**

Pharmacological Class	Risk of Hypoglycaemia	Weight Change
Biguanides	Low	Neutral
TZDs	Low	Weight Gain
Sulfonylureas	High	Weight Gain
Meglitinides	High	Weight Gain
GLP-1 agonists	Low	Weight Loss
DPP-4 inhibitors	Low	Neutral
SGLT2 inhibitors	Low	Weight Loss
α-Glucosidase inhibitors	Low	Weight Loss

Abbreviations: TZDs: thiazolidinediones; DPP-4: dipeptidyl peptidase 4; SGLT2: sodium-glucose cotransporter 2; GLP-1 agonists: glucagon-like peptide-1

1.10.2.7 Class/Medication-Specific Side Effects

According to safety studies and clinical reports, there are various side effects that are only observed in specific anti-diabetic classes; these effects are termed class-specific side effects. These side effects are often attributed to the class's unique pharmacological mode of action and correspondingly not observed with other classes. However, there are other side effects only shown in specific agents/ingredients within a pharmacological class. The following subsections discuss the side effects, which could be agent- or class specific.

1.10.2.7.1 Metformin

In extremely rare situations with estimated evidence of six cases per 100,000 person-years, metformin may cause lactic acidosis, especially in patients with pre-existing renal dysfunction (Zhou et al, 2018). Despite its low incidence, metformin-associated lactic acidosis remains a concern due to its high fatality rate (30 to 50%) (Zhou et al, 2018). Another potential issue associated with metformin use is the reduction in serum vitamin B12 and folic acid concentrations, which can cause megaloblastic anaemia (Zhou et al, 2018). Nonetheless, since the prevalence of vitamin B12 deficiency in metformin-treated patients has approached 20% over five years treatment; routine B12 monitoring is considered in elderly patients and those at risk for developing B12 deficiency because of low intake (e.g. vegan diet) or malabsorption issues (e.g. bariatric surgery) (Zhou et al, 2018).

1.10.2.7.2 DPP-4 Inhibitors

Several studies have reported severe forms of arthralgia and other musculoskeletal adverse effects, including myalgias, muscle weakness and muscle spasms, that are associated with the usage of DPP-4 inhibitors, such as sitagliptin, vildagliptin and saxagliptin (Schernthaner et al, 2010; Syed et al, 2019). Patients may develop these symptoms two days to five months after initiating DPP-4 inhibitors (Schernthaner et al, 2010; Syed et al, 2019). In many cases, these symptoms subsided within one month following discontinued use of the drug (Schernthaner et al, 2010; Syed et al, 2019).

1.10.2.7.3 SGLT2 Inhibitors

A meta-analysis of randomised controlled trials revealed higher incidence and risk of genitourinary tract infections among SGLT2 inhibitor recipients compared with those who were administered with placebo (Bailey et al, 2013; Bersoff-Matcha et al, 2019; Nyirjesy et al, 2012). Moreover, Fournier's gangrene is a new post-marketing safety concern associated with SGLT2 inhibitors (Bersoff-Matcha et al, 2019). Despite the rarity of its occurrence, it is a serious concern that warrants proper physician assessment of all patients on SGLT2 inhibitors presenting with fever, malaise or swelling from necrotizing fasciitis (Bersoff-Matcha et al, 2019). Furthermore, given their mechanism of actions, post-marketing cases of hypotension and acute kidney injury have been reported in some T2DM patients receiving SGLT2 inhibitors (Syed et al, 2019). In 2017, the FDA issued a black box warning on the increased risk of leg and foot amputations with the use of canagliflozin based on two large clinical trials (The Canagliflozin Cardiovascular Assessment Study (CANVAS) and The Canagliflozin Cardiovascular Assessment Study-Renal (CANVAS-R)) (Neal et al, 2013; Neal et al, 2017). However, in August 2020, the FDA withdrew this warning on account of new data derived from three clinical trials (Aschenbrenner, 2020). The latest data did not rule out the increased risk of amputation associated with canagliflozin, but found it to be lower than previously reported, especially when appropriately monitored (Aschenbrenner, 2020). Diabetic ketoacidosis is another safety concern that may arise from receiving SGLT2 inhibitors, particularly canagliflozin (Liu et al, 2020). A few cases have been documented in patients with T1DM and T2DM taking SGLT2 inhibitors (Liu et al, 2020). In light of the foregoing, the ADA recommends discontinuing the administration of SGLT2 inhibitors in patients with acidosis symptoms (e.g., nausea/vomiting, abdominal pain, generalised malaise) (ADA, 2023).

To sum up, the key evidence-based clinical data of current anti-diabetic agents are presented in **Table 1.3.**

Table 1.3 Key data of current pharmacological classes used for T2DM (ADA, 2023; Wajid et al, 2019).

Pharmacological Class	Mechanism of Action	HbA1c Reduction	Additional Benefits		Cost	Safety Concerns
			CV Effects	Renal Effects		
Biguanides	-Decrease hepatic gluconeogenesis and increase insulin sensitivity	1–2%	Potential ASCVD benefits	Neutral	Low	-GI (diarrhoea, abdominal pain) -Potential for B12 deficiency -Lactic acidosis
TZDs	-Increase insulin sensitivity	0.5–1.4%	Potential ASCVD benefits (Pioglitazone)	Neutral	Neutral	-Weight gain -Fluid retention -Congestive heart failure -Bone fractures
Sulfonylureas	-Enhance insulin secretion	1–2%	Neutral		Low	-Hypoglycaemia -Weight gain
Meglitinides	-Enhance insulin secretion	0.5–1.5%	Neutral		Low	-Hypoglycaemia -Weight gain
GLP-1 agonists	-Increase satiety, regulate gastric emptying, enhance insulin secretion and decrease glucagon release	0.5–1.5 %	ASCVD benefits	Reduce diabetic kidney disease progression (Liraglutide)	High	-GI (diarrhoea, abdominal pain) -Injection site reactions
DPP-4 inhibitors	-Increase endogenous GLP-1 levels	0.5–0.8%	Neutral		High	-Increased risk of infection -Headache -Arthralgia
SGLT2 inhibitors	-Induce glucosuria and prevent glucose reabsorption in the kidney's proximal tubule	0.3–1%	Both ASCVD and HF benefits	Reduce diabetic kidney disease progression	High	-Genitourinary infection -Hypovolemia -Renal insufficiency -Hypotension -Diabetic ketoacidosis
α-Glucosidase inhibitors	-Slow the absorption of carbohydrates	0.5–0.8%	Neutral		Mod.	-GI (flatulence, diarrhoea)

Abbreviations: TZDs: thiazolidinediones; DPP-4: dipeptidyl peptidase 4; SGLT2: sodium-glucose cotransporter 2; GLP-1 agonists: glucagon-like peptide-1

1.11 Toxicological Approaches for Side-Effect Exploration

With the unprecedented rise in the global prevalence of diabetes mellitus and its complications, optimising anti-diabetic agents' safety profile is urgently needed. The principal objective in managing diabetes and its related complications is maintaining adequate glycaemic control, which is primarily premised on the patient's medication adherence (Denicolo et al, 2021). Approximately 45% of diabetic patients fail to achieve their target HbA1c control (<7%) chiefly due to poor adherence (Currie et al, 2012). Non-adherence is a serious health concern that is subsequently associated with a higher incidence of diabetes-related complications, fatality rates and economic burden on the health care system (Denicolo et al, 2021). In the UK, among 15,984 participants treated with anti-diabetic agents, poor medication adherence was reported and independently associated with a significant 1.6-fold increase in all-cause deaths (Currie et al, 2012). Multiple factors are associated with anti-diabetic agent non-adherence. However, one of the significant determinants of poor adherence constitutes the adverse effects of medication (Denicolo et al, 2021).

In diabetes research, majority of the side effects summarised in **Table 1.3** are poorly characterised. In fact, the pathomechanisms underlying these adverse effects are still poorly defined, and there is a dearth of mechanistic studies addressing these issues. While most existing mechanistic studies have focused on elucidating the side effects of the prototype anti-diabetic drug metformin, particularly GI intolerance, these investigations have yielded valuable insights (Akhter & Uppal, 2020; DeFronzo et al, 2016; Piel et al, 2015; Thomas & Gregg, 2017). Studies suggest a direct effect of metformin on the gut mucosa, with jejunal concentrations reaching up to 300 times plasma levels (Thomas & Gregg, 2017). Additionally, research has explored the mechanisms underlying the rare side effect of lactic acidosis, revealing metformin's direct action on mitochondria, altering the balance between coupled and uncoupled reactions (DeFronzo et al, 2016; Piel et al, 2015). Specifically, metformin uptake via organic cation transporters followed by its targeting of mitochondria leads to inhibition of complex I respiration, increased uncoupled respiration, a slowdown of the tricarboxylic acid cycle, and ultimately, increased lactic acid formation (DeFronzo et al, 2016; Piel et al, 2015). This latter effect can potentially lead to lactic acidosis at high metformin concentrations (DeFronzo et al, 2016; Piel et al, 2015). Furthermore, investigations into the potential impact of SGLT2 inhibitors on renal function were conducted due to the mechanism of action of this drug class relying heavily on kidney

function. While some speculate on potential adverse events or even renoprotective benefits, initial studies suggest a transient decrease in GFR associated with SGLT2 inhibition (Minze et al, 2018). This decrease has been suggested to occur due to increased sodium delivery to the macula densa (Akhter & Uppal, 2020). This, in turn, leads to an increase in adenosine release, resulting in vasoconstriction of the afferent arteriole and subsequent reduction in renal plasma flow and GFR (Akhter & Uppal, 2020). Lastly, few proposed mechanisms attempt to explain the joint pain associated with DPP-4 inhibitors (Drucker, 2007; Mascolo et al, 2016). One possibility suggests these drugs may elevate levels of cytokines, chemokines, and matrix metalloproteinases, all of which can contribute to pain (Drucker, 2007; Mascolo et al, 2016). However, the exact mechanism underlying this side effect remains elusive. Therefore, further toxicological studies are warranted to unveil these mechanisms and give rise to the proposition of preventive and therapeutic strategies that could improve patient safety and, ultimately, medication adherence. Currently, several toxicological approaches are available to evaluate and predict drug safety endpoints (Jennings, 2015). These include *in vivo* testing, *in vitro* models, *in silico* and omics-based approaches (Jennings, 2015; Lankatillake et al, 2019).

1.11.1 *In Vivo* Toxicity Testing

In vivo animal models have been extensively used in T2DM research (Chatzigeorgiou et al, 2009). The etiopathogenesis of T2DM represented by insulin resistance and obesity has been substantially investigated using *in vivo* models (Chatzigeorgiou et al, 2009). The use of experimental animals is not restricted to disease pathogenesis but has been extended to drug applications in which animal models are utilised to determine drug efficacy, safety and drug-related parameters (pharmacokinetic and pharmacodynamic parameters) (Chatzigeorgiou et al, 2009). Rodent models are the most commonly used *in vivo* models for diabetes research, with Zucker diabetic Sprague-Dawley (ZDSD) rats being particularly valuable in this field (Rashmi et al, 2023). ZDSD rats are developed by breeding obese Sprague-Dawley rats, prone to obesity on a high-fat diet, with Zucker diabetic fatty rats that have impaired insulin production (Rashmi et al, 2023). These ZDSD rats develop a pre-diabetic state lasting over eight weeks, resembling the early stages of human T2DM (Rashmi et al, 2023). Another commonly employed model in diabetes research is the $Lep^{Ob/Ob}$ mouse, which carries a mutation in the leptin gene, leading to leptin deficiency (D'souza et al, 2016). This deficiency results in severe obesity, hyperphagia (excessive eating), IR, and hyperglycemia, closely mirroring T2DM (D'souza

et al, 2016). Given that the abovementioned rodent models exhibit key hallmarks T2DM pathogenesis, such as IR and hyperglycemia, and share the same metabolic and signaling pathways found in humans, these models are considered well-suited for diabetes research (Lankatillake et al, 2019).

Nevertheless, *in vivo* platforms have several drawbacks. Firstly, it is challenging to elucidate the mechanisms of drug perturbation or drug actions within biological systems since these mechanisms often arise from complex interactions between the complicated network of different organs and tissues within a living animal. Moreover, animal testing is costly and time consuming with low-throughput readouts (Lankatillake et al, 2019). Furthermore, the findings of animal studies are inconsistent and the validity of extrapolating these results to human cells is debatable (Lankatillake et al, 2019). Apart from the scientific and economic challenges, the use of experimental animals, particularly in toxicological studies, is fraught with other issues, including ethical and legislative constraints (Yu et al, 2020). As a consequence of the challenges mentioned above, the concept of next-generation risk assessments has emerged, providing new directions in toxicity testing (Yu et al, 2020). Toxicity testing of drugs is striving towards approaches that sustain the principles of replacement, reduction and refinement (3Rs), with the capability of developing reliable, robust and efficient findings in a high-throughput manner (Hemmerich & Ecker, 2020; Krewski et al, 2010). This includes the use of *in vitro* models, *in silico* approaches or a combination of both (hybrid projects) (Hemmerich & Ecker, 2020; Krewski et al, 2010).

1.11.2 *In Vitro* Toxicology

In vitro toxicology refers to the process of analysing the toxic effects of chemical substances in cellular systems selected to mimic the target tissues and organ toxicity (Jennings, 2015). There are numerous *in vitro* platforms, including (but not limited to) isolated organs, tissue slices, isolated primary cell cultures, immortalised cell lines, explant cultures and even subcellular organelles (e.g. mitochondria) (Jennings, 2015). The diversity in cellular systems enables testing of the toxic effects of drugs on specific cell types and determining the mode of toxicity at a fundamental level. Over the past decade, an upsurge in *in vitro* toxicology aspects has been reported (Jennings, 2015). This could be attributed to the advantages that *in vitro* toxicology testing offers in comparison with the *in vivo* approach. These include: (i) reduction of experimental animal utilisation following

the toxicology screening of drugs, (ii) consistency of the findings and less biological variations compared with *in vivo* testing, and (iii) availability of biotechnological advancements (e.g. high-throughput screens (HTS)) that provide reproducible and fast-tracked toxicology analyses (Jennings, 2015; Lankatillake et al, 2019).

To date, numerous *in vitro* modelling systems exist, including primary pancreatic cells and immortalised insulin-secreting cell lines (Bakhti et al, 2019).

1.11.2.1 Primary Islets

Primary islets are often derived from humans and rodents for *ex vivo* cell studies (Skelin et al, 2010). They are usually isolated either by enzymatic disaggregation (e.g. trypsin) or mechanical dispersion of pancreatic tissues (Skelin et al, 2010). Hence, primary islets retain many of their functional and differentiated characteristics despite their loss of microenvironment and vasculature supply (Skelin et al, 2010). Furthermore, they are phenotypically and genetically identical to their parental tissue (Skelin et al, 2010).

Nevertheless, the preparation of primary culture is labour intensive and the handling of these cells require extensive skills and careful planning (Lankatillake et al, 2019). The use of human primary islets in diabetes research is scarce due to limited tissue availability (Skelin et al, 2010). Another limitation of primary cells usage is their short lifespan attributed to cellular senescence genes (Skelin et al, 2010). In addition, the reproducibility of the findings is influenced by several confounders, which include the hormonal, cellular and genetic variabilities among individuals donors (Bakhti et al, 2019). Intra-donor differences due to sex, age, ethnicity, diet and body mass index could also impact the validity and efficiency of the results (Bakhti et al, 2019). Variations in the protocol followed in the primary islet isolation procedure, as well as the size and composition differences of these primary cells, are other obstacles for the comparative analyses of primary islets (Bakhti et al, 2019).

One of the suggested solutions to overcome these limitations is using the human micro-islets platform (Bakhti et al, 2019). The human micro-islets platform is a standardised alternative to human pancreatic islets as it enables the generation of clusters with defined size, identical cell number and uniform composition (Bakhti et al, 2019)**.** The process starts with primary islet disassociation accompanied by scaffold-free culturing that supports spontaneous re-aggregation of the dispersed endocrine cells to form homogenous human

micro-islets (Bakhti et al, 2019). Therefore, the resulting uniform human islet microtissues minimise the variations in the primary islet platform while ensuring robustness and reproducibility of the findings (Bakhti et al, 2019).

Another platform that relies on primary islets for research purposes is primary pancreatic tissue slice (Skelin et al, 2010). The preparation of slice culture is relatively quick and less damaging compared with primary culture (Bakhti et al, 2019). As a result, slice culture has the advantage of retaining tissue morphology and partially preserving the cellular microenvironment (Bakhti et al, 2019; Skelin et al, 2010). Furthermore, this platform (pancreatic slice) allows investigating the crosstalk between exocrine and endocrine compartments within the pancreatic tissue and the interactions between pancreatic and non-pancreatic tissues (Bakhti et al, 2019; Skelin et al, 2010). Nevertheless, limited availability and intra-donor variations remain as the challenges of this platform (Bakhti et al, 2019; Skelin et al, 2010).

1.11.2.2 Established Pancreatic Cell Lines

Owing to the finite lifespan of primary cells and their limited availability, immortalised cell lines have been generated to enable cells to overcome normal senescence and propagate indefinitely (Lankatillake et al, 2019; Persaud et al, 2014; Skelin et al, 2010). Several transformation approaches exist for the immortalisation of cells in culture conditions (Lankatillake et al, 2019; Persaud et al, 2014; Skelin et al, 2010). These include isolation of naturally occurring cancer cells, irradiation or chemical carcinogen induction of permanent genetic mutations or viral oncogene induction (e.g., simian vacuolating virus 40 (SV40) TAg) either by transfection or recombinant viral vector transduction (Lankatillake et al, 2019; Persaud et al, 2014; Skelin et al, 2010).

Besides their infinite lifespan, immortalised cell lines have several advantages. They are typically easy to handle and maintain in culture for an extended period of time (Skelin et al, 2010). Their fast proliferative property enables immortalised cells to continuously express target genes and, therefore, purify large amounts of the recommended proteins (Skelin et al, 2010). The unlimited availability of these homogeneous cell populations, in addition to their lower cost, enhances the consistency and reproducibility of the results compared with primary cells (Lankatillake et al, 2019; Persaud et al, 2014; Skelin et al, 2010).

Immortalised cell lines constitute powerful tools in diabetes research. In fact, they have been widely used for various purposes that cover both disease pathogenesis and pharmaceutical drug development process (e.g., safety studies) (Lankatillake et al, 2019; Persaud et al, 2014; Skelin et al, 2010). Currently, a number of pancreatic cell lines are commercially available. Some examples of commonly used immortalised cell lines include rat insulinoma cell line (RIN), insulinoma cell line (INS-1), hamster pancreatic β-cells (HIT), transgenic C57BL/6 mouse insulinoma cell line (MIN6) and β-tumour cell (β-TC) (Lankatillake et al, 2019; Persaud et al, 2014; Skelin et al, 2010). Each cell line has its own characteristics and limitations, and the choice should be tailored to the research goal being pursued. A brief description of commonly encountered cell lines is presented below.

1.11.2.3 Insulin-Secreting Cell Lines

The INS-1 cell line is a genetically modified cell line originally derived from rat insulinoma induced by X-ray irradiation (RIN) (Persaud et al, 2014). INS-1 is one of the relevant models displaying numerous characteristics that mimic pancreatic β-cells, including relatively high insulin content and secretory responsiveness to glucose within the physiological range (Skelin et al, 2010). Hence, the use of INS-1 is considered a suitable approach for investigating the effects of chemicals on glucose-stimulated insulin secretion (Persaud et al, 2014; Skelin et al, 2010). Furthermore, it has been shown that INS-1 cells can be passaged up to 80 times without substantial changes in cellular function or morphology (Persaud et al, 2014; Skelin et al, 2010). Nevertheless, the insulin release in response to glucose is as low as 20% of naive β-cells (Persaud et al, 2014; Skelin et al, 2010). In addition, the cell culture requires the presence of 2-mercaptoethanol for propagation (Skelin et al, 2010). Without this compound, the cells will lose various functional characteristics (Skelin et al, 2010). Despite these benefits of 2-mercaptoethanol, this toxic compound increases the intracellular levels of glutathione (GSH), which is associated with the irreversible denaturing of insulin production (Skelin et al, 2010).

HIT is a hamster insulinoma cell line produced by transforming hamster pancreatic β-cells with SV4 Tag (Lankatillake et al, 2019). HIT-T15 is the only sub-clone that responds to glucose stimulation (Lankatillake et al, 2019). Similar to mature hamster β-cells, HIT has a modest number of secretory granules (Persaud et al, 2014). It also has a low insulin content compared with normal hamster islets, and insulin production decreases with long-term subculturing (Skelin et al, 2010).

MIN6 is a transgenic C57BL/6 mouse insulinoma cell line established by SV40 transfection (Lankatillake et al, 2019). MIN6 cells express glucokinase and GLUT-2 and respond to glucose in a manner similar to that of naive β-cells (Persaud et al, 2014). They also have the advantage of retaining the morphological and functional characteristics of primary mice β-cells (Persaud et al, 2014). However, a high passage number of MIN6 cells should be generally avoided as a sudden loss of glucose-induced insulin release has been noticed (Skelin et al, 2010).

1.11.2.4 Human Pancreatic Cancer Cell Lines

Human pancreatic cancer cell lines constitute another *in vitro* model that is commonly used for molecular investigations of endocrinopathies, including diabetes mellitus (Deer et al, 2010). Numerous cell lines are available commercially; however, each cell line displays distinct phenotypic characteristics, such as adhesion, invasion, tumorigenesis and migration and genotypic status, thus requiring careful evaluation prior to cell line selection (Deer et al, 2010; Hiram-Bab et al, 2012). An overview of the commonly used human pancreatic cell lines is presented in **Table 1.4**.

The use of these cell lines in diabetes research has been achieved after several investigations involving the conversion of these immortalised cell lines into insulin-secreting cell lines (Hiram-Bab et al, 2012). A typical example is the PANC-1 epithelial cell line that has been transformed into a novel human insulin-secreting cell line (1.1B4, 1.4E7 and 1.1E7) after electrofusion with human pancreatic β-cells (Hiram-Bab et al, 2012; Persaud et al, 2014). The results showed that these electrofusion-derived cells display functional characteristics similar to those of naive pancreatic β-cells; however, the magnitude of insulin synthesis and secretory response is inferior to that of primary human β-cells and parallel or inferior to that of rodent-based cell lines (Hiram-Bab et al, 2012; Persaud et al, 2014). The studies by Hui et al., Hardikar et al., and Wu et al. showed that changing the growth medium of PANC-1 to serum-free medium (SFM) leads to cell line differentiation and induces the expression of insulin, glucagon and somatostatin (Hui et al, 2001; Wu et al, 2010). In the experiment, the cytosolic-free calcium of PANC-1 cells cultured in SFM was assessed following tolbutamide or glucose administration (Hui et al, 2001; Wu et al, 2010). Moreover, quantitative real-time polymerase chain reaction was used to measure the changes in the mRNA expression of glucokinase, GLUT2, L-type calcium channels, potassium ATP channels, glucagon and somatostatin (Hui et al, 2001;

Wu et al, 2010). The results showed cell response to tolbutamide or glucose that is similar to those exhibited by primary pancreatic islets (Hiram-Bab et al, 2012; Hui et al, 2001; Wu et al, 2010). This was parallel to a fivefold increase in glucokinase mRNA expression level and, to a lower degree, to L-type calcium channels and potassium ATP channels (Hiram-Bab et al, 2012; Hui et al, 2001). Furthermore, an increase in glucagon and somatostatin was detected, which altogether indicated changes in PANC-1 cell differentiation and gene expression (Hiram-Bab et al, 2012; Hui et al, 2001).

Table 1.2 Comparison of commonly used human pancreatic cancer cell line characteristics (Deer et al, 2010).

Cell Line	Disease	Cell Type/ Growth Mode	Patient Information	Differentiation	Proliferation
PANC-1	Epithelioid carcinoma	Epithelial/ Adherent	56-year-old Caucasian male	Poor	52 hrs
AsPC-1	Adenocarcinoma	NA/Adherent	62-year-old Caucasian female	Poor	38–40 hrs
BxPC-3	Adenocarcinoma	Epithelial/ Adherent	61-year-old Caucasian female	Poor to moderate	4–60 hrs
HPAC	Adenocarcinoma	Epithelial/ Adherent	64-year-old female	Moderate	41 hrs
MIA PaCa-2	Carcinoma	Epithelial/ Adherent	65-year-old Caucasian male	Poor	40 hrs

1.11.2.5 Stem Cell Lines

After the first report of the generation of insulin-producing β-like cells from the spontaneous differentiation of human embryonic stem cells (ESCs), a tremendous stride has been made towards the *in vitro* establishment of β-like cells (Bakhti et al, 2019). Stem cell research has revealed new horizons in the domain of diabetes mellitus therapy, including novel therapeutic approaches, such as human islet allotransplantation (Rickels & Robertson, 2019). Human islet allotransplantation has been successfully applied in selected T1DM patients, with results indicating 8% insulin independence achieved at one year (Rickels & Robertson, 2019). Aside from their involvement in cell-based therapy, stem cells have the ability to undergo unlimited cell division, differentiate into all specialised cells present in the human body and have the potential to regenerate and repair damaged tissue (Bakhti et al, 2019). Thus, stem cells could be used for multiple applications, including screening

and cytotoxicity testing of anti-diabetic drugs and disease modelling to explore new therapeutic targets for diabetes mellitus (Bakhti et al, 2019). Despite the advantages that the stem cell differentiation platform holds, several drawbacks exist. These include limited availability, high cost associated with the characterisation of each stem cell line and ethical concerns regarding the use of human stem cells, particularly ESCs, in laboratory research (Bakhti et al, 2019). In addition, stem cells require a long period of growth prior to their use (Skelin et al, 2010). Besides, the stem cell differentiation platform is not yet entirely understood, which means that it is still challenging to select the most appropriate type of stem cell needed to address the research objective (Bakhti et al, 2019). Moreover, differentiation protocols are still lacking and have not been developed for many cell types as they are hindered by limited knowledge and tissue availability (Bakhti et al, 2019).

1.11.2.6 Drawbacks of *In Vitro* Platforms

Despite the diversity and advantages of *in vitro* toxicology platforms, *in vitro* testing faces various challenges that need to be addressed. The lack of a reflecting cellular microenvironment, the complex human biology under disease conditions and loss of cell–cell interactions are the major drawbacks of *in vitro* studies (Langhans, 2018). This could raise a debate about result validity and pose a challenge in extending the experimental results to whole organisms or different species (Langhans, 2018). Although immortalised cell lines can address some limitations in primary islet cells, they also have their own pitfalls. Since the senescence genes have been mutated by different transformation techniques, cell lines may have abnormal chromosomal content and some form of genetic mutations that could consequently lead to atypical protein expression and modified metabolism (Skelin et al, 2010). Hence, collectively, the behaviour and characteristics of immortalised cell lines are not functionally comparable with those of primary cells (Skelin et al, 2010). The foregoing concerns should be considered when using these cell lines in diabetes mellitus research.

1.11.2.7 Recent Advancements in *In Vitro* Platforms

Recently, considerable progress has been attained in developing cell culture models that accurately mirror *in vivo* cellular microenvironments and replicate complex tissue structures (Langhans, 2018). This has enabled the transition from two-dimensional (2D) to three-dimensional (3D) cell culture experiments in which cells are permitted to grow and interact with their surroundings in a 3D environment (Langhans, 2018). Various 3D

culturing techniques are currently in use, often divided into two distinct categories: scaffold-based (i.e. polymeric hard scaffolds, micropatterned surface microplates) and scaffold-free systems (i.e. spheroid microplates containing ultra-low attachment (ULA) coating) (Langhans, 2018). Each has its advantages and disadvantages, which need to be considered prior to choosing the most suitable 3D system to achieve the research goal. The implication of 3D culture systems in diabetes mellitus research involves the use of pseudo-islet models and organoids (Bakhti et al, 2019; Kojima, 2014; Langhans, 2018).

1.11.2.7.1 Pseudo-Islets

In diabetes mellitus research, majority of cell culturing, mostly with immortalised cell lines, is carried out using conventional 2D techniques in which cells are propagated as adherent monolayers on tissue culture substrates (Persaud et al, 2014). Given that the anatomical configuration of islet cells is a major determinant of sustaining optimal insulin release responses, the configuration of cell lines as adherent monolayers is a major concern (Persaud et al, 2014). In previous studies, the functional characteristics of islet cells were evaluated after dispersing the cells into a cell suspension (Kojima, 2014). The results showed a significant reduction in insulin content in response to physiological signals (Kojima, 2014). Subsequently, when the islet cells were configured into the 3D structure, named pseudo-islets, restoration of the insulin secretion ability was established (Kojima, 2014). In agreement with the findings mentioned above, the reconfiguration of commonly used cell lines (MIN6, βTC6) into 3D pseudo-islet structures has also been shown to restore the cell line's differentiated functions, demonstrated as an improvement in the glucose-sensing characteristics compared with the monolayer culture (Bakhti et al, 2019). These observations collectively highlight the importance of cell–cell and cell–matrix interactions in the phenotypic and functional characteristics of pancreatic β-cells.

1.11.2.7.2 Organoids

An organoid is a 3D multicellular *in vitro* tissue culture that incorporates the key characteristics of its corresponding *in vivo* organ micro-architecture (Langhans, 2018). The 3D organoid system is a novel *in vitro* platform with promising potential for pharmaceutical testing and disease modelling (Langhans, 2018). This unique system replicates complex tissue structures and mirrors cellular microenvironments with superior reflections on cell differentiation, polarisation and intracellular interactions (Langhans, 2018). Several organoid structures have been established, such as mini-brain, kidney, liver and small

intestine (Langhans, 2018). To establish organoids, cells capable of self-renewing and multipotency are required. Hence, organoids are typically derived from a single adult stem cell (aSC), ESC and induced pluripotent stem cells (iPSC) (Bakhti et al, 2019). Different protocols are currently adopted with regards to organoid culture conditions; however, collectively agreeing on specific culture media with certain growth conditions (e.g. involvement of the basement matrix membrane) is essential to ensure proper development of the required organoid (Bakhti et al, 2019; Langhans, 2018). Since organoids are derived from stem cells, they preserve the long-term viability and maintenance characteristics (Bakhti et al, 2019; Langhans, 2018). Hence, organoids are suitable for replicative studies (Bakhti et al, 2019; Langhans, 2018). Going beyond diabetes research, pancreatic organoids were first generated by Anne Grapin-Botton's group using embryonic pancreatic cells (Greggio et al, 2015). In these generated organoids, the mouse progenitors successfully produced branched structures containing ductal, exocrine and endocrine lineages (Greggio et al, 2015). Furthermore, pancreatic organoids have been generated from CD133 (prominin-1) cells derived from adult mouse pancreas, and the results were comparable to those observed with embryonic cells (Greggio et al, 2015). Currently, the use of the 3D organoid system in diabetes research focuses on understanding pancreatic morphogenesis and differentiation (Bakhti et al, 2019). Its use in anti-diabetic agent screening is still lacking; however, it seems to be a promising *in vitro* platform candidate for pharmaceutical applications in the future.

1.11.3 Application of Omics in Toxicity Evaluation

Conventional toxicological methods have been mostly adopted to investigate the adverse effects of medications, mainly through observing toxicological endpoints. Despite the crucial input provided by these methods, a comprehensive description of the biological pathways underlying medications' toxic effects is still lacking. Thus, innovative methodological approaches are warranted to provide both comprehensive and targeted mechanistic data capable of filling the existing data gaps and ultimately improve the current understanding of drug toxicity.

To date, omics-based approaches have emerged as powerful tools in toxicological research (Hu & Jia, 2021; Li et al, 2021; Nguyen et al, 2022). The integration of omics-based studies in toxicity-related investigations has successfully shifted the scope of toxicological evaluation from an observational-based strategy to a more mechanical,

target-based analysis of the impact of chemicals on the human system (Marx-Stoelting et al, 2015). Various omics approaches currently exist – including toxicogenomics, toxicotranscriptomics, toxicometabolomics and toxicoproteomics, each of which has provided unprecedented insights into the toxicity pathways of various chemicals at different molecular levels (i.e., DNA, RNA, proteins and metabolites) in a high-throughput manner and acceptable time frame (Marx-Stoelting et al, 2015; Nguyen et al, 2022). Numerous technologies are available to perform such omics approaches (Li et al, 2021). These technologies can be broadly branched into two main categories that serve as the workhorse for performing different omics strands: technologies based on next-generation sequencing (NGS) and mass spectrometry (MS) **(Figure 1.20)** (Li et al, 2021).

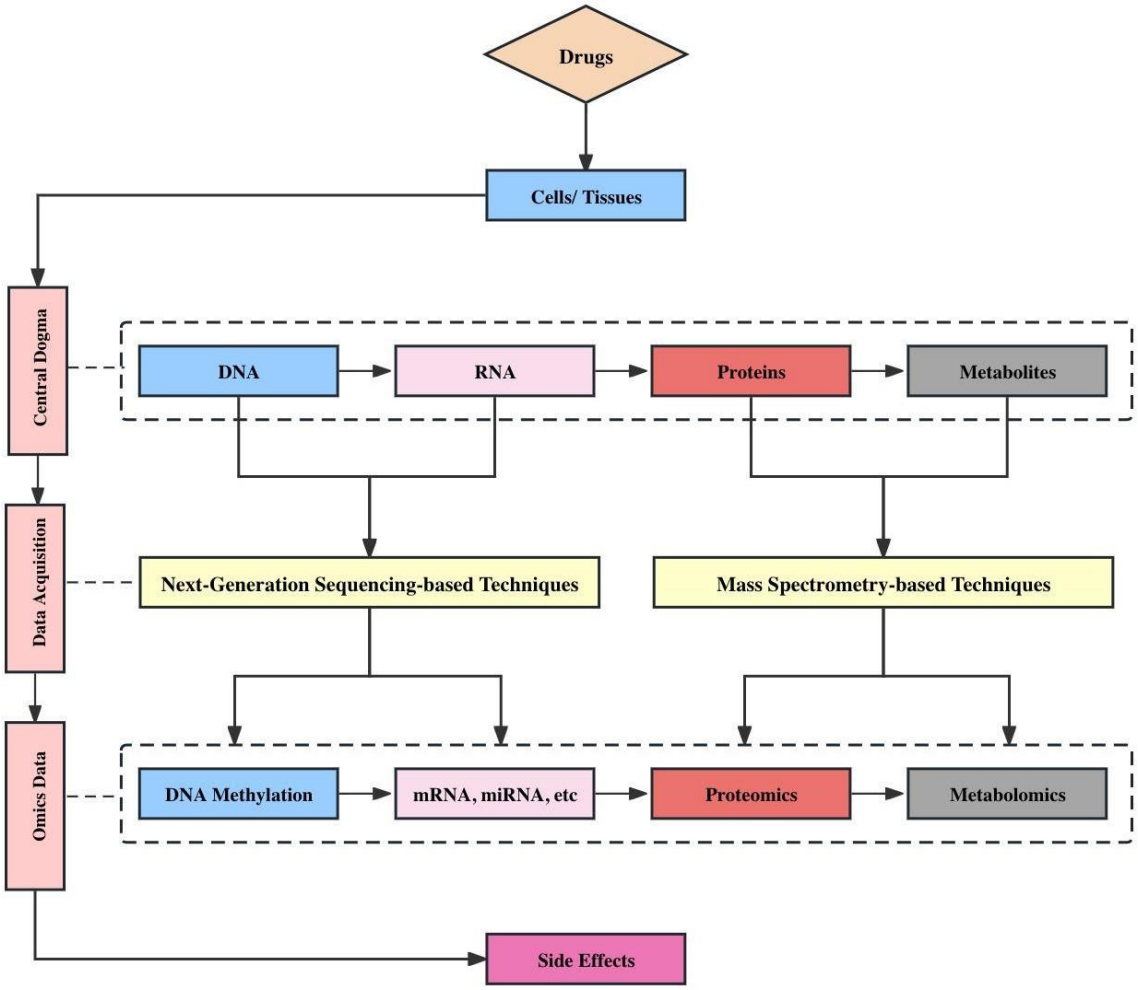

Figure 1.20 Integration of omics-based approaches in the investigation of drugs' side effects. Drugs, apart from their therapeutic effects, can disturb cells at different molecular levels, resulting in side effects. With the aid of omics-based technologies, these perturbations can be captured and translated into distinct types of omics data, enabling a comprehensive understanding of the toxic mechanisms that underpin drugs' unfavourable actions.

1.11.3.1 Toxicogenomics and Toxicotranscriptomics in Toxicological Studies

Francis Crick's central dogma of molecular biology, positing a unidirectional flow of genetic information from DNA to RNA to protein, laid the foundation for toxicogenomics (Mortimer et al, 2022). Advancements in sequencing technologies have enabled researchers to acquire genomic and transcriptomic data at unprecedented depth, driving the integration of these technologies into diverse fields, including toxicology (Mortimer et al, 2022).

Starting with toxicogenomics, various forms of genetic variants (i.e., single-nucleotide variations/polymorphisms [SNVs/SNPs], structural variation, insertion and deletion) may occur, resulting in variability in drug efficacy and safety (Nguyen et al, 2022). Genetic variation to variation in drug safety can be detected using whole-genome sequencing

(WGS) and whole-exome sequencing (WES) (Robinson et al, 2012). Moreover, advances in other sequencing techniques have enabled the deciphering of the dysregulated epigenome and its influence on gene expression and, ultimately, drug response (Li et al, 2021; Robinson et al, 2012). There are four well-recognised mechanisms that drive epigenetic modifications: DNA methylation, histone modifications, chromatin accessibility and compaction and nuclear architecture, each of which can be measured by certain techniques (Li et al, 2021). For instance, chromatin immunoprecipitation followed by sequencing (ChIP-Seq) is widely used for genome-wide mapping of DNA-binding proteins and histone modifications, whereas bisulfite sequencing (BS-Seq) is adopted for detecting DNA methylation patterns (Robinson et al, 2012). In addition, for the purpose of identifying chromatin accessibility across the genome, the assay for transposase-accessible chromatin with sequencing (ATAC-Seq) and DNase I hypersensitive sites sequencing (DNase-seq) have been commonly used (Li et al, 2021). Furthermore, Hi-C and chromatin interaction analysis with paired-end tag sequencing (ChIA-PET) have opened new horizons in the exploration of in situ chromatin interactions and transcription regulation (Li et al, 2021).

Moving to toxicotranscriptomics, the evolution of RNA-sequencing technologies has introduced a new perspective to transcriptome studies, producing valuable, increasingly accurate insights at a reasonable cost (Haimbaugh et al, 2022). The utilisation of RNA sequencing has enabled the quantification of the whole transcriptome and transcript isoforms, identification of aberrant splicing events and detection of gene fusions (Haimbaugh et al, 2022). The data extracted from this omics strand has significantly contributed to developing an inclusive list of differentially expressed gene candidates for adverse drug reaction exploration (Nguyen et al, 2022).

In toxicogenomics and toxicotranscriptomics, gene expression analysis has been primarily adopted to achieve two main key purposes: characterising the molecular signature of chemicals and discovering novel biomarkers. Genome-wide expression profiling offers unparalleled resolution for creating molecular fingerprints of toxicants, comprehensively capturing the impact of chemicals on molecular pathways (Mortimer et al, 2022). Given the vast number of genes in organisms (approximately 20,000 in humans), chemical exposures induce multiple simultaneous changes that necessitate comprehensive detection (Serra et al, 2020). Transcriptomics excels at identifying these changes, enabling the characterisation of molecular pathways perturbed by toxicants through the

simultaneous analysis of tens of thousands of gene expression profiles (Joseph, 2017). This comprehensive view encompasses intricate regulation and network interactions among genes throughout the genome and serves as a "molecular signature" that contains highly detailed biological information about chemicals (Mortimer et al, 2022). Hence, by comparing genome-wide expression profiles, researchers can effectively differentiate chemicals with distinct toxicity mechanisms and predict potential toxicity pathways for novel compounds based on similarities to known toxicants (Mortimer et al, 2022).

Furthermore, by analysing genome-wide expression profiles for a chemical, researchers can identify biomarkers based on classification criteria (Nguyen et al, 2022). Bioinformatics tools facilitate the discovery of marker genes consistently altered across expression profiles of chemically similar compounds (Li et al, 2021). These biomarkers streamline chemical classification. For instance, Li et al. compared transcriptome profiles of 14 genotoxic and 14 non-genotoxic chemicals, identifying 65 marker genes capable of accurately distinguishing between these chemical classes (Li et al, 2015). Despite the utility of toxicogenomics in biomarker discovery, solely relying on this approach for assessing chemical toxicity is insufficient, necessitating validation through traditional phenotyping experiments. It's crucial to interpret results cautiously, as molecular-level changes may not always translate into observable physiological effects.

Despite advancements in toxicogenomics, challenges persist in its application to toxicology studies. Firstly, lack of comprehensive transcriptomics databases hindering the ability of performing comprehensive chemical classification analysis (Mortimer et al, 2022). Secondly, the high cost of RNA-sequencing through which the expense of whole genome expression profiling restricts its widespread application (Zhang et al, 2018). Recent advancements have introduced reduced transcriptomics as a cost-effective method for comprehensively assessing chemical toxicity and identifying key molecular pathways (Zhang & Zhao, 2018; Zhang et al, 2018). This approach is predicated on the concept that a limited gene subset can effectively represent the behavior of entire gene networks (Zhang et al, 2018). Zhang and Zhao demonstrated the utility of reduced transcriptomics in identifying neurotoxicants induced by chemicals by using a reduced transcriptome atlas (RTA) approach which integrated transcriptomic data sets and a set of genes linked with neurogenesis and the early neurodevelopment of zebrafish (Zhang & Zhao, 2018). Analysing transcriptomic data from 74 chemicals and 736 genes yielded 135 distinct exposure signatures. A gene panel of 300 genes derived from gene expression index

(GEI) analysis effectively assessed neurotoxic potential and associated biological pathways. Thirdly, in the context of data interpretation, the substantial volume of data generated presents significant challenges in interpretation, necessitating advanced computational tools and expertise to establish connections between transcriptomic alterations and toxicological endpoints (Mortimer et al, 2022). Fourthly, transcriptomics analyses focus on RNA levels, which may not accurately reflect protein levels due to post-transcriptional regulation, limiting its ability to fully predict biological outcomes. Lastly, standardisation issues hinder the comparability of the findings and hence widespread application of transcriptomics in toxicology (Marx-Stoelting et al, 2015).

1.11.3.2 Toxicoproteomics and Toxicometabolomics in Toxicological Studies

While transcriptomics has been the predominant global approach in toxicology due to its well-established computational pipelines, toxicoproteomics is rapidly emerging as one of the most dynamic and fast-developing fields in toxicology for analysing changes in protein expression at the functional level (Yipel & İlhan, 2022). This dynamic field is gaining prominence due to its capacity to directly measure and quantify proteins, which are the ultimate effectors of biological processes. Proteomics encompasses not only the analysis of protein expression patterns but also their functions, localization, interactions, post-translational modifications (PTMs), and turnover (Suman et al, 2016). With an estimated 80,000 proteins encoded by approximately 20,000-25,000 genes in humans, and considering the vast array of PTMs, the protein landscape exceeds one million entities (Suman et al, 2016).

Toxicoproteomics is increasingly employed in toxicology to decipher the mode of action of chemicals through the investigation of the changes in protein expression profiles to pinpoint affected pathway processes (Thomas et al, 2023). Numerous papers in the literature have demonstrated the successful application of proteomics approaches in elucidating the mechanisms of action underlying chemical toxicity. In one paper, a comprehensive whole-cell proteomic analysis unveiled the molecular underpinnings of oxaliplatin's action, demonstrating its induction of DNA damage and perturbations in nucleolar and ribosomal function (Ozdian et al, 2017). Another untargeted proteomic examination in rifampicin-treated mice revealed proteomic alterations associated with hepatotoxic mechanisms (Kim et al, 2017). Hence, proteomic characterisation can

delineate cellular reactions to pharmaceutical interventions and facilitate the prediction of adverse drug effects.

Furthermore, toxicoproteomics has been widely utilised as a valuable platform for discovering protein biomarkers indicative of diverse chemicals within the realms of biomonitoring and human toxicology (Mortimer et al, 2022). For example, a study investigated changes in the rat serum proteome resulting from prepubertal exposure to bisphenol A (BPA) and genistein (Betancourt et al, 2014). By analysing the serum protein profiles of rats exposed to these compounds, the researchers aimed to identify alterations in protein expression and potential biomarkers associated with early exposure to endocrine-disrupting chemicals. The findings revealed elevated levels of ATPase family AAA domain containing 3A (ATAD3A), receptor tyrosine-protein kinase (ERBB3), and wingless-type MMTV integration site family (WNT). ATAD3A, a mitochondrial membrane protein crucial for stabilizing mitochondrial DNA-protein complexes (nucleoids), has been linked to lymphovascular invasion and exhibits anti-apoptotic properties in lung adenocarcinoma (Betancourt et al, 2014). The observed increases in ERBB3 and WNT align with previous research associating these factors with heightened carcinogenesis and mammary terminal end bud proliferation, respectively (Betancourt et al, 2014). These biomarkers provide insights into how BPA and genistein impact biological processes during critical developmental windows.

Metabolomics is a field of life science research that utilises high-throughput technologies to identify and characterise all small molecules or metabolites within a specific cell, tissue, or organism, collectively known as the metabolome (Olesti et al, 2021). Metabolomics represents the downstream consequence of genomic, transcriptomic, and proteomic processes, with metabolite fluctuations directly reflecting biochemical function and organismal phenotype (Olesti et al, 2021). The metabolome encompasses a comprehensive collection of low molecular weight compounds (≤1000 Da) present within biological samples, including endogenous and exogenous molecules as well as transient or even theoretical molecules (Fraga-Corral et al, 2022). The significance of metabolites is underscored by their diverse roles in biological systems. Over 95% of clinical diagnostic tests analyse small molecules, while 89% of pharmaceuticals and 50% of existing drugs are derived from them (Qiu et al, 2023). Additionally, 30% of identified genetic disorders stem from small molecule metabolism dysfunctions (Qiu et al, 2023). Metabolites function as essential cofactors and signaling molecules for thousands of proteins, highlighting their

intricate involvement in cellular processes (Olesti et al, 2021). Furthermore, the metabolome is intrinsically linked to other omics domains. Small molecules serve as fundamental building blocks for the genome and transcriptome, constituting nucleotides like adenosine monophosphate, cytidine monophosphate, guanosine monophosphate, and thymidine monophosphate (Rinschen et al, 2019). They also form the basis of the proteome as amino acids, and contribute to cellular architecture through lipids and glycolipids (Rinschen et al, 2019). Moreover, metabolites like sugars, lipids, amino acids, and ATP fuel cellular energy production (Qiu et al, 2023). Beyond structural and energetic roles, small molecules act as essential cofactors and signaling molecules, influencing both proteome and genome function (Rinschen et al, 2019). In essence, the genome and proteome have evolved to facilitate small molecule chemistry. To date, metabolomics is implicated in various applications, including toxicology (Toxicometabolomics) (Araújo et al, 2021). Toxicometabolomics explores how chemicals induce alterations in metabolite profiles, reflecting changes in biochemical processes (Araújo et al, 2021). This approach facilitates the early detection of toxic responses, preceding traditional toxicity assessments, and enables the application of toxicometabolomics across a wide range of toxicological studies (Olesti et al, 2021; Suman et al, 2016). These include the determination of the point of departure using benchmark dosing, elucidation of off-target toxicity mechanisms with high specificity, chemical grouping and cross-species extrapolation of toxicity data (Olesti et al, 2021). Furthermore, toxicometabolomics can simultaneously probe the toxicokinetic and toxicodynamic data of both parent drug and biotransformation products, which can further hasten the acquisition of mechanistic knowledge (Olesti et al, 2021). Recent studies, for example, have demonstrated its utility in characterising the effects of hepatotoxic drugs. In this study, Garcia-Canaveras et al. employed an MS-based metabolomics approach to categorise and investigate diverse mechanisms of drug-induced hepatotoxicity using HepG2 cells (García-Cañaveras et al, 2016). The research team profiled the metabolome of human-derived HepG2 cells exposed to various hepatotoxic drugs with distinct mechanisms: steatosis (doxycycline, tetracycline, valproate), phospholipidosis (amiodarone, clozapine, fluoxetine, tilorone, tamoxifen), and oxidative stress (cumene hydroperoxide, tert-butyl hydroperoxide). Glutathione and γ-glutamyl cycle metabolites emerged as potential oxidative stress biomarkers, while phospholipidosis was linked to inhibited phospholipid degradation and steatosis to increased triacylglyceride synthesis. Unique metabolic fingerprints for each

mechanism enabled the development of a predictive model with high accuracy (AUC of 0.97) in classifying hepatotoxicity based on drug mode of action.

Recent advancements in MS, particularly in liquid chromatography–mass spectrometry [LC–MS], with enhanced resolution and sensitivity, have significantly transformed the characterisation and profiling of proteomes and metabolomes in biological samples (Li et al, 2021). This technological leap has driven the increasing adoption of toxicoproteomics and toxicometabolomics in toxicological research (Li et al, 2021). The following section will describe the fundamental principles underlying LC–MS applications utilised in both toxicometabolomics and toxicoproteomics studies.

1.11.3.2.1 LC–MS Applications in Toxicometabolomics and Toxicoproteomics: Dissecting the Basic Principles

LC–MS is an analytical technique that merges the physical separation capabilities of liquid chromatography with the mass analysis power of mass spectrometry (Pitt, 2009). The LC–MS setup featuring the interface between the LC and MS components is shown in **Figure 1.21**.

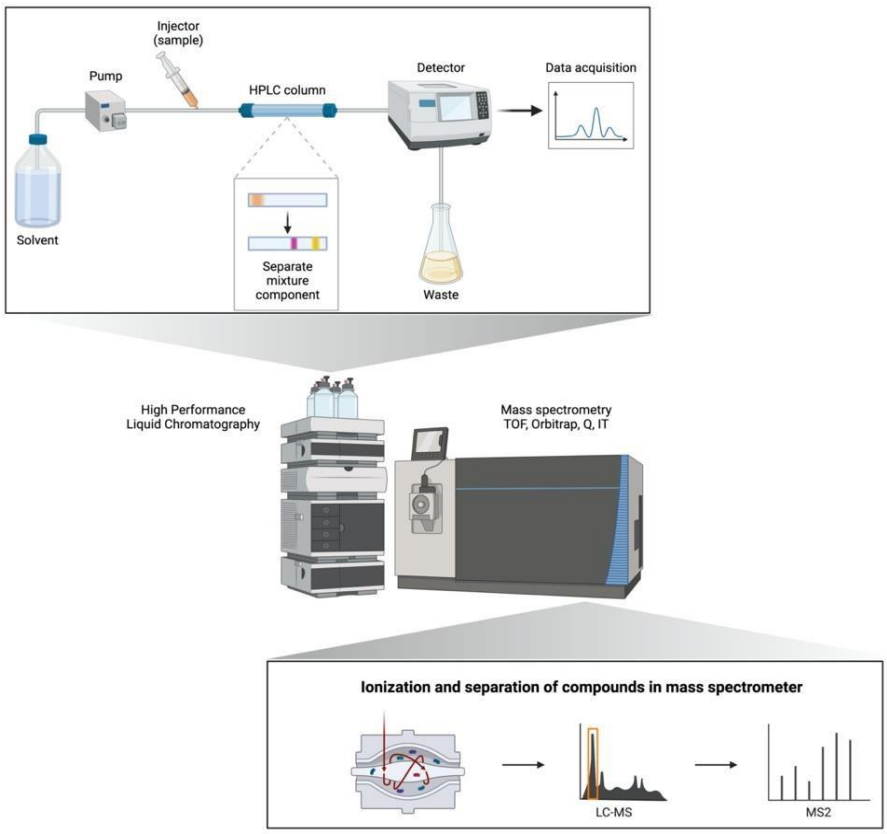

Figure 1.21. A schematic representation of LC–MS. An LC–MS system comprises several key components. The automated sample injector (autosampler) precisely introduces the sample into the high-pressure flow generated by the pump system. This flow carries the sample through a specialized column, where individual components separate based on their unique interactions with the stationary phase within the column. The separated analytes then enter the ion source, where they transition from a liquid state to gas-phase ions. These ionized molecules are then propelled through the mass spectrometer under progressively decreasing pressure, ultimately reaching the detector for analysis. LC–MS: liquid chromatography–mass spectrometry. Adopted from (Pitt, 2009).

The fundamental principle of an LC system relies on separating the components of a mixture (Coskun, 2016). This is achieved by passing the mixture dissolved in a mobile phase through a stationary phase (Coskun, 2016). The stationary phase interacts differently with the mixture's components, causing them to separate in accordance with their affinities for the two phases (Robards & Ryan, 2021). To date, a range of chromatographic separation techniques, most notably high-performance liquid chromatography (HPLC) and ultra-high-performance liquid chromatography (UHPLC), exist for complex sample analysis (Robards & Ryan, 2021). A standard HPLC system uses high pressure (up to 40 MPa) to propel the mobile phase through a compact column (Nahar et al, 2020). This column is typically 2.0–4.6 mm in diameter and 20– 250 mm in length and packed with a stationary phase, such as reversed-phase C18 silica particles, which are typically 2–5 µm in size (Nahar et al, 2020). UHPLC stands out as a cutting-

edge LC technique, achieving remarkably fast analysis times and using minimal mobile phase solvents (Cielecka-Piontek et al, 2013; Nahar et al, 2020). The defining characteristic of UHPLC instrumentation lies in its use of sub-2-micron stationary phase particles (Cielecka-Piontek et al, 2013; Nahar et al, 2020). This contrasts with conventional HPLC systems, which typically employ particles ranging from 2.5 to 10 microns (Nahar et al, 2020). The smaller particle size in UHPLC contributes to its superior separation efficiency and resolution (Robards & Ryan, 2021). However, these smaller particles necessitate significantly higher operating pressures, exceeding 6000 psi, which surpasses the capabilities of most classical HPLC systems (Cielecka-Piontek et al, 2013; Robards & Ryan, 2021).

LC relies on a mobile phase – a solvent or solvent mixture – to transport the sample through the column and achieve separation (Robards & Ryan, 2021). Two primary modes govern the delivery of this mobile phase: isocratic elution and gradient elution (Schellinger & Carr, 2006; Snyder & Dolan, 2007). Isocratic elution uses a single mobile phase composition throughout the separation (Schellinger & Carr, 2006). Hence, it offers the advantage of a constant mobile phase composition, simplifying setup and operation (Schellinger & Carr, 2006). However, the strength of this fixed solvent may not be sufficient to separate complex mixtures containing analytes with a wide range of polarities. To address this limitation, gradient elution emerged (Snyder & Dolan, 2007). This method dynamically changes the mobile phase composition over time, allowing for the separation of a broader spectrum of analytes with varying affinities for the stationary phase (Nahar et al, 2020).

In chromatographic separations, the columns play a crucial role in isolating and analysing the target compounds (Kirkland & DeStefano, 2006; Premnath & Zubair, 2024). These columns, typically made of stainless steel or glass, house the stationary phase, the key component responsible for separation (Kirkland & DeStefano, 2006). Selecting the most appropriate column hinges on several factors, including the properties of the analytes, the desired level of resolution, and the specific analytical technique employed. Currently, several types of LC columns are available, each offering unique properties for distinct applications, the most common of which are normal-phase and reversed-phase columns (Premnath & Zubair, 2024). Normal- phase chromatography employs stationary phases with hydrophilic surfaces, such as silica (Premnath & Zubair, 2024). In this setup, the mobile phase is typically a nonpolar solvent

like hexane or chloroform, causing nonpolar analytes to elute earlier (Premnath & Zubair, 2024). In contrast, reversed-phase chromatography uses a nonpolar stationary phase, often C18-bonded silica, paired with a polar mobile phase (Robards & Ryan, 2021). This versatile technique has demonstrably proven its worth in diverse applications, including the separation of drugs, metabolites, and bioactive molecules (Nahar et al, 2020). To sum up, operating an LC system effectively is akin to an art form, demanding meticulous selection of the stationary phase, mobile phase, and flow rate, all tailored to the specific properties of the analyte under investigation.

After the chromatographic separation resolves the analyte mixture into its individual components, these separated analytes are introduced into the MS system, where their mass-to-charge (m/z) ratios are measured (Medina et al, 2023). MS is an analytical technique that operates by transforming analyte molecules into charged particles (ions) through a process called ionization (Pitt, 2009). These ions, along with any fragment ions generated during ionization, are then accurately analysed based on their mass-to-charge ratio (m/z) (Pitt, 2009). Various ionization techniques have been devised to efficiently ionize molecules with diverse properties, including electrospray ionization (ESI), atmospheric pressure chemical ionization (APCI), and matrix- assisted laser desorption/ionization (MALDI), with ESI being the method most widely employed (Medina et al, 2023). ESI is a soft ionization technique applicable to a broad range of analytes, from small molecules to large biomolecules, such as proteins, with molecular weights of up to 200,000 Daltons (Banerjee & Mazumdar, 2012). In LC– ESI, the sample solution is introduced via a needle positioned within the probe (Pitt, 2009). Here, a high voltage (typically 3–4 kV) applied at the tip, coupled with a nebulizing gas flow, induces the sample to undergo nebulization, essentially forming an aerosol (Banerjee & Mazumdar, 2012; Medina et al, 2023). This aerosol is then directed through successive stages of increasing vacuum, where the solvent droplets evaporate to near-atomic size, generating highly charged analyte ions suitable for mass spectral analysis (Banerjee & Mazumdar, 2012; Pitt, 2009). Following ionization, the resulting ions are propelled into the mass spectrometer’s vacuum chamber and directed towards the mass analyser, which comes in various forms, including time-of- flight (ToF), quadrupole (Q), magnetic sector, ion trap, and Orbitrap mass analysers (Medina et al, 2023). Each type poses distinct characteristics in terms of resolution and mass accuracy that serve as key parameters for evaluating the efficiency of a mass analyser.

Within the realm of mass spectrometry, two prominent analysers stand out: Q and Orbitrap. The Q mass analyser functions by using four parallel metal rods with a distinctive, hyperbolic-shaped cross-section (Dawson, 2013; Haag, 2016). These rods are arranged around a central axis where ions travel (Dawson, 2013; Haag, 2016). The rods are linked to radiofrequency (RF) and direct current (DC) generators, and the adjacent rods are of the opposite RF phase (Dawson, 2013; Haag, 2016). By precisely controlling the RF and DC voltages applied, the Q analyser acts as a highly selective filter (Dawson, 2013; Haag, 2016). Only ions within a narrow m/z range possess a stable trajectory and reach the detector (Szyszka et al, 2024). All other ions, unable to maintain this path, collide with the rods and lose their charge (Szyszka et al, 2024). Hence, the Q analyser excels at filtering individual ions due to its unique operating principle (Szyszka et al, 2024). However, compared to other analysers, its lower mass resolution necessitates careful consideration for applications that demand high precision (Medina et al, 2023).

The Orbitrap, a powerful ion trap analyser, employs two outer electrodes and a central electrode, creating an ion trap configuration that allows it to function as both an analyser and a detector (Madeira et al, 2012). The Orbitrap applies a captivating technique called “electrodynamic squeezing” to trap incoming ions (Madeira et al, 2012). Once captured, these ions embark on a journey of oscillation within the trap (Madeira et al, 2012; Zubarev & Makarov, 2013). They travel around the central electrode while simultaneously oscillating between the two outer electrodes (Zubarev & Makarov, 2013). Notably, the frequency of these oscillations varies depending on the specific ion's m/z ratio (Madeira et al, 2012). This variation in frequency ultimately leads to the separation of the ions (Zubarev & Makarov, 2013). Then, the mass spectra of ions are acquired through image current detection by measuring the Fourier transform (FT) of the oscillation frequencies caused by ions on the outer electrodes (Madeira et al, 2012).

Recognising the strengths and weaknesses of individual mass analysers, scientists have increasingly adopted instruments that combine two analysers into a single (MS/MS) system. The Exploris 240 exemplifies this approach, integrating the previously mentioned analysers to offer enhanced capabilities (Sui et al, 2022). In MS/MS, a powerful technique for structural analysis, selected parent ions are fragmented using a process called collision-induced dissociation (CID) (Sui et al, 2022). These fragments, along with the parent ions, are then separated and measured by a second mass analyser

(Sui et al, 2022). This additional fragmentation step provides richer data than just the m/z value of the parent ion, revealing more detailed information about the molecule's structure (Yu et al, 2022). The MS/MS technique is currently compatible with a range of instruments, including a triple-quadrupole mass spectrometer (QqQ), QToF, and Orbitrap mass spectrometers (Zubarev & Makarov, 2013). MS/MS systems offer various data acquisition modes, broadly categorized as data-dependent acquisition (DDA) and data-independent acquisition (DIA). DDA selects the most abundant ions ("Top N", 10–15) and fragments them for detailed analysis, while DIA fragments all ions within a pre-defined mass range, resulting in a comprehensive fragmentation map of all ions present in the sample (Yu et al, 2022).

Following data acquisition, which generates a complex dataset, including retention time (RT), m/z ratio, and MS/MS spectra for each identified feature, the data undergo spectral processing. This processing often involves various software tools (i.e., XCMS, MetaboAnalyst, Proteome Discoverer™, R) and includes steps such as batch correction (i.e., peak matching and RT alignment) across samples to facilitate feature identification (Matthiesen, 2020). Once the raw spectra are converted into a list of features with their corresponding abundances, the data are further assessed and normalized to ensure a standardized final output, typically an X-Y matrix, suitable for downstream statistical analysis (Matthiesen, 2020).

Unravelling the complexities of omics data requires a toolbox of statistical analysis techniques encompassing both univariate and multivariate approaches (Todorov et al, 2020). Univariate analyses, well suited for examining single variables, such as changes in feature expression across samples, serve as a starting point (Todorov et al, 2020). However, the high dimensionality of omics data necessitates the use of multivariate statistical models. These models allow for a more holistic analysis and visualisation of the complex relationships between multiple variables within the data. In the realm of data analysis, multivariate statistical analysis and machine learning can be broadly categorized into supervised and unsupervised learning techniques (Bujak et al, 2015). Unsupervised learning techniques aim to find hidden patterns or structures within unlabelled data (Bujak et al, 2015). These include clustering algorithms (i.e., hierarchical clustering) and dimension reduction techniques, such as principal component analysis (Todorov et al, 2020). Supervised techniques use labelled data to train models for prediction (Lee et al, 2018). A common technique in the omics field is partial least-

squares discriminant analysis (PLS-DA), which uses labelled samples with known class membership to build a model that can predict the class of new unlabelled samples (Lee et al, 2018). Finally, pathway enrichment analysis is commonly performed to decipher the biological processes underlying the identified features (Chicco & Agapito, 2022). This technique compares the list of features against a reference pathway database, such Kyoto Encyclopedia of Genes and Genomes, to statistically assess the overrepresentation of specific biological functions or pathways within the feature set (Chicco & Agapito, 2022). To date, a growing body of evidence has underscored the remarkable effectiveness of LC–MS- based toxicometabolomics and toxicoproteomics workflows in toxicological research. These pipelines have proven instrumental in elucidating drugs' toxic mechanisms of action and identifying promising therapeutic targets (Li et al, 2022; Nury et al, 2023; Olesti et al, 2021; Thomas et al, 2023; Zaitsu et al, 2016).

Although toxicoproteomics and toxicometabolomics have expanded rapidly within toxicological research, significant challenges remain. Starting with toxicoproteomics, proteome is exceptionally complex, encompassing a vast array of proteins subject to dynamic expression changes and post-translational modifications. This complexity hinders comprehensive characterisation of protein diversity. Additional challenges in proteomics include sample preparation and data variability (Moulder et al, 2018). Protein extraction, digestion, and analysis processes can introduce artifacts that compromise protein integrity, affecting result accuracy (Moulder et al, 2018). Furthermore, inconsistencies in sample handling, experimental conditions, and analytical platforms contribute to data variability, hindering reproducibility and cross-study comparisons. Despite the critical role of PTMs in protein function and toxicity, current proteomics techniques often fail to comprehensively identify these modifications, hindering our understanding of protein activity and interactions (Nguyen et al, 2022). Similar to other omics-based approaches, proteomics studies necessitate specialised equipment, technical proficiency, and substantial computational resources, potentially limiting accessibility due to high costs. While regarding toxicometabolomics, standardisation of analytical procedures remains elusive due to the inability to comprehensively analyse all metabolites using a single extraction method. Metabolite identification, though improving, remains a hurdle as many NMR and MS detected metabolites remain chemically unidentified. While significant progress has been made in developing metabolite databases and automated identification

tools, a substantial portion of detected features lack definitive structural assignments (Borts, 2019). Similar to proteomics, metabolomics is hindered by the absence of amplification techniques, limiting the detection of low-abundance metabolites and providing an incomplete metabolic pathway overview (Mortimer et al, 2022). Additionally, metabolite databases, especially for plants and microorganisms, lag behind genomic and proteomic resources, impeding metabolite function annotation (Wu et al, 2019). Lastly, and within the context of biological interpretation of metabolomics data, major pathway databases like Kyoto Encyclopedia of Genes and Genomes (KEGG) were not primarily designed for metabolomics. The Human Metabolome Database (HMDB), while containing 114,100 metabolites, only maps approximately 22% to known pathways, highlighting the limited integration of metabolomics into pathway analysis tools (Chu et al, 2019).

Despite the unparallel insights obtained from the single-omics strand, toxicological studies have recently made the transition towards integrating multi-omics approaches (Hu & Jia, 2021; Xie et al, 2020). This paradigm shift in study design has been considered an attempt to yield a more comprehensive and complementary understanding of the adverse outcome pathways that underpin drugs' undesirable effects (Hu & Jia, 2021). For instance, since changes in metabolic profiles and protein expression can yield complementary data regarding drugs' adverse effects, the combination of toxicoproteomics and toxicometabolomics approaches has been shown to provide unparalleled opportunities to establish causality across different cellular function levels, thereby improving comprehension of the interplay between molecular alterations and phenotypic manifestations (Chen et al, 2020; Xie et al, 2020).

Collectively, the integration of omics-based studies either as a single strand or multi-omics strategies represents a powerful tool with great potential for supporting toxicology research outputs in different applications. Nevertheless, the variation in the sensitivity of the technologies adopted in different studies and the lack of harmonisation among the protocols followed for sample preparation and data acquisition hinder the comparability of the findings and therefore impede the reproducibility and replicability of the studies. Hence, efforts should be exerted and directed towards harmonising the designs of omics-based studies for the purpose of facilitating their incorporation into risk assessments and decision-making.

1.12 The Adverse Outcome Pathway Framework: A Mechanistic Approach to Toxicity Prediction

As the toxicity testing paradigm shifts from traditional *in vivo* methods to high-throughput *in vitro* and *in silico* approaches to support chemical risk assessments (**as described in section 11.1.1**), a critical challenge persists in the rapid, cost-effective prediction of a continuously growing number of chemicals. A key challenge in utilising alternative methods for chemical safety assessment lies in the absence of a cohesive framework for incorporating molecular-level measurements derived from high-throughput approaches and extrapolating these findings to apical endpoints relevant for risk assessment. These endpoints include impacts on survival, prediction of drug adverse outcomes and their underlying mechanisms, at individuals and population-level ecological impacts. The adverse outcome pathway (AOP) framework was established to tackle this translation challenge. AOPs offer a valuable framework for establishing biologically plausible and evidence-based connections between various molecular-levels along with their phenotypic manifestations (Halappanavar et al, 2020). The conceptual underpinnings of the AOP framework and its applications in drug toxicity are outlined below.

An AOP is a model that delineates the sequence of cellular and molecular events leading to a toxic effect following exposure to any poisonous substance (Gill et al, 2023). An AOP comprises a sequence of measurable key events (KEs) interconnected by key event relationships (Gill et al, 2023; Halappanavar et al, 2020). The initial KE is typically a molecular initiating event (MIE) that occurs when a chemical interacts with a biological macromolecule, triggering subsequent KEs culminating in an adverse outcome (AO) at the individual or population level (Gill et al, 2023; Halappanavar et al, 2020). An AOP explicitly defines sequential KEs as causally linked and describes toxicity responses across multiple biological levels, from cellular to organismal and population scales (Ankley & Edwards, 2018). Furthermore, a key characteristic of AOPs is their chemical agnosticism, allowing for the information they contain to be accessed, reused, updated, and applied to a diverse range of substances (Ankley & Edwards, 2018). Of importance, a prevalent misunderstanding is that AOPs can only illustrate KEs in a linear sequence, neglecting potential interactions between pathways. Nonetheless, linear AOPs can be integrated into AOP networks to encompass shared elements and pathway interconnections (Halappanavar et al, 2020). Additionally, quantitative AOPs (qAOPs) can be constructed to incorporate quantitative relationships between KEs, including feedback

model that mirror system regulation, to forecast AOs (Halappanavar et al, 2020). For instance, Conolly et al. introduced a qAOP employing a feedback-controlled hypothalamic-pituitary-gonadal axis model to predict reproductive capacity in fish exposed to sex steroid synthesis inhibitors (Conolly et al, 2017). In essence, the AOP framework is adaptable to accommodate the complexity of various assessment contexts.

1.12.1 **Omics-Driven AOP Development**

Omics-based approaches, encompassing high-throughput measurements of genes, proteins, and metabolites, allow researchers to comprehensively assess the transcriptional and translational responses of thousands of biological molecules within a single sample (Zhang et al, 2018). The substantial amount and breadth of omics data have elevated the toxicologists' expectations for their application in toxicology and risk assessment, particularly in the context of AOPs through identifying molecular-level changes, such as MIEs and early KEs, that underpin responses to chemical stressors (Brockmeier et al, 2017). Utilising acetylcholine esterase inhibition as a case study, transcriptomic data validated established MIEs and their corresponding KEs within the AOP framework (Russom et al, 2014). These KEs encompass an accumulation of acetylcholine at neural synapses and uncontrolled stimulation within muscular junctions (Russom et al, 2014). Furthermore, microarray analysis of *Caenorhabditis elegans*, a nematode model organism relevant to both ecotoxicology and human health, revealed affected pathways linked to electron transport activities and lipid metabolism (Viñuela et al, 2010). Within the AOP framework, omics datasets enhance the precision of MIE definition and biomarker selection for assessing effects and exposure (Brockmeier et al, 2017). Omics data offer both gene- and pathway-level insights, such as alterations in individual gene expression or statistical measures for differentially regulated gene sets within specific biological pathways, facilitating the identification of measurable and pertinent biomarkers (Viñuela et al, 2010). Within the realm of omics and drugs' mode of action elucidation, the use of high-content omics datasets has generated substantial research on chemical modes of action, nevertheless, there remains a scientific imperative to corroborate these findings through additional biochemical or physiological investigations (Brockmeier et al, 2017). The AOP framework offers a structured approach to fulfill this scientific need while optimising the integration of omics data into risk assessment (Ankley & Edwards, 2018).

In addition to the data generation capacity of omics-based approaches, the incorporation of computational biology tools for analysing omics datasets is another key driver for their integration into the AOP framework (Williams & Halappanavar, 2015). The emergence of computational tools designed for univariate and multivariate statistical analysis of omics datasets has facilitated groundbreaking discoveries in biomarker identification, network inference, and computational modelling (Schultz & Watanabe, 2018; Williams & Halappanavar, 2015). By incorporating these approaches into the AOP framework, network inference, for example, enables a deeper understanding of molecular network dynamics, contributing to the elucidation of the progression from an MIE or early KE to an AO (Schultz & Watanabe, 2018; Williams & Halappanavar, 2015).

Research in omics applications has successfully demonstrated the utility of omics data in developing and refining AOPs. For instance, Antczak et al. identified a potential mechanism for narcosis toxicity in *Daphnia magna* associated with calcium signaling (Antczak et al, 2015). Narcosis, a prevalent MOA for industrial chemicals, has an unclear underlying mechanism. Data from Antczak et al. and the University of Antwerp contributed to the Organisation for Economic Cooperation and Development (OECD's), an organization that play a role in advancing the development and application of AOPs, acceptance of a proposed AOP within their development program (Antczak et al, 2015).

To date, the AOP framework has been instrumental in revolutionising risk assessment by providing a mechanistic basis for understanding potential human health effects. This structured and systematic approach offers a significant leap forward for 21st century toxicity testing (Ankley & Edwards, 2018). Two key strengths contribute to this advancement: (i) a centralised repository and collaboration tools like AOP-Wiki (www.aopwiki.org), facilitating knowledge sharing and collaboration; and (ii) governance by OECD, ensuring broad support and adoption by major regulatory bodies worldwide (Ankley & Edwards, 2018). The AOP Wiki currently houses over 200 AOPs in various stages of development, encompassing processes and endpoints pertinent to both human health and environmental safety (Ankley & Edwards, 2018; Halappanavar et al, 2020). These robust frameworks are poised to transform risk assessment and usher in a new era of informed decision-making for chemical safety.

Currently, there are numerous proposed scenarios for applying AOPs to drug toxicities. In one study, an AOP network, encompassing thirteen individual nephrotoxicity-related

AOPs sourced from the AOP-Wiki, was developed to create a comprehensive map of the biological processes leading to kidney damage (Barnes et al, 2024). A topological analysis of the modeled network pinpointed mitochondrial dysfunction, oxidative stress, and tubular necrosis as the most interconnected and central KEs within the nephrotoxicity pathway. These KEs offer a potential framework for developing *in vitro* assays as alternatives to animal-based *in vivo* studies in predicting and evaluating chemical-induced nephrotoxicity in humans.

Another AOP framework was developed by Nymark, Penny, et al. to assess the potential lung carcinogenicity of nanoparticles (Nymark et al, 2021). The researcher formulated an AOP for lung cancer triggered by nanosized foreign matter, integrating both traditional and innovative new approach methodologies. Traditional *in vitro* assays, such as genotoxicity and mutagenicity tests, were combined with cutting-edge approaches centered on carcinogenic mechanisms, including including Multiple-Path Particle Dosimetry (MPPD) Model and *in silico* modeling *in vitro* Sedimentation, Diffusion, and Dosimetry, to identify and characterise key molecular and cellular events. The study meticulously delineates the critical stages of nanoparticle-induced lung carcinogenesis, commencing with the MIE, specifically the interaction between nanoparticles and lung cells. The pathway progresses through intermediate KEs encompassing oxidative stress, DNA damage, and chronic inflammation, culminating in tumor formation. This AOP framework is instrumental in elucidating and forecasting the carcinogenic risk posed by nanoparticles, thereby supporting informed risk assessment and regulatory strategies.

1.13 Research Aims

Diabetes mellitus is a pandemic that affects nearly half a billion people worldwide (ADA, 2023). The unprecedented rise in diabetes mellitus's global prevalence, incidence and related complications poses a heavy burden on healthcare expenditures and creates a cumulative impact on public health (ADA, 2023). Underlying drug toxicity is emerging as a threat to the favourable outcomes of commonly used cost-effective medication classes, such as TZDs (pioglitazone and rosiglitazone) (Wajid et al, 2019). TZDs, designed to tackle excess levels of both glucose and lipids within the blood, have been linked with cardiotoxicity in case reports (De Flines & Scheen, 2007). The mechanism of this deleterious off-target effect remains largely uncharacterised. Hence, the present thesis aims to elucidate the mechanism of TZD-induced cardiotoxicity through the integration of a novel adverse outcome pathway (AOP) framework. This novel conceptual framework provides a means to outline a knowledge-driven sequence of biological responses that relate a molecular initiating event (MIE) elicited by chemical exposure to an adverse outcome. The basis of this framework comprises two distinct disciplines: *in vitro* cytotoxicity testing and multi-omics strategies coupled with bioinformatics data modelling.

To establish an AOP framework for TZD-induced cardiotoxicity, the following thesis milestones were set:

- Develop cellular models for the *in vitro* toxicity testing of TZDs on both human adult cardiomyocytes and human cardiac fibroblasts (Chapter 2).
- Integrate the developed cellular toxicity models of TZDs to determine how drug-driven cardiotoxicity arises in mitochondria and develop strategies to avoid such events (Chapter 2).
- Introduce an untargeted LC–MS-based toxicometabolomics approach, followed by multivariate statistics to profile the biochemical pathways perturbed in TZD-treated human cardiomyocytes, and accordingly delineate the potential mechanisms implicated in the cardiotoxic actions of TZDs (Chapter 3).
- Establish a novel microflow LC–MS-based toxicoproteomics pipeline capable of profiling the proteome signatures of TZD-treated human adult cardiomyocytes and ultimately detecting hub proteins associated with TZDs' undesirable events (Chapter 4).

- Integrate multi-omics approaches by combining the untargeted toxciometabolomics and toxicoproteomics obtained data (Chapters 3 and 4) to further enhance comprehension of the findings and the interplay between molecular alterations and phenotypic manifestations (Chapter 5).

A graphical representation of the proposed framework is illustrated in **Figure 1.22.**

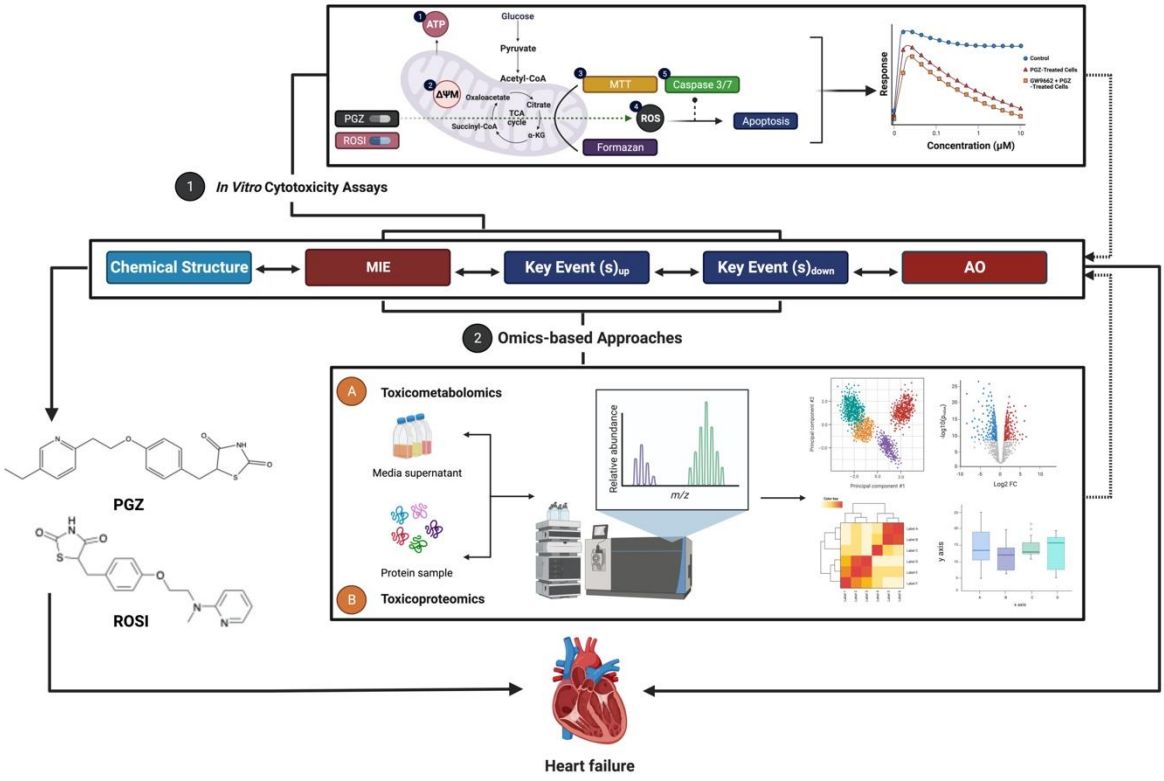

Figure 1.22 Adverse outcome pathway framework development for the assessment of thiazolidinedione cardiotoxicity. The proposed framework comprises two main distinct disciplines: (1) *in vitro* cytotoxicity testing of both TZD agents against cardiac cell lines and (2) multi-omics strategies and bioinformatics data modeling. The second discipline is subdivided into three subsections. The first and second subsections include toxicometabolomics and toxicoproteomics pipelines developed against the AC16 cellular model, while the third subsection represents an integrated multi-omics approach combining the untargeted toxicometabolomics and toxicoproteomics obtained data to further enhance comprehension of the findings and the interplay between molecular alterations and phenotypic manifestations. The ultimate aim of the proposed framework is to identify the MIE – which upon binding with TZD agents can lead to sufficient perturbation in the molecular-level homeostatic mechanisms (key events), resulting in an adverse outcome (heart failure) occurring in an organism or population. TZDs: thiazolidinediones; MIE: molecular initiating event; AO: adverse outcome; PGZ: pioglitazone; ROSI: rosiglitazone.

The primary knowledge developed in this project will contribute to the understanding of the molecular mechanisms responsible for TZDs' off-target effects. This knowledge may subsequently allow the proposal of potential therapeutic strategies that could improve TZDs' safety profile, promote the safety of patients with diabetes and support and enable the selection of cost-effective medications.

Chapter 2

Characterisation and *In Vitro* Cytotoxicity of Thiazolidinedione in Human Cardiac Cells

Abdullah Al Sultan[1,2] & Nicholas J. W. Rattray[1,3]*

[1]Strathclyde Institute of Pharmacy and Biomedical Sciences, University of Strathclyde, 161 Cathedral Street, Glasgow, UK, G4 0RE

[2]Faculty of Pharmacy, Kuwait University, Safat, 13110, Kuwait

[3]Strathclyde Centre for Molecular Bioscience, University of Strathclyde

Abstract

Thiazolidinediones (TZDs), such as pioglitazone and rosiglitazone, are selective and potent agonists of nuclear peroxisome proliferator-activated receptor gamma (PPAR-γ) used for managing insulin resistance in patients with type 2 diabetes mellitus. While TZDs initially showed promise in maintaining glycaemic control, safety concerns, particularly regarding heart failure, limited their use. The unclear mechanisms behind TZD-induced cardiotoxicity continue to spark debate, hindering their wider application as a treatment option. Hence, this study presented a comprehensive *in vitro* cytotoxicity approach designed to investigate the potential role of mitochondria as an off-target organelle contributing to the cardiotoxic effects of TZDs. In addition, it aims to elucidate their action mechanisms in terms of PPAR-γ dependency against selected cardiac cell types**.** Herein, AC16 human adult cardiomyocytes and primary human cardiac fibroblasts (HCFs) were used to evaluate the cytotoxicity of TZDs using mitochondrial assays with distinct endpoints. The concentration-response modelling of either pioglitazone or rosiglitazone (0.01–20 μM) revealed concentration-dependent loss in cell viability in both cardiac cell types. Analysis of caspase 3/7 activity revealed a drug and cell-type dependent response, with no significant increase observed in TZD-treated cardiac cells, except for the predefined endpoint noted in rosiglitazone-treated AC16 cells. Furthermore, significant depletion ($p < 0.05$) in mitochondrial adenosine triphosphate production was observed in both AC16 and HCFs upon TZD exposure (1–100 μM), which was not attenuated by a PPAR-γ inhibitor. Capitalising on TZD exposure and mitochondrial energetics, exposing cardiac cells to TZDs at concentrations ranging from 1 μM to 100 μM resulted in a marked perturbation in membrane depolarisation ($p < 0.05$). Moreover, the administration of TZD substantially triggered oxidative stress in both AC16 and HCFs ($p < 0.05$). In conclusion, our results indicated that TZDs exerted cytotoxic effects independently of PPAR-γ. The study's findings also pointed to a crosstalk between TZDs and mitochondrial dysfunction, as evidenced by perturbations in mitochondrial energetics and the induction of oxidative stress, highlighting two potential key mechanisms by which TZDs exert their cytotoxic actions on cardiac cells.

Keywords: Thiazolidinediones; Cardiotoxicity; Mitochondrial dysfunction; Oxidative stress; Apoptosis

2.1 Introduction

Thiazolidinediones (TZDs) (also called glitazones), including pioglitazone (PGZ) and rosiglitazone (ROSI), are a class of insulin-sensitising agents used for managing insulin resistance in patients with type 2 diabetes mellitus (T2DM) (ADA, 2023; Chaudhury et al, 2017; Wajid et al, 2019). TZDs are selective and potent ligands of nuclear peroxisome proliferator-activated receptor gamma (PPAR-γ), the molecular target responsible for their insulin-enhancing effects (ADA, 2023; Chaudhury et al, 2017; Wajid et al, 2019). Moreover, numerous *ex vivo* and *in vivo* studies have found that the ligand activation of PPAR-γ regulates endothelial nitric oxide synthase, the enzyme primarily responsible for vascular nitric oxide production, reduces blood pressure and improves the lipid profile, characteristically by elevating and reducing high- and low-density lipoproteins, respectively (Tan et al, 2021). Collectively, these promising data suggest that TZDs may exert cardioprotective effects in addition to their well-recognised hypoglycaemic effects. However, the cardiovascular effects of TZDs reported in clinical trials, pharmacovigilance reports and animal models have been surprisingly inconsistent and controversial (De Flines & Scheen, 2007; Erdmann et al, 2007; Home et al, 2007; Nissen & Wolski, 2007; Ntaios & Kent, 2016; Richter et al, 2007; Wallach et al, 2020; Zhou et al, 2020).

2.1.1 Effect of PGZ on Atherosclerotic Cardiovascular Events and Heart Failure

In the PROspective pioglitAzone Clinical Trial In macroVascular Events (PROactive), the effect of PGZ on cardiovascular events and mortality was evaluated in 5,238 patients with T2DM who demonstrated evidence of macrovascular disease (Erdmann et al, 2007). In this large randomised controlled trial (RCT) and following a mean follow-up period of 34.5 months, PGZ use failed to meet the predefined primary endpoints of the study: a composite of all-cause mortality, nonfatal myocardial infarction (MI) and silent MI, stroke, acute coronary syndrome, surgical intervention on coronary or leg arteries or leg amputation [19.7% versus 21.7%, hazard ratio (HR) 0.90, 95% confidence interval (CI) 0.80–1.02] (Erdmann et al, 2007). However, there was a significant reduction in the main secondary endpoint (composite of all-cause mortality, nonfatal MI or nonfatal stroke) in the PGZ group (11.6% versus 13.6%; HR 0.84; 95% CI 0.72–0.98) compared to the placebo arm (De Flines & Scheen, 2007; Erdmann et al, 2007). Additionally, there was a significant increase in hospitalisation

for heart failure (HF) in PGZ-treated patients: 149 versus 108 placebo-treated patients ($p = 0.007$) (De Flines & Scheen, 2007). The latter findings corroborated those of other large RCTs, including the studies titled “The Rosiglitazone Evaluated for Cardiac Outcomes and Regulation of Glycaemia in Diabetes” (RECORD) and “A Diabetes Outcome Progression Trial” (ADOPT), which illustrated an increased rate of hospitalisation for HF following TZD treatment (De Flines & Scheen, 2007). Moreover, animal models consistently confirmed the negative influence of PGZ treatment on HF progression, as PGZ administration exacerbated the cardiac damage associated with isoproterenol (ISO) injection in an ISO-induced HF rat model (Biswas et al, 2012). Another *in vivo* study evaluated an acute toxicity experiment with PGZ in mice (Chinnam et al, 2012). The results indicated ventricular hypertrophy in mice treated with large acute doses of PGZ (500 mg/kg and 1,000 mg/kg) (Chinnam et al, 2012).

However, in the Insulin Resistance Intervention after Stroke (IRIS) trial, PGZ treatment increased the risk of oedema without increasing the rate of hospitalisation for HF, although the dose titration of PGZ was allowed to compensate for oedema or weight gain during the trial (Ntaios & Kent, 2016). Corroborating the IRIS trial, a recent meta-analysis reported an increased risk of hospitalisation for HF in patients receiving PGZ [relative risk (RR) 1.34; 95% CI 1.11–1.57], although it was limited to those with overt cardiovascular diseases (Zhou et al, 2020).

2.1.2 Effect of ROSI on Atherosclerotic Cardiovascular Events and Heart Failure

Regarding ROSI and major adverse cardiovascular events, RECORD was designed primarily to evaluate cardiovascular death or hospitalisation due to the cardiovascular outcomes associated with ROSI exposure (Home et al, 2007). In this randomised, multicentre, open-label trial, 4,447 T2DM patients on metformin or sulfonylurea were randomly allocated to either receive ROSI as an add-on treatment (ROSI + metformin/sulfonylurea; n = 2,220) or undergo a combination therapy of metformin and sulfonylurea (n = 2,227) (Home et al, 2007). During a mean follow-up duration of 5.5 years, the trial’s findings reported 321 patients within the ROSI group experiencing the primary endpoint compared to 323 patients on standard glucose-lowering agents, with a HR of 0.99 (95% CI 0.85–1.16) (Home et al, 2007). The HR of each composite endpoint was 0.84 (95% CI 0.59–1.18), 1.14 (95% CI 0.80–1.63) and 0.72 (95% CI

0.49–1.06) for cardiovascular death, MI and stroke, respectively (Home et al, 2007). Furthermore, ROSI did not increase the risk of overall cardiovascular morbidity and mortality compared to the combination therapy (metformin and sulfonylurea) group (Home et al, 2007). The inconclusive effects of ROSI on cardiovascular morbidity and mortality were also reported in another systematic review of 18 trials (n = 3,888 patients; ≥ 24 weeks), which showed no evidence of an increased risk of MI in patients with ROSI treatment compared to other anti-diabetic agents (Richter et al, 2007).

Nevertheless, discrepant findings regarding ROSI and major adverse cardiovascular events have been conveyed elsewhere in other reports. One meta-analysis comprising 42 RCTs (n = 27,800 patients; ≥ 24 weeks) investigated the incidence of MI and cardiovascular death from cardiovascular causes associated with ROSI exposure (Nissen & Wolski, 2007). The analysis findings reported an increased risk of MI and cardiovascular mortality in the ROSI group compared to the control drugs group, with odds ratios of 1.43 (95% CI 1.03–1.98; p = 0.03) and 1.64 (95% CI 0.98–2.74; p = 0.06) for MI and cardiovascular death, respectively (Nissen & Wolski, 2007). Similar findings were reported in another systematic review and meta-analysis of 33 eligible randomised controlled trials (n = 21,156 patients; ≥ 24 weeks), in which a 33% heightened risk of the composite endpoint (composite of acute MI, HF, cardiovascular-related death and non-cardiovascular-related death) was reported in the ROSI group compared to the control arm (odds ratio 1.33; 95% CI 1.09–1.61) (Wallach et al, 2020). These findings highlight the fact that the effect of ROSI on cardiovascular events is uncertain.

Compared to PGZ, consistent findings of a greater risk of HF associated with ROSI exposure have been revealed in various reports, including RECORD and ADOPT (De Flines & Scheen, 2007; Home et al, 2007). **Table 2.1** provides an overview of key findings from meta-analyses of the TZDs used and their associated cardiovascular effects (de Jong, van der Worp, van der Graaf, Visseren, & Westerink, 2017; Lago, Singh, & Nesto, 2007; Liao et al., 2017; Nissen & Wolski, 2007, 2010; Richter, Bandeira-Echtler, Bergerhoff, Clar, & Ebrahim, 2007; S. Singh, Loke, & Furberg, 2007a, 2007b; Wallach et al., 2020; Zhou et al., 2020).

Table 2.1 Summary of the key findings of meta-analyses conducted on thiazolidinedione use and its associated cardiovascular effects. Colour shading donates the following: no significant treatment effect, lower risk and higher risk for grey, green and red, respectively.

Meta-analysis	Included Trials, n	TZD under Investigation	Treatment Duration	CV Risk				
				MI	Stroke	All-Cause Mortality	CV Mortality	HF
(Liao et al., 2017)	9 RCTs (n = 12,026)	PGZ	> 52 weeks	**RR, 0.8 (95% CI 0.62–1.03; p = 0.08)**	**RR, 0.78 (95% CI 0.60–1.02; p = 0.07)**	**RR, 0.93 (95% CI 0.80–1.09; p = 0.40)**		**RR, 1.32 (95% CI 1.14–1.54; p = 0.0003)**
(de Jong et al., 2017)	10 RCTs (n = 10,095)	PGZ	Not within the predefined inclusion criteria	**RR, 0.77 (95% CI 0.64–0.93; p = 0.007)**	**RR, 0.81 (95% CI 0.68–0.96; p = 0.02)**	**RR, 0.94 (95% CI 0.81–1.08; p = 0.38)**		**RR, 1.33 (95% CI 1.14–1.54; p = 0.0002)**
(Zhou et al., 2020)	26 RCTs (n = 19,645)	PGZ	Not within the predefined inclusion criteria	**RR, 0.8* (95% CI 0.6–1.0; p = 0.023)**	**RR, 0.8** (95% CI 0.7–0.9; p = 0.018)**	**RR, 1 (95% CI 0.8–1.1; p = 0.64)**	**RR, 1 (95% CI 0.7–1.2; p = 0.67)**	**RR, 1.3 (95% CI 1.1–1.6; p < 0.01)**
(Nissen & Wolski, 2007)	42 RCTs (n = 27,800)	ROSI	≥ 24 weeks	**OR, 1.43 (95% CI 1.03–1.98; p = 0.03)**			**OR, 1.64 (95% CI 0.98–2.74; p = 0.06)**	
(Nissen & Wolski, 2010)	56 RCTs (n = 35,531)	ROSI	≥ 24 weeks	**OR, 1.28 (95% CI 1.02–1.63; p = 0.04)**			**OR, 1.03 (95% CI 0.78–1.36; p = 0.86)**	
(Wallach et al., 2020)	33 RCTs (n = 21,156)	ROSI	≥ 24 weeks	**OR, 1.17 (95% CI 0.92–1.51; p < 0.05)**			**OR, 1.15 (95% CI 0.55–2.41; p < 0.05)**	**OR, 1.54 (95% CI 1.14–2.09; p < 0.05)**
(S. Singh et al., 2007a)	4 RCTs (n = 14,291)	ROSI	≥ 52 weeks	**RR, 1.42 (95% CI 1.06–1.91; p = 0.02)**			**RR, 0.90 (95% CI 0.63–1.26; p = 0.53)**	**RR, 2.09 (95% CI 1.52–2.88; p < 0.001)**
(Richter et al., 2007)	18 RCTs (n = 3,888)	ROSI	≥ 24 weeks	**No evidence**				**OR, 2.27 (95% CI 1.83–2.81; p < 0.05)**
(Lago et al., 2007)	7 RCTs (n = 20,191)	Both Agents	Not within the predefined inclusion criteria				**RR, 0.93 (95% CI 0.67–1.29; p = 0.68)**	**RR, 1.72 (95% CI 1.21–2.42; p = 0.002)**
(S. Singh et al., 2007b)	3 RCTs (n = 20,191)	Both Agents	≥ 24 weeks					**OR, 2.1 (95% CI 1.08–4.08; p = 0.03)**

Abbreviations: RCTs: randomised controlled trials; TZD: thiazolidinedione; PGZ: pioglitazone; ROSI: rosiglitazone; MI: myocardial infarction; HF: heart failure; CV: cardiovascular; RR: relative risk; OR: odds ratio; CI: confidence interval. *non-fatal MI; **non-fatal stroke

Although the mechanisms of the effects of TZDs on HF remain uncharacterised, a previous paper interestingly suggested mitochondrial dysfunction as a potential contributor to their cardiotoxic effects (Zhong et al, 2018). Since the scope of T2DM management has undergone major revisions and the selection of anti-diabetes medications is evolving towards those with cardiovascular benefits, it is imperative to expand our understanding of anti-diabetic agents that have potential cardiovascular benefits, including TZDs. Hitherto, and within the confines of TZDs' HF-inducing capacity, various platforms have been adopted, including *in silico* (PGZ only) (Zhong et al, 2018), *in vivo* and *in vitro* models (Asakawa et al, 2002; Biswas et al, 2012; Chinnam et al, 2012; Duan et al, 2005; Festuccia et al, 2009; Gouni-Berthold et al, 2001; Liu et al, 2012; Lygate et al, 2003; Qi et al, 2015; Son et al, 2007; Zhong et al, 2018), to explore such toxic effects (**Figure 2.1**).

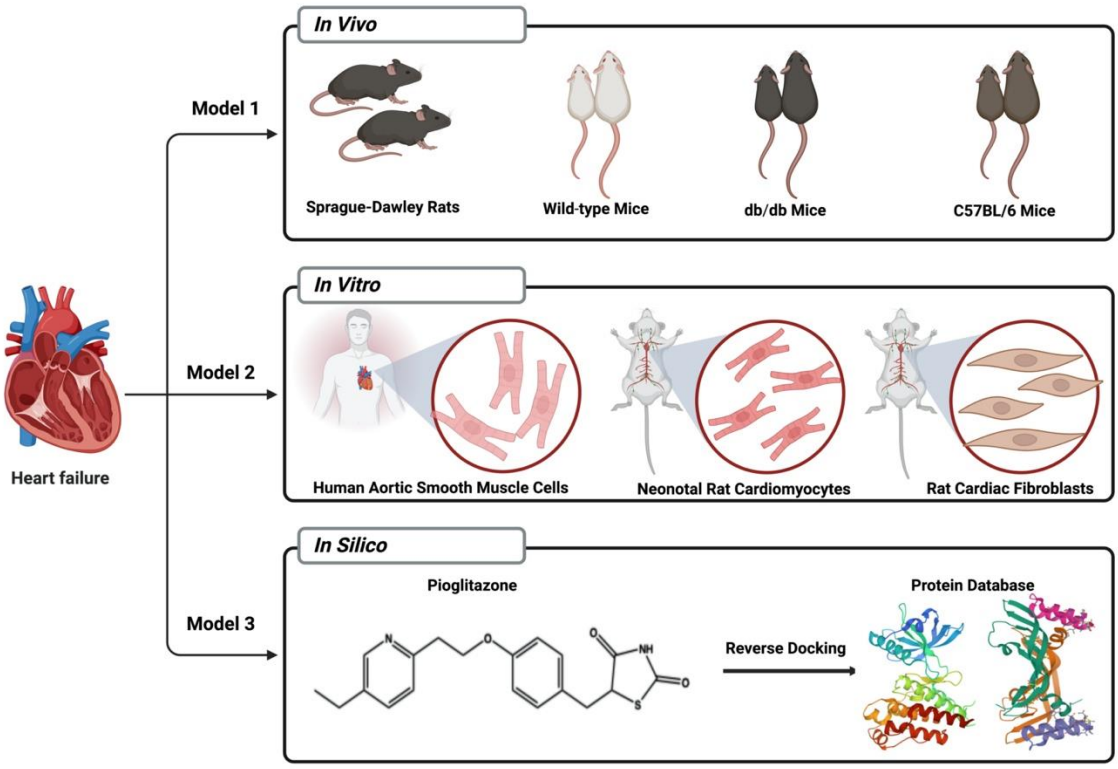

Figure 2.1 Overview of reported platforms adopted for TZD cardiotoxicity investigations. ROSI treatment induced diverse cardiac effects across *in vivo* models. In Sprague-Dawley rats, it triggered hypertrophy via the mTOR pathway, while wild-type mice exhibited increased lipid accumulation and cardiac damage. *db/db* mice experienced fluid retention upon ROSI administration, and supratherapeutic doses (10 and 30 μM) in C57BL/6 mice resulted in cardiac dysfunction (decreased pressure and relaxation rates, increased end-diastolic pressure). Both PGZ and ROSI displayed cytotoxic effects against vascular smooth muscle cells, but through distinct pathways: PPAR-γ signaling for PGZ and an ERK1/2-independent pathway for ROSI. PGZ exhibited dose-dependent inhibition of neonatal rat cardiomyocyte viability (higher doses up to 20 μmol/L showing a stronger effect). Conversely, ROSI treatment in neonatal rat cardiac fibroblasts increased connective tissue growth factor expression and decreased nitric oxide production at doses ranging from 0.1 to 10 μmol/L after a 48-hour pretreatment. Interestingly, *in silico* analysis using GOLD v5.3 software predicted VEGFR-2 as a potential target for PGZ in cardiovascular disease, suggesting that PGZ may influence cardiomyocyte hypertrophy through VEGFR-2 binding. PGZ: pioglitazone; ROSI: rosiglitazone; PPAR-γ: peroxisome proliferator-activated receptor gamma; mTOR: mammalian target of rapamycin; ERK1/2: extracellular signal-regulated kinase 1/2; GOLD: Genetic Optimization for Ligand Docking; VEGFR-2: vascular endothelial growth factor receptor 2. Adopted from (Asakawa et al, 2002; Biswas et al, 2012; Chinnam et al, 2012; Duan et al, 2005; Festuccia et al, 2009; Gouni-Berthold et al, 2001; Liu et al, 2012; Lygate et al, 2003; Qi et al, 2015; Son et al, 2007; Zhong et al, 2018).

Nevertheless, the application of human cardiac cell lines is limited. Therefore, the aims of this chapter are to traverse the potential implications of mitochondria as an off-target organelle for the cardiotoxic actions of TZDs by characterising the *in vitro* cytotoxicity of TZDs on AC16 human adult cardiomyocytes and primary human cardiac fibroblasts (HCFs) using various mitochondrial assays.

2.2 Methods

2.2.1 Drugs and Chemicals

PGZ, ROSI and the PPAR-γ antagonist GW9662 were purchased from Sigma-Aldrich (St Louis, MO, USA). For the *in vitro* studies, all drugs were dissolved in sterile dimethyl sulphoxide (DMSO) (Cat. No. 12611P; Cell Signaling Technology, Beverly, MA, USA), and the stock solutions (100 mM) were subsequently diluted to the appropriate concentrations with culture medium. The final concentration of DMSO in the medium was ≤0.1% (v/v).

2.2.2 Cells and Culture Conditions

The AC16 cell line was derived from adult human ventricular cardiomyocytes and was purchased from Sigma-Aldrich (Product No. SCC109; St. Louis, MO, USA). The cells were cultured in Dulbecco's Modified Eagle's Medium/Nutrient Mixture F-12 (DMEM/F-12) (Product No. D6434; Sigma-Aldrich, St Louis, MO, USA) supplemented with 12.5% foetal bovine serum, 1% antibiotics (streptomycin and penicillin) and 2 mM L-glutamine at 37 °C in a humid atmosphere of 5% CO_2 and 95% air.

HCFs obtained from the ventricles of the adult heart were purchased from PromoCell GmbH (Product. No. C-12375; Heidelberg, Germany). The HCFs were cultured using Fibroblast Growth Medium 3 (Product. No. C-23025; PromoCell GmbH, Heidelberg, Germany) and kept in a humidified incubator at 37 °C and 5% CO_2.

2.2.3 Cell Viability Assay

The cytotoxic effect of TZDs on cardiomyocyte and cardiac fibroblast proliferation was measured using an MTT [3-(4,5-dimethylthiazol-2-yl)-2,5-diphenyltetrazolium bromide] assay kit (Cat. No. V13154; Thermo Fisher, Eugene, OR, USA). The cells were seeded in 96-well microplates (Cat. No. 655180; Greiner Bio-One, Gillingham, Dorset, UK) (1×10^4 cells/well) and exposed to increasing concentrations of the TZD agent (0.01, 0.1, 0.5, 1, 5, 10, and 20 μM) for 24 h. Following the incubation period, 10 μL of the MTT solution (5 mg/mL) was added to each well, the supernatants were removed and 50 μL of DMSO was used to dissolve the yielded formazan precipitate. A plate reader (GloMax Explorer Multimode Microplate Reader; Promega, Madison, WI, USA) was used to measure the formazan absorbance at 560 nm.

Cell viability was expressed as a percentage and calculated as follows:

$$(\text{A-treatment} - \text{A-blank})/(\text{A-control} - \text{A-blank}) \times 100\%$$

where *A* is absorbance. The half maximal inhibitory concentration (IC_{50}) value was determined from a three-parameter nonlinear regression curve fitted to TZD concentration and the obtained absorbance values using GraphPad Prism 9 software (San Diego, CA, USA).

2.2.4 Luminescence Assay Used to Detect Caspase Activity

The activity of caspase 3 and caspase 7 was assessed using a Caspase-Glo 3/7 assay kit (Part No. G8090; Promega, Madison, WI, USA) according to the manufacturer's protocol. Cells were seeded in white-walled 96-well plates (1×10^5 cells/well) and incubated overnight. Following exposure to various concentrations of either PGZ or ROSI (0.01, 0.1, 1, 5, 10 and 20 μM) for 24 h, the cells were lysed by adding 100 μL of the Caspase-Glo 3/7 reagent to each well. Subsequently, equal volumes of the samples and reagent were mixed and incubated for 1 h at room temperature. Luminescence was measured using a plate reader (GloMax Explorer Multimode Microplate Reader). The activity was expressed as relative luminescence units (RLU) and calculated using the following formula:

$$\text{RLU} = \text{luminescence (sample)} - \text{luminescence (blank)}$$

2.2.5 Measurement of Adenosine Triphosphate Production

The CellTiter-Glo Luminescent Assay (Part No. G7570; Promega, Madison, WI, USA) was used to determine the level of cellular metabolism by measuring adenosine triphosphate (ATP) levels. Cells were seeded in white 96-well microplates (1×10^4 cells/well) and incubated for 24 h. The cells were then exposed to increasing concentrations of PPAR-γ agonist (1, 5, 10, 50 and 100 μM) in the presence or absence of GW9662 (5 μM) and incubated for a further 24 h. Subsequently, 100 μL of the CellTiter-Glo reagent was added to each well and the plates were agitated for 1 min in a shaking incubator. A luminometer (GloMax Explorer Multimode Microplate Reader) was then used to measure the luminescence.

2.2.6 Mitochondrial Membrane Potential Measurement

TZD-stimulated changes in the mitochondrial membrane potential (ΔΨm) were assessed using the JC-1-Mitochondrial Membrane Potential Assay Kit (Cat. No. ab113850; Abcam, Cambridge, UK). Cells were seeded (50,000 cells/well) and allowed to adhere overnight in a black, clear-bottom 96-well plate (Cat. No. 165305; Thermo Fisher, Rochester, NY, USA). The cells were exposed to various concentrations of PGZ or ROSI (1, 5, 10, 50 and 100 μM) and incubated for 24 h. Afterwards, the cells were washed once with phosphate-buffered saline (PBS) and then incubated with 10 μM JC-1 dye for 10 min at 37 °C while protected from light. Following incubation, the wells were washed with 1× dilution buffer (provided in the kit). The fluorescence related to the mitochondrial membrane potential (MMP) was measured immediately using a FlexStation 3 Multi-Mode Microplate Reader (Molecular Devices, Sunnyvale, CA, USA) at the maximum excitation and emission spectra of 531 and 595 nm, respectively, as well as 485 and 535 nm for aggregate and monomer forms, respectively. Background fluorescence was subtracted from the fluorescence of the treated cells, and the ratio of red (polarised) fluorescence to green (depolarised) fluorescence was obtained.

2.2.7 Determination of Reactive Oxygen Species Production

To examine the ability of TZDs to induce the production of reactive oxygen species (ROS) in the cells, the intracellular level of the ROS was estimated using a fluorescent 2′7′-dichlorodihydrofluorescein diacetate dye (H_2DCFDA) (Cat. No. D399; Thermo Fisher, Waltham, MA, USA). H_2DCFDA, a chemically reduced form of fluorescein, is a nonpolar compound converted into a polar and membrane-impermeable derivative of H_2DCF under the presence of cellular esterases (Wu & Yotnda, 2011). The latter compound is nonfluorescent (Wu & Yotnda, 2011). However, upon oxidation through the intracellular level of ROS, H_2DCF is oxidised to highly fluorescent 2',7'-dichlorofluorescein (DCF) (Wu & Yotnda, 2011).

Cells were seeded in a dark, clear-bottomed 96-well microplate (50,000 cells/well) and incubated overnight. Following 24 h of incubation, the cells were washed once with PBS and loaded with 5 μM H_2DCFDA for 30 min at 37 °C in the dark. Subsequently, the dye was removed, and the cells were exposed to various concentrations of PGZ or ROSI (1, 5, 10, 50 and 100 μM) and incubated for 6 h. DCF fluorescence was

measured using a FlexStation 3 Multi-Mode Microplate Reader (Molecular Devices, Sunnyvale, CA, USA) at the maximum excitation and emission spectra of 492 and 517 nm, respectively.

A detailed description of the mechanisms underlying each assay can be found in **Table S1** of **Appendix Section 7.1.**

2.2.8 Statistical Analysis

Cytotoxicity data are expressed as mean ± SD. At least three independent experiments were performed for each cytotoxicity assay, with three or more technical replicates for each experimental group tested. Statistical significance was determined using Student's or Welch's *t*-test when comparing two groups. A non-repeated one-way analysis of variance (ANOVA), followed by Dunnett's post-hoc test, was used for multiple comparisons. A p-value < 0.05 was considered statistically significant.

The experimental design employed in this study is depicted in **Figure 2.2**.

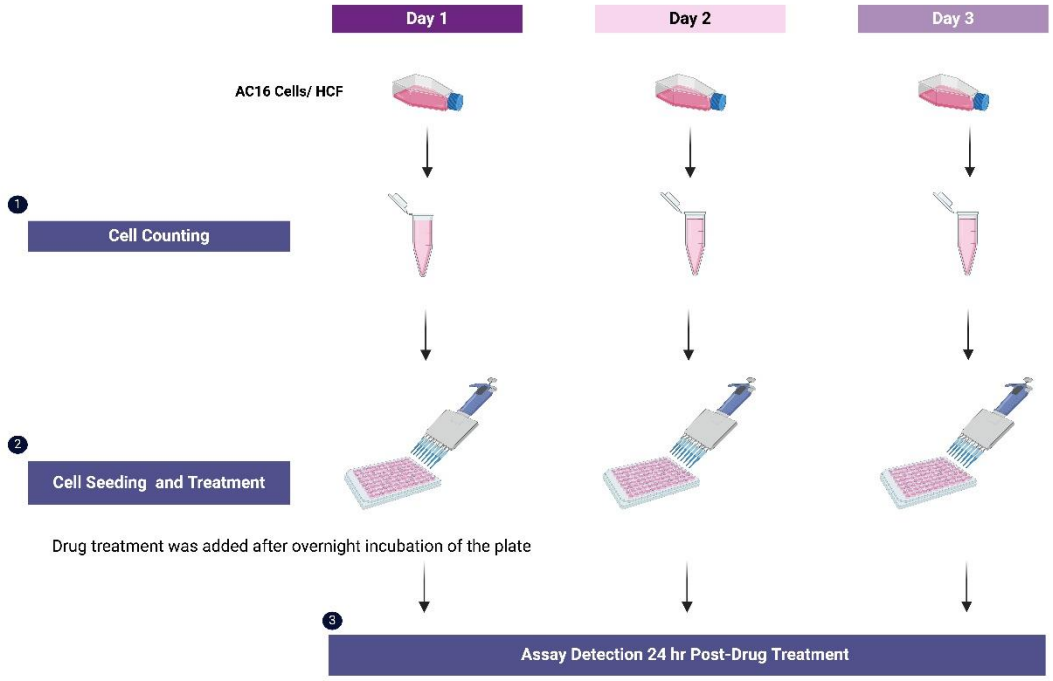

Figure 2.2 Experimental design for functional assays. Each experimental group was subjected to three independent cytotoxicity assays (biological replicates n=3), each with at least three technical replicates, for each experimental group. In each assay, the cells were pre-cultured for 24 h in 96-well plates and incubated with increasing concentrations of either PGZ or ROSI for another 24 h. *In vitro* endpoints were then assessed according to the manufacturer's protocol.

2.3 Results

2.3.1 Effect of TZDs on Cell Viability

The effects of PGZ and ROSI on the viability of the two human cardiac cell types, AC16 and HCF, were assessed using the MTT assay. Cells were treated with a wide range of concentrations of either PGZ or ROSI (0.01, 0.1, 0.5, 1, 5, 10 and 20 μM). Then, after a 24-h incubation period, the cytotoxic effect was measured. As shown in **Figures 2.3A and 2.3C**, the PGZ treatment resulted in concentration-dependent cell death, and the IC_{50} values against AC16 cells and HCFs, calculated using the Hill equation (Goutelle et al, 2008), were 4.74 μM (R^2 = 0.99; 95% CI 3.842–5.894) and 0.37 μM (R^2 = 0.96; 95% CI 0.1472–0.9358), respectively. The exposure of both AC16 and HCFs to ROSI led to a notable decrease in cell viability, which closely resembled the concentration-dependent manner observed with PGZ. As seen in **Figures 2.3B** and **2.3D**, the IC_{50} values of ROSI against AC16 cells and HCFs were 2.05 μM (R^2 =

0.98; 95% CI 1.270–3.495) and 0.95 μM (R^2 = 0.90; 95% CI 0.1865–6.006), respectively.

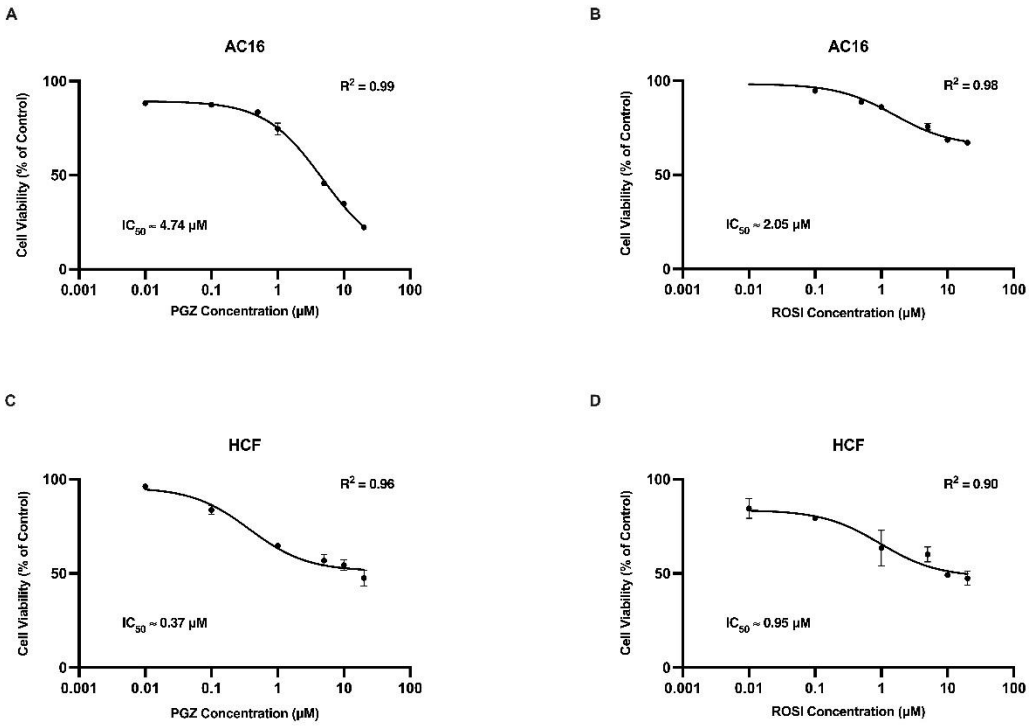

Figure 2.3 Cytotoxic effects of TZDs on selected cardiac cell types. Concentration-response modelling (applying the Hill equation) and corresponding IC_{50} values for PGZ (A, C) and ROSI exposure (B, D) in AC16 cells and HCFs, respectively. In each experiment, cells were pre-cultured for 24 h in 96-well plates (1×10^4 cells/well) and incubated with increasing concentrations of either PGZ or ROSI for another 24 h. Each point is the average of four independent experiments (each in quadruplicate), with standard deviation indicated by error bars. R^2 indicating goodness of fit of the model.
TZDs: thiazolidinediones; IC_{50}: half maximal inhibitory concentration; PGZ: pioglitazone; ROSI: rosiglitazone; HCFs: human cardiac fibroblasts

2.3.2 Effect of TZDs on Caspase 3/7 Activity

To investigate the molecular mechanisms underlying the TZD-induced loss of cell viability, we first determined whether apoptosis occurred by measuring caspase 3/7 activity—a gold standard measure of apoptosis (Niles et al, 2008). This assay produces a luminescent substrate that has a four-peptide sequence, which, after cleavage by caspase 3/7, generates a light signal produced by luciferase (Niles et al, 2008). As shown in **Figures 2.4A** and **2.4C**, PGZ did not activate caspase 3/7 activity. The observed effect was noted in both AC16 and HCFs at all tested concentrations.

Furthermore, caspase 3/7 activity was lower in ROSI-treated HCFs than in cells treated with the control medium (**Figure 2.4D**). However, the activation of caspase 3/7 activity was observed in ROSI-treated AC16 cells that reached significance at 0.01, 0.1, 1, 5, 10 and 20 μM (**Figure 2.4B**).

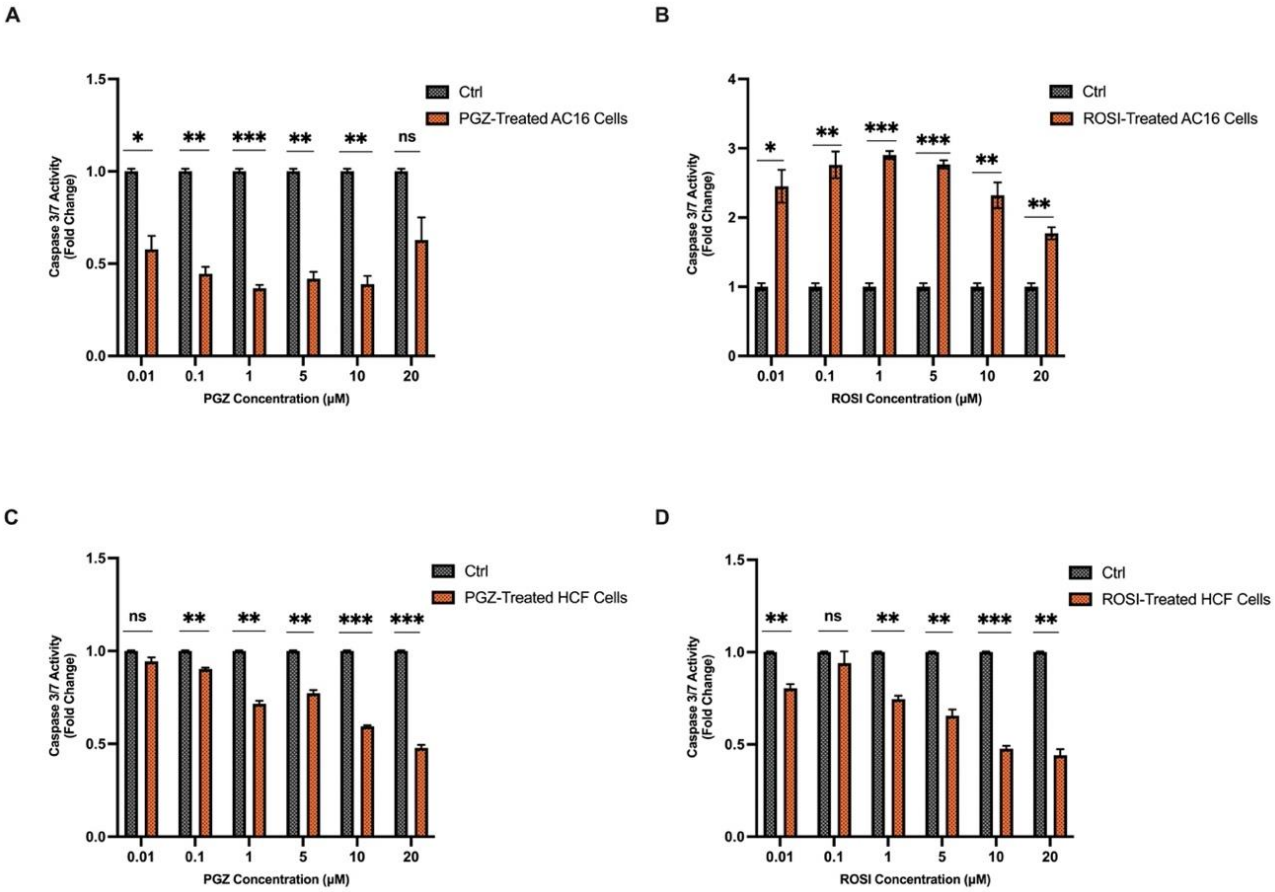

Figure 2.4 The effect of TZDs on caspase 3/7 activity. The fold change in the *y*-axis represents the level of caspase 3/7 activity in the TZD-treated AC16 (A, B) or HCF cells (C, D) relative to that of the control group. The data are from three independent experiments, each performed in triplicate, and are expressed as the mean ± SD. Statistical significance was assessed using Student's *t*-test (each concentration of TZD vs. control).
* $p < 0.05$, ** $p < 0.01$, *** $p < 0.001$ and **** $p < 0.0001$
TZDs: thiazolidinediones; HCFs: human cardiac fibroblasts; ns: non-significance

2.3.3 Involvement of PPAR-γ in TZDs' Effects on Cell Viability

Figures 2.5A–D show the effect of TZD on mitochondrial ATP production and the involvement of PPAR-γ in TZD-induced cell death. In both cardiac cell types, the administration of PGZ or ROSI markedly decreased mitochondrial ATP production in a concentration-dependent manner.

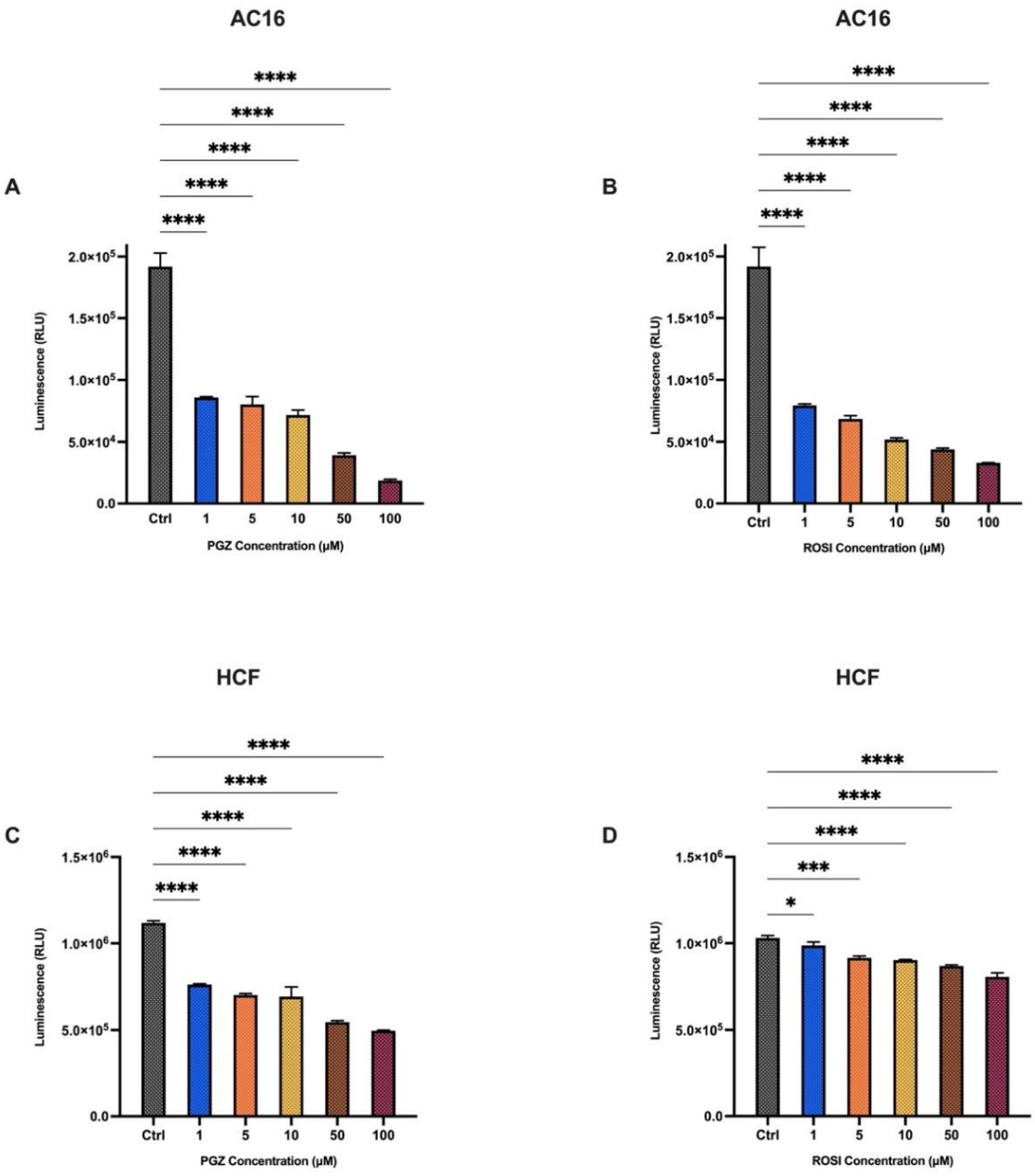

Figure 2.5 The effect of TZDs on mitochondrial ATP production. Quantifying cellular ATP production levels of AC16 cells (A, B) and HCFs (C, D) after 24 h of exposure to increasing concentrations of either PGZ or ROSI using the CellTiter-Glo luminescent assay. The data are from three independent experiments, each performed in triplicate, and are expressed as the mean ± SD. Statistical significance was determined using a one-way ANOVA and Dunnett's multiple comparisons test (control vs. each concentration of TZD).
* $p < 0.05$, ** $p < 0.01$, *** $p < 0.001$ and **** $p < 0.0001$
TZDs: thiazolidinediones; ATP: adenosine triphosphate; HCFs: human cardiac fibroblasts; PGZ: pioglitazone; ROSI: rosiglitazone

Interestingly, the co-administration of TZDs and PPAR-γ antagonist GW9662 (5 μM) resulted in multi-faceted effects (**Figure 2.6**). The presence of GW9662 partially

attenuated the cytotoxic effect of PGZ on AC16 cells. Nevertheless, its presence worsened the cytotoxicity of PGZ in HCFs and further decreased the ATP levels of both AC16 and HCFs following ROSI exposure.

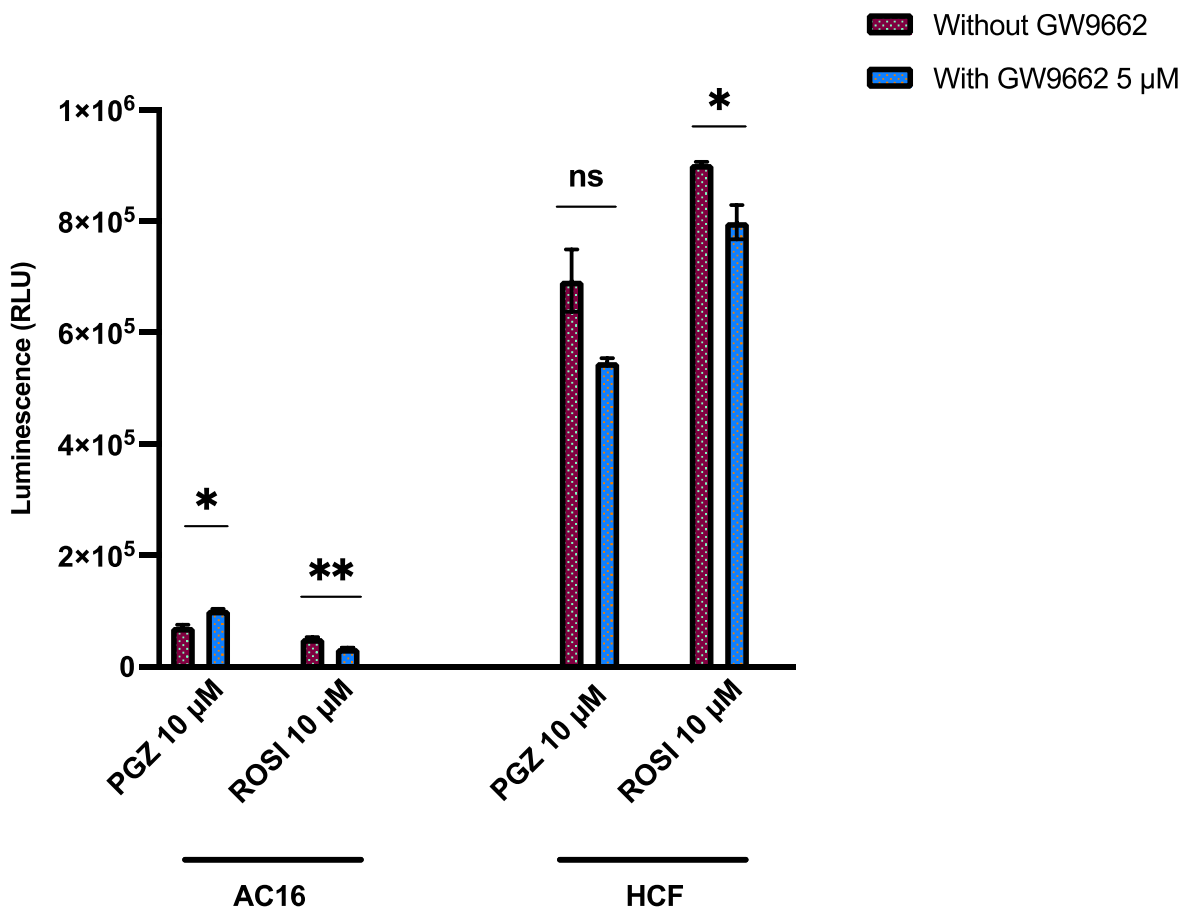

Figure 2.6 The effect of the PPAR-γ inhibitor GW9662 on TZD-induced cytotoxicity. AC16 cells or HCFs were pre-cultured for 24 h in 96-well plates (1 × 10^4 cells/well) and exposed to either PGZ (10 µM) or ROSI (10 µM) with or without GW9662 (5 µM) for another 24 h. The data are from three independent experiments, each performed in triplicate, and are expressed as mean ± SD. Statistical significance was assessed using Student's *t*-test (TZD vs. TZD + GW9662).
* $p < 0.05$, ** $p < 0.01$
PPAR-γ: peroxisome proliferator-activated receptor gamma; TZD: thiazolidinedione; HCFs: human cardiac fibroblasts; PGZ: pioglitazone; ROSI: rosiglitazone; ns: non-significant

2.3.4 Effect of TZDs on MMP Depolarisation

MMP is a key hallmark of the mitochondrial bioenergetic state, as it reflects the cells' capability to generate ATP through oxidative phosphorylation (Zorova et al, 2018). Due to the decrease in ATP production observed following 24 h of TZD treatment (**Figure 2.5**), it is highly anticipated that TZDs act on the motive force processes that

drive ATP production, oxidative phosphorylation and glycolysis. Given that the majority of ATP generated in the heart is through oxidative phosphorylation (>95%), the effect of TZDs on MMP was therefore assessed using the fluorescent reagent JC-1. Treatment with TZDs showed a marked decrease in ΔΨm in both AC16 cells and HCFs, as illustrated in **Figure 2.7**.

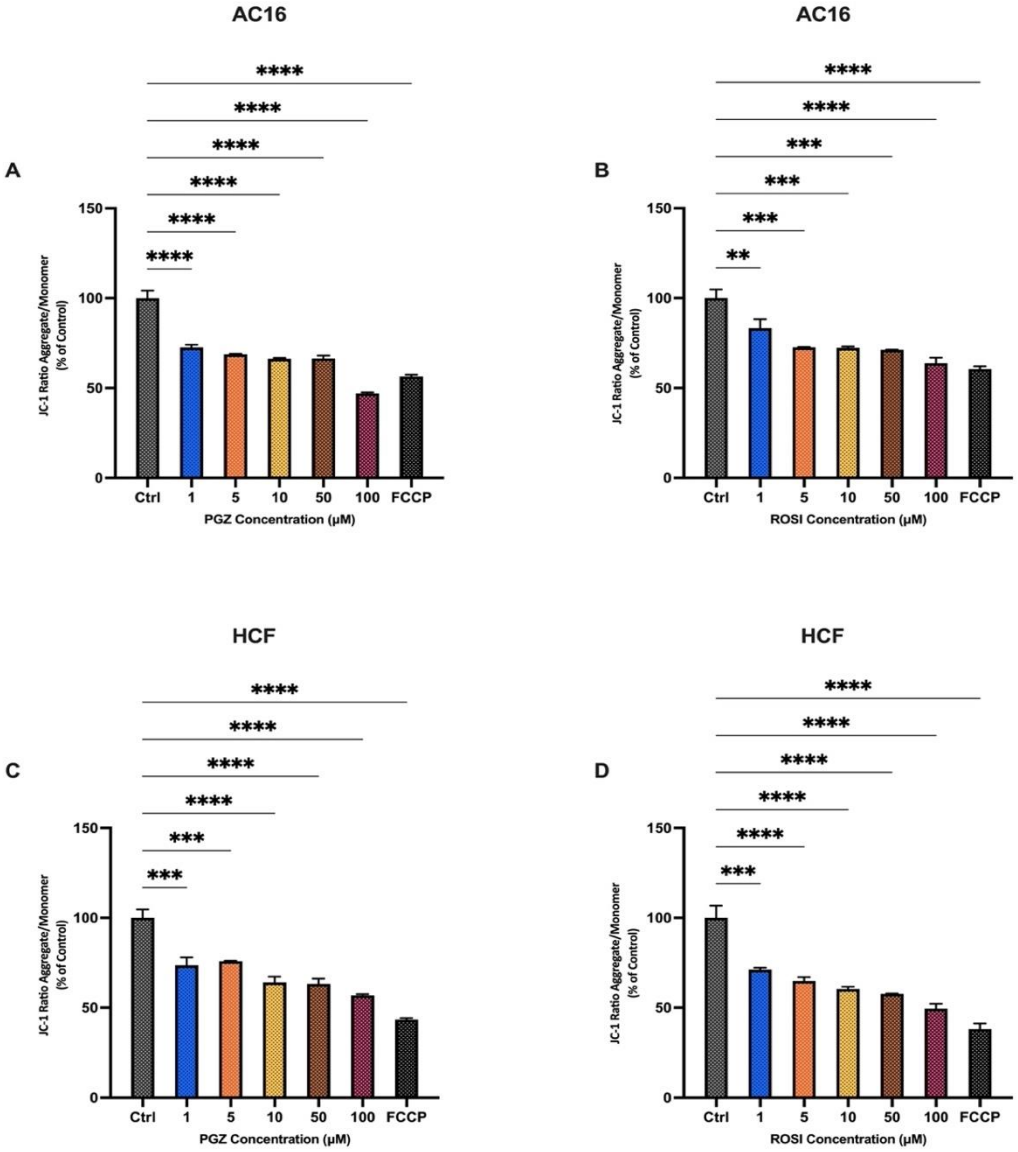

Figure 2.7 The ΔΨm of selected cardiac cell types following TZD treatment. Cells were pre-cultured for 24 h in 96-well plates (5 × 10^4 cells/well) and exposed to various concentrations of PGZ (A, C) or ROSI (B, D) for another 24 h. FCCP (100 μM), the depolarizing agent, served as a positive control for this assay. Afterwards, the cells were loaded with 10 μM JC-1 dye and fluorescence was measured using a microplate reader. The data are from three independent experiments, each performed in triplicate, and are expressed as the mean ± SD. Statistical significance was determined using a one-way ANOVA and Dunnett's multiple comparisons test (control vs. each concentration of TZD).
* $p < 0.05$, ** $p < 0.01$, *** $p < 0.001$ and **** $p < 0.0001$
TZDs: thiazolidinediones; MMP: mitochondrial membrane potential; PGZ: pioglitazone; ROSI: rosiglitazone; FCCP: carbonyl cyanide 4-phenylhydrazone

2.3.5 Effect of TZDs on ROS Production

To determine the role of oxidative stress in TZD-induced cytotoxic effects, the fluorogenic dye H_2DCFDA, a marker of a broad spectrum of ROS, was used to measure the intracellular levels of ROS in selected cardiac cell types following TZD treatment. The results showed that PGZ significantly increased ROS levels at concentration ranges of 10–100 μM and 1–100 μM in AC16 cells and HCFs, respectively (**Figures 2.8A and 2.8C**). ROSI treatment markedly elevated ROS levels in both AC16 and HCFs at a concentration range of 1–100 μM (**Figures 2.8B and 2.8D**).

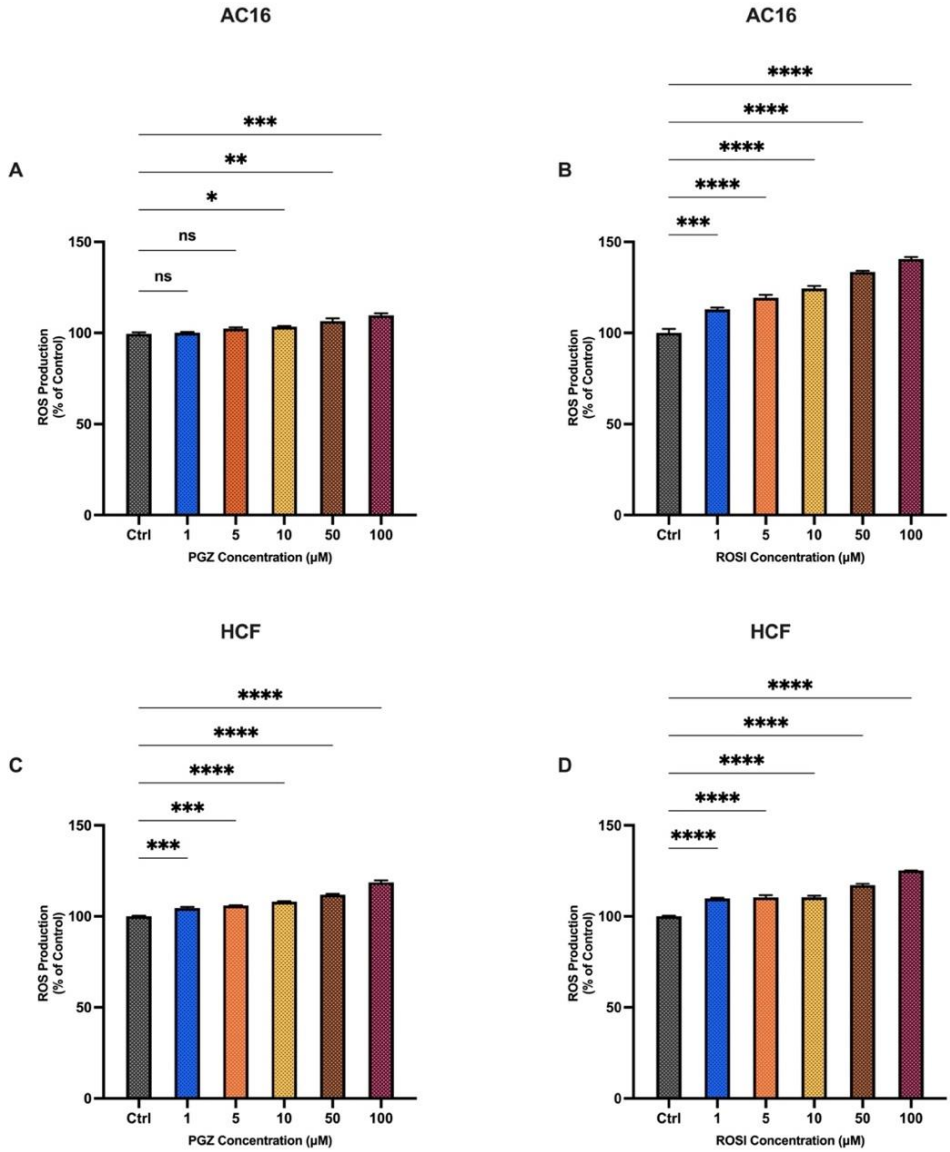

Figure 2.8 Effect of TZDs on ROS production. AC16 cells (A, B) and HCFs (C, D) were pre-cultured for 24 h in 96-well plates (50,000 cells/well). Afterwards, the cells were loaded with 5 μM H_2DCFDA and exposed to various concentrations of either PGZ or ROSI. The data are from three independent experiments, each performed in triplicate, and are expressed as the

mean ± SD. Statistical significance was determined using a one-way ANOVA and Dunnett's multiple comparisons test (control vs. each concentration of TZD).
* $p < 0.05$, ** $p < 0.01$, *** $p < 0.001$ and **** $p < 0.0001$
TZDs: thiazolidinediones; ROS: reactive oxygen species; HCFs: human cardiac fibroblasts; PGZ: pioglitazone; ROSI: rosiglitazone; ns: non-significance

2.4 Discussion

2.4.1 Research Design Rationale

As clinical practice is evolving towards a new, evidence-based era of T2DM management guidelines, it is imperative to enrich our understanding of anti-diabetic agents, especially those that carry potential benefits against cardiovascular disease, including TZDs (ADA, 2023). Since their approval for T2DM management in the early 2000s, TZDs have demonstrated a range of cardiovascular effects that have ultimately limited their selection as anti-diabetic agents of choice (ADA, 2023; Starner et al, 2008). For instance, despite large clinical trials that have evidenced a reduced risk of atherosclerosis progression, in-stent restenosis after coronary stent implantation, MI and ischaemic stroke in TZD-treated patients, the reported consensus is that increased risk of HF is associated with TZD use (De Flines & Scheen, 2007). Nevertheless, few mechanistic studies have addressed the TZD-induced HF mode of toxicity, leaving us with inconclusive evidence on the role of TZDs in cardiovascular disease risk.

Today, emerging evidence implicates mitochondrial dysfunction as a potential determinant of the unfavourable effects of various off-target medications (Varga et al, 2015; Vuda & Kamath, 2016). Troglitazone, a member of the TZD family, is an example of an anti-diabetic agent with toxicity linked to mitochondrial damage (Julie et al, 2008; Rachek et al, 2009). Troglitazone was first introduced into the US market in 1997 for the management of T2DM (Rachek et al, 2009). However, a few months after its approval, numerous hepatotoxicity cases were reported, including hepatic failure necessitating hepatic transplantation and even instances of death (Rachek et al, 2009). These eventually led to its withdrawal from the UK and US markets in late 1997 and 2000, respectively (Julie et al, 2008; Rachek et al, 2009). Mechanistic studies have proposed that a decline in mitochondrial ATP production and the

induction of oxidative stress, which contribute to mitochondrial damage, are potential mechanisms for troglitazone-induced hepatotoxicity (Julie et al, 2008; Rachek et al, 2009). Interestingly, a previous paper also suggested that damage to the mitochondria, an off-target organelle, may be responsible for the cardiotoxic effects of both PGZ and ROSI (Zhong et al, 2018). Hence, to gain deeper insight into this specific potential effect, the cytotoxicity of TZDs on selected human cardiac cell types, AC16 cells and HCFs, as well as their action mechanisms in terms of PPARγ dependency, were investigated in this study primarily using mitochondrial assays, each of which carries a different endpoint (MTT assay: implication of mitochondrial dehydrogenases; ATP assay: measurement of oxidative phosphorylation; caspase 3/7 assay: activity of caspase 3/7 in cellular apoptosis; MMP: reflection of membrane depolarisation, electron transfer and oxidative phosphorylation; and ROS: measurement of oxidative stress).

2.4.2 Interpretation of Results

2.4.2.1 Crosstalk Between TZDs and Mitochondrial Functions

The results from the MTT assay indicated that TZDs exhibited cytotoxicity against AC16 cells with high potency, reflected by IC_{50} values of 4.74 μM and 2.05 μM at 24 h for PGZ and ROSI, respectively. Our results correspond with those of a previous study in which rat cardiomyocytes exhibited a dose-dependent loss of viability following PGZ administration, with effective concentrations ranging from 0 to 20 μM/L (Zhong et al, 2018). Analogously, dose-dependent reduction in H9c2 (rat cardiomyocyte) proliferation in response to ROSI exposure was also reported elsewhere, but at doses that ranged between 1 and 100 μM (Mishra et al, 2014). Our study also shed light on TZDs' effects on cardiac fibroblast viability, suggesting detrimental cytotoxic effects of TZDs on HCFs, as indicated by lower IC_{50} values of both PGZ and ROSI compared to the AC16 cell line. The effect of TZDs on cardiac fibroblasts was reported only once, when an *in vitro* study showed a reduction in cardiac fibroblast viability following ROSI exposure (Li et al, 2008). These cytotoxic effects potentially indicate a mitochondrial involvement in TZDs' cytotoxicity, as the MTT assay relies on mitochondrial respiration (mitochondrial succinate dehydrogenase) for the enzymatic reduction of MTT to the MTT-formazan product (Ghasemi et al, 2023).

In this study, the role of mitochondrial dysfunction in TZD-induced cardiotoxicity was examined further by measuring the effect of TZDs on mitochondrial ATP production. Consistent with the aforementioned MTT assay findings, TZD treatment led to a marked reduction in the intracellular ATP production in both cardiac cell types. To investigate TZDs' cytotoxicity in terms of PPAR-γ dependency, the effect of TZDs on ATP production was assessed in the presence and absence of a PPAR-γ antagonist (GW9662). The partial restoration of ATP production noted in PGZ-treated AC16 cells and the further decrease in the ATP levels in PGZ-treated HCFs and in both AC16 and HCFs following ROSI exposure strongly indicated that the observed cytotoxicity was not fully PPAR-γ dependent and that potentially an off-target effect was involved. As such, it seems that TZDs induced mitochondrial damage that led to AC16 cells' and HCFs' death due to a decline in ATP production. These findings correspond with a previous *in vivo* study performed in mice, in which ROSI treatment significantly compromised mitochondrial respiration and substrate oxidation, resulting in decreased ATP production and deterioration of cardiac function, notably at a concentration of 10 μM (He et al, 2014). These findings also agree with those of several other studies that showed a correlation between the cytotoxic effects of various chemicals and insufficient ATP levels (Julie et al, 2008; Rachek et al, 2009).

The exact mechanism behind the induced mitochondrial dysfunction is complex. However, our analysis findings strongly suggest that the uncoupling of oxidative phosphorylation is involved in mediating mitochondrial damage. Mitochondria are well-recognised as the cellular 'powerhouse', orchestrating cardiac energy production primarily through oxidative phosphorylation (Stoker et al, 2019). The latter biological process involves a flow of electrons through five electron transport chain complexes (ETC I–V) (Deshpande & Mohiuddin, 2020). The passage of electrons generated from energy-rich molecules nicotinamide adenine dinucleotide and flavin adenine dinucleotide, through glycolysis, fatty acid oxidation and the citric acid cycle to oxygen, which occurs through the ETC located in the inner membrane of the mitochondria, pumps hydrogen ions out of the matrix (Deshpande & Mohiuddin, 2020). This pumping generates an electrochemical gradient and a membrane voltage that creates a high proton motive force (PMF) (Deshpande & Mohiuddin, 2020). This high PMF, which is the driving force of MMP, will eventually generate ATP from ADP and phosphate through the flow of protons back to the mitochondrial matrix through the ATP synthase

enzyme (Zorova et al, 2018). Therefore, when considering the decrease in MMP noted in both cardiac cell types following TZD exposure (**Figure 2.7**) and when referring to the prominent role that MMP has in ATP production, it can be postulated that cells treated with TZD agents exhibited a mitochondrial uncoupling that potentially led to sequelae of events initiated with disruption in the PMF and MMP defects and ending up with a loss of ATP production. There is cumulative evidence of similar results, in which the cytotoxic effects of chemicals including bisphenol A and *N*-nitrosofenfluramine arose from the interplay between MMP defects and ATP depletion (Khan et al, 2016; Nakagawa et al, 2005).

To explain the association between MMP defects and mitochondrial uncoupling further, TZDs' effect on oxidative stress was evaluated. The results indicated that TZD exposure induced ROS generation in both AC16 and HCFs. These findings may have one of two theoretical underpinnings, as follows: (i) First, the cellular redox imbalance state generated following TZD exposure may be the implicated mechanism behind mitochondrial uncoupling and subsequent MMP defects, eventually leading to mitochondrial damage, ATP depletion and cell death. This notion is supported by other studies' findings, one of which evaluated the mechanism of usnic-acid-induced liver toxicity, finding usnic acid to induce ROS generation in HepG2 cells, which resulted in MMP loss and cell death (Sahu et al, 2012). The second explanation (ii) is that the TZD-induced oxidative stress is secondary to the mitochondrial uncoupling and membrane depolarisation, with the increase in electron leakage from the electron transport chain resulting from mitochondrial damage and leading to excessive generation of ROS species (Zorova et al, 2018). In alignment with TZDs' effect on redox homeostasis, consistent findings in regard to the induction of oxidative stress following ROSI exposure were reported both from studies *in vivo* and *in vitro* (He et al, 2014; Riess et al, 2020).

2.4.2.2 Insights into Molecular Mechanisms for TZD-Induced Cell Death

Cell death is a common pathological mechanism that underpins all cardiovascular diseases, regardless of whether it is the endpoint or a sign of impending disease progression. However, there are distinct types of cell deaths, and those are greatly disease dependent. To investigate the type of cell death in the cardiac cells treated with TZD agents, the level of apoptosis was examined by measuring caspase 3/7

activity. It was found that this activity was not markedly elevated in the TZD-treated cardiac cells apart from the observation endpoints noted in ROSI-treated AC16 cells, suggesting the following: (i) PGZ could have inhibitory effects on caspase-dependent apoptosis. In a previous study conducted on adult male Sprague–Dawley rats, the effect of PGZ on cardiomyocyte apoptosis was investigated (Li et al, 2008). In this *in vivo* model, rats were randomly divided into four groups: a sham-operated control group (treated with 0.9% saline), an ischaemia/reperfusion (I/R) group (treated with 0.9% saline), a PGZ-treated group (3 mg/kg) and a group treated with 5-hydroxydecanoate (5-HD, 10 mg/kg) and PGZ (3 mg/kg). After 24 h of treatment, the rats were subjected to 30 min of ischaemia followed by 4 h of reperfusion (Li et al, 2008). The apoptosis rate and three proteins (B-cell lymphoma 2 (Bcl-2), Bcl-2-associated X protein (BAX) and caspase-3) were detected using immunohistochemistry staining. The PGZ-treated group had a significantly lower ($p < 0.05$) apoptosis rate and positive cell index (PCI) for Bax and caspase-3 compared to the I/R group, and a marked increase in the PCI for Bcl-2 was noted (Li et al, 2008). Together, these findings revealed the inhibitory effects that PGZ has on cardiomyocyte apoptosis. (ii) Caspase assay findings imply that other types of cell death—particularly necrosis—might underpin TZD's cell death effects. The defects in MMP and the depletion of mitochondrial ATP observed in cardiac cells exposed to TZD are characteristic biochemical features of necrosis. Various mechanistic studies have reported cellular necrosis as common sequelae of chemical-induced ATP depletion (Julie et al, 2008; Rachek et al, 2009); nevertheless, further investigations are warranted to examine its implication for TZDs' cardiotoxicity. (iii) The activation in caspase 3/7 that we noted in ROSI-treated AC16 cells was also noted in another *in vitro* study, in which ROSI treatment induced apoptosis at 50 and 60 μM in cultured H9c2 cells (Mishra et al, 2014). A possible explanation is that apoptosis activation could be secondary to mitochondrial uncoupling, through which the collapse in MMP defects noted after ROSI treatment could result in increased calcium influx into the mitochondria, triggering cytochrome c release from the mitochondria to the cytoplasm (Zorova et al, 2018). The presence of cytochrome c in the cytoplasm allows for binding of cytochrome c to apoptotic protease activating factor 1, leading to activation of the caspase cascade (Zorova et al, 2018). Another mechanistic insight regarding the observed caspase activation concerns elevated ROS levels. High levels of ROS were reported to activate caspase 3/7 through multiple pathways including direct oxidising

of caspases that trigger apoptosis, or via activating mitogen-activated protein kinase (MAPK) signalling pathways, which can eventually lead to caspase activation and apoptosis (Yue & López, 2020).

In light of the observational endpoints outlined, the mechanistic basis for the disparity between PGZ and ROSI in caspase activation remains elusive. Nevertheless, it is well-recognised that there are slight differences in chemical structure and stereochemistry between PGZ and ROSI (e.g. the presence of a methyl group on the 5-position of the thiazolidinedione ring in PGZ and not in ROSI) (Naim et al, 2017) (**As illustrated in Figure 1.10 from Chapter 1**). On account of these differences, TZDs have distinct PPAR selectivity, with ROSI purely selective to PPAR-γ, while PGZ also exerts some PPAR-α actions (Naim et al, 2017). These detailed divergences in the chemical and pharmacological properties between the two TZD agents could possibly explain the variation in caspase activation noted in the present study.

2.4.3 The Study's Limitations and Future Directions

We caution that this study has potential limitations, which should frame how the findings are interpreted. First, all cytotoxic assays were conducted using an *in vitro* platform; therefore, it is imperative to address the limitations associated with each cardiac cell line. HCFs are primary cells isolated from the ventricles of human adults; hence, they are phenotypically and genetically identical to their parental tissue (Jonsson et al, 2016). As with most primary cells, HCFs' have been shown to retain many of their functional and differentiated characteristics (Jonsson et al, 2016). Yue et al. also reported these cells' ability to express various receptors including cardiac-delayed-rectifier potassium channels, inward-rectifier potassium channels and the swelling-activated chloride current, which collectively make them candidates for investigating various cardiovascular pathologies, including cardiac hypertrophy (Yue et al, 2013). Nevertheless, the preparation of HCFs is labour intensive and the handling of these cells requires extensive skills and careful planning (Eckerle et al, 2014).

Another limitation of this study concerning primary cells' usage is their short lifespan, attributed to cellular senescence genes (Eckerle et al, 2014). In addition, the reproducibility of the findings could be influenced by several confounders, which

include the hormonal, cellular and genetic variabilities among individual donors (Ng & Schantz, 2010). Intra-donor differences due to sex, age, ethnicity, diet and body mass index could also impact the validity and efficiency of the results (Ng & Schantz, 2010). Meanwhile, the AC16 cell line is an immortalised, stable cell line, derived from adult human ventricular cardiomyocytes, which has been used widely in toxicology research (Davidson et al, 2005). It expresses adult cardiomyocyte-specific biomarkers (α-myosin heavy chain [α-MHC], β-MHC, α-actin and troponin I) and displays electrophysiological properties comparable with primary human cardiomyocytes, which generally explains its wide application in *in vitro* studies (Davidson et al, 2005). Nonetheless, while immortalised cell lines can address some limitations in primary cells, they also have their own pitfalls. Since the senescence genes have been mutated using different transformation techniques, the cell lines may have abnormal chromosomal contents and forms of genetic mutations that could consequently lead to atypical protein expression and modified metabolism (Irfan Maqsood et al, 2013). Hence, collectively, the behaviour and characteristics of immortalised cell lines are not functionally comparable with those of primary cells (Irfan Maqsood et al, 2013).

Lastly, in both primary and immortalised cell lines, failure to grow these cells in a 3D environment while performing the cytotoxicity assays and the loss of cell–cell interaction could limit the extrapolation of the obtained *in vitro* results to *in vivo* environments and hence confound their validity. Furthermore, aside from the limitations of the *in vitro* platform, the cytotoxic effects of PPAR-γ agonist drugs are clearly cell-type dependent, as we have shown. Unfortunately, few extant studies have addressed the implications of mitochondrial dysfunction in TZDs' cardiotoxic effects, and particularly PGZ, limiting the chance of conducting a comparative analysis.

In conclusion, our results indicated that TZDs exerted cytotoxic effects on both cardiac cell types in a PPAR-γ-independent manner. The results also suggest that TZDs induced mitochondrial dysfunction through oxidative stress and MMP defects, subsequently leading to insufficient ATP production and eventually cell death. Despite the findings' importance, as mentioned earlier, more mechanistic details of TZDs' cytotoxic effects are needed to further understand and confirm the study's results, including the following: In the aforementioned results, TZDs were found to induce oxidative stress and MMP defects, both of which are determinant factors triggering

mitophagy activation. Furthermore, caspase 3/7 activity was found not to be highly implicated following TZD treatment. Thus, other forms of cell death, particularly necrosis and mitophagy, need to be assessed. The investigation of the latter form of cell death is crucial in accordance with a previous *in vitro* study performed in human neuroblastoma SH-SY5Y cells, in which low MMP arose from elevated ROS levels led to phosphatase and tensin homolog-induced kinase protein 1 accumulation in the outer mitochondrial membrane (Lee et al, 2017). This subsequently resulted in Parkin recruitment to the damaged mitochondria and excessive mitophagy (Lee et al, 2017). Furthermore, ROS levels were elevated in TZD-treated cells, as the H_2DCFDA assay confirmed. Nevertheless, the pathways involved in this observed effect were not investigated. Thus, future assessment of the pathways involved in this effect is warranted for further mechanistic data acquisition. Extending the findings presented herein, these proposed research directions will collectively improve our understanding of the mode of toxicity of TZD-induced cardiotoxicity and further clarify the implications of mitochondrial dysfunction for such toxic effects.

Chapter 3

Toxicometabolomics-Based Cardiotoxicity Evaluation of Thiazolidinedione Exposure in Human-Derived Cardiomyocytes

Abdullah Al Sultan[1,2] , Zahra Rattray[1,3] & Nicholas J. W. Rattray[1,3]*

[1]Strathclyde Institute of Pharmacy and Biomedical Sciences, University of Strathclyde, 161 Cathedral Street, Glasgow, UK, G4 0RE

[2]Faculty of Pharmacy, Kuwait University, Safat, 13110, Kuwait

[3]Strathclyde Centre for Molecular Bioscience, University of Strathclyde

Received: 2 January 2024 / Accepted: 29 January 2024

Al Sultan, A., Rattray, Z. & Rattray, N.J.W. Toxicometabolomics-based cardiotoxicity evaluation of Thiazolidinedione exposure in human-derived cardiomyocytes. *Metabolomics* **20**, 24 (2024). https://doi.org/10.1007/s11306-024-02097-z

Abstract

Introduction: Thiazolidinediones (TZDs), represented by pioglitazone and rosiglitazone, are a class of cost-effective oral antidiabetic agents posing a marginal hypoglycaemia risk. Nevertheless, observations of heart failure have hindered the clinical use of both therapies.

Objective: Since the mechanism of TZD-induced heart failure remains largely uncharacterised, this study aimed to explore the as-yet-unidentified mechanisms underpinning TZD cardiotoxicity using a toxicometabolomics approach.

Methods: The present investigation included an untargeted liquid chromatography–mass spectrometry-based toxicometabolomics pipeline, followed by multivariate statistics and pathway analyses to elucidate the mechanism(s)of TZD-induced cardiotoxicity using AC16 human cardiomyocytes as a model, and to identify the prognostic features associated with such effects.

Results: Acute administration of either TZD agent resulted in a significant modulation in carnitine content, reflecting potential disruption of the mitochondrial carnitine shuttle. Furthermore, perturbations were noted in purine metabolism and amino acid fingerprints, strongly conveying aberrations in cardiac energetics associated with TZD usage. Analysis of our findings also highlighted alterations in polyamine (spermine and spermidine) and amino acid (L-tyrosine and valine) metabolism, known modulators of cardiac hypertrophy, suggesting a potential link to TZD cardiotoxicity that necessitates further research. In addition, this comprehensive study identified two groupings – (i) valine and creatine, and (ii) L-tryptophan and L-methionine – that were significantly enriched in the above-mentioned mechanisms, emerging as potential fingerprint biomarkers for pioglitazone and rosiglitazone cardiotoxicity, respectively.

Conclusion: These findings demonstrate the utility of toxicometabolomics in elaborating on mechanisms of drug toxicity and identifying potential biomarkers, thus encouraging its application in the toxicological sciences.

Keywords: Thiazolidinediones; Toxicometabolomics; LC–MS; Cardiotoxicity; Amino acids; Carnitines

3.1 Introduction

Thiazolidinediones (TZDs), represented by pioglitazone (PGZ) and rosiglitazone (ROSI) agents, are a class of oral insulin-sensitising agents used to manage type 2 diabetes mellitus, or T2DM (DeFronzo et al, 2019; Wajid et al, 2019). Moreover, TZDs are cost-effective, potent insulin sensitisers that pharmacologically mediate their action by activating the peroxisome proliferator-activated receptor-gamma (PPAR-γ) nuclear receptor (Wajid et al, 2019). Independent of their metabolic actions, TZDs have been shown to exert several pleiotropic effects involving improvements in insulin resistance, endothelial dysfunction, dyslipidaemia and vascular inflammation (Chaudhury et al, 2017; DeFronzo et al, 2019). These polyhedric effects suggest a cardiovascular protective potential that encourages the selection of TZDs in T2DM treatment in parallel with the new T2DM treatment paradigm (ADA, 2023).

Despite the initially encouraging profile of TZDs, PGZ and ROSI have been widely used globally for the initial management of T2DM. However, a few years after their approval, case reports of heart failure (HF) emerged, leading to a progressive decline in TZD prescriptions (ADA, 2023; Wajid et al, 2019).

In recent decades, toxicometabolomics has progressively been established as a powerful tool in regulatory toxicology (Olesti et al, 2021). Toxicometabolomics can be broadly defined as the comprehensive and simultaneous analysis of large sets of endogenous metabolites presented in a biological sample in response to chemical exposure (Karahalil, 2016). Broadly speaking, toxicometabolomics has two major strategies: targeted and untargeted (Turi et al, 2018). As reflected by its term, the untargeted approach, also termed a global approach, involves the comprehensive analysis of all metabolites within the biological sample, whereas the targeted approach entails the study of a certain subset of metabolites characterised structurally and annotated biochemically (Turi et al, 2018). In regards to toxicometabolomic-based analytical techniques, the most commonly used methods include liquid chromatography–mass spectrometry (LC–MS), gas chromatography–mass spectrometry (GC–MS) and nuclear magnetic resonance (NMR) spectroscopy (Fraga-Corral et al, 2022). Each of these has its own metabolic coverage, advantages and disadvantages that define its application (**Table 3.1**).

Table 3.1 Overview of commonly used toxicometabolomic-based analytical techniques. Adopted from (Fraga-Corral et al, 2022).

Characterisations	LC–MS / GC–MS	NMR
Sample Preparation	Extensive	Simple
Sample Volume	Low sample consumption (~ 10 µL)	High sample consumption (~ 500 µL)
Sample Destructive	Destructive; derivatisation is needed for GC–MS	Non-destructive
Metabolic Coverage	Wide	Narrower than MS techniques
Sensitivity	High	Low
Reproducibility	Moderate	High
Experiment Cost	High	Low

Abbreviations: NMR: nuclear magnetic resonance; LC–MS: liquid chromatography–mass spectrometry; GC–MS: gas chromatography–mass spectrometry.

To date, extensive toxicometabolomic studies have been devoted to revealing the toxicity modes of various drugs (Cabaton et al, 2018; Li et al, 2020). These studies have led to the discovery of toxicity biomarkers and a deeper understanding of the underlying toxicological pathways (Cabaton et al, 2018; Li et al, 2020).

Thus, the present study was designed to introduce an untargeted LC–MS-based toxicometabolomic approach, followed by multivariate statistics to elucidate the mechanism of TZD-induced cardiotoxicity using AC16 human cardiomyocytes. The AC16 cell line is derived from adult human ventricular cardiomyocytes (Davidson et al, 2005). This immortalised, stable cell line has been increasingly used in both metabolomics and toxicology research because it expresses adult cardiomyocyte-specific biomarkers, which are α-myosin heavy chain (α-MHC), β-MHC, α-Actin and troponin I (Davidson et al, 2005). In addition, it displays electrophysiological properties comparable to primary human cardiomyocytes, which makes it a suitable candidate for toxicological studies (Davidson et al, 2005). Hence, the primary aim of this study was to **(i)** profile the biochemical pathways perturbed in TZD-treated AC16 human cardiomyocytes and, accordingly, **(ii)** identify biomarker candidates associated with

such an effect that could serve as potential therapeutic targets for TZDs' undesirable effects.

3.2 Methods

3.2.1 Reagents and Chemicals

PPARγ agonists, PGZ and ROSI, were purchased from Sigma-Aldrich (St. Louis, MO, USA). PGZ and ROSI 100 mM stock solutions were prepared in sterile dimethyl sulphoxide (DMSO) (Cat. No. 12611P; Cell Signalling Technology Beverly, MA, USA), and diluted to the appropriate half maximal inhibitory concentration (IC_{50}) with culture medium for *in vitro* experiments. The final concentration of DMSO in the medium was ≤0.1% (v/v). The reagents used for the LC–MS analysis consisted of high-performance liquid chromatography (HPLC)-grade acetonitrile, methanol, analytical-grade formic acid and ultrapure water and were purchased from Fisher Scientific (Loughborough, Leicestershire, UK).

3.2.2 Cells and Cell Culture

The AC16 cell line was purchased from Sigma-Aldrich (Product. No. SCC109; St Louis, MO, USA). The cells were cultured in Dulbecco's Modified Eagle's Medium (DMEM/F-12, Product. No. D6434; Sigma-Aldrich, St Louis, MO, USA) supplemented with 12.5% foetal bovine serum (FBS), 1% antibiotics (streptomycin and penicillin) and 2 mM L-glutamine at 37°C in a humid atmosphere of 5% CO_2 and 95% air.

3.2.3 Sample Preparation and Metabolite Extraction

To profile changes in the endogenous metabolites, AC16 cells were seeded at a density of 2×10^6 cells/well in six-well plates (Cat. No. 140675; Thermo Fisher Scientific, Roskilde, Denmark) containing 2 mL of medium per well and incubated for 24 h. Following a 24-h incubation period, the cells were washed once with phosphate-buffered saline (PBS) and supplemented with either a new phenol red-free medium alone or exposed to the half-maximal inhibitory concentration of either PGZ or ROSI (Details on IC_{50} determination are included in Chapter 2, Section 2.3.1). After the 24 h treatment period, the plates were placed on an ice-cold metal plate, and the AC16 cells were washed with 500 µL of ice-cold PBS. Using a pre-chilled plastic cell scraper, the cells were harvested three times with 500 µL of ice-cold methanol/water (50/50,

v/v) and aliquoted in microcentrifuge tubes. Subsequently, the microcentrifuge tubes were placed in liquid nitrogen. The samples were then allowed to sit for a few seconds and vortexed for 2 min. The resultant extracts were centrifuged at 12,000 g for 15 min at 4°C. The supernatant was then collected into new microcentrifuge tubes and evaporated using a Thermo Scientific™ Savant™ SpeedVac™ (Thermo Fisher, San Jose, CA, USA) to form dried metabolite extract pellets, while the recovered sediment pellets were retained for total protein quantification using the Bradford assay (Product. No. 10495315; Thermo Fisher, Rockford, IL, USA). The dried metabolite pellets were reconstituted in water/0.1% formic acid at volumes normalised to the relative protein content. Eventually, the reconstituted solutions were transferred to 300µL fixed insert glass vials (Cat. No. 6PSV9-03FIVAPT; Thermo Fisher, Langerwehe, Düren, Germany) for LC–MS analysis. Following sample preparation, quality control (QC) and blank samples were prepared. The QC samples were prepared by mixing equal volumes of all the prepared and tested samples. The blank sample, typically used to monitor background contamination or interference acquired through sample preparation, was prepared by pooling methanol/water (50/50, v/v) **(Figure 3.1)**.

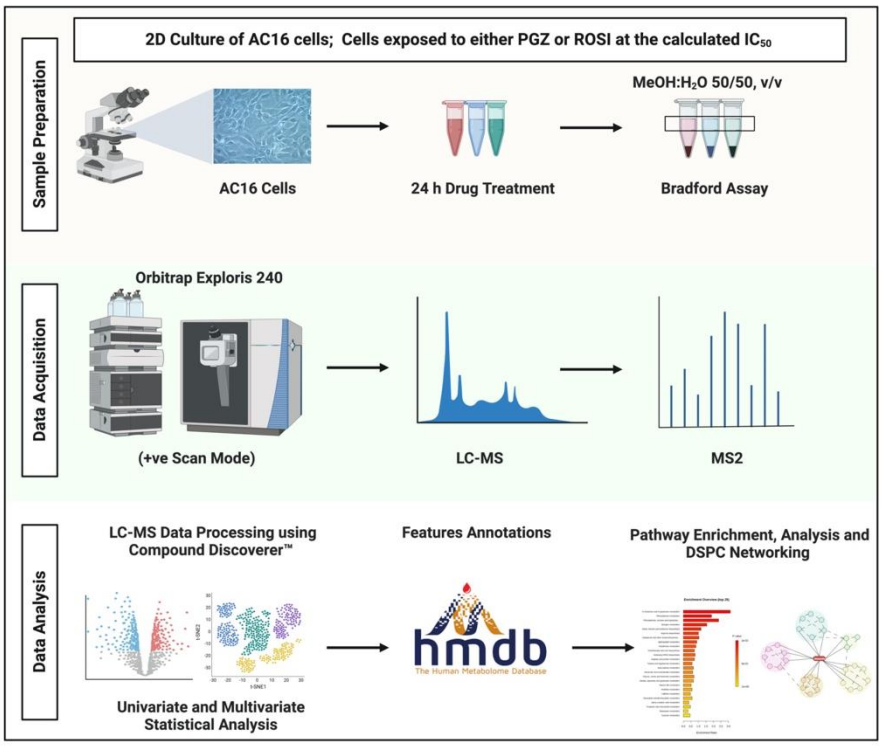

Figure 3.1 Schematic flow chart of the toxicometabolomic profiling strategy employed for LC–MS data collection and analysis.
PGZ: pioglitazone; ROSI: rosiglitazone; LC–MS: liquid chromatography–mass spectrometry; DSPC: debiased sparse partial correlation.

3.2.4 LC–MS Data Acquisition

Metabolite extracts of the AC16 cell biomass and corresponding culture media were randomised and subsequently analysed by high-performance liquid chromatography-electrospray ionisation quadrupole orbitrap mass spectrometry (HPLC-ESI-HRMS) using a Thermo Scientific™ Vanquish™ binary LC system coupled to a Thermo Scientific™ Orbitrap Exploris™ 240 mass spectrometer. The LC separations were carried out on an Accucore C18 HPLC column (2.6 µm, 100 mm × 2.1 mm I.D.; Thermo Fisher) thermostatted at 40°C and operated at a flow rate of 400 µl/min. A 5 µl sample injection was used with an elution gradient consisting of water (eluent A) and acetonitrile (eluent B), each containing 0.1% formic acid (**Table 3.2**).

Table 3.2 HPLC gradient mode of the mobile phase

No.	Time	Flow (ml/min)	%B
1	0.000	Run	
2	0.000	0.400	1.0
3	0.500	0.400	1.0
4	2.000	0.400	50.0
5	10.500	0.400	99.0
6	11.000	0.400	99.0
7	11.500	0.400	1.0
8	14.900	0.400	1.0
9	15.000	0.400	1.0
10			
11	15.000	Stop Run	

The mass spectrometer (Orbitrap Exploris™ 240) was equipped with a heated electrospray ion source (HESI-II). The HESI-II was operated in positive (+ESI) mode and set as follows: spray voltage 3700 V; sheath gas flow rate: 40 (arbitrary units); auxiliary gas flow rate: 10 (arbitrary units); sweep gas flow rate: 1 (arbitrary units); ion transfer tube temperature: 300°C; and vaporiser temperature: 280°C. The duty cycle consisted of a full MS scan with an MS1 resolution of 60,000 and then 5 subsequent data dependent acquisition scans using 30,000 resoluiton and an RF lens of 70% in

an m/z scan range of 70–1050. XCalibur ™ 4.2 software (Thermo Fisher Scientific) was used for data acquisition.

3.2.5 Data Processing Using Compound Discoverer 3.2

The acquired LC–MS data were processed using Compound Discoverer 3.2 software (Thermo Fisher, San Jose, CA, USA) featuring a processing workflow and its associated data processing nodes, as depicted in **Figure 3.2**. The workflow applied herein and its associated nodes are described as follows.

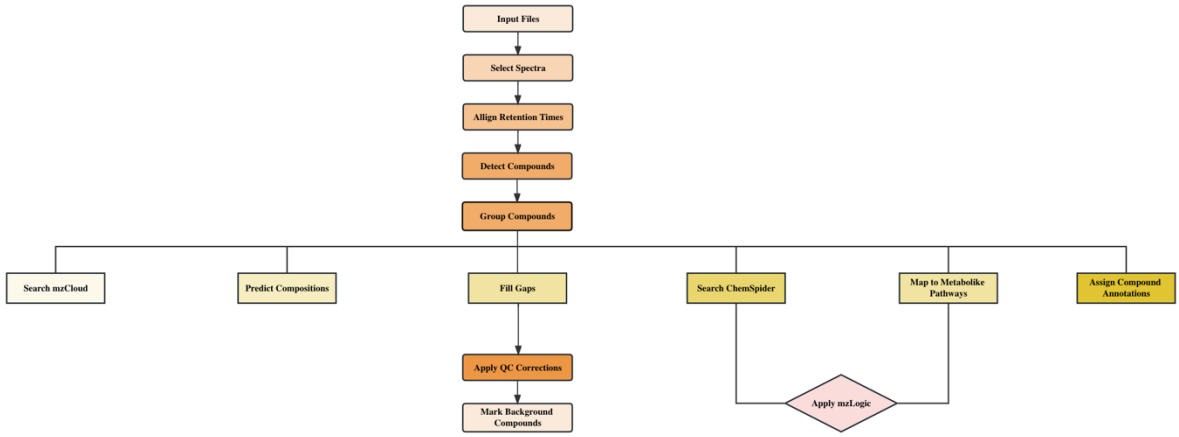

Figure 3.2 Flow chart of the Compound Discoverer workflow applied to the acquired LC–MS data.

LC–MS: liquid chromatography–mass spectrometry.

Briefly, the Select Spectra node was used with open settings and a default 1.5 signal-to-noise ratio (S/N) threshold. The raw data files were aligned with adaptive curve settings with 3 ppm mass tolerance and a 0.3 min retention time shift. The Detect Compounds node was used with 5 ppm mass tolerance, 10,000 minimum peak intensity, peak detection S/N threshold 1.5, remove baseline true, and compound detection of $[M+H]^{+1}$, $[M+ACN+H]^{+1}$, $[M+MeOH+H]^{+1}$, $[M+H-H_2O]^{+1}$, $[M+H-NH_3]^{+1}$ ions for polar sample positive mode, $[M-H]^{-1}$, $[M+FA-H]^{-1}$, $[M-H-H_2O]^{-1}$ ions for polar sample negative mode, $[M+H]^{+1}$, $[M+ACN+H]^{+1}$, $[M+H-H_2O]^{+1}$, $[M-NH_3+H]^{+1}$, $[M+NH_4+1]^{+1}$ ions for non-polar sample positive mode, and $[M-H]^{-1}$, $[M+FA-H]^{-1}$, $[M-H-H_2O]^{-1}$, $[M-H+HAc]^{-1}$ ions for non-polar sample negative mode. The Group

Compounds node was tuned with 5 ppm mass tolerance, 0.2 min retention time tolerance and a peak rating filter threshold of 4 for a minimum of 2 files. The Fill Gaps node was used with 5 ppm mass tolerance, the QC Correction node was used with max QC area relative standard deviation (RSD) 30%, max corrected QC area RSD 25%, and the Mark Background Components node was enabled with max sample/blank 5. The Predict Compositions node was set at 5 ppm mass tolerance with element counts C90 H190 Br3 C14 N10 O18 P3 S5. The Apply mzLogic and Apply Spectral Distance nodes were set with 5 ppm mass tolerances. Subsequently, the normalisation procedure took place, at which peak areas across all the samples were normalised to the total area of the corresponding samples. Features identified in the processed raw data of mass spectral peaks within a 5-ppm mass error were searched against the mzCloud spectral library and ChemSpider™ databases. Databases selected by ChemSpider were the Human Metabolome Database (HMDB), BioCyc, Chemical Entities of Biological Interest (ChEBI), Kyoto Encyclopaedia of Genes and Genomes (KEGG), Taneisa Grier, Toxin, Toxin-Target Database, WikiPathways and xPharm. All data reported align to MSI Level 2 identification. Only known features with full matches across at least two annotation sources and supported by MS2 data (DDA for the preferred ion) were included in the subsequent analysis.

3.2.6 Data Analyses and Statistical Interpretation

3.2.6.1 Chemometric Analyses and Characteristic Features Selection Criteria

Univariate and multivariate statistical analyses were performed using R v4.3.0 and MetaboAnalyst v6.0 (https://www.metaboanalyst.ca) webserver. Before the data analyses and through Compound Discoverer 3.2 software, the spectral data were filtered by annotation filters (i.e., a full match with the predefined databases). This was followed by data normalisation using the *MSPrep R package* (Hughes et al., 2014), with the normalisation mode applied being median mode. Regarding multivariate analysis, principal component analysis (PCA) and orthogonal partial least squaresdiscriminant analysis (OPLS-DA) were developed to inspect the clustering of biological samples and model the discriminations between the experimental groups. Furthermore, random forest analysis (RF), was performed to identify the features that had the highest discriminatory power between the two experimental groups. The number of trees in this study was set to 500. Univariate analysis, Student's *t*-test, was

conducted to identify differentially expressed features (DEFs) between control and TZD-treated groups. The *p* and FDR values were set at 0.05. Through combining univariate and multivariate analyses findings, features that fit on one of the following criteria— (i) variable importance in the projection (VIP) value >1 of the OPLS-DA model, (ii) discriminant features identified by RF and (iii) significant features extracted from univariate analysis (*p*-value ≤ 0.05)—were labelled in this study as characteristic features and hence subjected for debiased sparse partial correlation analysis (DSPC)–weighted network analysis, metabolite set enrichment analysis (MSEA) and pathway analysis.

3.2.6.2 DSPC Weighted Network, MSEA and Pathway Analyses of the Characteristic Features

To further explore the metabolic alteration underpinning treatment conditions, the correlation among the characteristic features was determined through DSPC weighted network analysis. Using MetaboAnalyst, the DSPC network was performed on the basis of the graphical lasso modelling procedure. The significance cutoff for correlation (*p*-value) was set to 0.01. The specific range for correlation coefficients was from −1 to 1. The constructed network was accordingly exported to the Cytoscape software platform (Cytoscape; https://cytoscape.org; v3.10) for visualisation.

In addition, MSEA and pathway analyses were performed to profile the perturbed biochemical pathways in response to TZD treatment. Initially, the characteristic features were annotated using HMDB v5.0 (https://hmdb.ca). MSEA and pathway analysis were then deduced by mapping the annotated metabolites against known metabolic pathways for homo sapiens (i.e., Kyoto Encyclopedia of Genes and Genomes (KEGG)) using MetaboAnalyst. The hypergeometric test's *p*-values determined the pathway impact and statistical significance of the identified metabolic pathways**.**

3.2.6.3 Selection of Biomarker Candidates

To identify biomarker candidates associated with the cardiotoxicity of TZDs, univariate receiver operating characteristic (ROC) curves were applied. Initially, hub feature(s) identified from the DSPC network (feature(s) with the highest degree score) that were also enriched in pathways linked with TZDs' cardiotoxicity were defined in this study

as biomarker candidates. Thereafter, ROC curves were constructed and the area under the curve (AUC) was calculated to evaluate the prognostic potential of these features.

3.2.7 Statistical Analysis

Statistical analysis was conducted using R v4.3.0. Three independent experiments were performed, each conducted in triplicate (biological replicates), yielding nine samples per group. The experimental design employed in this study is illustrated in **Figure 3.3**. Statistical significance was determined using Student's or Welch's t-tests when comparing the two groups. A non-repeated one-way analysis of variance (ANOVA), followed by Dunnett's post hoc test, was used for multiple comparisons. The correlation coefficient was assessed using Pearson and distance correlation analyses. A p-value ≤ 0.05 was considered statistically significant. All the downstream analyses were performed using MetaboAnalyst, otherwise delegated to R. A schematic flowchart of the toxicometabolomics pipeline applied for downstream analyses is illustrated in **Figure 3.4**.

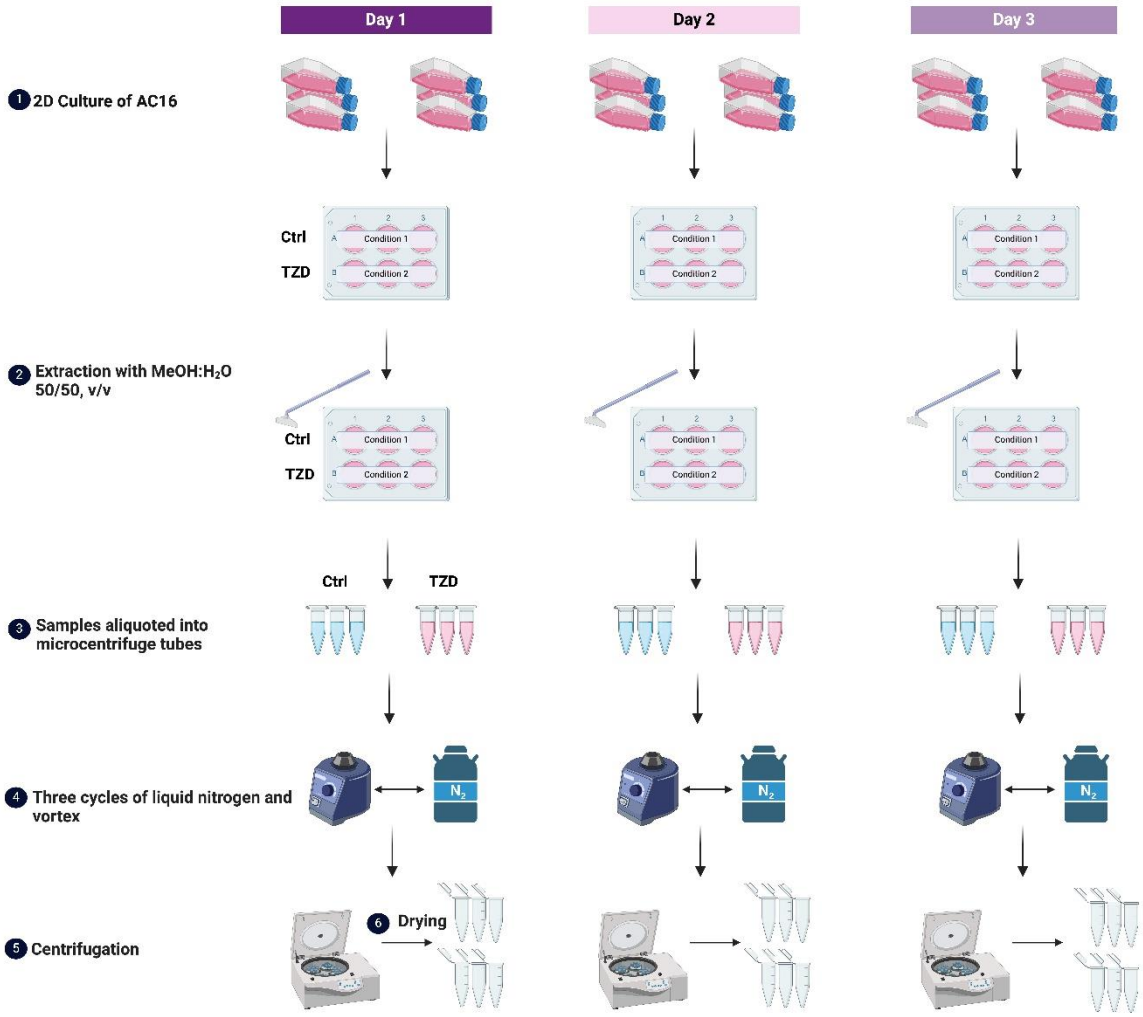

Figure 3.3 Experimental design for toxicometabolomics analysis. Three independent toxicometabolomics experiments were performed. Each experiment involved (1) cell seeding, followed by (2) metabolite extraction. The resulting extracts were transferred to (3) microcentrifuge tubes and (4) quenched in liquid nitrogen. After (5) centrifugation, the supernatant was collected in new microcentrifuge tubes and (6) evaporated using a Thermo Scientific™ Savant™ SpeedVac™.

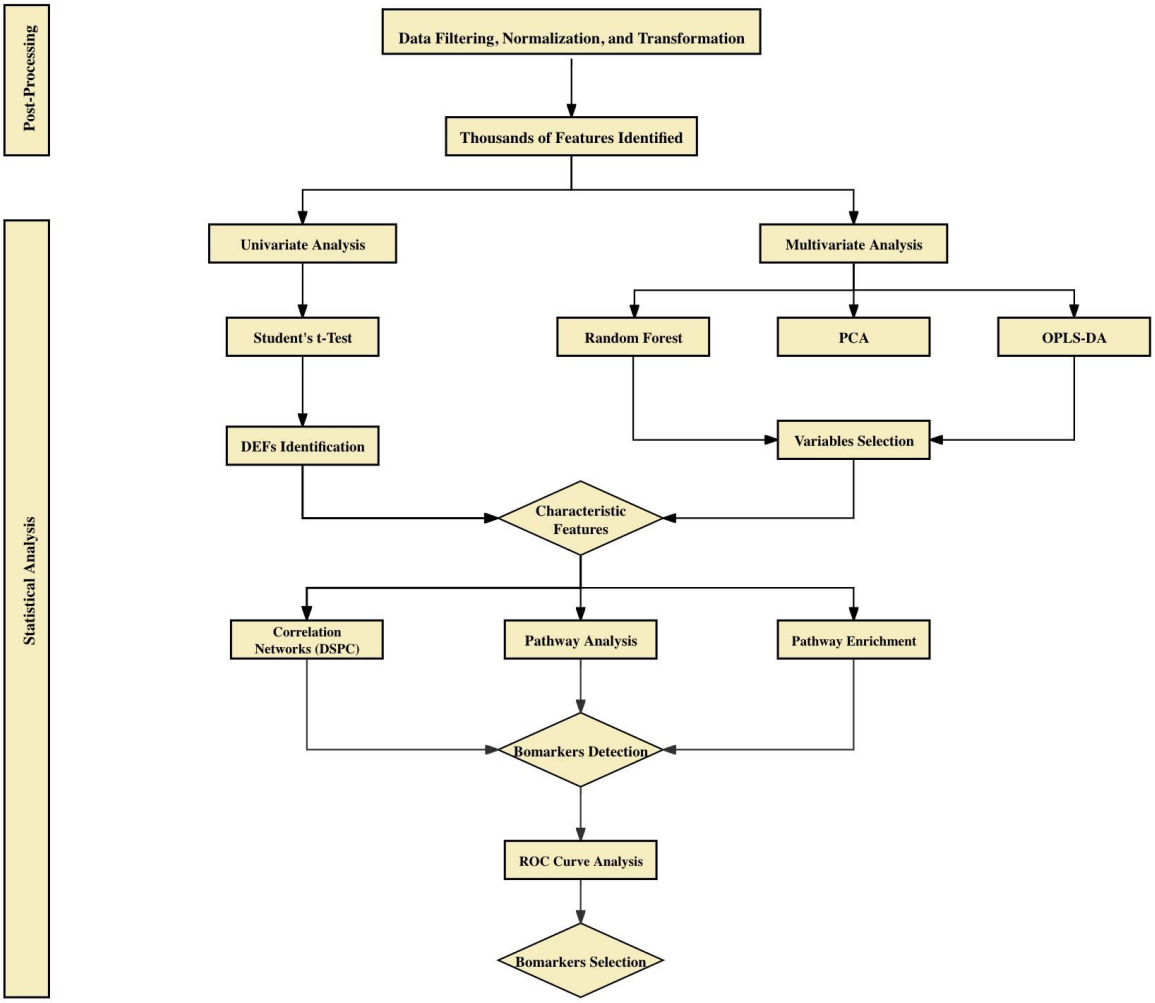

Figure 3.4 Flowchart of the toxicometabolomics pipeline applied for downstream analyses. The metabolic profiling of AC16 cells produced in response to the TZDs was characterised using an untargeted LC–MS approach. First, the raw LC–MS data were processed using Compound Discoverer, after which further data filtering and normalisation were conducted using the *MSPrep* R package. Thereafter, downstream analysis, including uni- and multi-variate analyses, was performed on the identified features. PCA was performed to identify potential outliers. Subsequently, OPLS-DA and RF analysis, both supervised techniques, were adopted as feature selectors and classifiers. Alongside the multivariate analysis, univariate analysis, Student's t-test, was conducted to identify differentially expressed features (DEFs) between control and TZD-treated groups. The *p* and FDR values were set at 0.05. Accordingly, the characteristic features were first selected by combining the univariate and multivariate findings and then subjected to DSPC weighted network analysis, metabolite set enrichment analysis and pathway analysis. Finally, this study defined the hub features identified from the DSPC network, which were also observed to be enriched in the pathways linked to TZD's cardiotoxicity pathogenesis, as biomarker candidates. Additionally, ROC curves were applied to evaluate the prognostic potential of the chosen candidates.

LC–MS: liquid chromatography–mass spectrometry; TZDs: thiazolidinediones; DEFs: differentially expressed features; PCA: principal component analysis; OPLS-DA: orthogonal partial least squares-discriminant analysis; RF: random forest; DSPC: debiased sparse partial correlation; KEGG: Kyoto Encyclopaedia of Genes and Genomes; ROC: receiver operating characteristic.

3.3 Results

3.3.1 Overview of Cellular Metabolome Profiling under TZD Treatment

To unveil TZDs' cardiotoxic mode of action and delineate the perturbation of the cellular metabolome in response to their exposure, a toxicometabolomics approach featuring untargeted LC–MS followed by computational bioinformatics analyses was introduced, as depicted in **Figure 3.4**.

However, prior to data analysis, data inspection and quality assessment involved generating box plots of log_2-transformed abundance data with corresponding retention times and plotting coefficient of variation (CV%) against raw intensity. In both experiments, box plots (**Figures 3.5B and 3.5D**) revealed comparable medians across samples within the same group. **Figures 3.5C and 3.5D** demonstrated a clustering of features at low intensity values with correspondingly high CVs, suggesting increased relative variability for less abundant features, likely due to noise. Conversely, as raw intensity increased, CV values tended to decrease, indicating improved measurement consistency for more abundant features. Overall, these findings suggest robust and reproducible LC-MS system performance.

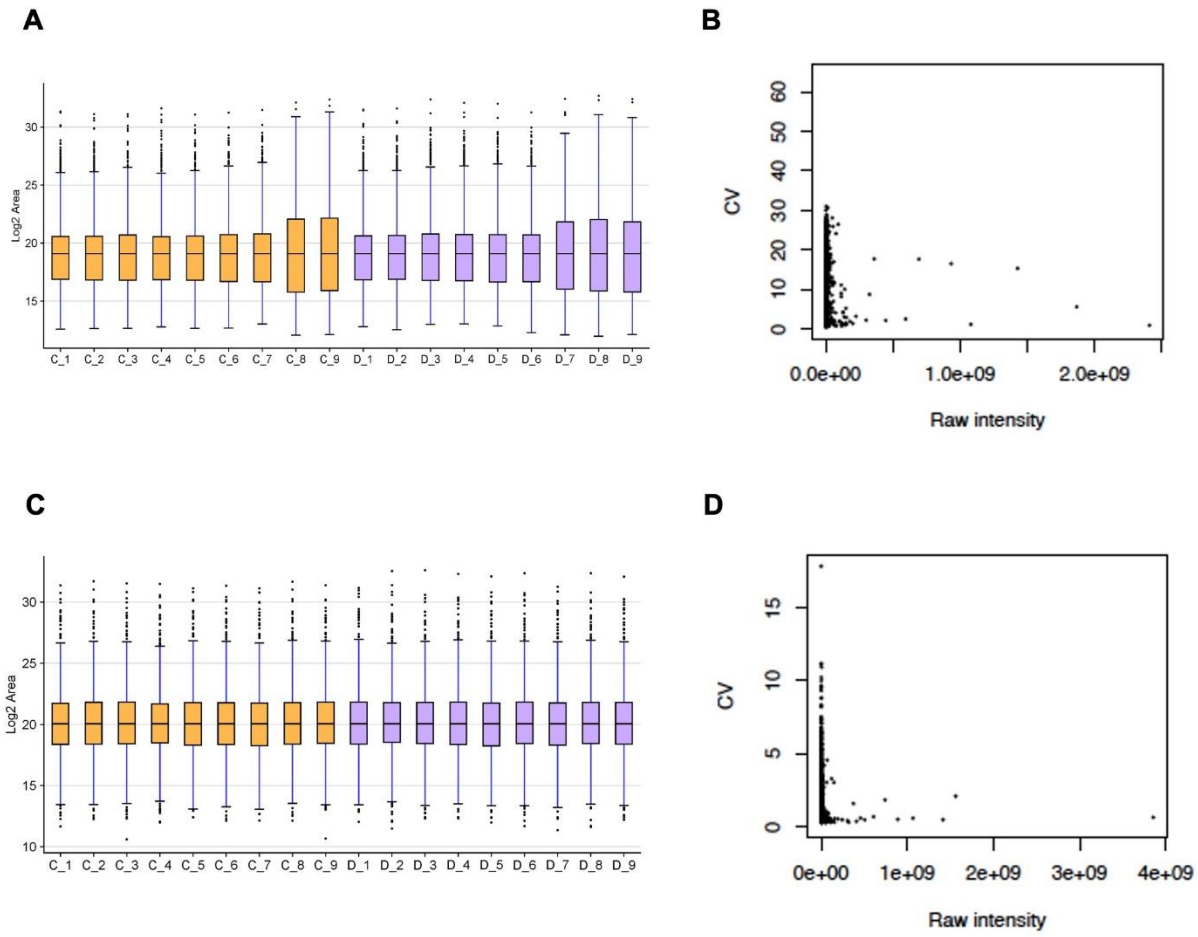

Figure 3.5 Quantitative profiling of AC16 cells in response to TZD treatment. Box plots of $\log_2$ area for each tested sample using PGZ and ROSI datasets are shown in figures A and C. Control and TZD-treated samples are colored orange and purple, respectively. Figures B and D depict the coefficient of variation (CV%) in raw PGZ and ROSI data.

PGZ: pioglitazone; ROSI: rosiglitazone; CV: coefficient of variation

Univariate and multivariate statistical analyses were performed to decipher the metabolic perturbation in AC16 cells following TZD exposure. An unsupervised two-component PCA plot was constructed to delineate the overall similarities and heterogeneity in the clustering of the biological samples.

In both experiments, the PCA scores plots indicated marked separation among the sampling data, showing a distinct metabolic profile that was yielded after TZD exposure (**Figures 3.6A and 3.6B**). In addition to its role in assessing sample group heterogeneity, the PCA plot was utilised as a QC and QA tool to evaluate the reliability and quality of LC–MS-based toxicometabolomics data. As depicted in **Figures 3.6A**

and 3.6B, all QC samples clustered within the PCA plot and 95% CIs, indicating a robust and reproducible performance of the LC-MS system.

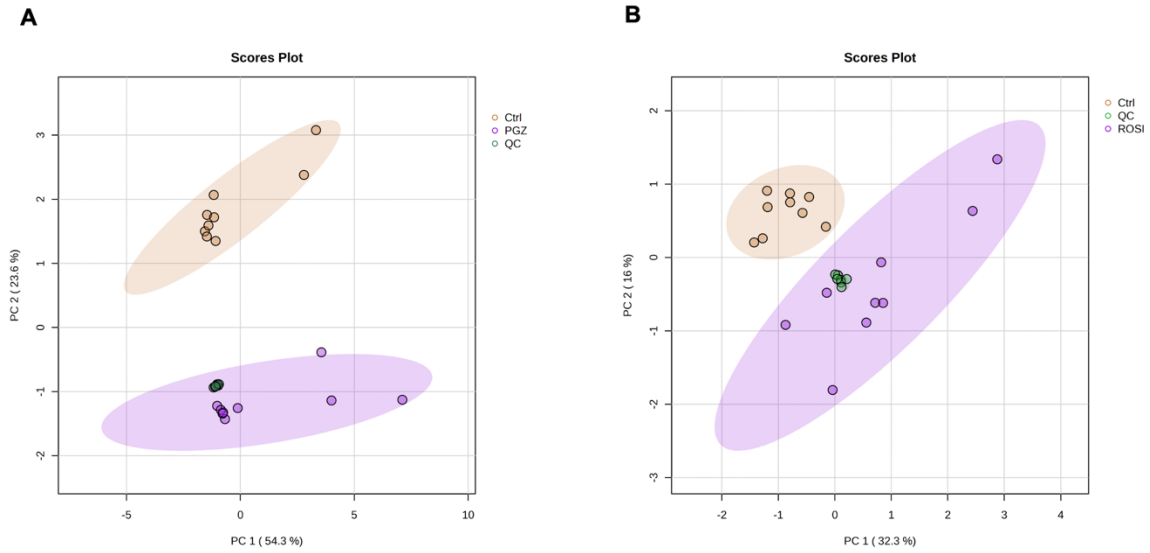

Figure 3.6 Multivariate analysis of the metabolomics data. (A and B) PCA plots comparing the LC–MS metabolic profiles of TZD-treated and control samples. (A) The PCA scores plot of PGZ-treated and control samples; (B) scores plot of PCA of the ROSI-treated vs. control samples. In both (A and B), shaded circles represent 95% confidence intervals, while colored dots illustrate individual samples. The plot shows the separation between sample groups and the cluster of QC samples, which are colored in green.

PGZ: pioglitazone; ROSI: rosiglitazone; LC–MS: liquid chromatography–mass spectrometry; PCA: principal component analysis; QC: quality control.

This distinct metabolic profile observed by PCA plots was also confirmed following the application of the OPLS-DA supervised model illustrated in **Figures 3.7A and 3.7C**. In both experiments, the constructed supervised OPLS-DA model yielded a satisfactory fitness of the model and a high predictive ability value of (R^2 = 0.747 and Q^2= 0.618) and (R^2 = 0.805 and Q^2= 0.717), in PGZ and ROSI datasets, respectively (**Figures 3.7B and 3.7D)**.

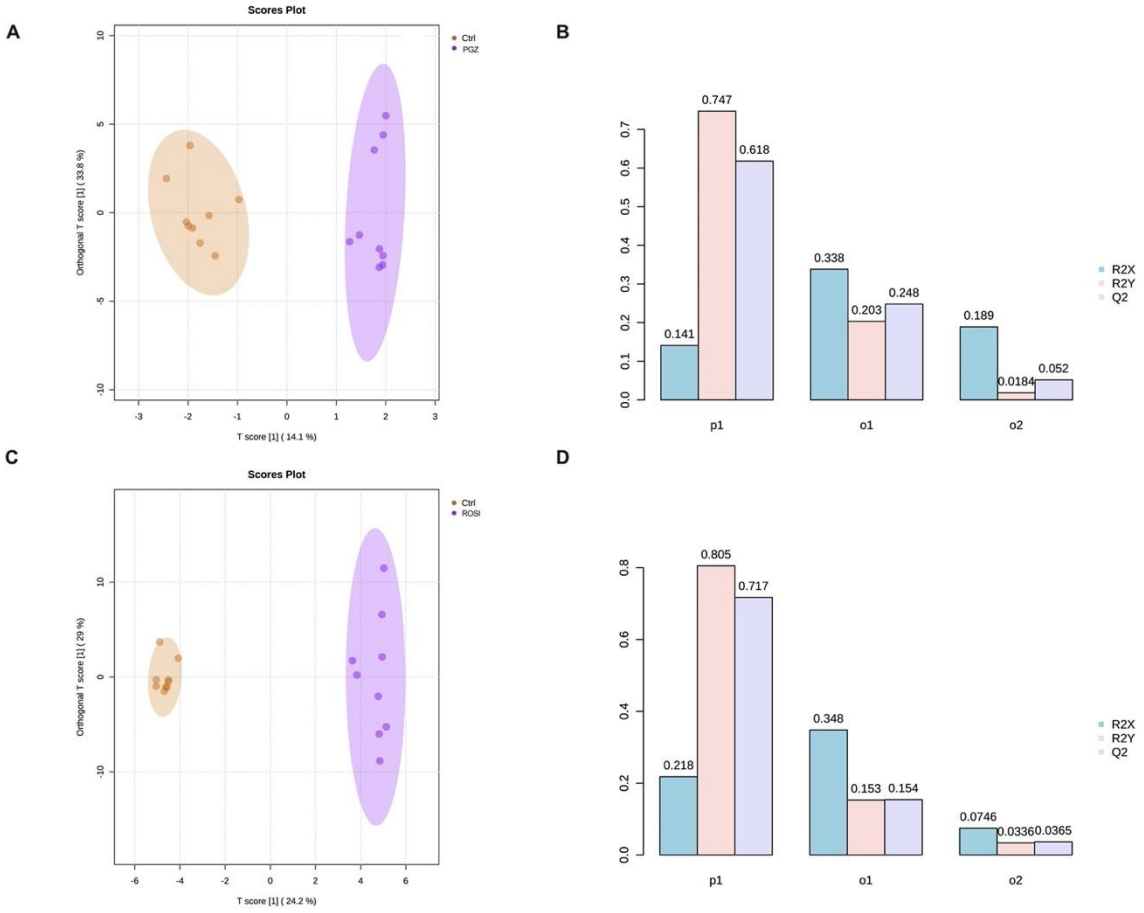

Figure 3.7 Multivariate statistical analysis of the acquired LC–MS data. OPLS-DA plots showing the separation between the (a) PGZ-treated vs. control groups and the (c) ROSI-treated vs. control groups. (b) and (d) show the cross-validated cumulative modelled variation R^2X, R^2Y and Q_2 coefficients of the predictive loading (p1) and orthogonal (o1, o2) components applied on OPLS-DA data. The supervised OPLS-DA model illustrated in (a) yielded satisfactory fitness and a high predictive ability value (R^2 = 0.747 and Q^2 = 0.618, respectively), while the OPLS-DA score plot of the metabolite profiling data in (c) demonstrated a similar clustering panel between the experimental groups, exhibiting satisfactory fitness and predictive ability values (R^2 = 0.805 and Q^2 = 0.717, respectively).

PGZ: pioglitazone; ROSI: rosiglitazone; OPLS-DA: orthogonal partial least squares-discriminant analysis.

Furthermore, the Variable Importance in Projection (VIP) measure was adopted to fingerprint the important features responsible for clustering separation. With respect to PGZ treatment, 9 features were found with VIP scores > 1, as listed in **Figure 3.8A**. In contrast, several influential features were extracted from the later model in response to ROSI exposure (**Figure 3.8B)**, including amino acid-related products (e.g. L-glutamine), purines and purine derivatives (hypoxanthine), polyamines (spermidine), inosine and others.

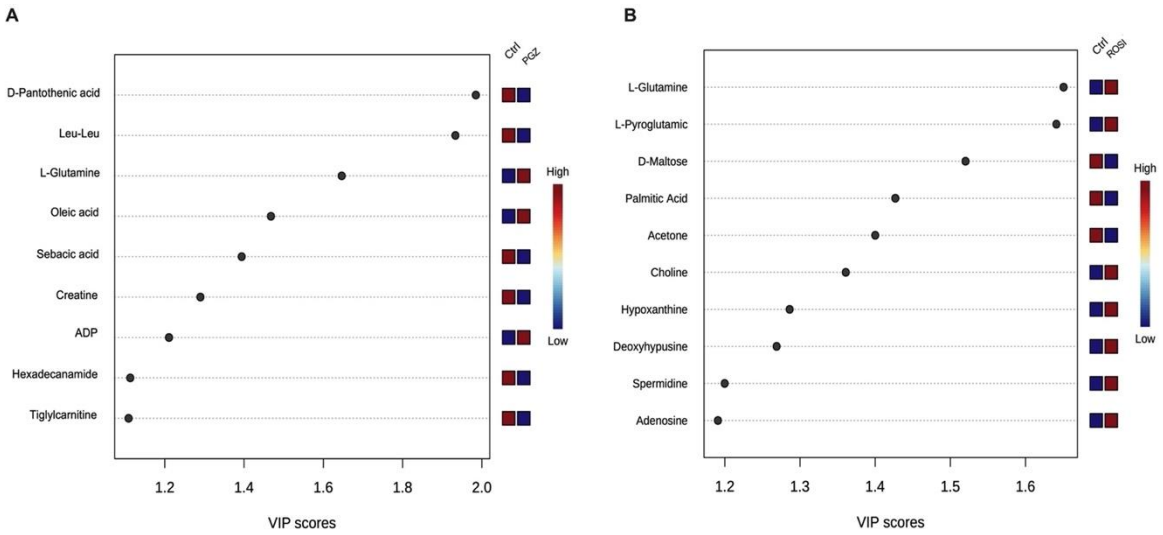

Figure 3.8 Variable importance in projection (VIP) scores for the top 10 features. (A) and (B) illustrate the VIP score plots of the 10 most influential features responsible for the separation noted between the PGZ-treated vs. control groups and the ROSI-treated vs. control groups in the OPLS-DA model, respectively. In (A and B), the colour code indicates higher (red) or lower (blue) concentrations.

VIP: variable importance in projection; PGZ: pioglitazone; ROSI: rosiglitazone; OPLS-DA: orthogonal partial least squares-discriminant analysis.

Furthermore, the putative features were ranked using the mean decrease accuracy measure integrated into the RF analysis. Regarding the PGZ experiment, the RF classification, as shown in **Figure 3.9A,** demonstrated an outstanding prediction of the treated group; nevertheless, the classification exhibited less accuracy in the control group, with a 0.0556 out-of-bag (OOB) error rate. The RF variable importance plot identified a number of discriminant features important in classifying the data, including amino acid products (e.g., L-tyrosine, valine), creatine and mitochondrial-derived metabolites such as triglylcarnitine (**Figure 3.9B**). However, the RF classification model extracted from ROSI data, as illustrated in **Figure 3.9C,** predicted the control excellently, while the prediction of the treated class was less accurate, with a 0.056 OOB rate. The features identified by RF that had the most influence on data classification are listed in **Figure 3.9D**. In an attempt to further identify the DEFs, univariate analysis, Student's *t*-test, was conducted, yielding 16 and 53 DEFs in response to PGZ and ROSI exposure, respectively.

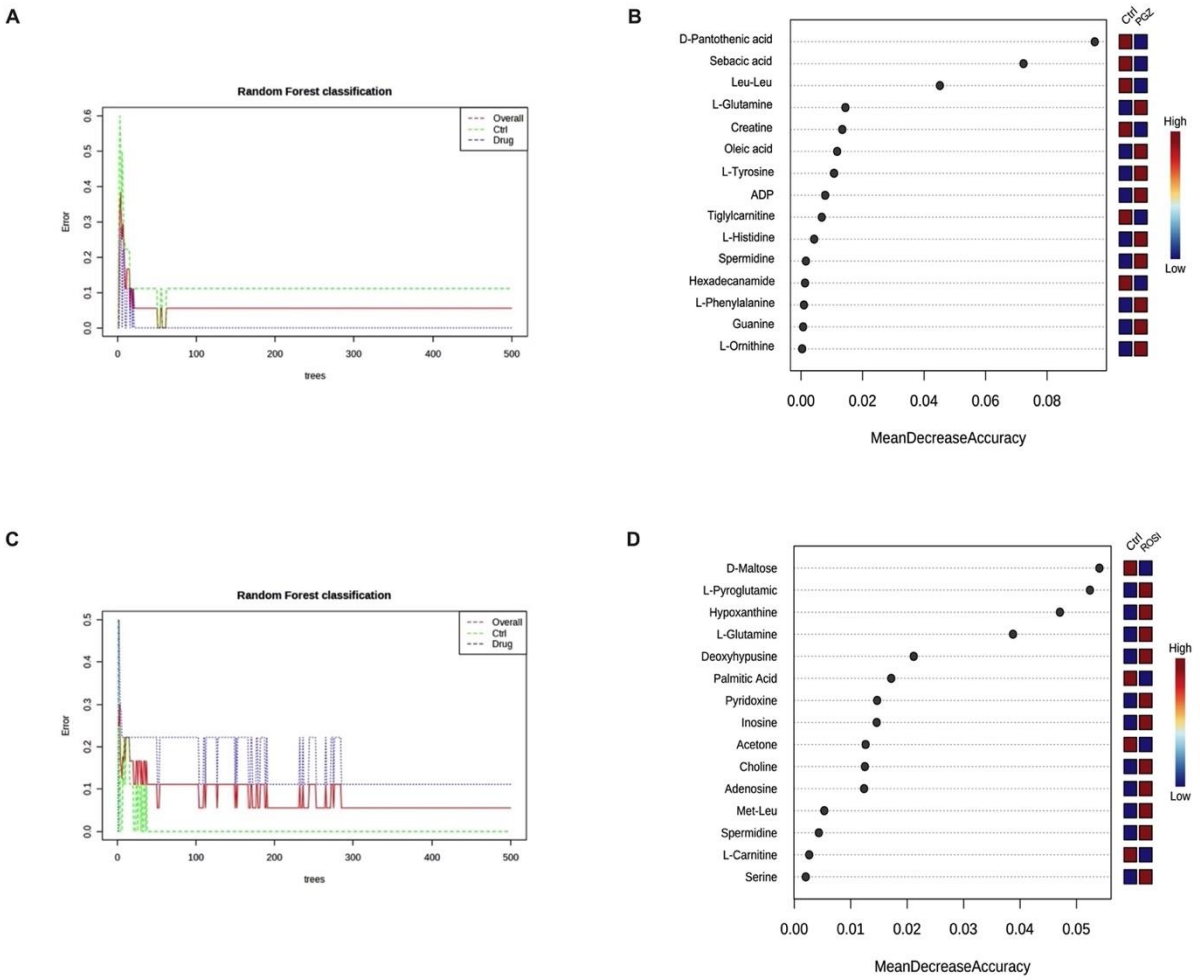

Figure 3.9 Random forest classification model. (A) and (C) represent the random forest classification model of the PGZ and ROSI experiments, respectively, illustrating the cumulative error rates measured for each experimental group using the machine learning approach. (B) and (D) demonstrate the discriminant features with the highest discriminatory power between the treated and control groups (PGZ in (B) and ROSI in (D)). In (B and D), the colour code indicates higher (red) or lower (blue) concentrations.

PGZ: pioglitazone; ROSI: rosiglitazone.

Thereafter, a combination of multivariate and univariate analyses was performed to define PGZ's and ROSI's characteristic features. The combination analysis resulted in 27 and 63 characteristic features extracted from the PGZ and ROSI datasets, respectively, discriminating the experimental groups.

The relative distribution of these defined characteristic features across TZD-treated and control groups was measured by calculating the z-score using the following formula (Wei et al, 2012):

$$z = (x - \mu)/\sigma$$

where x indicates sample abundance; μ represents average and σ denotes the standard deviation.

The z-score plot of the 27 features in the PGZ-treated group relative to the control group, as presented in **Figure 3.10A**, exhibited metabolic perturbation in the treated group, with a z-score range of −6 to 14 compared to the control group (z-score range: −2 to 2). The relative distribution of the 63 features altered following ROSI exposure showed z-score ranges of (−15 to 20) and (−2 to 2) in the treated and control groups, respectively (**Figures 3.10B and 3.10C**). The chemical taxonomy classification of the characteristic features of each TZD agent is described in **Figures 3.10D and 3.10E**.

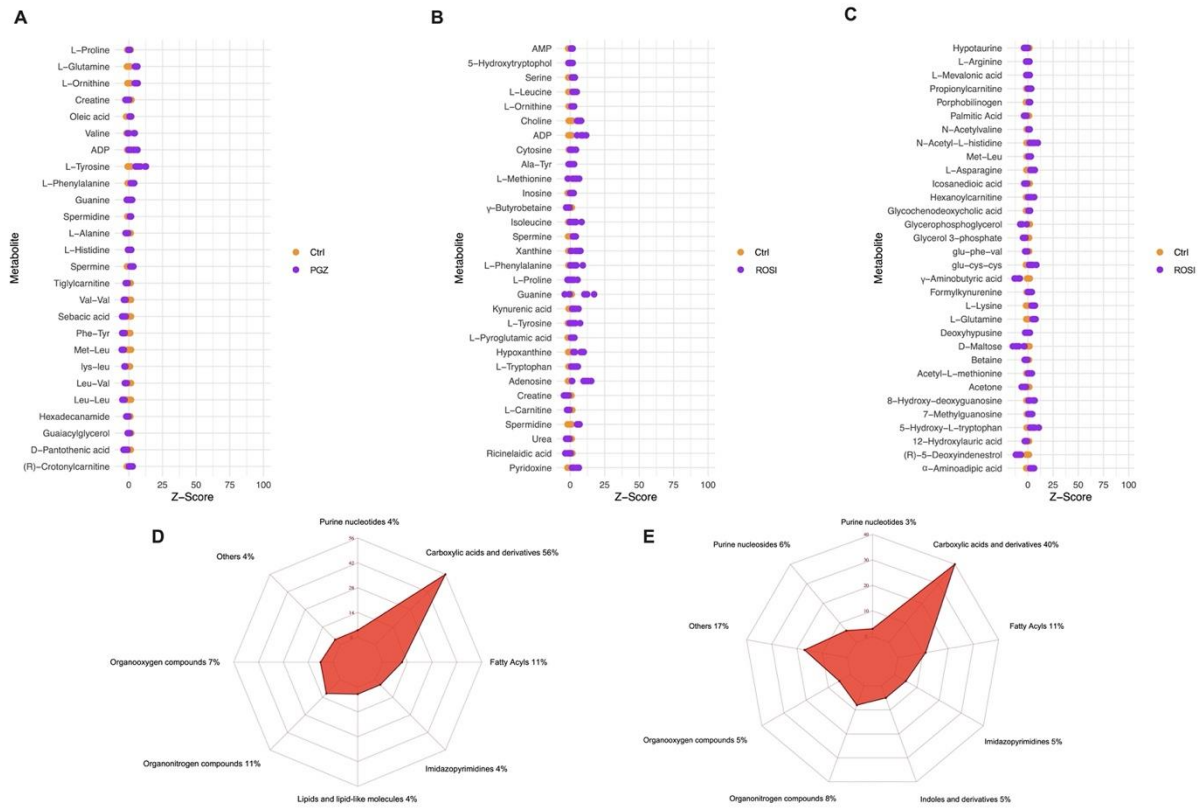

Figure 3.10 z-score plot of the characteristic features and their chemical classification. (A) and (B and C) present z-score plots of the characteristic features altered in the PGZ-treated and ROSI-treated samples relative to the mean in the control cells, respectively. Each point represents one metabolite in one sample, coloured according to the sample grouping. (D) and (E) show the chemical classification of the characteristic features identified from the PGZ and ROSI datasets, respectively.

PGZ: pioglitazone; ROSI: rosiglitazone.

3.3.2 DSPC Algorithm and Correlation Network Construction

Debiased sparse partial correlation (DSPC) was applied to explore the connectivity among PGZ's and ROSI's characteristic features. The PGZ-constructed network, as illustrated in **Figure 3.11A**, revealed dense interactions among amino acids, amino acids with purine ribonucleotide (ADP) and amino acids with both polyamines (spermine and spermidine). In addition to the identified positive correlations, negative interactions were also noted, including valine with L-histidine, L-phenylalanine with guanine, and creatine with spermidine. Valine and creatine represented the main hubs with the highest degree score in the PGZ network.

Conversely, ROSI's DSPC network, as shown in **Figure 3.11B**, revealed dense interactions among amino acids and their derivatives, similar to PGZ. Furthermore, kynurenic acid, which is a vital bioproduct of tryptophan's catabolism, has demonstrated strong interactions with amino acid derivatives (i.e., acetyl-L-methionine) and purine nucleosides (methylguanosine). The main hubs represented in the ROSI network include L-tryptophan and L-methionine.

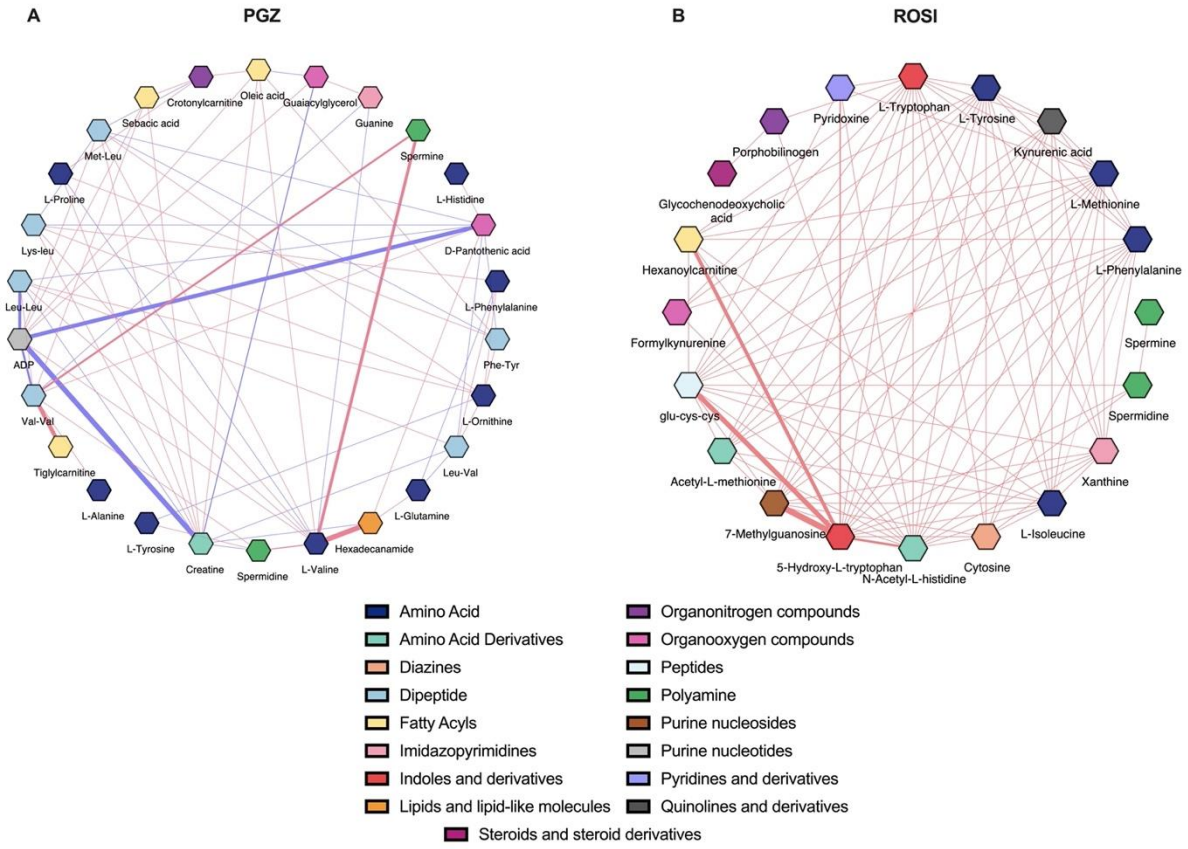

Figure 3.11 DSPC correlation network using characteristic features. (A) and (B) denote the DSPC network using PGZ's and ROSI's characteristic features, respectively. In both networks, the nodes represent metabolites, the red lines indicate a direct positive correlation between features, and the blue lines signify an inverse correlation. The thickness of the lines donates significance. The DSPC network analysis was performed on the basis of the graphical lasso modelling procedure, with the significance cutoff for correlation (*p*-value) set to 0.01. The range specified for the correlation coefficients was from −1 to 1. The constructed networks were exported to the Cytoscape software platform (Cytoscape; https://cytoscape.org; v3.10.1) for visualisation.

DSPC: debiased sparse partial correlation; PGZ: pioglitazone; ROSI: rosiglitazone.

3.3.3 MSEA and Pathway Analysis

To profile the biochemical pathways perturbed in PGZ- and ROSI-treated AC16 cells, MSEA and pathway analyses were performed by mapping the drug's characteristic features against the Kyoto Encyclopedia of Genes and Genomes (KEGG) using the MetaboAnalyst webserver. The MSEA analysis revealed that the PGZ's characteristic features were significantly enriched in pathways linked to amino acid metabolism, energy metabolism, polyamine biosynthesis, metabolism of cofactors and others as listed in **Figure 3.12A (Table S2, Appendix Section 7.2)**. The pathway analysis results, on the other hand, showed that the highest number of metabolites were

products of various amino acid metabolism and amino acid and cofactor biosynthesis **(Figure 3.12B, [Table S3, Appendix Section 7.2])**.

Regarding ROSI, the MSEA, as shown in **Figure 3.12C (Table S4, Appendix Section 7.2)**, revealed that the characteristic features were significantly enriched in pathways belonging to amino acid (i.e., methionine metabolism), polyamines (spermidine and spermine biosynthesis) and betaine metabolism. The pathway-topology analysis showed a significant association between the characteristic features and pathways linked to purine metabolism, amino acid metabolism and amino acid biosynthesis, as illustrated in **Figure 3.12D (Table S5, Appendix Section 7.2)**.

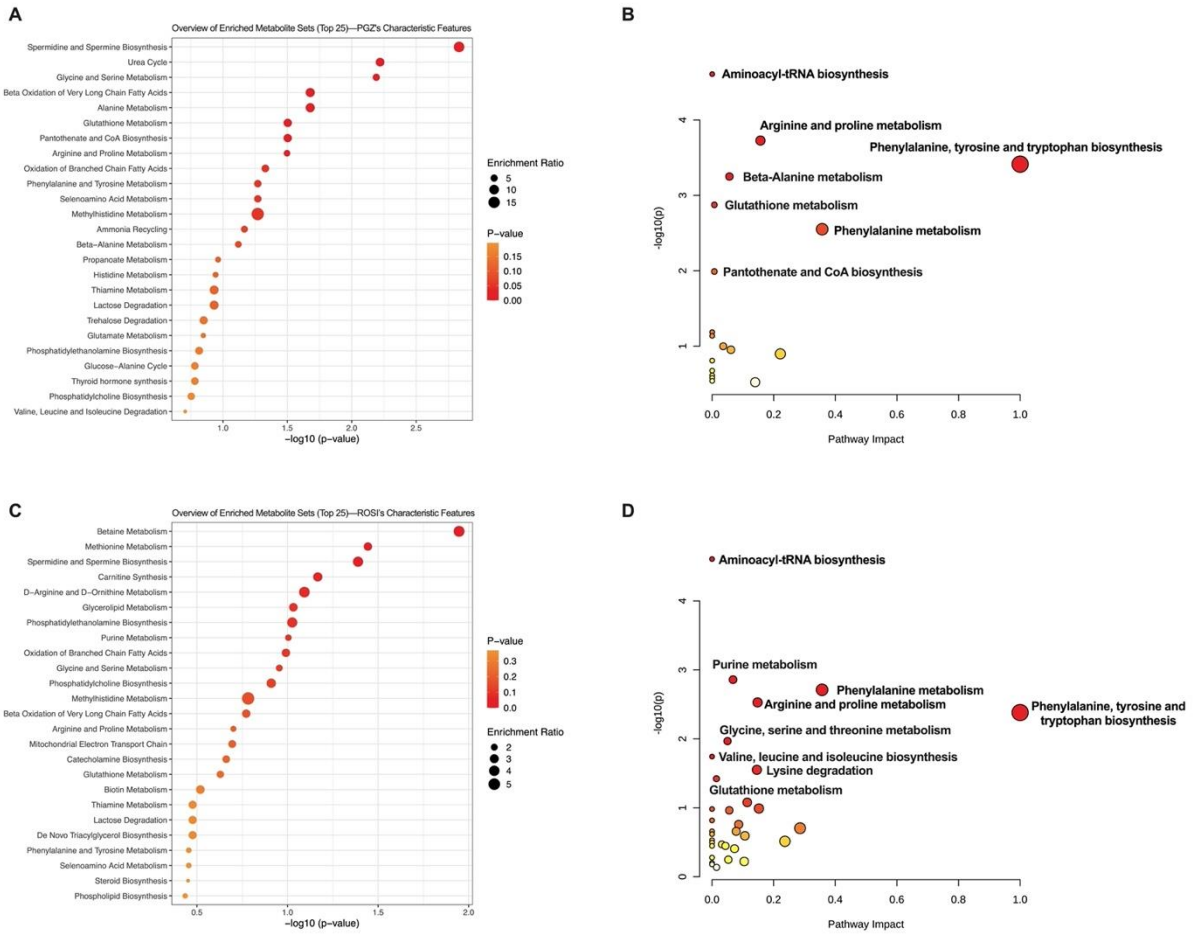

Figure 3.12 The MSEA and metabolic pathways of the characteristic features. The top 25 enriched pathways of (A) PGZ's and (C) ROSI's characteristic features. (B) and (D) denote the pathway analysis of the characteristic features identified from the PGZ and ROSI datasets, respectively. The size and colour of each circle in (A) and (C) reflect the enrichment ratio and significance, respectively, while those in (B) and (D) represent the pathway impact value and the *p*-value, respectively.

PGZ: pioglitazone; ROSI: rosiglitazone; MSEA: metabolite set enrichment analysis.

3.3.4 Identification and Validation of Biomarker Candidates for TZDs' Cardiotoxicity

The hub features identified through PGZ's and ROSI's DSPC networks that were also enriched in pathways linked with TZDs' cardiotoxicity were subjected to ROC analysis to evaluate their prognostic potential (**Figure 3.13**). The ROC findings revealed excellent biomarker prediction for PGZ's hub features; these results included valine with an AUC value of 0.938 ($p < 0.05$), as well as creatine with AUC value of 1 and $p < 0.05$. Regarding ROSI, the ROC curves had an AUC value of 0.802 ($p < 0.05$) and 0.778 ($p < 0.05$) for both L-tryptophan and L-methionine, reflecting a satisfactory overall score performance.

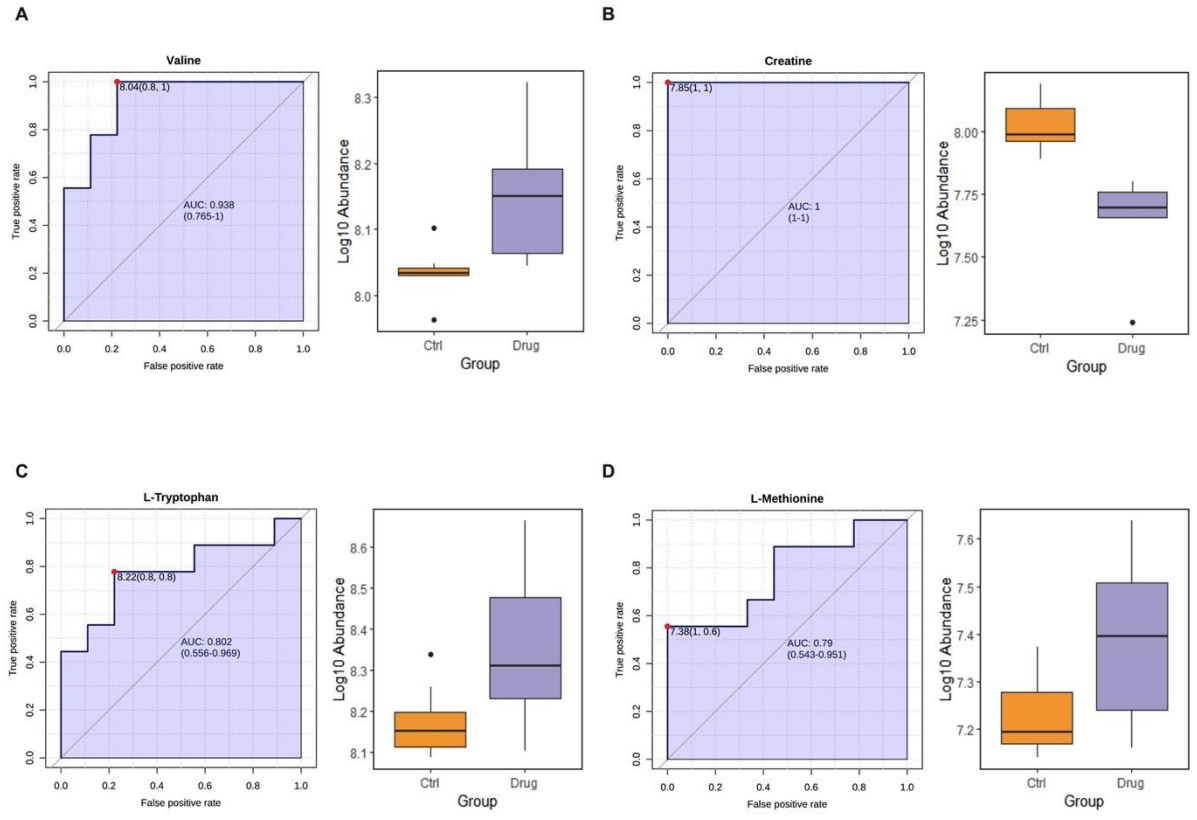

Figure 3.13 Receiver operating characteristic curves and box-plot representation for the hub features of the TZDs. (A) and (B) illustrate the receiver operating characteristic curves, along with the corresponding AUC and considering 95% confidence intervals, for PGZ's chosen biomarkers, while (C) and (D) indicate the receiver operating characteristic analysis findings for ROSI's biomarker candidates.

TZD: thiazolidinedione; PGZ: pioglitazone; ROSI: rosiglitazone; AUC: area under the curve.

3.4 Discussion

The latest T2DM management guidelines have placed growing emphasis on the concept of maintaining tight glycaemic control as a means to delay disease progression and prevent T2DM complications (ADA, 2023). The primary cornerstone to achieving the envisioned goal is pharmacological modalities. TZDs are insulin sensitisers with outstanding pharmacoeconomic attributes (DeFronzo et al, 2019). The efficacy of TZDs, as measured by the Hb_{A1c} index, and their costs have been categorised by the American Diabetes Association as highly effective and economical, cost-effective agents (ADA, 2023). Despite the fruitful profile of TZDs, their clinical use in T2DM has been hindered due to safety concerns, which are characterised chiefly by HF cases associated with their usage (Administration, 2012). To date, the TZD class has been forgotten, and its application has been restricted.

Toximetabolomic tools have been successfully and widely employed in toxicological studies to reveal novel biochemical sequelae and molecular biomarkers underpinning the mode of toxicity of various drugs, including dexamethasone, bisphenol A, doxorubicin and 17β-oestradiol (Cabaton et al, 2018; Dahabiyeh et al, 2020; Geng et al, 2020). However, a limited number of pharmacometabolomic studies on TZDs have been reported thus far. In a rat model, Yang et al. showed that PGZ had an ameliorative effect on hepatic steatosis, predominantly due to the regulation of lipid metabolism, including fatty acids (FAs) and phosphatidylcholines (Yang et al, 2018). In another study, Vinaixa et al. reported a reduction in metabolic oxidation in women with polycystic ovary syndrome after PGZ treatment in combination with flutamide-metformin (Vinaixa et al, 2011). Furthermore, the lipid metabolome effects of ROSI on obese (NZO x NON) F1 male mice were assessed, with observations suggesting a hypolipidemic effect (in the form of triacylglycerides and cholesterol esters) associated with its use (Watkins et al, 2002). Nevertheless, toxicometabolomic studies have yet to address the toxic effects associated with TZD usage (e.g., cardiotoxicity). Thus, this study was designed to employ an untargeted, LC–MS-based toxicometabolomic pipeline for comprehensive metabolic profiling of the AC16 cellular metabolome in response to the acute exposure of TZDs as a means to elucidate the hitherto uncharacterised pathomechanisms that basis TZDs' cardiotoxicity.

3.4.1 Interpretation of Results

The heterogeneity and similarity between the metabolic fingerprints of the drug-treated and control groups were assessed using multivariate statistical analyses. PCA was initially performed to inspect the clustering of the biological samples and determine potential outliers. The PCA model identified group separation, as illustrated in **Figures 3.6A and 3.6B**. Thereafter, the supervised methods OPLS-DA and RF analysis were carried out as feature identifiers and classifiers. By combining the univariate and multivariate analysis findings, the characteristic features of each experiment were identified. In both experiments, these features predominantly include modulation in amino acids (e.g., glutamine, glycine, valine and asparagine); energy metabolites, including glutamate; and lipid content, including prenol lipids, glycerophospholipids and glycerolipids. The common and unique characteristic features, MSEA and pathway findings isolated from each experiment are illustrated via an UpSet plot in **Figure 3.14**. The modulation in characteristic features expression following TZD treatment suggests perturbation in the following major biological processes: cardiac energy metabolism and cardiac hypertrophy.

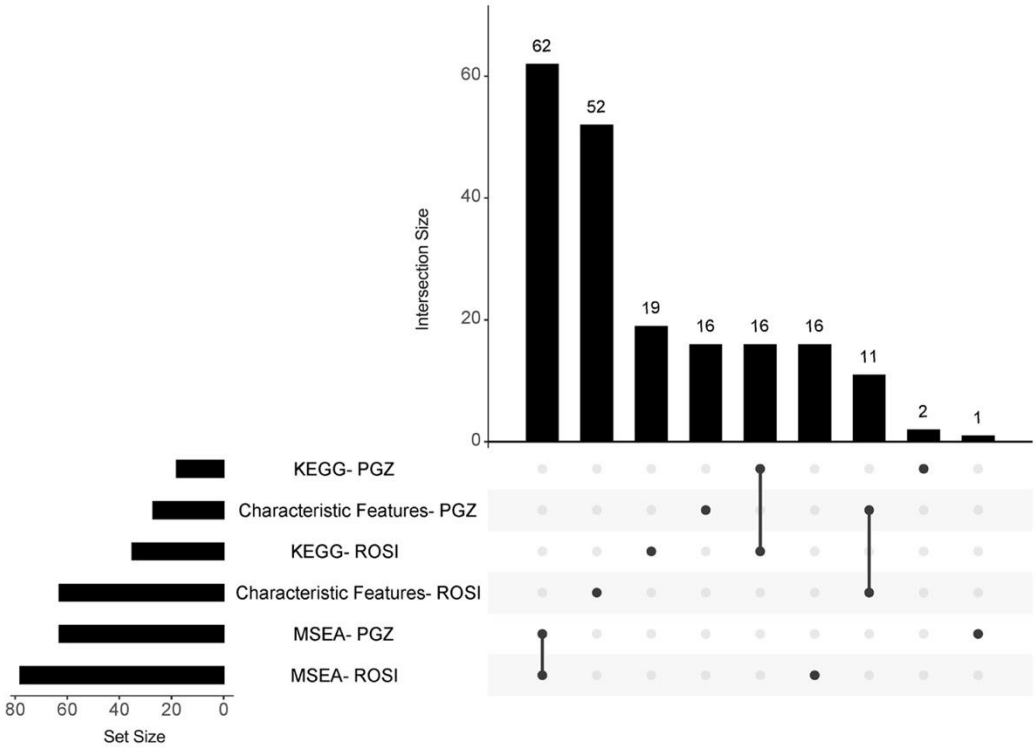

Figure 3.14 UpSet plot illustrating the overlapping and specific characteristic features, MSEA and pathway analysis findings for the two experiments. The *x*-axis (set size) represents the size of each set, while the intersection size indicates the number of each set's measures that are common between sets. The black points denote the intersections, while the grey points represent no intersections.

PGZ: pioglitazone; ROSI: rosiglitazone; MSEA: metabolite set enrichment analysis; KEGG: Kyoto Encyclopedia of Genes and Genomes.

3.4.1.1 TZDs and Cardiac Energetics

It is well acknowledged that a cardiac energy deficit is a hallmark characteristic of HF. The contractile and mechanical properties of the myocardium demand a substantial, steady energy supply; hence, any disruption in the energy metabolic pathways results in drastic reduction in efficient cardiac function. Our toxicometabolomics analysis revealed modulation in the carnitine pool, including L-carnitine and triglylcarnitine, which are crucially integrated in mitochondrial fatty acid oxidation. The carnitine pool represents mitochondrial-derived metabolites primarily responsible for importing long-chain fatty acids into the mitochondria for subsequent beta-oxidation, providing roughly 70–90% of cardiac adenosine triphosphate (ATP), a process referred to as the carnitine shuttle (McCann et al, 2021). The analysis findings showed a decrease in the carnitine pool associated with TZD treatment. Of importance, enrichment in beta oxidation of very long-chain fatty acids was noted with MSEA findings, reinforcing the potential of cardiac energy failure associated with TZD administration secondary to disruption in the carnitine shuttle system and a decrease in substrate oxidation. To date, a cumulative amount of evidence has linked disruption in the carnitine profile with HF pathogenesis in both human and rodent models (Schenkl et al, 2023). Furthermore, our analysis findings revealed an increase in D-glucose levels, which could be interpreted as a compensatory mechanism to meet the energy demand in response to the disruption of fatty acid oxidation.

In the same context, our analysis revealed alterations in purine metabolites, including inosine, hypoxanthine, adenosine, and adenosine monophosphate/diphosphate (AMP/ADP), suggesting modulation in purine biosynthesis/catabolism pathways accompanying TZD treatment. It is well established that purine nucleotides play crucial roles in the synthesis of the genetic material and the energy currency of the cells, ATP (Lane & Fan, 2015). The cross-linking between the modulation in purine metabolites and TZD treatment is explained through the need to compensate for the shortage of cellular ATP. The elevated levels of both inosine and hypoxanthine suggest upregulation of the purine salvage pathway, which is a process of synthesizing purine nucleotides from nucleosides recovered from RNA and DNA degradation as a

response to mitigate cardiac energy failure and increase the energy supply (Johnson et al, 2019). Nevertheless, the purine catabolism end product, hypoxanthine, has been reported to induce reactive oxygen species (ROS) generation, elevate serum cholesterol levels and worsen the progression of cardiotoxicity (Ryu et al, 2016). Therefore, the unbalancing between purine salvage and catabolism noted in our analysis could have catastrophic consequences for cardiac tissue, which necessitates further investigation.

Reflecting on the amino acid profile, modulation in branched-chain amino acids (BCAAs) represented with high levels of L-leucine, L-isoleucine and valine was noted in our analysis. Growing clinical and preclinical evidence has proposed elevated levels of BCAAs as a predictor of a wide range of cardiovascular diseases, including HF (Xiong et al, 2022). These findings surprisingly contradict the crucial roles that BCAAs play in cardiac energy metabolism. It is well recognised that BCAA oxidation acts as another fuel supply in the heart. Therefore, the high levels of BCAAs noted, and through various clinical studies performed on patients with overt cardiovascular diseases, could potentially be interpreted as a cardioprotective mechanism to promote cardiomyocyte survival. Nevertheless, the reported outcomes are inconsistent with the above-mentioned predictions. High levels of BCAAs have been shown to worsen the progression of cardiotoxicity for the following proposed reasons: **(i)** The contribution of BRAAs to cardiac ATP is marginal, accounting for approximately 2% of the total cardiac energetics. Therefore, elevated levels of these amino acids are not adequate for overcoming the shortage in cardiac ATP levels (Karwi & Lopaschuk, 2023). **(ii)** On account of recent *in vivo* cardiovascular studies, downregulations in key enzymes involved in BCAA oxidation have been reported, resulting in impairment in energy supply, contractile dysfunction and further accumulation of BCAAs in the myocardium (Lai et al, 2014; Sun et al, 2016). **(iii)** Elevated levels of BCAAs have been reported to induce mitochondrial dysfunction through mechanisms involving interfering with the electron transport chain and hence oxidative phosphorylation and altering mitochondria biogenesis through activating eNOS/NO/SIRT1 pathways (Ye et al, 2020).

3.4.1.2 TZDs and Cardiac Hypertrophy

Cardiac hypertrophy is an adaptive response prompted by physiological and pathological stressors. However, sustained hypertrophy causes a myriad of negative consequences, including the progression to HF. In our analysis, the modulation of a number of putative features that are evidently associated with cardiac hypertrophy was identified. For instance, elevated levels of polyamines, spermine and spermidine, noted in our analysis, have been linked through numerous *in vivo* models with cardiac hypertrophy (Giordano et al, 2010; Meana et al, 2016). Several mechanisms have been postulated to explain the cross-link association, one of which is attributed to the intrinsic ability of polyamines to modulate β-adrenoceptor signalling pathways and therefore cardiac remodelling (Giordano et al, 2010). In addition, modulation of amino acids has been associated with cardiac remodelling (Geng et al, 2020; Karwi & Lopaschuk, 2023). The high levels of BCAAs found in our toxicometabolomics analysis have been reported to activate the mammalian target of the rapamycin (mTOR) signalling pathway, a crucial hypertrophic signalling pathway implicated in HF patho-mechanisms (Xiong et al, 2022). L-tyrosine is another amino acid that has been hooked with cardiac hypertrophy, as its involvement was supported by a recent study performed to investigate the pathophysiological process of doxorubicin-induced cardiotoxicity (Geng et al, 2020). Furthermore, low levels of the nonproteinogenic amino acid γ-aminobutyric acid (GABA) were detected with TZDs. GABA is well recognised as a major inhibitory neurotransmitter with vital biological roles that are not restricted to the central nervous system but also function in peripheral tissues (Rashmi et al, 2018). In spontaneously hypertensive rats, the oral administration of GABA led to a reduction in cardiac hypertrophy (Lin et al, 2012). Hence, the low levels of GABA found in our analysis could be secondary to TZD-induced modulation of amino acid metabolism, an additional contributor factor involved in TZD cardiotoxicity. While the above-mentioned findings provide a valuable starting point, additional experiments are crucial to validate the cross-link between TZDs and cardiac hypertrophy and unravel the specific molecular pathways involved.

3.4.2 Limitations and Future Directions

When all the results are taken together, some limitations should be addressed before drawing conclusions. Initially, in accordance with the 3Rs principle of animal

experimentation, the transition in toxicological research is evolving towards animal-free *in vitro* and *in silico* approaches (Yu et al, 2020). This also explains the rationale behind selecting AC16 cells for our analysis. Furthermore, the well-defined cardiac signaling pathways and responsiveness to stimuli in AC16 cells, combined with their ease of culture, rapid growth, and relative cost-effectiveness compared to other models, justified their selection for our research, allowing us to effectively investigate the effects of TZDs on cardiomyocyte metabolism. While AC16 cells offer advantages for studying cardiac function, their inherent limitations, including glycolysis-dependence and fibroblast-like morphology, coupled with their dedifferentiation potential and challenges in maintaining differentiated cultures, necessitated our focus on proliferative cells for this investigation. Also, the validity of *in vitro* models in accurately estimating the biological complexity of the human body is still lacking (Graudejus et al, 2018; Yu et al, 2020). Moreover, when investigating the metabolic activity of cells, an *in vitro* model could be a limitation due to its limited metabolic activity compared to *in vivo* systems (Graudejus et al, 2018; Yu et al, 2020). Lastly, a significant limitation of this study is the lack of internal standards. Internal standards are essential for normalising variations that can arise during sample preparation, instrument performance, and data acquisition (Wang et al, 2017). They help to control for factors like variable metabolite recovery, matrix effects, and MS drift. Without internal standards, the ability to accurately quantify metabolite levels is reduced, and relative quantification becomes more susceptible to technical variability. This also limits confidence in comparing metabolite changes across samples, batches, or experiments, and may affect the reproducibility of the results. Furthermore, the absence of internal standards complicates the detection of low-abundance metabolites and increases the risk of RT shifts, which can hinder metabolite identification (Wang et al, 2017). However, a future direction for our research group is to address this limitation by developing a comprehensive internal standard library tailored for our system. This effort will enhance data reliability and improve the robustness of our metabolomics analysis in future studies.

In conclusion, the present study is the first to profile the broad-scale metabolic perturbations of human AC16 induced by the TZD class of medications. The comprehensive toxicometabolomics approach employed herein has unveiled modulations in the carnitine shuttle, purine metabolism and amino acid fingerprint,

each of which strongly indicate aberration in cardiac energetics associated with TZD usage. Our analysis has also pinpointed changes in polyamines and BCAA levels that are evidently associated with phenotypic alterations of cardiac tissues (hypertrophy), which indeed represents another hallmark characteristic of cardiotoxicity and a potential mechanism implicated in it. This comprehensive study also suggests the following two groupings – (i) valine and creatine, and (ii) L-tryptophan and L-methionine – which were significantly enriched in the above-mentioned mechanisms, as potential fingerprint biomarkers for PGZ and ROSI cardiotoxicity, respectively. Collectively, the results of this study suggest the LC–MS toxicometabolomics approach as a powerful platform for exploring chemical-induced perturbation in downstream molecular phenotypes, in turn pointing out a promising route for designing therapeutic targets capable of tackling these chemicals' adverse effects.

Chapter 4

Toxicoproteomics-Based Cardiotoxicity Evaluation of Thiazolidinedione Exposure in Human-Derived Cardiomyocytes

Abdullah Al Sultan[1,2] , Zahra Rattray[1,3] & Nicholas J. W. Rattray[1,3]*

[1]Strathclyde Institute of Pharmacy and Biomedical Sciences, University of Strathclyde, 161 Cathedral Street, Glasgow, UK, G4 0RE

[2]Faculty of Pharmacy, Kuwait University, Safat, 13110, Kuwait

[3]Strathclyde Centre for Molecular Bioscience, University of Strathclyde

Received: 17 February 2024 / Accepted: 2 April 2024

Al Sultan A, Rattray Z, Rattray NJ. Cytotoxicity and toxicoproteomics analysis of thiazolidinedione exposure in human-derived cardiomyocytes. Journal of Applied Toxicology. 2024 Apr 2. https://doi.org/10.1002/jat.4613

Abstract

Thiazolidinediones (TZDs) (e.g., pioglitazone and rosiglitazone), known insulin sensitiser agents for type II diabetes mellitus, exhibit controversial effects on cardiac tissue. Despite consensus on their association with increased heart failure risk, limiting TZD use in diabetes management, the underlying mechanisms remain uncharacterised. Herein, we report a comprehensive *in vitro* investigation utilising a novel toxicoproteomic pipeline on human adult cardiomyocytes to elucidate mechanistic insights into TZD cardiotoxicity. Our toxicoproteomic analysis revealed mitochondrial dysfunction accompanying TZD exposure. This dysfunction primarily stemmed from impaired oxidative phosphorylation, with distinct signalling mechanisms observed for both agents. The type of cell death differed strikingly between the two agents, with rosiglitazone exhibiting features of caspase-dependent apoptosis and pioglitazone implicating mitochondrial-mediated necroptosis, as evidenced by the protein upregulation in the phosphoglycerate mutase family 5–dynamin-related protein 1 axis. Furthermore, our analysis revealed additional mechanistic aspects of cardiotoxicity, showcasing drug specificity. The downregulation of various proteins involved in protein machinery and protein processing in the endoplasmic reticulum was observed in rosiglitazone-treated cells, implicating proteostasis in the rosiglitazone cardiotoxicity. Regarding pioglitazone, the findings suggested the potential activation of the interplay between the complement and coagulation systems and the disruption of the cytoskeletal architecture, which was primarily mediated through the integrin-signalling pathways responsible for pioglitazone-induced myocardial contractile failure. Collectively, this study unlocks substantial mechanistic insight into TZD cardiotoxicity, providing the rationale for future optimisation of antidiabetic therapies.

Keywords: Thiazolidinediones; mitochondrial dysfunction; WGCNA; label-free protein quantification

4.1 Introduction

Over the past few decades, dramatic advances in analytical techniques for high-throughput experimentation and computational tools have been achieved, revolutionising the landscape of toxicological science (Karahalil, 2016; Li et al, 2021; Nguyen et al, 2022). Simultaneously with revolutionary discoveries, the US National Research Council (NRC) published a turning point report, 'Toxicity Testing in the 21st Century', setting up a long-term strategic plan to encourage the transition towards advanced *in vitro* and *in silico* high-throughput technologies over the costly and time-consuming traditional toxicity testing that primarily relies on animal experimentation (Krewski et al, 2020). The long-term strategic vision of the NRC, which is rooted in embracing the technologies mentioned above, has a two-component toxicity testing paradigm (Krewski et al, 2020). The first component encourages the elucidation of the signalling pathways perturbed by chemicals, preferably through adapting omics-based *in vitro* cell-line studies, and the second envisioned point focuses on validating the first component's findings by performing targeted testing on the identified pathway using *in vivo* models or clinical samples (Krewski et al, 2020). These two components collectively aim to provide more comprehensive insights into the toxicity mode and open up new horizons into the identification of toxicity biomarkers associated with hazardous substances.

In alignment with the NRC's strategic vision, several omics-based approaches have emerged and been integrated into mechanistic toxicological studies, including toxicoproteomics (Brewer et al, 2020; Nguyen et al, 2022; Nury et al, 2023; Thomas et al, 2023). Toxicoproteomics is a rapidly expanding field of omics that can be broadly described as the global characterisation of protein expression profiling in response to stressors (Nguyen et al, 2022). Toxicoproteomics encompasses a triangle of three disciplinary areas: traditional toxicology, proteomics applications and the biological system to fulfil two main research aims: (i) deciphering the mode of toxicity associated with adverse chemical effects and (ii) governing and identifying molecular targets that could act as candidate biomarkers for toxicants (Suman et al, 2016). Depending upon the research question, toxicoproteomic approaches constitute a large-scale characterisation of either the whole proteome or are restricted to a class of proteins of interest, processes termed the shotgun approach and targeted proteomics, respectively (Deracinois et al, 2013). To date, numerous proteomic platforms are

available to apply this approach (Aslam et al, 2016). This includes gel-based and gel-free techniques. An overview of the principle and the advantages and drawbacks of the commonly used techniques is summarised in **Table 4.1.**

Table 4.1 Overview of commonly used proteomics approaches.

Technique	Principle	Pros	Cons
Gel-Based Techniques (Abdallah et al, 2012; Aslam et al, 2016; Deracinois et al, 2013)			
2D Gel Electrophoresis	Separation and profiling complex protein mixtures as per isoelectric point and protein mass	-Cost-effective compared to existing methods -Reasonable sensitivity and resolution -Can detect protein complexes	-Limited reproducibility and dynamic range -Low throughput -Time consuming -Labour intensive -Difficulty in separating basic and hydrophobic proteins -Differential analysis is challenging -Inter-gel variability
2D-DIGE	Fluorescent protein sample labelling before gel separation	-Improved sensitivity -Enables comparative analysis -Overcomes inter-gel variation with 2D gel electrophoresis	-Time consuming -Labour intensive -Limited reproducibility and dynamic range -Low throughput
Gel-Free Techniques (Abdallah et al, 2012; Al-Amrani et al, 2021; Deracinois et al, 2013)			
HPLC	Fractionating and separating protein complexes as per to their distribution equilibrium differences between stationary and mobile phases	-Availability of stationary and mobile phases -Accuracy, precision and reproducibility -Low sample consumption -Wide dynamic range	-Costly and complex -Solvent consumption
Analytical Protein and Peptide Microarrays	Proteins identified after antibody capture with direct protein labelling	-High-throughput technology -Versatile: Utilised in a broad spectrum of applications -Low sample consumption -Rapid and sensitive technique	-Lack of standardised protocol methods -Highly specific antibodies are imperative for each assay; otherwise, non-specific binding could arise, leading to false positive results -Stability of proteins on the array surface
MS	Profiling and quantifying simple and complex mixtures according to their mass-to-charge ratio of ions	-High-throughput technique -Distinctive array of applications (i.e., de novo sequencing, post-translational modification identification) -Highly sensitive, precise and accurate -Can be coupled with other techniques (i.e., HPLC) -Low sample consumption	-Costly -Sample handling, refinement and manipulation -Technical expertise required
NMR	Determination of the molecular structure at the atomic level via measuring the interaction of the radio frequency electromagnetic radiations and the nuclei of atoms	-High-throughput technology -Non-destructive -Rapid	-Costly -Lack of sensitivity -Not applicable for large proteins (molecular weight > 800 Da)
LC–MS/ GC–MS	Coupling of the separation feature of the chromatography technique with the detection power of MS	-Gold standard; superior sensitivity and specificity -Multiplexing capabilities -High-throughput technique -Broad array of applications (i.e. de novo sequencing, post-translational modification identification) -Low sample consumption	-Time consuming -Complex -Costly -Technical expertise required

Abbreviations: 2D-DIGE: 2D differential gel electrophoresis; HPLC: high-performance liquid chromatography; MS: mass spectrometry; NMR: nuclear magnetic resonance; LC–MS: liquid chromatography–mass spectrometry; GC–MS: gas chromatography–mass spectrometry

Among these proteomics techniques, increasing attention has been paid to integrating liquid chromatography–mass spectrometry (LC–MS) into mechanistic toxicology (Al-Amrani et al, 2021; Li et al, 2021). The increased sensibility and specificity of LC–MS has revitalised the ability to profile and quantify the proteome, generating high-throughput data acquisition with unprecedented mass accuracy, sensitivity and resolving power. Emphasising proteome quantification, another distinctive feature of integrating MS technology is the usability of numerous strategies for relevant and absolute protein quantification (Aslam et al, 2016). The multitude of quantitative MS applications can be broadly categorised based on sample labelling into label-based and label-free quantification methods (**Figure 4.1**) (Abdallah et al, 2012; Al-Amrani et al, 2021; Aslam et al, 2016; Deracinois et al, 2013).

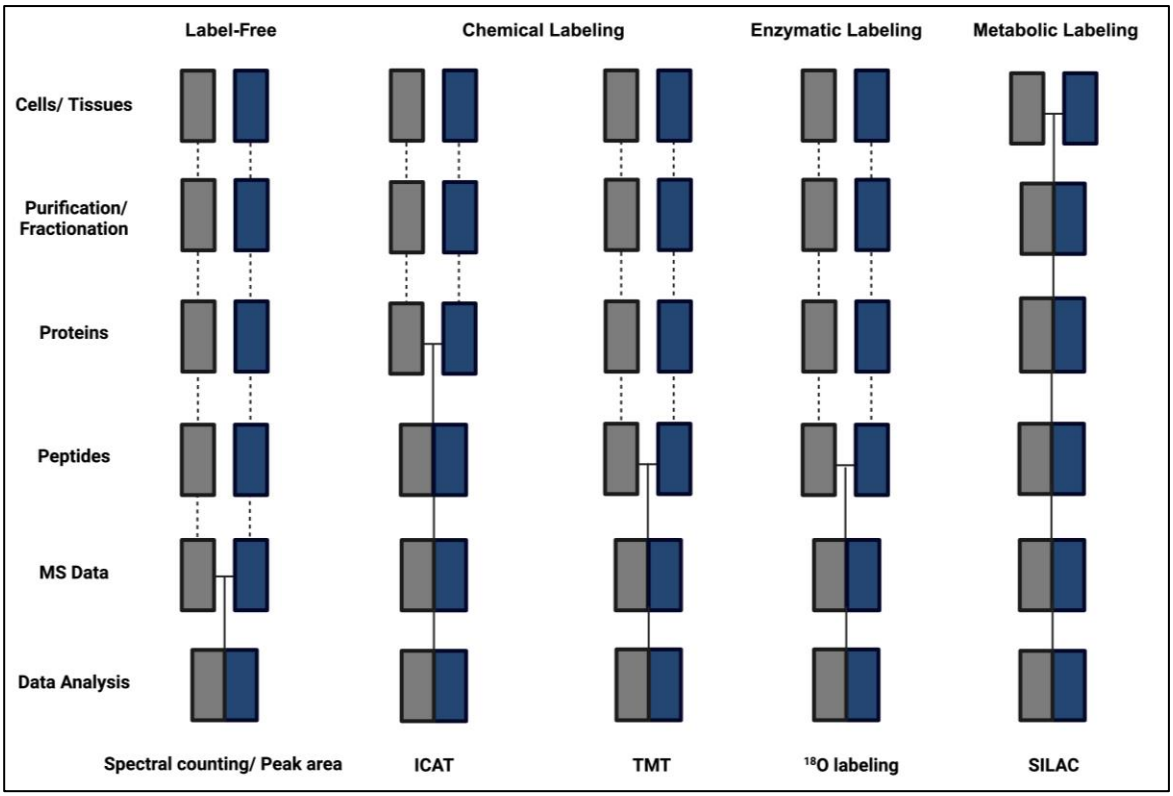

Figure 4.1 Quantitative mass spectrometry-based proteomics. Boxes in blue and grey indicate the two experimental conditions. The dashed lines indicate the parallel processing of the experimental conditions at each workflow step. The horizontal lines represent the step whereupon the blue and grey samples are pooled for the upcoming experimental workflow. Adopted from (Abdallah et al, 2012; Al-Amrani et al, 2021; Aslam et al, 2016; Deracinois et al, 2013).

MS: mass spectrometry; ICAT: isotope-coded affinity tag; TMT: tandem mass tagging; SILAC: stable-isotope labelling by amino acids in cell culture.

Label-based quantification analysis entails the introduction of stable isotope labels within the samples, thereby providing a predictable mass difference within the tested groups (Abdallah et al, 2012; Al-Amrani et al, 2021). Examples of well-recognised isotope labelling strategies involve metabolic labelling, such as isotope labelling with amino acids in cell culture (SILAC); chemical labelling, which includes isobaric labelling techniques, such as tandem mass tag and isobaric tag for absolute and relative quantitation (TMT/iTRAQ); and enzymatic labelling (i.e., ^{18}O-labeling) (Anand et al, 2017; Aslam et al, 2016). Notably, each labelling technique has its pros and cons that, therefore, affect its scope of application. In contrast, the label-free technique, as the term implies, provides a large-scale proteome quantification independent of sample labelling (Anand et al, 2017). The adoption of this technique has been widespread in recent years due to the straightforward principle of label-free quantification (LFQ), the simplicity of the protocol required to implement such an experiment and the fact that it is time saving and cheaper than the other label-based methods (Aslam et al, 2016).

Therefore, with the envisioned NRC and motivated by the successful application of toxicoproteomics in mechanistic toxicology, as reported extensively in the literature (Al-Amrani et al, 2021; Nury et al, 2023; Pizzatti et al, 2020; Thomas et al, 2023), this study aimed to implement a toxicoproteomic approach to elucidate the cardiotoxicity effects associated with a class of insulin-sensitising agents termed thiazolidinediones (TZDs). The objectives of this study were to (i) establish a novel micro-flow LC–MS-based toxicoproteomic pipeline capable of profiling the proteome signatures of TZD-treated AC16 cells, (ii) elucidate the biochemical pathways underpinning the cardiotoxic effects of TZD agents and (iii) identify the driver proteins associated with such effects through analysing differential expressed proteins (DEPs) and performing a weighted correlation network analysis (WGCNA).

4.2 Material and Methods

4.2.1 Drugs and Chemicals

PGZ and ROSI were purchased from Sigma-Aldrich (St Louis, MO, USA). For the *in vitro* studies, PGZ and ROSI 100 mM stock solutions were prepared in sterile dimethyl sulphoxide (DMSO) (Cat. No. 12611P; Cell Signaling Technology Beverly, MA, USA), and diluted to the appropriate IC_{50} concentrations with culture medium for *in vitro* experiments. The final concentration of DMSO in the medium was ≤0.1% (v/v).

The EasyPep Mini MS Sample Prep Kit that was used for the proteomic profiling of cultured cells was purchased from Thermo Fisher Scientific (Cat. No. A40006; Rockford, IL, USA). The following items were included in the kit: lysis solution, universal nuclease, reduction solution, alkylation solution, Pierce™ Trypsin/Lys-C Protease Mix (MS Grade), digestion stop solution, peptide clean-up columns, wash solution A, wash solution B, elution solution and low protein-binding collection tubes. The reagents used for the LC–MS analysis consisted of high-performance liquid chromatography (HPLC)-grade acetonitrile, methanol, analytical-grade formic acid and ultrapure water and were purchased from Fisher Scientific (Loughborough, Leicestershire, UK).

4.2.2 Cells and Cell Culture

The AC16 cell line is derived from adult human ventricular cardiomyocytes and was purchased from Sigma-Aldrich (Product. No. SCC109; St Louis, MO, USA). Cells were cultured in Dulbecco's Modified Eagle's Medium (DMEM/F-12, Product. No. D6434; Sigma-Aldrich, St Louis, MO, USA) supplemented with 12.5% foetal bovine serum, 1% antibiotics (streptomycin and penicillin) and 2 mM L-glutamine at 37 °C in a humid atmosphere of 5% CO_2 and 95% air.

4.2.3 Sample Preparation for Proteomic Profiling

Rigorous optimisation of sample preparation and protein extraction protocols was conducted to ensure reproducible and reliable analytical outcomes. The EasyPep™ MS Sample Prep Kits served as the foundation, with further optimisation focused on cell density and trypsin digestion (**Figure 4.2**).

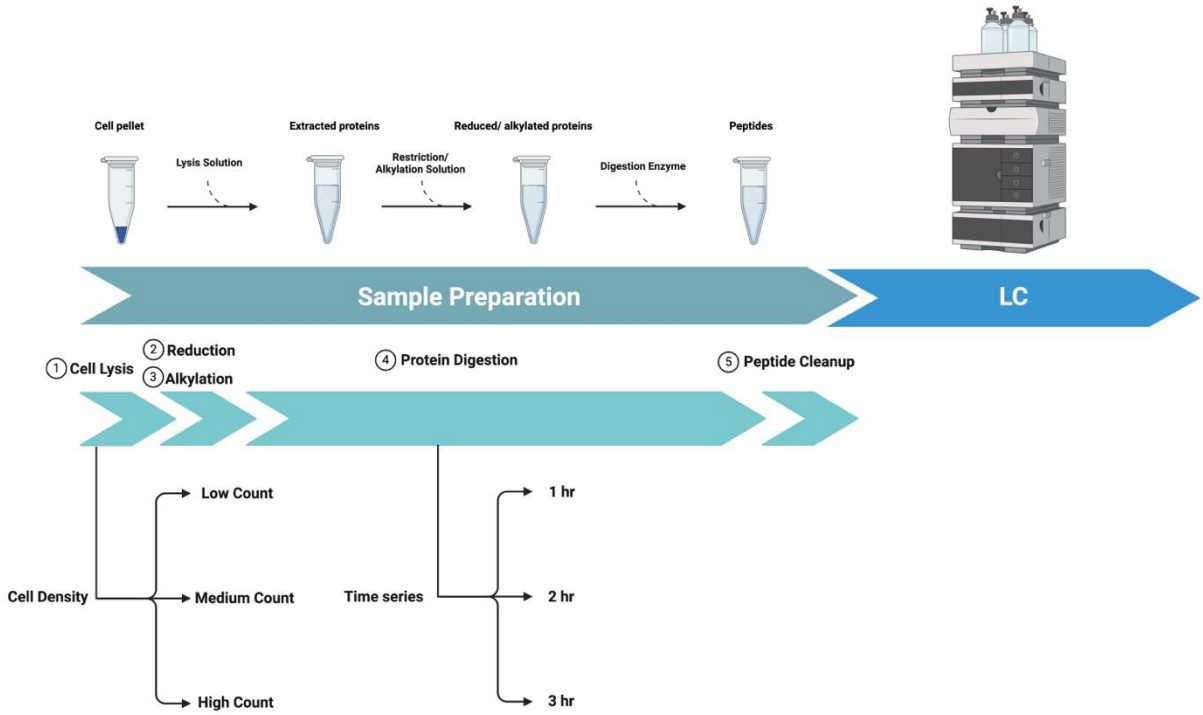

Figure 4.2 Optimisation workflow for proteomics sample preparation techniques. This figure outlines the sample preparation and analysis workflow employed in the study. The process involved (1) cell lysis, (2) reduction and (3) alkylation, (4) protein digestion, and (5) peptide cleanup, followed by LC–MS analysis. Optimisation was conducted for key steps, including cell density and trypsin digestion incubation period. Three different cell densities were evaluated, with two million cells selected as the optimal concentration. Trypsin digestion time was optimised through time-series experiments, resulting in a two-hour incubation period as the preferred choice. These optimised parameters ensured reliable and robust findings throughout the study.
LC–MS: Liquid chromatography–mass spectrometry

Cell seeding count is a crucial factor in the efficiency of cell lysis and protein extraction, the essential initial steps in bottom-up proteomics. To achieve consistent and reliable protein yield, various cell densities were evaluated. The cell seeding densities were categorised into three groups: low, moderate, and high cell counts. The low count included cell numbers up to 1 million, moderate ranged from 1 to 2 million cells, and the high count consisted of a minimum of 2 million cells.

The results demonstrated a direct correlation between cell seeding concentration and the mean number of identified proteins and peptides (**Figure 4.3**). The low-cell group exhibited the lowest counts, with an average of 813 proteins and 1543 peptides. The moderate group showed an increase to 3026 proteins and 13,928 peptides. However, the group with the highest cell count (2 million) yielded the most comprehensive proteomic coverage, with an average of 3285 proteins and 15,804 peptides. These findings, based on the results of two experimental replicates per group, suggest that a minimum cell seeding count of 2 million is necessary to ensure adequate protein coverage and maximize the identification of biologically relevant molecules in subsequent proteomic analyses.

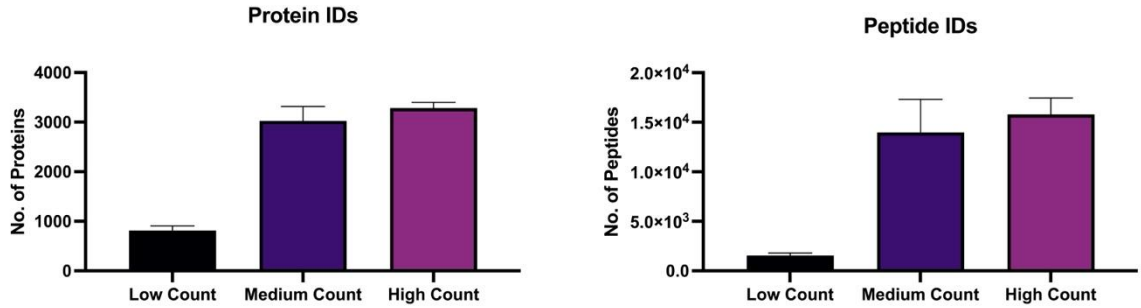

Figure 4.3 Effect of cell seeding density on proteomic coverage. This figure compares the proteomic coverage achieved using different cell seeding densities (low, moderate, and high). The number of identified proteins (A) and peptides (B) were evaluated for each seeding density. The results demonstrate that higher seeding densities led to increased proteomic coverage.

Following cell count optimisation, proteolytic digestion is another critical step in bottom-up proteomics sample preparation. The duration and completeness of digestion can significantly impact the overall performance of the proteomic analysis. While the EasyPep™ MS Sample Prep Kits protocol recommended a 1-3 h incubation period, our optimisation procedure focused on assessing the percentage of zero missed cleavages at 1, 2, and 3 h to determine the ideal digestion duration. The results, based on two experimental replicates per group, were comparable across the three time points, with a slightly higher percentage of zero missed cleavages observed at 2 hours (**Figure 4.4**).

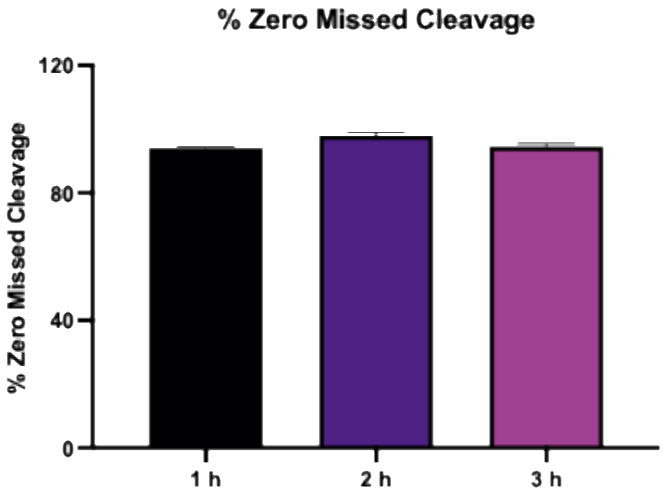

Figure 4.4 Effect of trypsin incubation time on digestion efficiency. This figure illustrates the impact of varying trypsin incubation times (1, 2, and 3 h) on protein digestion efficiency. The percentage of peptides with zero missed cleavages was assessed to evaluate digestion quality. The findings demonstrate comparable digestion efficiency across all incubation times.

Collectively, based on the findings presented, a minimum of 2 million cells and a 2 h incubation period were selected as optimal parameters, ensuring robust peptide cleavage and enhanced protein identification. These optimisations established a robust and reproducible sample preparation process, which is essential for accurate mass spectrometry analysis. A detailed explanation of the protocol followed is provided below.

AC16 cells were cultured to 70–80% confluence and seeded at 2×10^6 cells/well in six-well plates (Cat. No. 140675; Thermo Fisher Scientific, Roskilde, Denmark). Following attachment, the medium was replaced with either fresh medium (control) or medium containing TZD agent at the calculated IC_{50} and incubated for 24 h. Cells were scraped from the six-well plates, aliquoted into 1.5 mL Eppendorf microtubes (Eppendorf, Hamburg, Germany) and centrifuged at 3,000 g for 10 min (4 °C). The supernatant was discarded, and cell pellets retained for proteomics profiling using EasyPep Mini MS Sample Prep Kits.

4.2.4 Protein Extraction, Trypsin Digestion and Peptide Clean-up

For the protein identification and proteomic profiling steps, the cell pellets were lysed with 100 µL lysis buffer and resuspended thoroughly in 1 µL of universal nuclease for 10–15 cycles until the sample viscosity was reduced. The lysates were collected, and the supernatant protein concentration was determined using the Pierce BCA Protein Assay Kit (Product. No. 10495315; Thermo Fisher, Rockford, IL, USA). For the protein digestion step, an aliquot containing 100 µg of protein was taken from each sample and transferred into a new 1.5 mL Eppendorf microtube, and the final volume was adjusted to 100 µL with the lysis solution. The samples were then reduced by the addition of 50 µL of reduction solution and alkylated by the addition of 50 µL of alkylation solution. The alkylated protein samples were then incubated at 95 °C for 10 min using a heat block. The samples were then left to cool to room temperature. Subsequently, 50 µL of the reconstituted enzyme solution (Trypsin/Lys-C Protease Mix) was added to each sample, and the sample tubes were incubated for 2 h at 37 °C in an Eppendorf ThermoMixer C (Thermo Fisher, San Jose, CA, USA) with agitation (600 rpm). Following the incubation period, 50 µL of digestion stop solution was added to each sample to terminate trypsin digestion.

Following the instructions supplied with the EasyPep Mini MS Sample Prep Kit, peptide clean-up was performed after the enzymatic sample processing. The peptide clean-up columns provided with the kit were first placed in 2 mL microcentrifuge tubes and centrifuged at 3,000 g for 2 min until dry. The protein samples were then transferred into the dry peptide clean-up columns and centrifuged at 1,500 g for 2 min. The flowthrough was discarded from each column. Subsequently, 300 µL of wash solution A was added to each column, the tubes were centrifuged at 1,500 g for 2 min, and the flowthrough was discarded. The same step was repeated with 300 µL of wash solution B. For the elution step, the peptide columns were transferred into new 2 mL microcentrifuge tubes. The elution solution (300 µL) was added to each column, and the sample tubes were centrifuged at 1,500 g for 2 min. The eluted peptides were then collected and evaporated to dryness using a Thermo Scientific Savant SpeedVac (Thermo Fisher, San Jose, CA, USA). The dried samples were reconstituted in 100 µL of 0.1% formic acid in water and eventually transferred to 1.5 mL LC–MS glass vials (Cat. No. 6PSV9-03FIVAPT; Thermo Fisher, Langerwehe, Düren, Germany) for LC–MS analysis. In addition to the experimental samples, quality control (QC) and

blank samples were prepared. The QC sample was prepared by pooling equal volumes of all the experimental samples, while the blank sample consisted of 50 µL of acetonitrile: water (50:50).

4.2.5 Micro-flow LC–MS-based Toxicoproteomic

4.2.5.1 Data Acquisition

Peptide separation was performed on a binary Thermo Vanquish ultra-high-performance liquid chromatography system where 20 µL of the reconstituted peptide mixture extract was injected onto a Thermo Acclaim C_{18} PepMap 100 column (150mm x 1mm, particle size 3µm) and separated over a 100min method. The column was maintained at 40 °C, while the autosampler temperature was set at 5 °C. For chromatographic separation, a consistent flow rate of 50 µl/min was used where the mobile phase in positive and negative heated electrospray ionisation mode (HESI+/-) was composed of Solvent A (99.9% water with 0.1% formic acid) and solvent B (99.9% acetonitrile with 0.1% formic acid) (**Table 4.2**). All post columns viper fittings had a 75 µm internal diameter (black colour code).

Table 4.2 HPLC gradient mode of the mobile phase

No.	Time	Flow (ml/min)	%B
1	0.000	Run	
2	0.000	0.050	3.0
3	65.000	0.050	20.0
4	70.000	0.050	40.0
5	74.000	0.050	95.0
6	79.000	0.050	95.0
7	84.000	0.050	3.0
8	100.000	0.050	3.0
9			
10	100.000	Stop Run	

A high-resolution Exploris 240-Orbitrap mass spectrometer (Thermo Fisher Scientific) was used to perform bottom up proteomics analysis. Operating parameters were set as follows: spray voltages of 3400V in HESI +ve mode. The temperature of the ion transfer tube was set at 320°C with a vaporiser temperature of 75°C. Sheath, aux gas and sheath gas flow rates were set at 25, 5 and 0 Arb, respectively. A Top-20 Data-Dependent Acquisition (DDA) was performed using the following parameter: survey scan range was 275-1500 m/z with MS1 resolution of 120,000, RF Lens of 70% and an intensity threshold of $1.0e^4$. Subsequent MS/MS scans were collected with a resolution of 15,000, isolation window of 1.2 m/z, and with a normalised HCD Collision Energy of 30%. A data dependent cycle time of 3 seconds between master scans was also employed. High-purity nitrogen was used as nebulising and as the collision gas for higher energy collisional dissociation.

4.2.5.2 Data Processing

Using Proteome Discoverer (PD) v3.0 software (Thermo Fisher, San Jose, CA, USA), the MS raw data were used to search the UniProtKB Human Reference Proteome database (v22.07.13; 79,740 entries), including common contaminants (247 entries), using the SEQUEST and Percolator algorithms involved in modified label-free quantification (LFQ) standard processing and consensus workflows. **Figure 4.5** outlines the processing and consensus workflows used in this study, which are described in detail in [**Tables S6 and S7, Appendix Section 7.3**] and summarised below (Orsburn, 2021; Zhao et al, 2020).

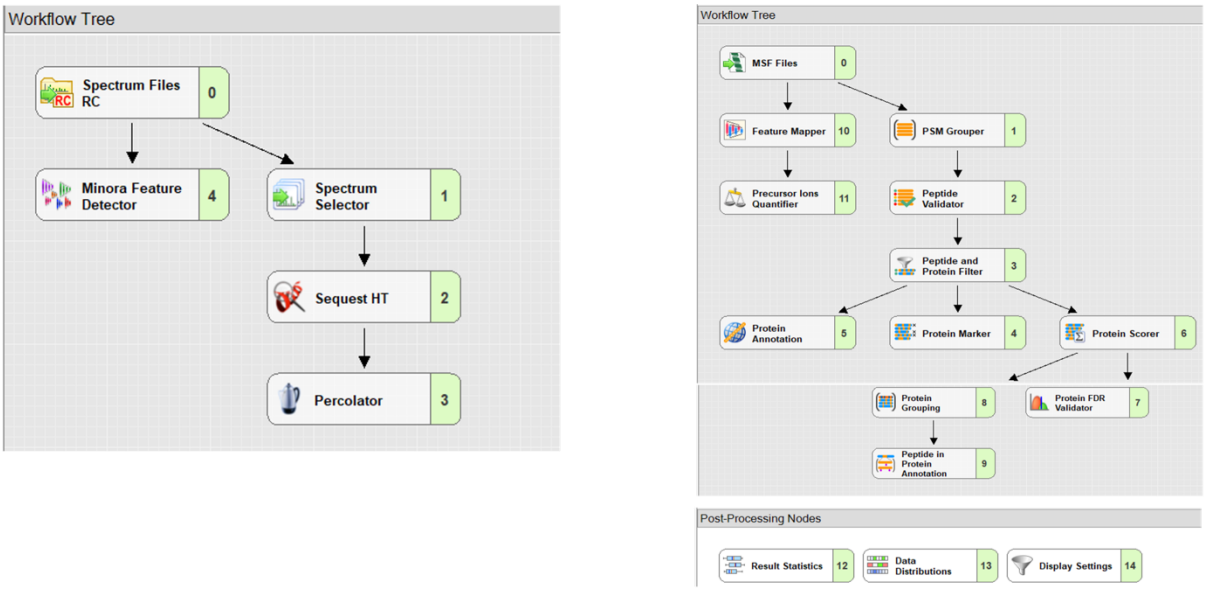

Figure 4.5 Flow chart of the Proteome Discoverer workflows applied to the acquired LC–MS data.

The precursor mass tolerance was set to 10 ppm and 0.02 Da for fragment mass tolerance. Full tryptic digestion was selected, with up to two missed cleavages allowed. The minimum and maximum peptide lengths were set at 6 and 144 amino acids, respectively. Cysteine carbamidomethylation was set as a static modification, and oxidation of methionine (Met), Met loss and N-terminal acetylation were set as dynamic modifications. A maximum of three modifications were allowed per peptide. A concentrated target–decoy approach was applied for the false discovery rate (FDR) calculation, which was set to 1% for highly confident peptide hits.

For protein abundance, the Feature Mapper node was enabled. The raw files were chromatographically aligned with a 10-min retention time shift. The minimum signal-to-noise threshold for feature linking and mapping was set at a value of 5. For precursor peptide abundance, precursor chromatographic intensities were used for precursor quantification results, and the total peptide amount was the selected normalisation mode to correct for experimental bias. Unique and razor peptides were used to quantify the identified proteins. Following data processing, the search results were filtered to include only peptides with a confidence level greater than 95% and "Master proteins" with a confidence level greater than 99%. This stringent filtering ensured that only high-quality identifications were retained for further

analysis. Proteins with an FDR of less than 1% were classified as "High" confidence, corresponding to an experimental q-value no greater than 0.01. These criteria were applied to the resultant outcome features, which were subsequently subjected to statistical analyses.

4.2.6 Bioinformatic Analyses of Proteomics Data

4.2.6.1 Dimensionality Reduction Approaches and Identification of DEPs

To capture the underlying uniformity and heterogeneity within the data obtained from the two sample groups, dimensionality reduction and clustering methodologies were performed in R v4.3.0, including principal component analysis (PCA), t-stochastic neighbour embedding (t-SNE) and generation of a hierarchical clustering heatmap. Notably, the *mixOmics* R package (Rohart et al, 2017) was used on the linearly transformed data to generate the PCA scatter plot, and two components were extracted. In contrast, the *Rtsne* (Krijthe et al, 2018) and *ggplot2* (Wickham et al, 2016) packages were utilised to perform the nonlinear t-SNE, and the resultant output data were clustered based on the protein expression data.

To identify differentially expressed proteins (DEPs), a $\log_2$ fold change (FC) value of 1 and a *p*-value ≤ 0.05 were set as cutoffs. A volcano plot was accordingly generated to visualise the discriminant proteins using the *ggplot2* package (Wickham et al, 2016).

4.2.6.2 GO, DO and KEGG Pathway Analyses

To acquire a systematic understanding of the biological functions and pathways associated with the identified DEPs, an overrepresentation analysis of the Gene Ontology (GO) and Kyoto Encyclopedia of Genes and Genomes (KEGG) enrichment pathways was performed utilising the *enrichDAVID* function of the *clusterProfiler* package (Yu et al, 2012). Furthermore, mining protein–disease associations has opened a new avenue for exploring protein recruitment from the disease perspective. Therefore, disease ontology (DO) enrichment analysis was also performed using the Genetic Association Database, which is based on the Database for Annotation, Visualization and Integrated Discovery (DAVID; https://david.ncifcrf.gov; v2023q1). The GO, DO and KEGG enrichment terms that had a cumulative hypergeometric *p*-value < 0.05 and a minimum count of 2 were considered statistically significant.

4.2.6.3 WGCNA and Module Identification

WGCNA is an established analytical co-correlation tool that was originally developed for analysing high-throughput genomic datasets predominantly via unsupervised clustering (Langfelder & Horvath, 2008; Liu et al, 2021). The unsupervised clustering method is used to classify genomic data into biologically meaningful modules of coexpressed genes and can be used to identify regulatory networks, disease-associated modulation in genomic networks and the 'driver genes' that are critical in disease onset and progression (Langfelder & Horvath, 2008; Liu et al, 2021). Recent studies have highlighted the successful deployment of WGCNA in quantitative proteomics (Wu et al, 2021; Zhang et al, 2018). Here, a WGCNA was constructed using the *WGCNA* r-package (Langfelder & Horvath, 2008; Wu et al, 2021) and the entire proteomic dataset excluding the outliers. A similarity matrix was constructed by measuring each pairwise protein correlation and then converted to an adjacency matrix using an appropriate soft threshold power (β) estimated using the *pickSoftThreshold* function (Wu et al, 2021). The obtained adjacency matrix was used to calculate the topology overlap matrix accompanied by the calculation of corresponding dissimilarity (1-TOM). Accordingly, hierarchical clustering based on the distance measure (1-TOM) was performed to generate a clustering dendrogram. Using the dynamic tree-cut algorithm, dendrogram branches with similar co-expression were clustered into several modules, each assigned a different colour, and the parameter value of the minimum cluster size was set to 30. Lastly, module–trait correlation analysis was conducted to correlate the modules with the TZD-treated samples that potentially had a 'high HF risk' compared to the control samples that had a 'low HF risk'. Only modules with a significant positive correlation with high HF risk were subjected to subsequent analysis (WGCNA's module–GO, DO, and KEGG pathway analyses).

4.2.6.4 Protein–Protein Interactions of the Key Module Proteins and Identification of Hub Proteins

The list of identified proteins was uploaded to the Search Tool for the Retrieval of Interacting Genes/Proteins (STRING; https://string-db.org; v11.5) database to generate a full protein–protein interaction (PPI) STRING network limited to *Homo sapiens* with the highest confidence interaction score of 0.9. The developed network

was exported to the Cytoscape software platform for visualisation (Cytoscape; https://cytoscape.org; v3.10). The cytoHubba plugin in Cytoscape, which provided topological algorithms for ranking nodes, was used to identify the top 20 proteins. Proteins that were cytoHubba-identified driver proteins as well as enriched in pathways linked with HF pathogenesis from both the DEPs and WGCNA KEGG analyses were labelled in this study as feature proteins.

4.2.7 Statistical Analysis

Statistical analysis was conducted using R v4.3.0. Three independent experiments were performed for each proteomics analysis. Statistical significance was determined using Student's or Welch's t-tests when comparing the two groups. The experimental setup for this study is presented in **Figure 4.6**. A non-repeated one-way analysis of variance (ANOVA), followed by Dunnett's post hoc test, was used for multiple comparisons. The correlation coefficient was assessed using Pearson and distance correlation analyses. A p-value ≤ 0.05 was considered statistically significant. A schematic flowchart of the toxicoproteomics pipeline applied for downstream analyses is illustrated in **Figure 4.7**.

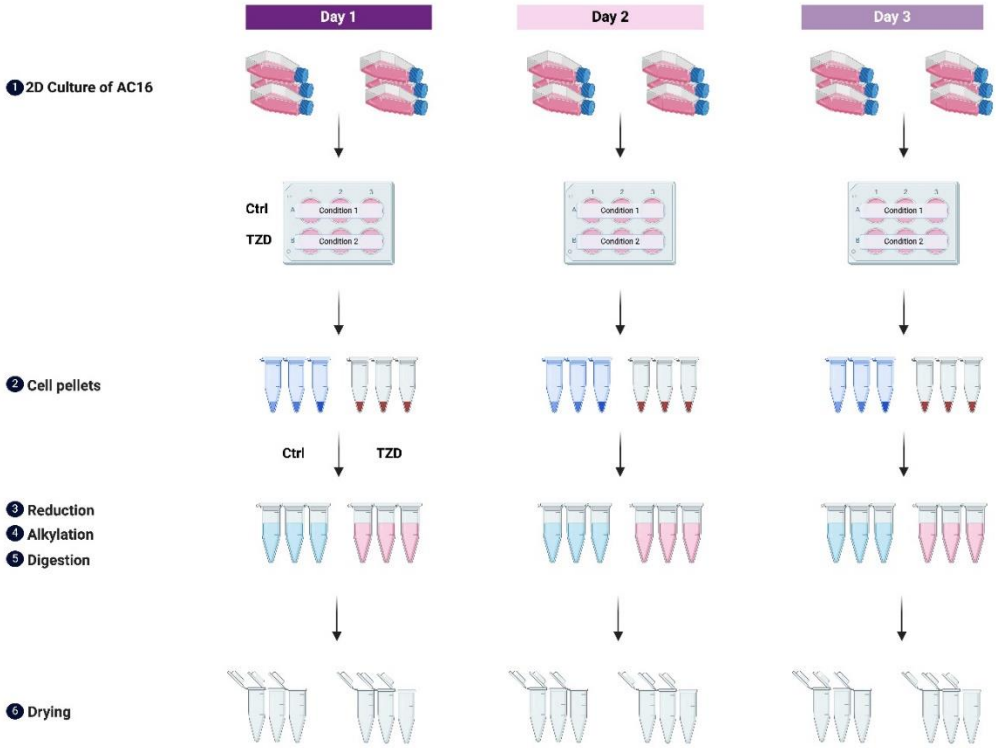

Figure 4.6 Experimental design for toxicoproteomics analysis. Three independent toxicoproteomics experiments were performed. Each experiment involved (1) cell seeding followed by (2) pellet preparation. The resulting cell pellets were subjected to (3) reduction, (4) alkylation, and (5) digestion. The tryptic peptide samples were dried, reconstituted with the extraction solvent and subsequently analyzed by LC-MS.

LC–MS: liquid chromatography–mass spectrometry; TZD: thiazolidinedione

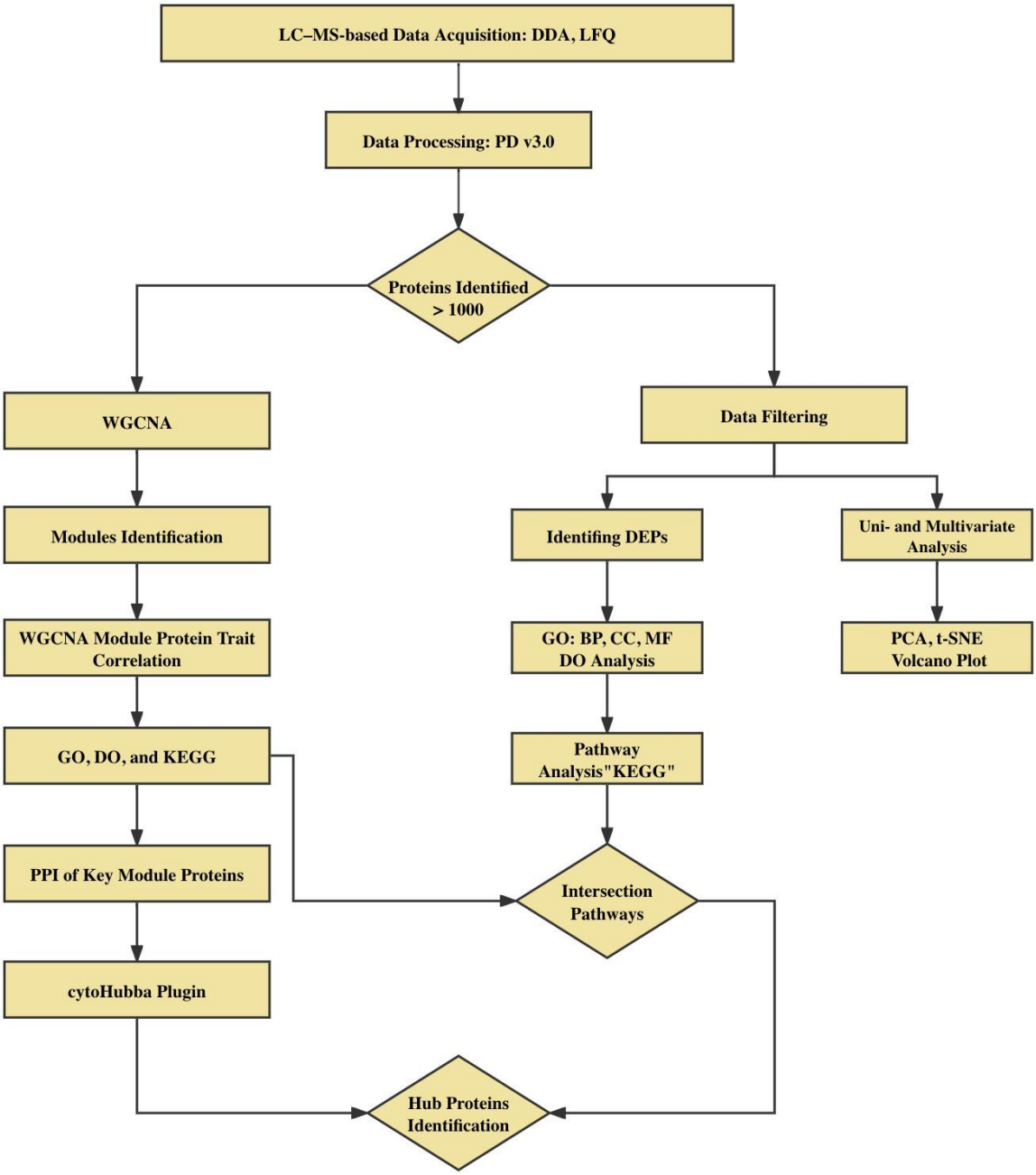

Figure 4.7 Flowchart of the toxicoproteomics pipeline used in this study for the downstream analyses. The total proteome of the AC16 cells produced in response to TZD was characterised using a novel microflow label-free shotgun toxicoproteomics approach. Initially, the raw LC–MS data were processed using PD, followed by further data filtering, normalisation and imputation, yielding a total of >1000 proteins in each experiment. Accordingly, downstream analysis, represented by uni- and multi-variate analyses, was performed on the identified proteins. WGCNA was conducted on all identified proteins. In parallel to WGCNA, the DEPs under the threshold values ($log_2FC > 1$ and $p \leq 0.05$) were captured. Further functional (GO), disease (DO) and pathway (KEGG) analyses of both the WGCNA results and DEPs were performed. The pathways significantly implicated in HF pathogenesis, which were identified from the examination of the DEPs and the WGCNA, were intersected. The key module proteins extracted from the WGCNA were mapped to the PPI network, and then the top 20 driver proteins were identified using the cytoHubba plugin.

Finally, proteins that were cytoHubba-identified driver proteins as well as enriched in pathways linked with HF pathogenesis from both the DEPs and WGCNA KEGG analyses were labelled in this study as feature proteins.

LC–MS: liquid chromatography–mass spectrometry; DDA: data-dependent acquisition; LFQ: label-free quantitation; PD: Proteome Discoverer; TZD: thiazolidinedione; DEP: differentially expressed protein; PCA: principal component analysis; t-SNE: t-stochastic neighbour embedding; GO: Gene Ontology; BP: biological process; CC: cellular component; MF: molecular function; DO: Disease Ontology; KEGG: Kyoto Encyclopedia of Genes and Genomes; WGCNA: weighted correlation network analysis; PPI: protein-protein interaction.

4.3 Shotgun Proteomics and Protein-Based Bioinformatics Analysis Results of TZD-Treated Human AC16 Cells

4.3.1 Characterisation of the Proteome of TZD-Treated Human AC16 Cells

To characterise the proteins and the mechanism(s) of action underlying the cardiotoxic activity of TZDs and identify the implicated targets, a label-free quantitative proteomic pipeline was applied, as depicted in **Figure 4.7.** After processing the raw data of the tryptic peptides using PD, further data filtering (FDR < 1% for both peptides and proteins), normalisation and imputation were conducted via *NormalyzerDE* (Willforss, Chawade, & Levander, 2018) and *NAguideR* (S. Wang et al., 2020) packages, yielding thousands of proteins in both PGZ and ROSI experiments. In both experiments, median normalisation was applied, followed by data imputation using the KNN method.

As part of the data inspection and quality assessment, box plots of the $\log_2$ transformed LFQ intensities for the control and the treated samples with their corresponding peptide retention times were plotted. Plotting box plots of $\log_2$-transformed LFQ intensities along with peptide retention times in proteomics serves as an important quality control step (Pan et al, 2017). It aids verifying data normalisation, ensuring consistent distributions across control and treated samples, and detect any systematic biases or outliers. Additionally, it allows to assess experimental variability by comparing the spread of intensities within each group. By including peptide retention times, the analysis ensures consistent peptide detection and alignment across runs, minimising technical artifacts. Overall, this approach helps confirm that differences between control and treated samples are biologically meaningful and not due to technical issues. In both experiments, the boxplot results (**Figures 4.8A and 4.8C**) revealed a comparable median across samples within the same group; nevertheless, the following samples, labelled Drug-2 and Drug-7, in PGZ

and ROSI experiments, respectively, were flagged as potential outliers and therefore excluded from the subsequent analyses. To further assess data quality, coefficient of variation (CV%) was plotted against raw intensity. This approach highlights technical variability, as lower CV% at higher intensities indicates better reproducibility, while higher CV% often points to noise in low-abundance signals. The plot also reveals intensity-dependent variability, helping identify the most reliable data range. It serves as a quality control tool, allowing the filtering of low-quality data with high CV%, and provides insights into the overall performance of the analytical workflow, ensuring more robust and accurate results (Mendoza-Porras et al, 2024). **Figures 4.8B and 4.8D** depict a clustering of features at low intensity values with correspondingly high CVs, suggesting increased relative variability for less abundant features, likely due to noise. Conversely, as raw intensity increased, CV values tended to decrease, indicating improved measurement consistency for more abundant features. Overall, these findings suggest robust and reproducible LC-MS system performance.

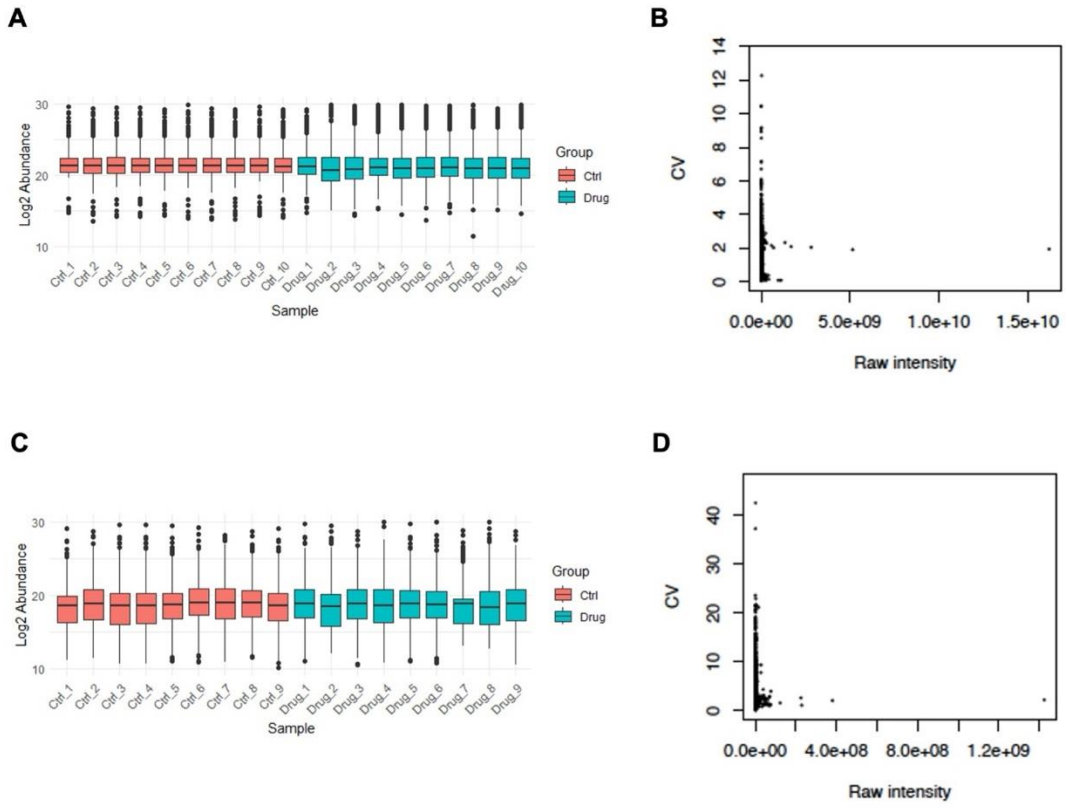

Figure 4.8 Quantitative profiling of AC16 cells in response to TZD treatment. (A, C) Box plots of log_2 abundance for each tested sample using PGZ and ROSI datasets. (B, D) Visualization of coefficient of variation (CV%) in PGZ and ROSI raw data.

PGZ: pioglitazone; ROSI: rosiglitazone; CV: coefficient of variation

Various chemometric analyses were performed to profile TZD-induced, proteome-wide changes in expression in AC16 cells. In both experiments, the multivariate PCA technique was employed to visualise the heterogeneity in the expression data among the studied samples. The PCA scores plots revealed that the control and PGZ-treated samples, shown in **Figure 4.9A**, and the control and ROSI-treated samples (**Figure 4.9B**), were distinct. Nevertheless, PCA analysis identified samples labeled Drug-2 (PGZ) and Drug-7 (ROSI) as potential outliers and therefore, these samples were excluded from further analyses. Besides its function in evaluating sample group heterogeneity, the PCA plot was employed as a quality control and assurance tool to assess the reliability and quality of LC-MS-based toxicoproteomics data. As shown in Figures **4.9A and 4.9B**, all QC samples grouped together within the PCA plot and 95% confidence intervals, demonstrating consistent and reproducible performance of the LC-MS system.

Distinct proteomic profiles differentiating control and treated groups were further validated following the application of t-SNE; sample separation was also achieved using the first two t-SNE components (**Figures 4.9C and 4.9D**). To discern the protein expression trends of the two studied genotypes globally, another t-SNE plot was generated in which the quantified proteins were projected into the t-SNE space and clustered accordingly based on their expression patterns. The t-SNE plot in **Figures 4.9E and 4.9F** shows the expression-driven separation of the control and treated groups and highlights the downregulation trend observed in a large set of proteins following treatment of cells with the TZD agent.

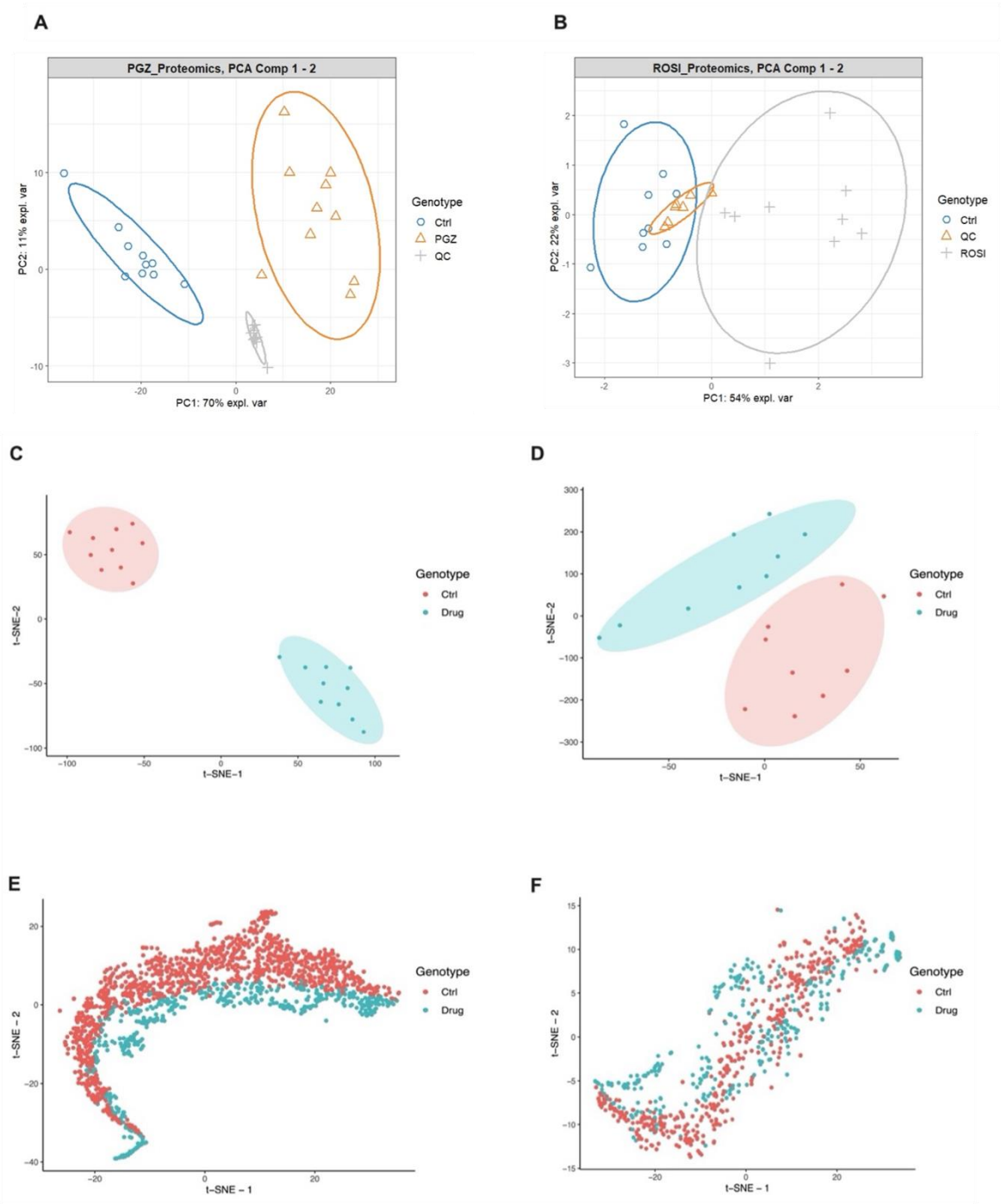

Figure 4.9 Chemometric analyses of proteomics data. (A, B) 2D PCA scores plots showing the trend of separation between the control and TZD-treated groups. (A) The PCA scores plot of the PGZ-treated and control samples. (B) PCA scores plot between the ROSI-treated and control groups. In both (A and B), the plots demonstrate the separation between sample groups and the clustering of QC samples, which are colored gray and orange in A and B, respectively. (C, D) t-SNE plots comparing the LC–MS proteomic profiles of the control and TZD-treated samples. (C) The plot represents the PGZ-treated and control cells. (D) The separation between the ROSI-treated and control samples. In both C and D, the *Rtsne* values used were $Perp$ = 5, η = 200, and T = 5,000. The shaded circles in plots A–D represent 95% confidence intervals, while the coloured dots illustrate the individual samples. (E, F) Clustered protein visualised within t-SNE across samples on the basis of expression. (E, F) Proteome datasets of PGZ and ROSI, respectively. In both E and F, the *Rtsne* values applied were $Perp$ = 50, η = 200, and T = 5,000.

PCA: principal component analysis; t-SNE: t-stochastic neighbour embedding; LC–MS: liquid chromatography–mass spectrometry; $Perp$: perplexity; η: learning rate; T: maximum number of iteration; DEPs: differentially expressed protein.

To capture the DEPs responsible for the separation and clustering observed in the PCA and t-SNE results, a volcano plot was generated using data that fell under the threshold values ($log_2FC > 1$ and $p \leq 0.05$), and 237 upregulated and 368 downregulated proteins were identified after PGZ exposure (Figure **4.10A**). Proteins significantly affected after ROSI exposure yielded 198 significant proteins (97 upregulated and 101 downregulated), as shown in **Figure 4.10B**.

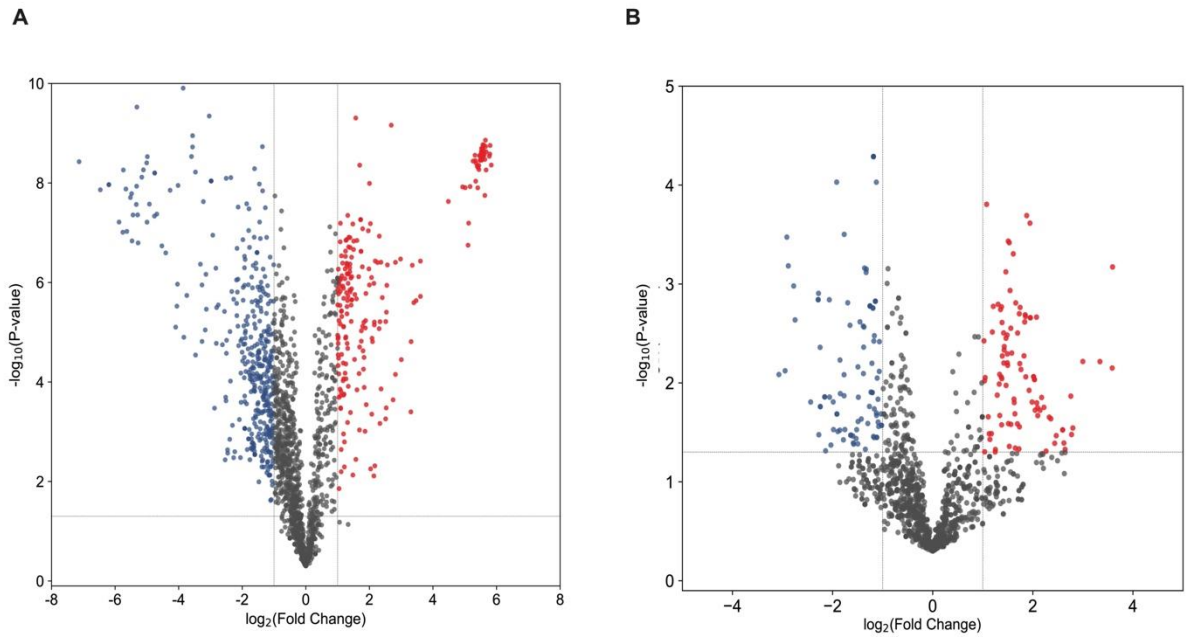

Figure 4.10 Volcano plots of label-free quantitative proteomic data. Volcano plot showing the DEPs (log_2 fold change value of 1 and a $-log_{10}$ p value < 0.05) identified between (A) the PGZ-treated and control samples and (B) the ROSI-treated and control samples. The red and blue dots denote significant upregulated and downregulated proteins, respectively. The grey dots represent the non-significant altered proteins.

DEP: differentially expressed protein; PGZ: pioglitazone; ROSI: rosiglitazone.

4.3.2 Functional, Disease and Pathway Analyses of the DEPs

To gain insights into the implicated molecular mechanisms and further delineate the cellular responses to TZD treatment, GO, DO and KEGG pathway analyses of the DEPs were performed.

4.3.2.1 Functional, Disease and Pathway Analyses of the DEPs

To gain insights into the implicated molecular mechanisms and further delineate the cellular responses to TZD treatment, GO, DO and KEGG pathway analyses of the DEPs were performed.

Regarding PGZ exposure, the GO enrichment analysis based on biological process (BP) revealed that the DEPs were associated with various processes, including intermediate filament organisation, oxygen transport, blood coagulation, the mitogen-activated protein kinase (MAPK) cascade and mitochondrial translation (**Figure 4.11A**). Furthermore, the DEPs were found to be markedly enriched in molecular functions (MFs) associated with protein binding, haptoglobin binding, oxygen transporter activity and extracellular matrix (ECM) structural constituents (**Figure 4.11A**). Parallel to the BP and MF analysis findings, the DEPs were overrepresented in compartments, including the cytosol, extracellular exosome and cytoplasm (**Figure 4.11A**). In response to ROSI treatment, the GO functional analyses showed that the DEPs were predominantly assembled into BP linked to nucleosome assembly, intermediate filament organisation, protein folding, telomere organisation, innate immune response in mucosa and Rab protein signal transduction (**Figure 4.11B**). On the MF level, the DEPs were mainly involved in structural constituents of chromatin, RNA binding, protein heterodimerization activity, ATPase activity, nucleosomal DNA binding and DNA binding (**Figure 4.11B**). On the CC levels, the DEPs were predominantly localised in the nucleosome, cytosol, blood microparticle, membrane, nuclear chromosome and nucleus (**Figure 4.11B**).

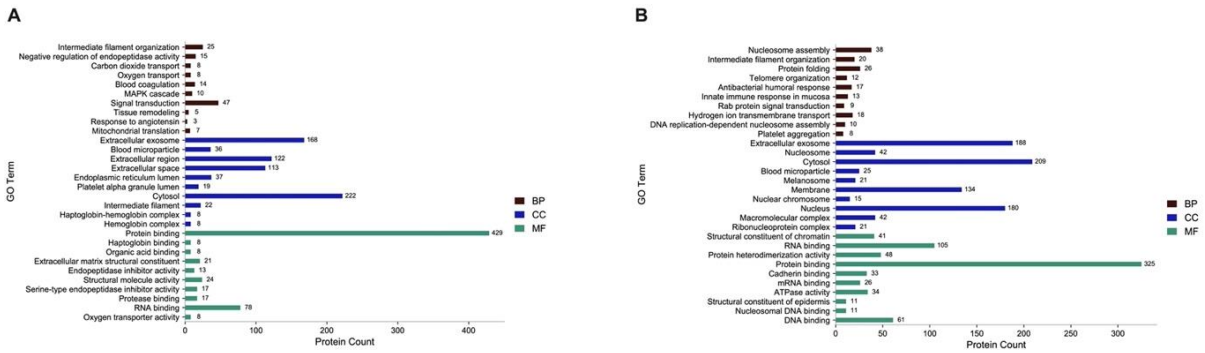

Figure 4.11 Functional analysis of the DEPs. The top 10 enriched GO terms for the BP, CC and MF categories of the DEPs of PGZ (A) and ROSI (B).
DEP: differentially expressed protein; PGZ: pioglitazone; ROSI: rosiglitazone; GO: Gene Ontology; BP: biological process; CC: cellular component; MF: molecular function

The DO analysis revealed that the PGZ's DEPs were predominantly associated with cardiovascular diseases (CVDs), such as atherosclerotic CVD, myocardial infarction (MI), peripheral (i.e., venous thromboembolism) and cerebrovascular (i.e., stroke) diseases (**Figure 4.12A**). Interestingly, as shown in **Figure 4.12A**, 103 DEPs were enriched in the DO termed 'type 2 diabetes-oedema-rosiglitazone'. This finding could potentially explain the worsening body congestion noted in diabetic patients who use PGZ as part of their treatment, as evidenced in numerous case reports (De Flines & Scheen, 2007).

However, the DO enrichment analysis of the DEPs induced by ROSI revealed their implications in various diseases, including blood disorders (glucosephosphate dehydrogenase deficiency, sickle cell anaemia), neurodegenerative disorders (e.g., Alzheimer's disease, Parkinson's disease) and peripheral diseases, such as venous thrombosis. Similar to PGZ's DO findings, the majority of DEPs were markedly enriched in the DO termed 'type 2 diabetes-oedema-rosiglitazone', signifying the implication of oedema in cardiotoxicity pathogenesis (**Figure 4.12B**).

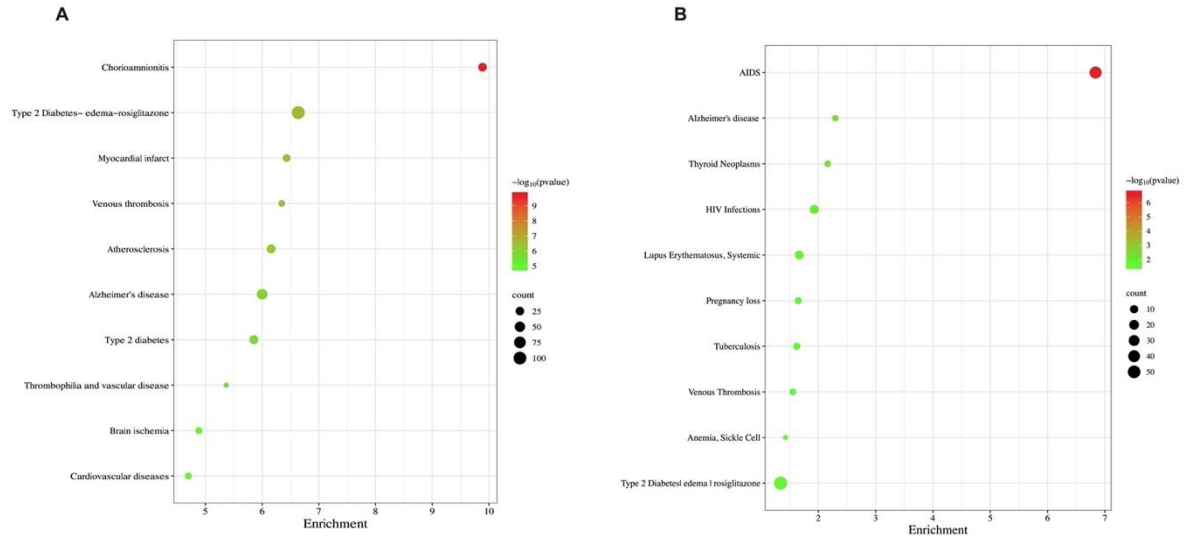

Figure 4.12 DO enrichment analysis results for the DEPs. (A and B) The bubble plots represent a subset of the enriched DO terms of the DEPs identified in the PGZ and ROSI data, respectively. In A and B, the bubble size and colour represent the number of DEPs enriched in the pathway and the enrichment significance, respectively.

DEP: differentially expressed protein; PGZ: pioglitazone; ROSI: rosiglitazone; DO: Disease Ontology.

The KEGG pathway analysis revealed 37 enriched pathways that fulfilled the applied criteria of a *p*-value < 0.05 and a minimum count of 2 **(Figure 4.13A, [Table S8, Appendix Section 7.3])**. The KEGG pathway analysis findings also showed that the screened proteins were associated with pathways primarily involved in immune-related cellular processes and signal transduction-based pathways, which include the complement and coagulation cascades (KEGG: 04610), platelet activation (KEGG: 04611), neutrophil extracellular trap formation (KEGG: 04613), the Wingless-related integration site (Wnt) signalling pathway (KEGG: 04310), the phosphatidylinositol 3' kinase-protein kinase B (PI3K-Akt) signalling pathway (KEGG: 04151), extracellular matrix (ECM)-receptor interaction (KEGG: 04512), focal adhesion (KEGG: 04510) and the regulation of the actin cytoskeleton (KEGG: 04810). The pathway-topology analysis **(Figure 4.13B, [Table S9, Appendix Section 7.3])** of the proteins markedly altered in response to ROSI showed a significant association between the DEPs and pathways linked to immune-related systems (i.e., neutrophil extracellular trap formation (KEGG: 04613)), circulatory system and cardiovascular disease (e.g., cardiac muscle contraction (KEGG: 04260), diabetic cardiomyopathy (KEGG: 05415)) and excretory system (e.g., endocrine and other factor-regulated calcium reabsorption (KEGG: 04961), proximal tubule bicarbonate reclamation (KEGG: 04964) and collecting duct acid secretion (KEGG: 04966)). Furthermore, the KEGG analysis revealed the involvement of DEPs in pathways related to the following: carbohydrate metabolism (i.e., glycolysis / gluconeogenesis (KEGG: 00010)), citrate cycle (TCA cycle (KEGG: 00020), pyruvate metabolism (KEGG: 00620)), energy metabolism (i.e., oxidative phosphorylation (KEGG: 00190)) and cellular processes (i.e., phagosome (KEGG: 04145), ferroptosis (KEGG: 04216), necroptosis (KEGG: 04217)).

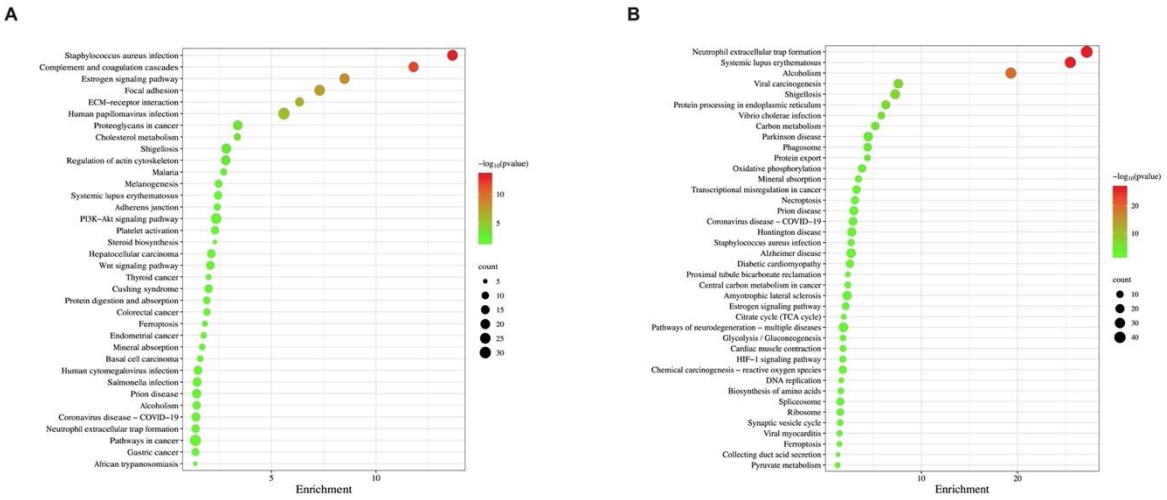

Figure 4.13 KEGG pathway analysis results for the DEPs. The bubble plots in A and B list all the significantly enriched pathways of the DEPs of PGZ and ROSI, respectively. In A and B, the bubble size and colour represent the number of DEPs enriched in the pathway and the enrichment significance, respectively.

DEP: differentially expressed protein; PGZ: pioglitazone; ROSI: rosiglitazone; KEGG: Kyoto Encyclopedia of Genes and Genomes.

4.3.3 WGCNA and Module Identification

A WGCNA was constructed using a PGZ dataset that included 19 samples by adopting the *WGCNA* package. To ensure a scale-free network, a soft threshold power (β = 8; scale free R^2=0.85) was selected as shown in **Figures 4.14A and 4.14B**, yielding four protein co-expression modules (blue, yellow, turquoise and brown), which ranged in size from 60 to 904 proteins (**Figure 4.15A**).

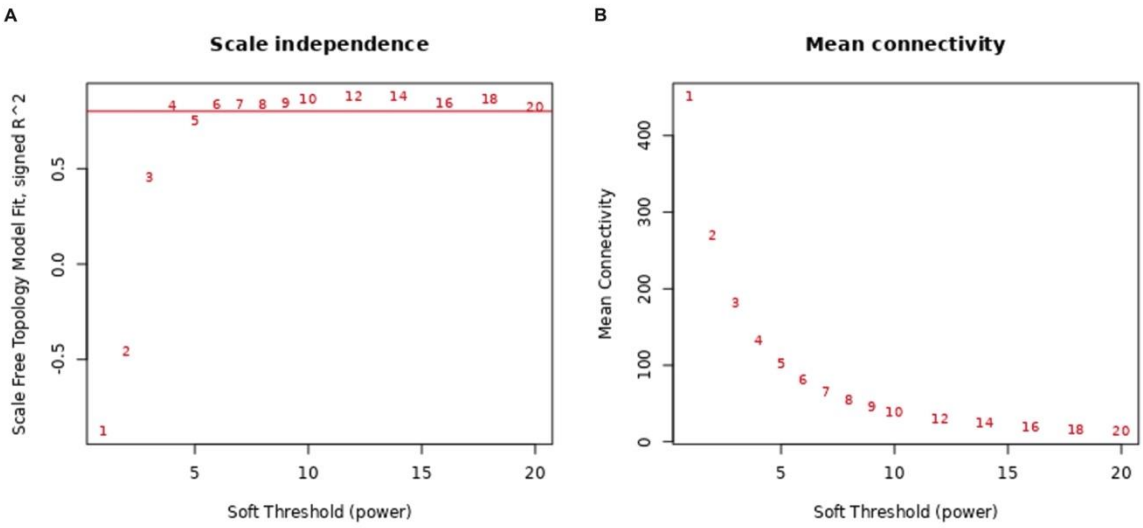

Figure 4.14 WGCNA network construction using PGZ dataset. (A, B) Determination of optimal soft threshold power for scale-free topology. (A) and (B) show the scale-free topology index and the mean connectivity for each power value between 1 and 20, respectively.

WGCNA: weighted correlation network analysis; PGZ: pioglitazone

To achieve a clear understanding of the molecular changes that occur in AC16 cells following PGZ treatment, a module–trait correlation analysis was conducted to correlate the identified modules with the PGZ-treated samples that potentially had a 'high HF risk' compared to the control samples that had a 'low HF risk'. It was found that only the blue module demonstrated a strong positive correlation with the high-HF-risk samples (correlation coefficient = 0.964, $p < 0.001$) (**Figure 4.15B**). An intramodular analysis demonstrating the correlation between blue module members (MMs) and protein significance for the chosen trait is illustrated in **Figure 4.15C**.

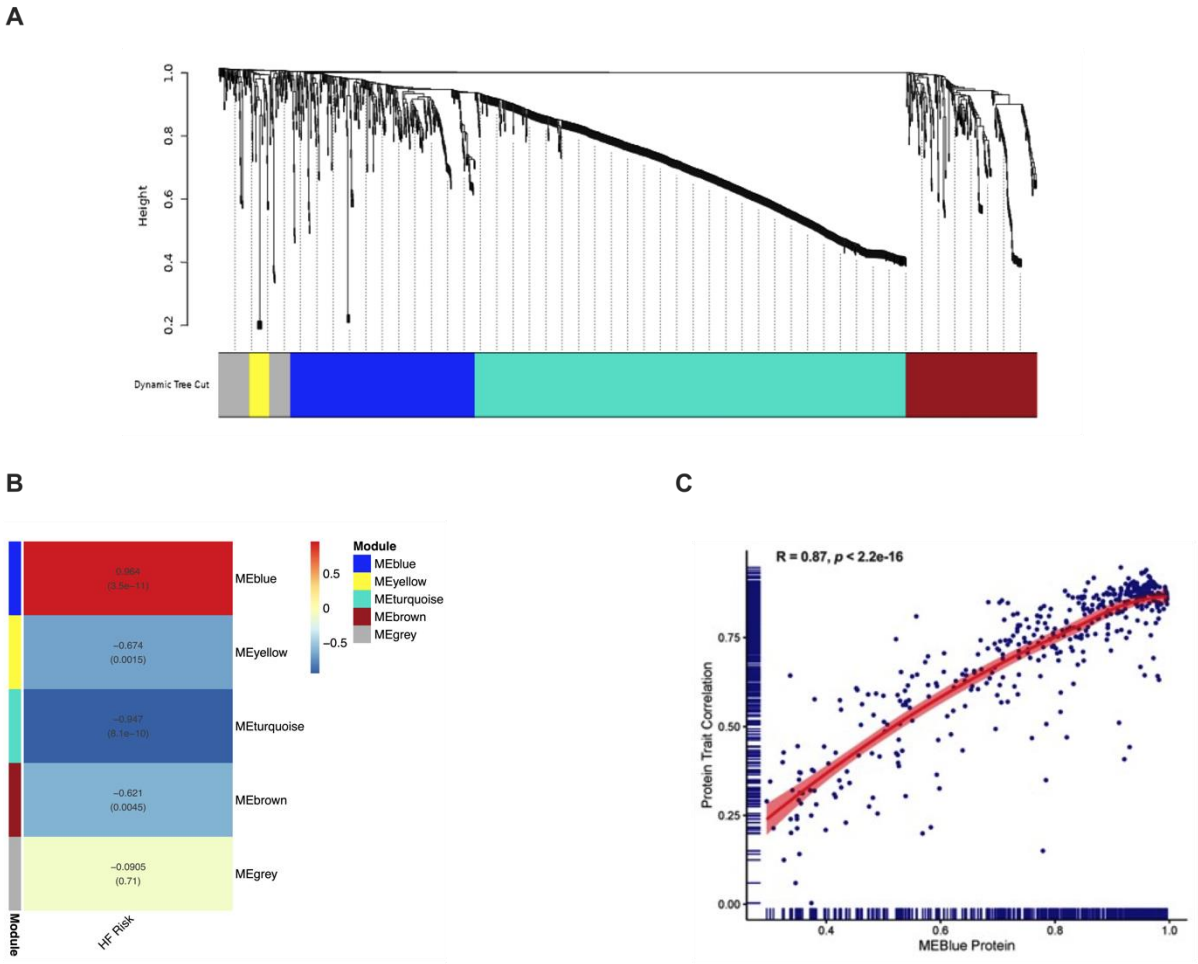

Figure 4.15 Analysis of the protein coexpression modules. (A) Dendrogram of all proteins, with dissimilarity clustered on topological overlap. (B) Diagram showing the correlation between each of the five modules and the HF-risk trait. The blue module significantly correlated with the chosen trait (R = 0.964, p < 0.001). (C) Scatterplot and correspondent regression line (in red) with 95% confidence interval of the blue MMs versus protein significance for HF risk.

HF: heart failure; MMs: module members.

Regarding the ROSI dataset, a soft-threshold power of 8 was selected on the basis of the scale-free fit index and mean connectivity values illustrated in **Figures 4.16A and 4.16B** (β = 8; scale free R^2 = 0.85).

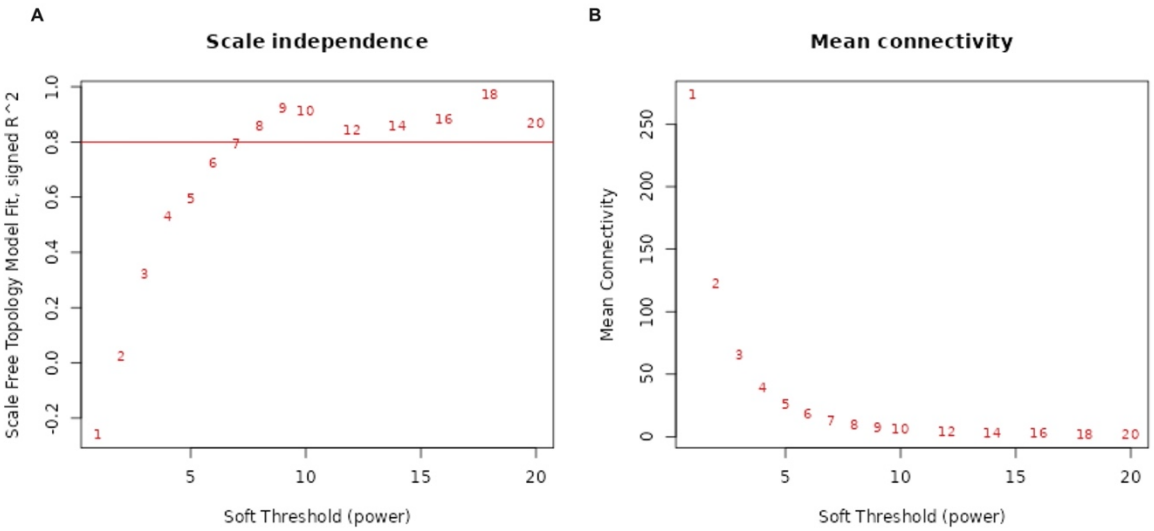

Figure 4.16 WGCNA network construction using ROSI dataset. (A, B) Determination of optimal soft threshold power for scale-free topology. (A) and (B) show the scale-free topology index and the mean connectivity for each power value between 1 and 20, respectively.

WGCNA: weighted correlation network analysis; ROSI: rosiglitazone

The WGCNA algorithm clustered proteins into eight co-expression modules, which were blue, turquoise, black, red, brown, green, pink and yellow modules, ranging in size from 45 to 148 proteins (**Figure 4.17A**). In regard to module–trait correlation analysis, the brown module showed the highest positive correlation with the high-HF-risk samples, with a correlation coefficient value of (correlation coefficient = 0.701, $p < 0.05$) (**Figure 4.17B**). A scatter plot of brown MMs vs. protein significance is shown in **Figure 4.17C**.

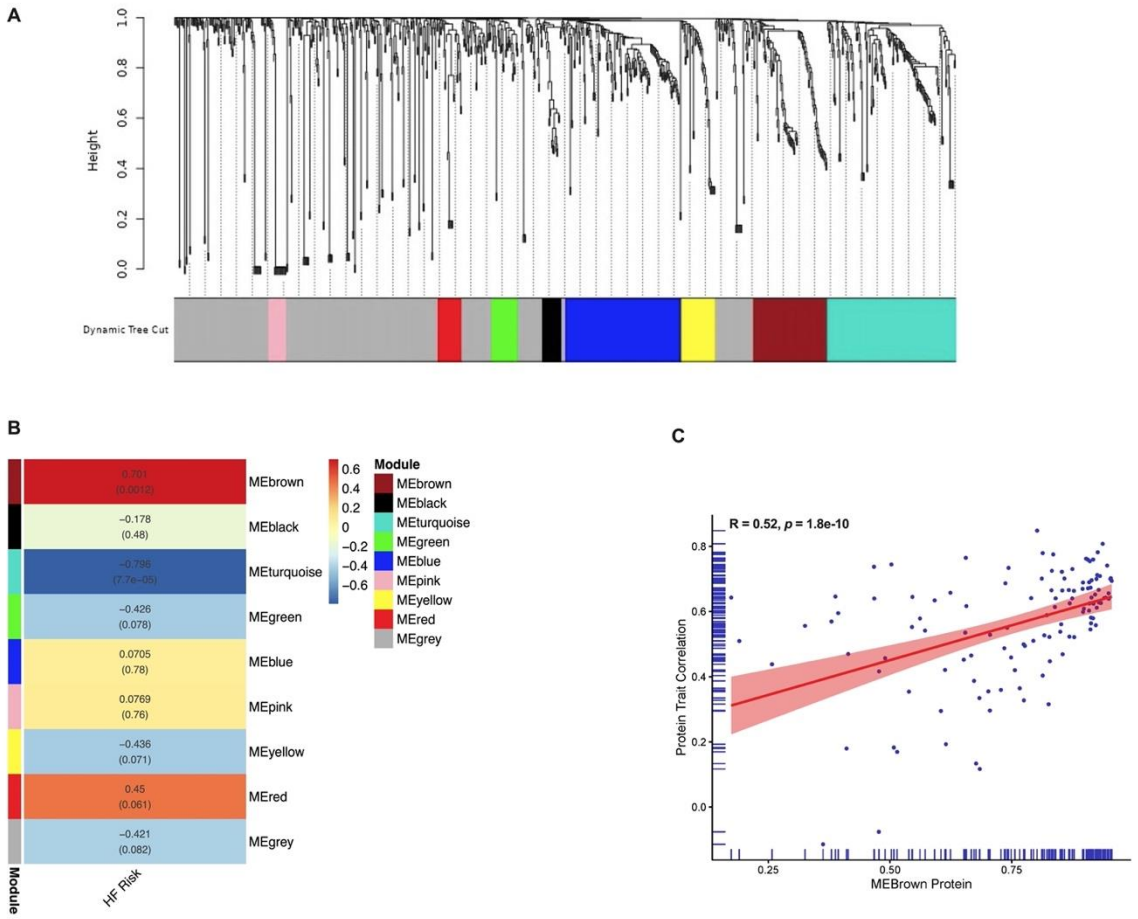

Figure 4.17 Analysis of the protein coexpression modules. (A) Dendrogram of all proteins, with dissimilarity clustered on topological overlap. (B) Diagram showing the correlation between each of the eight modules and the HF-risk trait. The brown module significantly correlated with the chosen trait (R = 0.701, p < 0.001). (C) Scatterplot and correspondent regression line (in red) with 95% confidence interval of the brown MMs versus protein significance for HF risk.

HF: heart failure; MMs: module members.

4.3.4 Functional, Disease and Pathway Analyses of the Chosen Modules

Given that only the blue and brown modules demonstrated a positive correlation with HF risk in the PGZ and ROSI datasets, additional GO, DO and KEGG enrichment analyses were performed with these modules to further characterise the biological relevance of the MMs and their roles in pathway and disease processes.

4.3.4.1 Biological Inferences of the Blue Module–PGZ

The GO enrichment analysis revealed that the blue MMs were associated with BPs linked to nucleosome assembly, fibrin clot formation, mitochondrial ATP synthesis and the tricarboxylic acid cycle (**Figure 4.18A**). In terms of MFs, the blue MMs were implicated in protein binding, RNA binding, ATPase activity, haptoglobin binding and calcium-ion binding (**Figure 4.18A**). The analysis also revealed that most of the blue MMs were localised in the extracellular exosome, cytosol, mitochondria and nucleus (**Figure 4.18A**).

The DO enrichment analysis revealed that the blue MMs were primarily associated with the same heart diseases associated with DEPs and other lipid disorders (**Figure 4.18B**). It was also found that 86 blue MMs were enriched for 'type 2 diabetes-oedema-rosiglitazone', which was consistent with the results of the DO enrichment analysis of the full set of DEPs.

The KEGG pathway analysis revealed that the blue MMs were significantly enriched in pathways related to CVDs, the immune system, cellular processes and energy metabolism. The immune-related pathways included the complement and coagulation cascades (KEGG: 04610), platelet activation (KEGG: 04611) and neutrophil extracellular trap formation (KEGG: 04613). The CVD-related pathways included diabetic cardiomyopathy (KEGG: 05415) and lipid and atherosclerosis (KEGG: 05417). The cellular processes–related pathways included ferroptosis (KEGG: 04216), necroptosis (KEGG: 04217), the phagosome (KEGG: 04145), the ECM-receptor interaction (KEGG: 04512), focal adhesion (KEGG: 04510) and the regulation of the actin cytoskeleton (KEGG: 04810). The energy metabolism–related pathway was the oxidative phosphorylation pathway (KEGG: 00190) **(Figure 4.18C, [Table S10, Appendix Section 7.3])**.

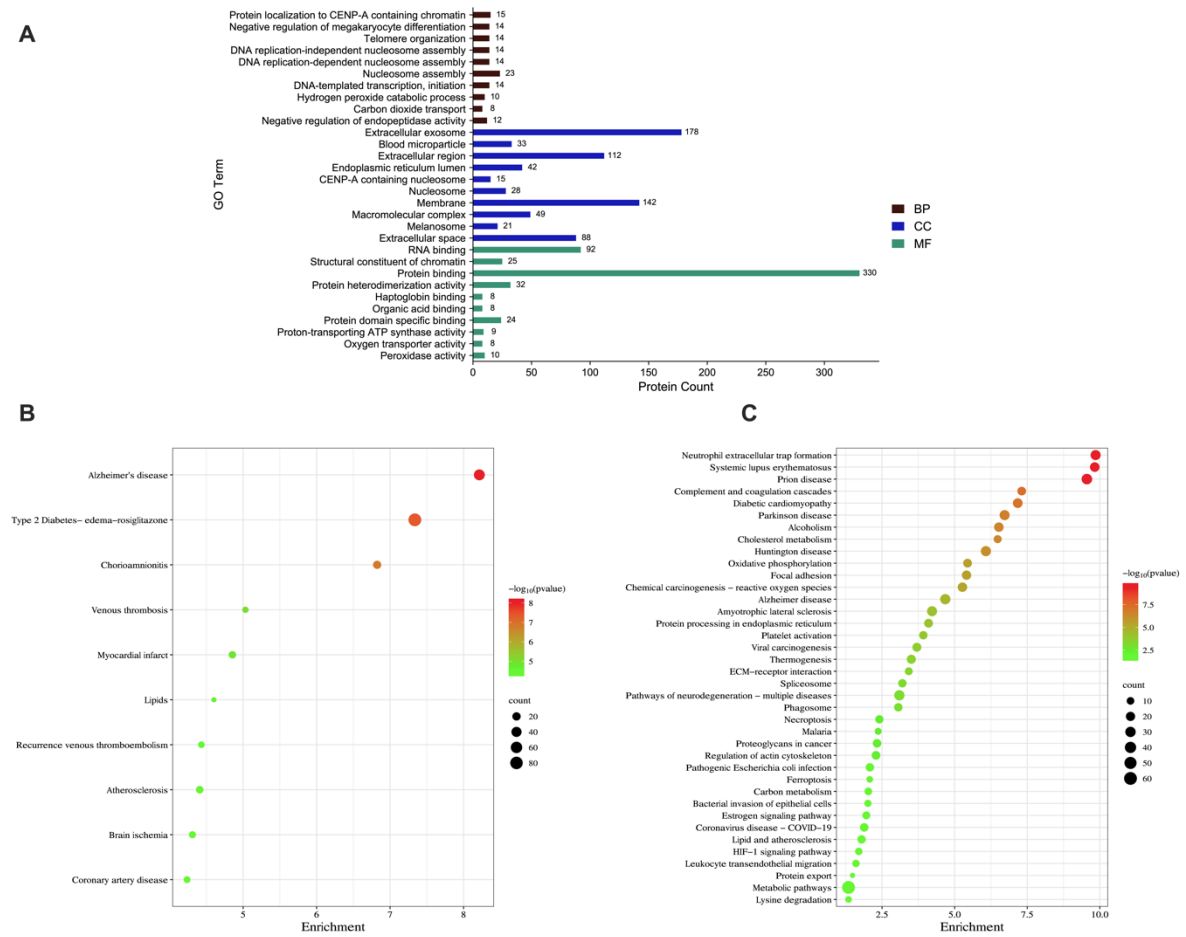

Figure 4.18 Functional, disease and pathway analyses of the blue module. (A) The top 10 enriched GO terms for the BP, CC and MF categories. (B) DO enrichment analysis results (top 10) for the blue module. (C) KEGG enrichment analysis results for the blue module. In (B) and (C), the bubble size and colour represent the number of blue MMs enriched in the pathway and the enrichment significance, respectively.

GO: Gene Ontology; BP: biological process; CC: cellular component; MF: molecular function; DO: Disease Ontology; KEGG: Kyoto Encyclopedia of Genes and Genomes; MMs: module members.

4.3.4.2 Biological Inferences of the Brown Module–ROSI

The GO functional analysis of the brown MMs (**Figure 4.19A**) revealed their implication in BPs associated with cellular oxidant detoxification, hydrogen peroxide catabolic process, cytoplasmic translation, negative regulation of growth and intermediate filament organisation. In addition, the brown MMs were markedly enriched in MFs related to endopeptidase inhibitor activity, organic acid binding, serine-type endopeptidase inhibitor activity, oxygen transporter activity and oxygen binding. The proteins in the brown module were found to be predominantly localised

in the extracellular exosome, blood microparticle, cytosol, extracellular space, focal adhesion, haptoglobin-haemoglobin complex and extracellular regions.

Regarding the DO ontology, the proteins in the brown module were mainly enriched in blood disorders (i.e., α-thalassemia, β-Thalassemia, anaemia), dyslipidaemias and neurodegenerative disorders, including Alzheimer's disease. Interestingly, consistent with the findings for PGZ, 'type 2 diabetes-oedema-rosiglitazone' was also enriched (**Figure 4.19B**).

Lastly, KEGG pathway enrichment analysis suggested that 133 proteins in the brown module were significantly enriched in the following pathways: mineral absorption (KEGG: 04978), ribosome (KEGG: 03010), and complement and coagulation cascades (KEGG: 04610) **(Figure 4.19C, [Table S11, Appendix Section 7.3]).**

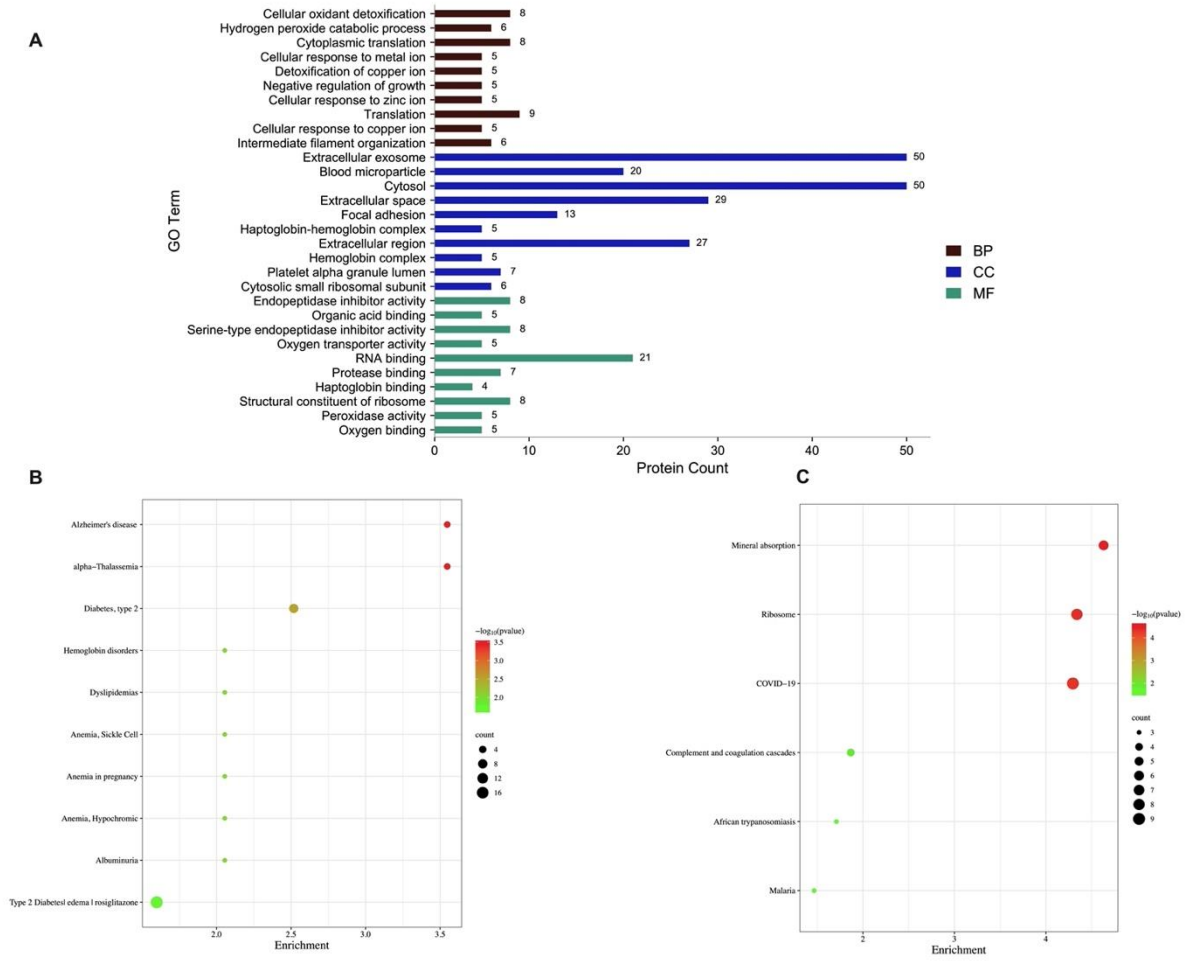

Figure 4.16 Functional, disease and pathway analyses of the brown module. (A) The top 10 enriched GO terms for the BP, CC and MF categories. (B) DO enrichment analysis results (top 10) for the brown module. (C) KEGG enrichment analysis results for the brown module.

In (B) and (C), the bubble size and colour represent the number of brown MMs enriched in the pathway and the enrichment significance, respectively.

GO: Gene Ontology; BP: biological process; CC: cellular component; MF: molecular function; DO: Disease Ontology; KEGG: Kyoto Encyclopedia of Genes and Genomes; MMs: module members.

4.3.5 WGCNA and Identification of Hub Proteins

To further identify the key proteins (prognostic biomarkers) implicated in the pathoetiology of TZD use and HF risk, the pathways significantly implicated in HF pathogenesis, which were identified from the examination of the DEPs and the WGCNA, intersected. In the PGZ dataset, this resulted in the identification of seven pathways: the complement and coagulation cascades (KEGG: 04610), platelet activation (KEGG: 04611), neutrophil extracellular trap formation (KEGG: 04613), ferroptosis (KEGG: 04216), the ECM-receptor interaction (KEGG: 04512), focal adhesion (KEGG: 04510) and the regulation of the actin cytoskeleton (KEGG: 04810) (**Figure 4.20A**). In the context of the ROSI dataset, two pathways were identified: mineral absorption (KEGG: 04978) and ribosome (KEGG: 03010) (**Figure 4.20C**).

Subsequently, the hub proteins of each chosen module (blue module–PGZ; brown module–ROSI) were extracted. The MMs were mapped to the PPI network, and then the top 20 driver proteins were identified using the cytoHubba plugin. Brief descriptions of the identified top 20 driver proteins for each module, as well as their expression levels, are summarised in **(Figure 4.20B, Table 4.3) and (Figure 4.20D, Table 4.4)** for the blue and brown modules, respectively.

With respect to blue module–PGZ, among the 20 listed proteins, eight (P60709, P05556, P00533, P02751, P00734, P21796, P02679 and P02452) intersected with the proteins enriched in the seven pathways (DEPs and WGCNA) mentioned above and were therefore labelled as feature proteins. For brown module–ROSI, eight proteins, which were P30050, Q9UNX3, P61254, P46777, P62277, P39019, P62857 and P62081, were also found to fulfil the proposed criteria and hence recognised as feature proteins.

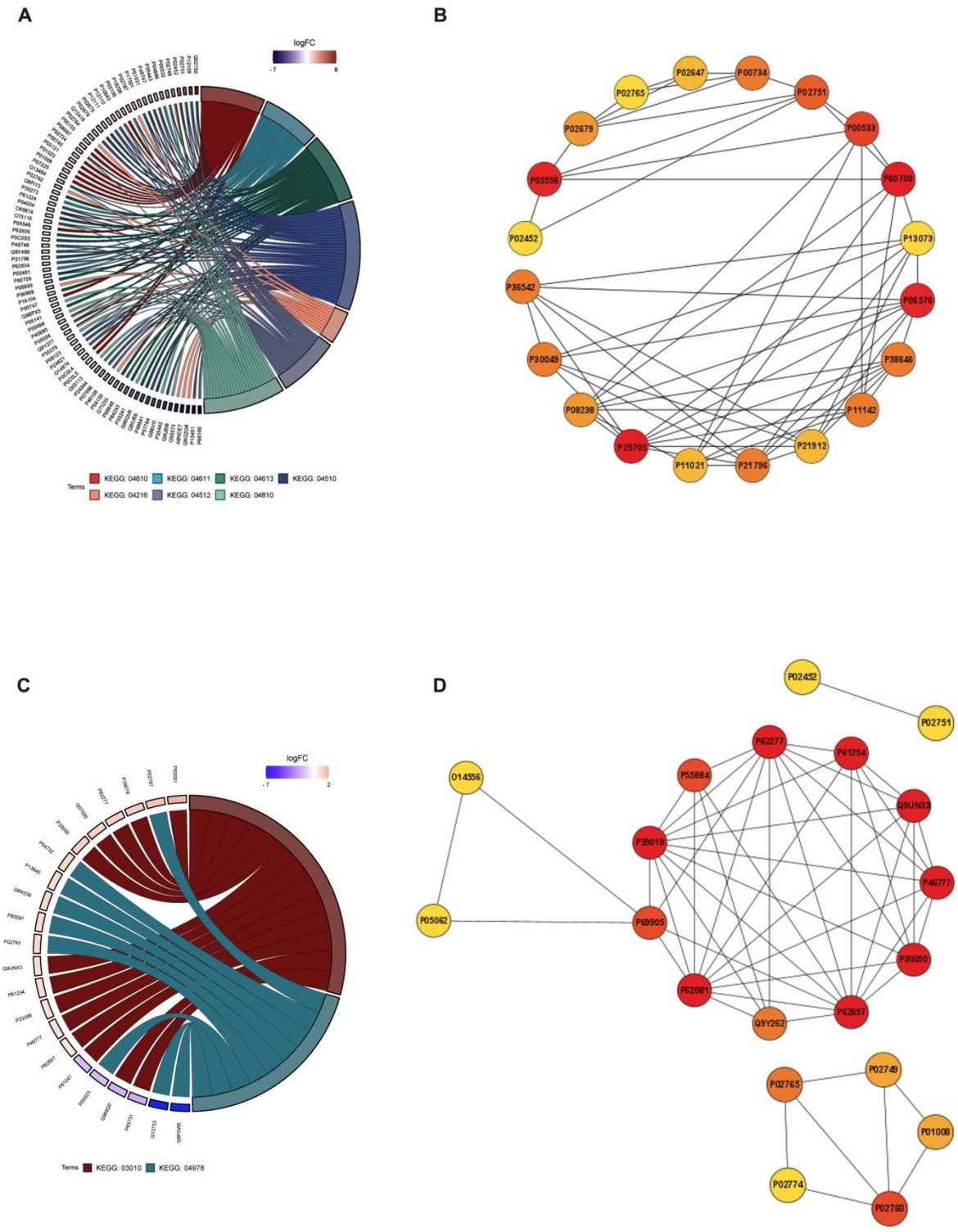

Figure 4.20 Chord diagrams and identification of hub proteins. The common pathways enriched with both (the DEPs of PGZ and blue MMs–PGZ) and (the DEPs of ROSI and brown MMs–ROSI) are presented in plots A and C, respectively. The top 20 hub proteins in the blue module (B) and brown module (D) identified using Cytoscape's cytoHubba plugin. The node colour denotes the ranking score (red = high score, orange = intermediate score and yellow = low score).
PGZ: pioglitazone; ROSI: rosiglitazone; DEP: differentially expressed protein; KEGG: Kyoto Encyclopedia of Genes and Genomes; MM: module member.

Table 4.3 The top 20 hub proteins in the blue module identified using Cytoscape's cytoHubba plugin.

Rank	Accession No.	Score	Protein Name	Gene Symbol	log_2 FC	*p*-value
1	P60709	32	Actin, cytoplasmic 1	*ACTB*	0.45	1.80E-03
2	P25705	30	ATP synthase subunit-α, mitochondrial	*ATP5A1*	0.37	4.05E-04
3	P06576	28	ATP synthase subunit-β, mitochondrial	*ATP5B*	0.24	9.71E-03
3	P05556	28	Integrin β-1	*ITGB1*	0.14	1.04E-02
5	P00533	27	Epidermal growth factor receptor	*EGFR*	2.54	3.95E-06
6	P02751	25	Fibronectin	*FN1*	4.48	2.35E-08
7	P00734	23	Prothrombin	*F2*	1.08	2.89E-06
7	P30049	23	ATP synthase subunit-δ, mitochondrial	*ATP5D*	0.40	3.22E-03
7	P11142	23	Heat shock cognate 71 kDa protein	*HSPA8*	0.09	2.96E-02
7	P21796	23	Voltage-dependent anion-selective channel protein 1	*VDAC1*	0.52	2.80E-05
7	P38646	23	Stress-70 protein, mitochondrial	*HSPA9*	0.07	1.47E-01
7	P36542	23	ATP synthase subunit-γ, mitochondrial	*ATP5C1*	0.12	2.39E-01
13	P08238	22	Heat shock protein HSP 90-β	*HSP90AB1*	0.10	5.19E-02
13	P02679	22	Fibrinogen-γ chain	*FGG*	1.25	1.31E-05
15	P21912	21	Succinate dehydrogenase [ubiquinone] iron-sulphur subunit, mitochondrial	*SDHB*	0.69	8.11E-04
15	P02647	21	Apolipoprotein A-I	*APOA1*	1.44	3.10E-07
15	P11021	21	Endoplasmic reticulum chaperone BiP	*HSPA5*	0.12	4.42E-02
18	P02765	20	α-2-HS-glycoprotein	*AHSG*	0.95	6.44E-05
18	P02452	20	Collagen α-1(I) chain	*COL1A1*	3.61	3.71E-07
18	P13073	20	Cytochrome c oxidase subunit 4 isoform 1, mitochondrial	*COX4I1*	0.08	3.29E-01

Table 4.4 The top 20 hub proteins in the brown module identified using Cytoscape's cytoHubba plugin.

Rank	Accession No.	Score	Protein Name	Gene Symbol	log_2 FC	*p*-value
1	P62277	10	Small ribosomal subunit protein uS15	*RPS13*	1.28	7.55E-02
1	P39019	10	Small ribosomal subunit protein eS19	*RPS19*	1.46	3.53E-03
1	P62081	10	Small ribosomal subunit protein eS7	*RPS7*	2.08	1.59E-02
1	P62857	10	Small ribosomal subunit protein eS28	*RPS28*	0.62	4.89E-02
5	P30050	7	Large ribosomal subunit protein uL11	*RPL12*	1.17	3.26E-02
5	Q9UNX3	7	Ribosomal protein uL24-like	*RPL26L1*	0.89	4.43E-02
5	P46777	7	Large ribosomal subunit protein uL18	*RPL5*	0.73	2.10E-01
5	P61254	7	Large ribosomal subunit protein uL24	*RPL26*	0.89	4.43E-02
9	P02760	6	α-1-microglobulin	*AMBP*	2.22	1.77E-02
9	P55884	6	Eukaryotic translation initiation factor 3 subunit B	*EIF3B*	1.35	1.81E-03
9	P69905	6	Hemoglobin subunit α	*HBA1; HBA2*	0.23	3.32E-01
12	P02765	5	α-2-HS-glycoprotein	*AHSG*	1.42	3.12E-03
12	Q9Y262	5	Eukaryotic translation initiation factor 3 subunit L	*EIF3L*	1.27	7.16E-02
14	P01008	3	Antithrombin-III	*SERPINC1*	2.33	2.22E-02
14	P02749	3	β-2-glycoprotein 1	*APOH*	0.29	1.54E-01
16	P02452	2	Collagen α-1(I) chain	*COL1A1*	1.43	4.65E-03
16	P02751	2	Fibronectin	*FN1*	1.53	4.38E-02
16	O14556	2	Glyceraldehyde-3-phosphate dehydrogenase	*GAPDHS*	1.41	1.57E-01
16	P05062	2	Fructose-bisphosphate aldolase B	*ALDOB*	1.74	6.38E-03
16	P02774	2	Vitamin D-binding protein	*GC*	2.07	2.16E-03

4.4 Discussion

TZDs are a class of antidiabetic agents approved for the management of T2DM. Besides their well-recognised capability in improving insulin sensitivity, TZDs have been shown to exert multiple pleotropic effects, including anti-inflammatory, potential neuroprotective, and blood pressure-lowering effects (DeFronzo et al, 2013). These pleotropic actions have extended TZDs' therapeutic horizons beyond glycaemic control and encouraged their application in managing T2DM and its related complications (DeFronzo et al, 2013). Nevertheless, the widespread use of TZDs in clinical practise has shortly been hampered following reports of HF cases associated with their usage (De Flines & Scheen, 2007). Owing to the uncharacterised mechanisms underpinning TZD-induced HF, TZD agents have failed to garner widespread clinical interest, and further exploration of their pleotropic effects has been hindered, resulting in their gradual disappearance from the realm of active research.

To date, the exponential growth of proteomics techniques, along with bioinformatic tools, has fuelled a surge in their application within the areas of pharmacology and mechanistic toxicology (Karahalil, 2016; Li et al, 2021; Nguyen et al, 2022). Substantial evidence from various papers has corroborated the successful integration of the toxicoproteomics approach in devoting and predicting the mechanisms of drugs' adverse effects (Karahalil, 2016; Li et al, 2021; Nguyen et al, 2022). Hence, by exploiting the innovative potential of toxicoproteomics while upholding the long-term strategic vision of the NRC, this study aims to clarify the controversy behind the cardiotoxic potential of TZDs and to elucidate the molecular mechanisms behind TZDs' deleterious effect by deciphering the AC16 cellular proteome following TZD administration using a novel, label-free, quantitative shotgun toxicoproteomics pipeline.

Using the LFQ shotgun proteomic pipeline outlined in **Figure 4.7**, the heterogeneity and similarity between the proteome signatures of the two cohorts (TZD-treated cells and control cells) were assessed using two unsupervised dimensionality reduction techniques, namely PCA and t-SNE. Although both methods fall under the umbrella of dimensionality reduction, each utilises a unique algorithm, which enables their use in a variety of contexts. In our analysis, these two techniques were initially used to visualise the clustering of biological samples. Consistently, the overall results

represented by the PCA and t-SNE plots in both experiments showed that the control and treated groups had distinct proteome patterns, as illustrated in **Figure 4.9**. Since PCA is a linear dimensionality reduction tool, and the presence of outliers could distort the linear relationship between features, PCA was also used to identify the potential outliers among the included samples (de Oliveira Andrade et al, 2022). D2 in PGZ-treated AC16 and D7 in ROSI-treated cells were found to be outliers and were therefore excluded from the subsequent analysis. t-SNE, on the other hand, constitutes a nonlinear mapping approach to the dataset that preserves the local structure of the data; thus, it is less sensitive to outliers and is not an ideal tool for outlier detection (Bajal et al, 2022; de Oliveira Andrade et al, 2022). However, the effectiveness of t-SNE at the local level and its ability as a nonlinear stochastic model to capture the complex interplay between features/data points empowers its use for clustering (Bajal et al, 2022; de Oliveira Andrade et al, 2022). Hence, based on the aforementioned characteristics of t-SNE and given that t-SNE is an unsupervised method, an attempt to elucidate the biological factor that mediated the separation of the two tested groups was made by taking advantage of the clustering feature of t-SNE and performing t-SNE-based cluster analysis. Notably, whole-proteome clustering based on protein expression levels was performed, and the generated t-SNE plots (**Figures 4.9E** and **4.9F**) showed that expression-mediated clustering effectively distinguished the two cohorts. The clustering analysis also sheds light on the trend of protein downregulation, which was observed in the majority of proteins following TZD agent treatment. These two findings extracted from the t-SNE plot strongly indicate the potential for acquiring output on biological prevalence when using an unsupervised technique, such as t-SNE.

Correspondingly, DO, functional and pathway enrichment analyses of each TZD agent's DEPs and the TZD agent's-chosen MMs (WGCNA) were performed. Within each experiment, the overall results suggest shared functional proteomic signatures between the 'PGZ-DEPs vs. PGZ-blue MMs' and 'ROSI-DEPs vs. ROSI-brown MMs', as considerable intersections were noted in most of the findings obtained from the DO, GO and KEGG pathway analyses. However, from a macro perspective, a holistic examination of PGZ and ROSI analysis findings uncovered common and unique functional and pathway findings that could explain the molecular basis underpinning the cardiotoxicity of each agent. A detailed description of the overlapping and distinct

molecular mechanisms that each TZD agent elicits to induce heart failure will be provided accordingly.

4.4.1 Converging Pathways to Cardiotoxicity: Unravelling the Shared Molecular Signatures of PGZ and ROSI

4.4.1.1 Distorted Cardiac Energetics and Mitochondrial Dysfunction

The biological inferences of TZD-induced alteration in the AC16 proteome suggest that PGZ and ROSI exhibit cytotoxicity due to mitochondrial impairment. The exact mechanism behind the induced mitochondrial dysfunction is complex. However, our analysis of the GO and KEGG pathways strongly suggests perturbation in mitochondrial cardiac energetics as the hallmark characteristic of TZD cardiotoxicity. Intriguingly, a significant downregulation in crucial pathways implicated in cardiac energetics involving oxidative phosphorylation, citrate cycle (TCA cycle) and pyruvate metabolism were noted in both TZD agents. However, the signalling pathways underpinning these processes revealed a striking divergence between PGZ and ROSI.

With regard to PGZ, the results of our enrichment analyses suggested that the treated cells exhibited mitochondrial uncoupling, represented by significant upregulation of uncoupling proteins referred to as adenine nucleotide translocators (ANTs), including ANT2. ANTs belong to a large mitochondrial solute carrier family of proteins that catalyse the ATP/ADP exchange across the inner mitochondrial membrane and therefore play a crucial role in energy homeostasis (Busiello et al, 2015; Demine et al, 2019). Apart from their role in mitochondrial energy output, ANTs also exhibit uncoupling properties (Busiello et al, 2015; Demine et al, 2019). The uncoupling properties of ANTs are reported to be secondary to their intrinsic ability to mediate H^+ leakage across the inner mitochondrial membrane, which leads to mitochondrial membrane potential disruption, proton gradient dissipation and, eventually, mitochondrial uncoupling (Busiello et al, 2015; Demine et al, 2019). The ability of PGZ to induce ANT-mediated uncoupling was also suggested in a recent study performed with isolated rat liver mitochondria (Kharechkina et al, 2021). Kharechkina et al. investigated the role that mitochondrial carriers (ANTs) play in mitochondrial depolarisation and the uncoupling effects associated with PGZ exposure in liver mitochondria (Kharechkina et al, 2021). They found that the coadministration of carboxyatractyloside (an ANT inhibitor) with PGZ-containing medium ameliorated

PGZ-induced mitochondrial depolarisation and uncoupling activities, suggesting that the latter effects were mediated by ANTs (Kharechkina et al, 2021).

With respect to ROSI, our toxicoproteomics analysis revealed a significant perturbation in crucial proteins involved in the oxidation of pyruvate and the citric acid cycle. For instance, a marked downregulation of fumarate hydratase (FH), the homotetrameric mitochondrial enzyme that catalyses the reversible hydration of fumarate to malate as a step in the citric acid cycle (Valcarcel-Jimenez & Frezza, 2023), was associated with ROSI-treated cells. This downregulation of FH could result in excessive accumulation of fumarate, disrupting this vital metabolic pathway and thereby impeding cellular energy production. Another perturbated protein in response to ROSI treatment and crucially involved in the pyruvate and citric acid cycle was malate dehydrogenase, a member of the malate–aspartate shuttle (Ahn et al, 2020). The malate shuttle is a metabolic pathway that serves as a conduit for electrons produced during glycolysis, enabling their translocation from the cytosol to the mitochondria for oxidative phosphorylation (Ahn et al, 2020). The primary role of malate dehydrogenase is to catalyse the reversible conversion of malate to oxaloacetate, facilitating the transfer of NADH from the cytoplasm to mitochondria (Ahn et al, 2020). Hence, with the recognition of the malate dehydrogenase role, its disruption markedly disrupts the malate–aspartate shuttle, leading to reduced NADH transfer to the mitochondria and thus compromising oxidative phosphorylation. The influence of ROSI on oxidative phosphorylation also reverberates by modulating the expression of mitochondrial complexes, the driving force of mitochondrial ATP production. The treatment of ROSI is associated with downregulation of human ubiquinol-cytochrome c reductase core protein 1 (UQCRC1), a vital subunit of the mitochondrial complex Ⅲ (Yi et al, 2020). The UQCRC1 protein plays an essential role in the catalytic activity of complex Ⅲ,serving as key facilitator of electron transport from ubiquinol to cytochrome c, thus contributing to the overall functionality of complex Ⅲ (Yi et al, 2020). Hence, downregulation of this vital subunit could dramatically disrupt the complex Ⅲ role, resulting in compromised electron flow and diminished ATP production. These findings were consistent with an *in vivo* study through which disrupting one UQCRC1 allele in mice showed perturbed complex Ⅲ formation, leading to a decrease in complex Ⅲ activity and ATP content in the brain at baseline

(Shan et al, 2019). Furthering the understanding of ROSI's impact on mitochondrial complexes, an additional marked downregulation in mitochondrially encoded cytochrome c oxidase I (MT-CO1) was observed. The MT-CO1 protein is a pivotal subunit of cytochrome c oxidase, the terminal enzyme in the electron transport chain, serving as an electron acceptor, mediating the transfer of electrons from cytochrome c to oxygen and driving the synthesis of ATP (Singh et al, 2019). Its downregulation strongly reflects the direct interplay between ROSI and mitochondrial complexes. In parallel with the downregulation in pyruvate metabolism and the citric acid cycle noted in response to TZD treatment, an upregulation in lactate dehydrogenase was observed, suggesting an adaptive response to limited oxygen availability (hypoxic state), allowing cells to compensate for the limited energy supply. This proposed theory is strongly supported by the upregulation of the hypoxia-inducible factor 1 (HIF-1) pathway identified in the PGZ- and ROSI-KEGG analyses. As such, it seems that TZDs induced mitochondrial damage that led to AC16 cells' death due to a decline in ATP production. These findings correspond with a previous *in vivo* study performed in mice, in which ROSI treatment significantly compromised mitochondrial respiration and substrate oxidation, resulting in decreased ATP production and deterioration of cardiac function (He et al, 2014). These findings also agreed with those of several other studies that showed a correlation between the cytotoxic effects of various chemicals and insufficient ATP levels (Julie et al, 2008; Rachek et al, 2009).

The KEGG pathway analyses also suggested that the impact of TZD on oxidative phosphorylation extends beyond the confines of ATP production, influencing a diverse array of cellular mechanisms, including redox status. In both TZD agents, the reactive oxygen species pathway showed significant enrichment of proteins also involved in oxidative phosphorylation, implying a shared mechanistic basis underlying both processes. One possible explanation for the convergence of both pathways with a noteworthy degree of similarity in the protein profile is that the TZD-induced oxidative stress is secondary to mitochondrial uncoupling and the interruption in oxidative phosphorylation, with the increase in electron leakage from the electron transport chain resulting from mitochondrial damage and leading to excessive generation of ROS species (Zorova et al, 2018).

4.4.1.2 Molecular Insights Into TZD-Induced AC16 Cellular Death

The induction of energy deficit, oxidative stress and hypoxia often culminates in cellular death. Regardless of whether cell death is an endpoint or a sign of impending disease progression, it is a common pathological mechanism that underpins all CVDs. However, there are distinct types of cell death, and they are disease dependent to a substantial extent. Our toxicoproteomics analysis uncovered that two forms of cell death were shared between PGZ and ROSI: ferroptosis and necroptosis.

Interestingly, our analysis of the DEPs identified in the present study and our WGCNA pathway analysis revealed that TZDs had an inhibitory effect on a distinct type of cell death: ferroptosis. Ferroptosis is defined as an iron-dependent type of non-apoptotic cell death that is primarily characterised by two main biochemical features: iron accumulation and lipid peroxidation (Hu et al, 2022). There have been mixed results regarding the effect of TZDs on ferroptosis (Chen et al, 2020; Liang et al, 2022). However, in our analysis, TZDs showed a strong ferroptosis inhibitory effect mediated by glutathione peroxidase-4 (GPX4)-dependent (PGZ only) and independent pathways (PGZ & ROSI). Exposing AC16 cells to PGZ led to significant upregulation of the antioxidant defence enzyme GPX4, a cornerstone regulator of ferroptosis (Hu et al, 2022). Since ferroptosis is triggered by iron-dependent lipid peroxidation accumulation, the induction of GPX4 production, which functionally disrupts lipid peroxidation by converting lipid hydroperoxides into nontoxic lipid alcohols, will eventually result in ferroptosis suppression. In addition to this GPX4-dependent inhibitory effect, the expression of ferritin was significantly upregulated in both ROSI- and PGZ-treated cells, suggesting a GPX4-independent mechanism for ferroptosis inhibition. Upregulation of ferritin, the iron-storage form, can limit the availability of iron in the body and thus limit ferroptosis (Ma et al, 2022). Another GPX4-independent pathway revealed by our analysis and implicated only in PGZ-mediated ferroptosis inhibition is the interaction of PGZ with CDGSH iron-sulphur domain-containing protein 1 (mitoNEET), an outer mitochondrial membrane protein that plays a crucial role in mitochondrial iron homeostasis (Kharechkina et al, 2021). MitoNEET is reportedly a mitochondrial PGZ target and has been shown to be overexpressed in various compartments, including the heart (Kharechkina et al, 2021; Yuan et al, 2016). Loss of mitoNEET, as reported by cumulative evidence, leads to intracellular iron accumulation that results in excessive reactive oxygen species (ROS) generation and,

therefore, ferroptosis (Yuan et al, 2016). In our analysis, upregulation of the anti-ferroptosis activity of mitoNEET was noted in the PGZ-treated samples. Together with the abovementioned findings, this result supports the notion that PGZ and ROSI have anti-ferroptosis activity.

The second pathway that exhibited enrichment in both drugs was necroptosis. Necroptosis is an emerging mode of programmed cell death that shares hallmark features with both apoptosis and necrosis (Hu et al, 2022). Compared to apoptosis, necroptosis is a regulated caspase-independent process that correlates at the molecular level with the activation of receptor-interacting protein kinases 1 and 3 (RIPK1 and RIPK3) (Dhuriya & Sharma, 2018; Xue et al, 2020). When RIPK3 is activated, it phosphorylates its substrate (mixed-lineage kinase domain-like pseudokinase (MLKL)), which results in cell death via disruption of plasma membrane permeability and cell lysis (Dhuriya & Sharma, 2018; Xue et al, 2020).

With reference to the PGZ dataset, enrichment in the necroptosis pathway, which was characterised primarily by upregulation of phosphoglycerate mutase family member 5 (PGAM5) and dynamin-related protein 1 (Drp1), strongly suggested that mitochondrial-mediated necroptosis occurred in PGZ-treated AC16 cells. PGAM5 is a mitochondrial phosphatase integral in the regulation of mitochondrial dynamics (i.e., mitochondrial fission) and various types of cell death, including mitophagy and necroptosis (Cheng et al, 2021). In the context of necroptosis, emerging evidence indicates that PGAM5 is the point of convergence for multiple necrosis pathways (Cheng et al, 2021; Wang et al, 2012). Nevertheless, it is defined as a downstream molecule of RIP3/MLKL, and its RIPK3-dependent activation results in its recruitment to the mitochondria (Cheng et al, 2021; Wang et al, 2012; Xue et al, 2020). Activated PGAM5 subsequently dephosphorylates and activates the mitochondrial fission factor Drp1 and its GTPase activity, leading to mitochondrial fragmentation, an obligatory step in the execution of necroptosis (Cheng et al, 2021; Wang et al, 2012; Xue et al, 2020). In a study conducted with a human tumour cell line, knockdown of PGAM5 attenuated ROS and tumour necrosis factor-α, as well as calcium ionophore-mediated necroptosis (Wang et al, 2012). Surprisingly, our toxicoproteomic analysis indicated that the enhanced expression of proteins in the PGAM5–Drp1 axis was independent of the canonical necroptosis pathway. This finding has also been reported elsewhere,

with PGAM5 reported to play an indispensable role in mediating concanavalin A-induced liver injury without being implicated in the execution of the canonical necroptosis pathway (He et al, 2017). Collectively, these findings may suggest that a novel form of PGAM5–Drp1 axis-mediated necrosis exists, and this necessitates further investigation.

Surprisingly, ROSI counteracts the effect of PGZ on necroptosis. The proteome profile of ROSI-treated cells showed downregulation of glutamate dehydrogenase (GLUD), a protein reported to play a role in the initiation and execution of necroptosis (Morgan & Kim, 2022). An explanation of GLUD enzyme contribution to necroptosis execution is its interaction with RIPK3 and thereby activating necroptosis signalling (Morgan & Kim, 2022). Hence, the dysregulation of GLUD suggests an inhibitory effect of ROSI against necroptosis.

4.4.2 Deciphering the Molecular Mechanisms of Cardiotoxicity: A Drug-Specific Perspective

4.4.2.1 ROSI and Alteration in Myocyte Contractility

The present study has revealed the “cardiac muscle contraction” pathway as a novel contributor to ROSI-induced cardiotoxicity, representing a significant advancement in our understanding of this adverse drug reaction. The characterisation of the enriched proteins in this tightly regulated pathway points towards four possible explanations by which ROSI modulates cardiomyocyte contraction: (i) impediment in cardiac muscle metabolism primarily through interrupting the oxidative phosphorylation process via altering mitochondrial complexes levels (MT-CO1 and UQCRC1) and (ii) alteration in muscle coordination, as significant downregulation in myosin light chain 3 (MYL3) was noted. This downregulation in MYL3 could drastically reduce myosin phosphorylation, disrupting the myosin–actin interaction and thereby compromising muscle contractility (Sitbon et al, 2020). (iii) Perturbation in catecholamine synthesis is another mechanism suggested herein, following the downregulation in aspartate beta-hydroxylase (ASPH) noted with ROSI-treated cells. The dysregulation in ASPH enzymes involved in catecholamine synthesis could principally lead to a reduction in sympathetic nervous system activity manifested in low heart rate, decreased contractility and impaired blood pressure regulation (Brewitz et al, 2020), and finally, (iv) modulation in cardiac sodium pump (Na^+/K^+ ATPase) function. Our findings

revealed significant downregulation of ATPase Na^+/K^+ transporting subunit alpha 1(ATP1A1), a major component of Na^+/K^+ pump that has a recognizable role in maintaining the electrochemical gradient that arises from the difference in electrical potential and ion concentration across the cell membrane (Obradovic et al, 2023). Maintaining this gradient by ATP1A1 is crucial to drive the Na^+/Ca^{2+} exchanger that works in extruding calcium ions from the cell, contributing to the regulation of cytosolic calcium levels and thereby ensuring muscle relaxation (Obradovic et al, 2023). Hence, dysregulation in ATP1A1 associated with ROSI exposure could have a dramatic effect on the contractile machinery, at which it could potentially result in elevating cytosolic calcium levels, leading to sustained muscle contraction and, eventually, muscle weakness.

4.4.2.2 ROSI Influence on Protein Synthesis Machinery

Noticeably reported in association with ROSI, the GO and KEGG observations suggest modulation in the cellular machinery responsible for the protein synthesis reflected by “ribosome pathway”, “protein export” and “protein processing in the endoplasmic reticulum (ER)”. The analysis revealed a downregulation of various numbers of ribosomal proteins, including ribosomal protein L24, which play a crucial role in the decoding of mRNA during translation and thus impede protein synthesis (Kisly et al, 2019). Moreover, downregulation of SEC61 translocon subunit alpha 1 (SEC61A1), a pivotal subunit of the transmembrane protein SEC61 that mediates the translocation of the newly synthesised proteins from the cytoplasm to the ER for proper folding and protein maturation (i.e., glycosylation and disulfide bond formation) (Lang et al, 2017), was noted. The effect of ROSI on protein machinery also extends to involving other proteins localized in the ER, with crucial roles in protein folding. This includes downregulation in ribophorin 1, a chaperone-like protein that facilitates N-linked glycosylation to the asparagine residues on proteins (Wilson & High, 2007), and protein disulfide isomerase family A member 3, which catalyses the formation and isomerization of disulfide bonds between cysteine residues in proteins (Ali Khan & Mutus, 2014). Altogether, the decreased expression of the abovementioned proteins reveals critical insights into the disruption of protein machinery, protein export and protein processing in the ER that could massively lead to defects in protein maturation, accumulation of unfolded or misfolded proteins in the ER and, ultimately, disruption in ER homeostasis.

4.4.2.3 Immunothrombotic Dysregulation and Cytoskeleton Architecture Alteration in PGZ-treated AC16 Cells

4.4.2.3.1 The Interplay between the Complement and Coagulation Cascades

HF is well-recognised as a disorder of cardiac contractility. Despite the phenotypic and pathophysiological heterogeneity of contractile failure, alterations in blood coagulation status and cardiomyocyte cytoskeleton components responsible for preserving cell morphology and orchestrating contractile activity play a central part. In the current study, PGZ treatment led to activation of the complement system and coagulation cascade, and this was reflected by enhanced expression of numerous complement proteins, including complement C5, C7 and C9, and various coagulation factors (i.e. coagulation factor II, V and IX). Three potential mechanisms responsible for this upregulation in the complement and coagulation cascades and their interconnectivity are briefly explained below. First, the upregulation noted in the complement components, coagulation factors and scar constituents (i.e. collagens) may suggest that their enhanced expression was part of an adaptive response to PGZ-induced myocardial damage/stress that led to an immune-cell response and scar formation. Clinically, the involvement of the complement system in HF pathogenesis is well-known. For example, Aukrust et al. reported an increase in complement activation in patients with HF, including those with dilated and ischaemic cardiomyopathies (Aukrust et al, 2001). Second, our data showed that there was molecular alteration in coagulation proteins and upregulation in the platelet activity pathway, suggesting an increased risk of blood clotting associated with PGZ exposure. Interestingly, these findings are in agreement with those from clinical cases that have reported an increase in blood coagulation with PGZ treatment (Jarrar et al, 2022). Therefore, PGZ's intrinsic ability to increase blood clotting and thrombus formation may result in complement activation by way of thrombus-mediated complement activation, as described in detail by de Bont et al. (de Bont et al, 2019), and consequently immunoinflammatory reactions. Third, necroptosis induced by PGZ exposure could lead to complement activation. In turn, complement activation can promote fibrin and clot formation. In an in vivo experimental model, C3 knockout (KO) mice experienced prolonged bleeding compared to wild-type mice, and this effect was ameliorated by reconstituting C3 KO mice with the serum of wild-type mice (Subramaniam et al, 2017). Hence, at the molecular level, the activation of the complement system, namely through the

production of C3a and C5a, aids the recruitment of platelets and immune cells to the injured site, which triggers the coagulation cascade (Rafail et al, 2015; Subramaniam et al, 2017).

4.4.2.3.2 Perturbation of Cell–Matrix Adhesion in PGZ-treated Cells

The cardiac ECM is a highly dynamic non-cellular network that plays a crucial role in cellular development and haemostasis by providing structural integrity and various functions; for example, it can elicit cellular responses and transduce signalling cascades (Frantz et al, 2010). However, aberrant protein expression in the ECM could adversely impact cellular integrity and ultimately contribute to various CVD pathologies, including HF (Frangogiannis, 2019; Frantz et al, 2010). In addition, it is widely acknowledged that the massive loss of cardiomyocytes in response to external stimuli limits their endogenous regeneration. In fact, the healing process often modifies the functional ECM to an acellular fibrotic-scar matrix with a profoundly different composition (Frangogiannis, 2019). There is mounting evidence that these changes in the ECM's profile have a dramatic impact that not only modulates the heart's structural/mechanical segments but also affects the cellular phenotype and function, leading to myocardial stiffness, diastolic dysfunction and adverse cardiac remodelling (Frangogiannis, 2019). The current study's findings showed that there was upregulation in the ECM receptor–focal adhesion–cytoskeleton pathway axis. The upregulation of ECM proteins was reflected by increased myocardial collagen and fibronectin levels, along with enhanced expression of the integrin receptors, heterodimeric transmembrane proteins consisting of α and β subunits, suggesting that the cell–matrix adhesion/linkages were modulated by PGZ exposure.

Changes in the ECM profile can be sensed by cells via active mechanosensing, a process primarily mediated by integrins (Hu et al, 2023; Huveneers & Danen, 2009). When integrins bind their adhesive ligands, a conformational change occurs in the integrin's cytoplasmic domain, and this triggers the formation of docking sites, allowing the recruitment of anchor and cytoskeleton proteins, such as talin and vinculin, which are responsible for initiating signalling cascades and links to the cytoskeleton (Hu et al, 2023; Huveneers & Danen, 2009). These proteins were overexpressed in PGZ-treated cells. The resultant integrin–anchor protein complexes ultimately support integrin clustering and the formation of focal adhesions (FAs) between a cell and the

ECM (Hu et al, 2023; Huveneers & Danen, 2009). The formation of FAs results in the activation and recruitment of other adapter proteins, including integrin-linked kinase (Yen et al, 2014), which was overexpressed in the treated cells in this study. This subsequently causes the activation of various downstream signalling pathways implicated in regulating cell behaviour and cytoskeleton organisation (Yen et al, 2014).

It is likely that PGZ affects the the cytoskeleton of cardiomyocytes by targeting the talin–vinculin axis and the Rho-associated kinases (ROCK1 and ROCK2) pathway (**Figure 4.21**). The crosslinking of vinculin with talin and actin is fundamental in the orchestration of the actomyosin cytoskeleton's actions (Meagher et al, 2021). Aberrant expression in the talin–vinculin axis could result in detrimental effects in actin polymerisation and, ultimately, myocardial stiffness. Our findings align with those from an RNA-sequencing analysis performed to investigate changes in cytoskeletal genes in patients with ischaemic and dilated cardiomyopathy (Herrer et al, 2014). In that analysis, increased vinculin expression was noted and reported to be associated with HF pathogenesis (Herrer et al, 2014; Meagher et al, 2021; Yen et al, 2014). Furthermore, in another study, knocking out mouse cardiomyocyte talin-1 resulted in a reduction in cardiac hypertrophy and fibrosis compared to that in wild-type mice (Manso et al, 2017).

Integrin activation following PGZ exposure has also been shown to upregulate the Rho/ROCK pathway. When Rho is activated via integrins, it activates ROCK1 and ROCK2, and this leads to the phosphorylation of several downstream substrates, including myosin phosphatase target subunit 1, ezrin-radixin-moesin and myosin light chain (MLC), which is crucial for diverse cellular responses (Hartmann et al, 2015). Nevertheless, the high expression of ROCK1 and ROCK2 found in our analysis was concomitant with the downregulation of MLC and myosin light chain kinase, which may be an attempt to compensate for the increased Rho kinase activity, as explained by Kirschstein et al. (Kirschstein et al, 2015). This downregulation of MLC may ultimately result in a decrease in myocardial flexibility and increased myocardial stiffness, as proven by numerous studies (Hartmann et al, 2015; Herrer et al, 2014; Manso et al, 2017).

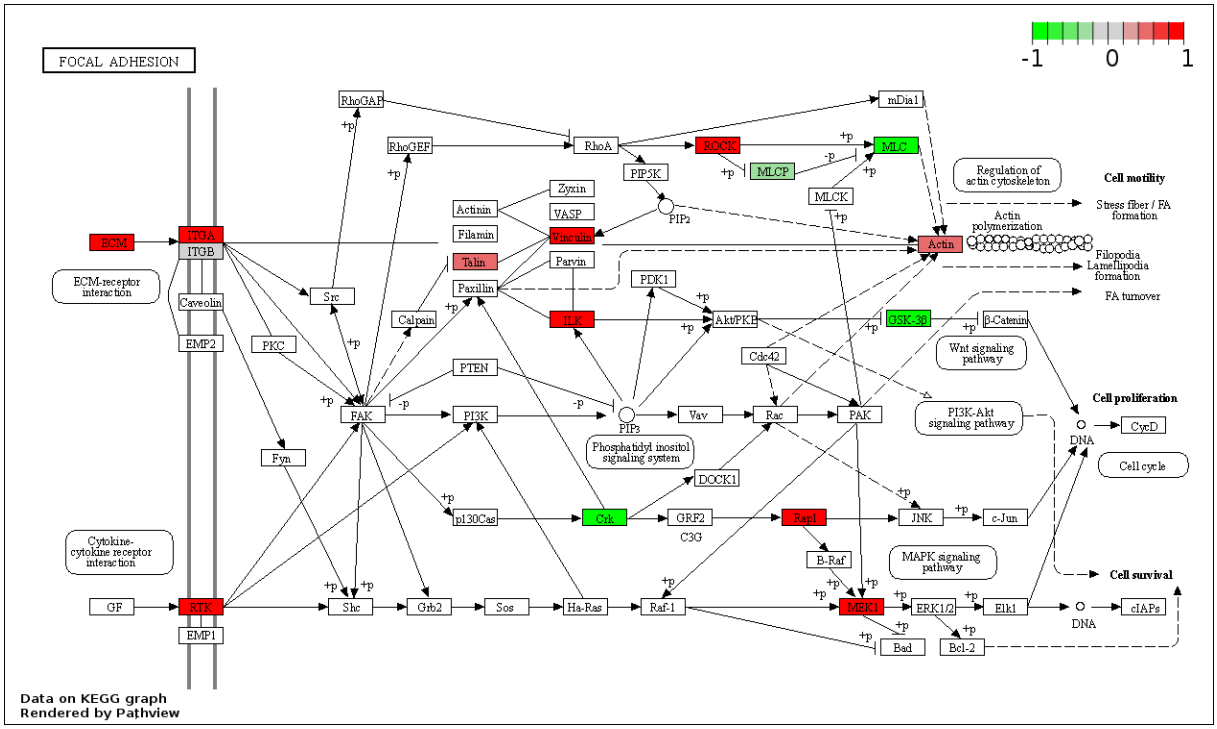

Figure 4.21 The focal adhesion signaling pathway. Proteins expression in the focal adhesion pathway (KEGG: 04510) with respect to our measured proteomics data. Red represents up-regulated proteins, while green represents down-regulated proteins. The plot was generated using PATHVIEW (available online: https://pathview.uncc.edu/analysis).

4.4.3 Limitations and Future Directions

Although the study provides valuable insights, it is crucial to acknowledge that it has a few limitations that should be considered before drawing a definitive conclusion. In response to the NRC's call, the adoption of *in vitro*–to–*in vivo* extrapolation methodologies over animal experimentation is becoming increasingly popular in mechanistic toxicology studies. Motivated by this rationale, a cell model represented by AC16 cells was employed in this study. The AC16 cell line is derived from adult human ventricular cardiomyocytes (Davidson et al, 2005). This immortalised, stable cell line has been used widely in toxicology research, as the cells express adult cardiomyocyte–specific biomarkers (α-myosin heavy chain [α-MHC], β-MHC, α-actin and troponin I) and display electrophysiological properties that are comparable to those of primary human cardiomyocytes (Davidson et al, 2005). While cell models offer numerous advantages, they have some limitations. *In vitro* models, despite their contributions, cannot accurately reflect the biological complexity of the human body. Also, when investigating the proteomic activity of cells, using an *in vitro* model could be a limitation, since such models exhibit restricted proteomic activity compared to *in*

vivo systems. In addition, our findings strongly suggest that PGZ may induce immune-mediated cardiotoxic effects; however, the interplay between immune and cardiac cells and the consequences cannot be studied using an *in vitro* model alone. Lastly, the small sample size and the absence of clinical data directly associated with the expression data may limit the utility of the results of this study.

In conclusion, we conducted a comprehensive study that used a novel proteomic pipeline to investigate the effects of TZDs on the heart. The findings provide substantial mechanistic insight into the role that mitochondrial dysfunction plays in TZDs' undesirable actions. The in-depth differential and WGCNA correlation analyses showed that the cardiotoxicity of TZDs primarily stemmed from mitochondrial oxidative phosphorylation impairment, with distinct signalling mechanisms observed for PGZ and ROSI. The type of cell death was also found to be related to the mitochondria—protein upregulation in the PGAM5–Drp1 axis, as noted in PGZ-treated cells, suggested mitochondrial-mediated necroptosis. As well as the influence of TZD on mitochondrial cardiac energetics, our toxicoproteomics findings revealed additional mechanistic aspects of cardiotoxicity; however, these findings showcased drug specificity.

Notably, dysregulation in cardiomyocyte contractility and its regulation were noted in the ROSI-treated cells, with potential mechanisms related to perturbation in mitochondrial complex expression (MT-CO1 and UQCRC1) and cardiac sodium pump (Na^+/K^+ ATPase) function, impeding cytosolic calcium homeostasis. Surprisingly, and apart from ROSI's influence on calcium levels, the analysis sheds light on potential perturbation in sodium homeostasis, represented as enrichment in 'proximal tubule bicarbonate reclamation' and 'mineral absorption'. Due to the protein profiles of both pathways, the potential disruption in sodium levels is anticipated to be secondary to the alteration of the Na^+/K^+ ATPase pump, with the potential consequence of sodium and water retention. Interestingly, a previous mechanistic study suggested the possibility of sodium and water retention in TZDs' cardiotoxicity (Horita et al, 2015); thus, further investigation of TZDs' effects on the kidney is needed to validate the reported findings. Furthermore, impairments in protein homeostasis, or proteostasis, were found following ROSI treatment, potentially contributing to cardiac myocyte dysfunction and, ultimately, cell death. In accordance with ROSI's impact on protein

synthesis and maturation, the identified hub proteins were found to be exclusively engaged in pathways relating to protein machinery, further suggesting the significance of proteostasis in ROSI-induced cardiotoxicity.

With respect to PGZ treatment, the findings suggest a potential interplay between the complement and coagulation systems induced by PGZ exposure that could trigger immunothrombosis, resulting in blood clotting and scar formation. Recent evidence has highlighted the presence of a tripartite interconnection among the complement and coagulation systems, neutrophil extracellular trap formation (NETosis) and CVDs (51). Interestingly, NETosis (KEGG: 04613) was enriched in our study; hence, understanding the interplay between PGZ and this tripartite interconnection is imperative for the examination of NETosis as a potential therapeutic target for reducing PGZ cardiotoxicity. Our findings also suggest that the disruption of the cytoskeletal architecture, which was primarily mediated through integrin-signalling pathways (namely, the talin–vinculin axis and the Rho/ROCK pathway), was responsible for myocardial contractile failure. In alignment with the findings on the ECM–integrin interaction, the hub proteins identified using the cytoHubba plugin included ECM-receptor interaction pathway proteins, such as P60709, P05556, P02751, P02679 and P02452, reinforcing the notion that the ECM is central to PGZ's undesirable actions.

Our findings provide novel information on the mechanisms, pathways and proteins that may mediate the detrimental effects that TZD has on cardiomyocytes. Thus, these mechanisms, pathways and proteins represent potential targets for the development of technologies and methodologies designed to mitigate TZDs' undesirable actions and improve their safety profiles. Further functional and clinical investigations are needed to confirm the roles that these potential targets play in the cytotoxicity of TZD.

Chapter 5

Integrative Analysis of Toxicometabolomics and Toxicoproteomics Data: New Molecular Insights into Thiazolidinedione-Induced Cardiotoxicity

Abdullah Al Sultan[1,2] & Nicholas J. W. Rattray[1,3]*

[1]Strathclyde Institute of Pharmacy and Biomedical Sciences, University of Strathclyde, 161 Cathedral Street, Glasgow, UK, G4 0RE

[2]Faculty of Pharmacy, Kuwait University, Safat, 13110, Kuwait

[3]Strathclyde Centre for Molecular Bioscience, University of Strathclyde

Abstract

Introduction

Despite the well-established efficacy of thiazolidinediones (TZDs), including pioglitazone and rosiglitazone, in type II diabetes management, their potential contribution to heart failure risk remains a significant area of uncertainty. This incomplete understanding, which persists despite decades of clinical use of TZDs, has generated ongoing controversy and unanswered questions regarding their safety profiles, ultimately limiting their broader clinical application.

Objective and Methods

This study presented a multi-omics approach, integrating toxicoproteomics and toxicometabolomics data with the goal of uncovering novel mechanistic insights into TZD cardiotoxicity and identifying molecular signatures predictive of side effect progression.

Results

Network analysis of proteo-metabolomic data revealed a distinct fingerprint of disrupted biochemical pathways, which were primarily related to energy metabolism. Downregulation of oxidative phosphorylation and fatty acid synthesis was coupled with increased activity in anaerobic glycolysis, the pentose phosphate pathway, and amino acid and purine metabolism. This suggests a potential metabolic shift in AC16 cells from fatty acid oxidation towards anaerobic glycolysis, potentially contributing to observed cardiotoxicity. Additionally, the study identified a marked disruption in the glutathione system, indicating an imbalanced redox state triggered by TZD exposure. Importantly, our analysis identified key molecular signatures across omics datasets, including prominent signatures of amino acids like L-ornithine, L-tyrosine and glutamine, which are established heart failure biomarkers, supporting their potential use for the early prediction of cardiotoxicity progression.

Conclusion

By uncovering a novel mechanistic explanation for TZD cardiotoxicity, this study simultaneously illuminates potential therapeutic interventions, opening avenues for future research to improve the safety profile of TZD agents.

Keywords: Thiazolidinediones; Toxicometabolomics; Toxicoproteomics; Cardiotoxicity; Mitochondrial energetics; Oxidative stress

5.1 Introduction

Within the last decade, the concept of medication safety has risen to the forefront of the healthcare and drug development agenda in recognition of the fact that it plays a pivotal role in patients' clinical outcomes (Alshammari, 2016). The overarching purpose of medication safety is to prevent or at least reduce the occurrence of adverse drug reactions (ADRs), which are broadly defined by the National Patient Safety Agency (NPSA) as 'any unintended or unexpected incident which could have or did lead to harm for one or more patients' (Courtenay & Griffiths, 2010). According to the latest Centers for Disease Control and Prevention (CDC) report, ADRs necessitate 1.3 million emergency department visits annually (Thacker et al, 2020). It has also been estimated by the CDC that 350,000 patients per year require hospitalisation following emergency visits for ADRs (Thacker et al, 2020). Within the context of ADRs and drug development, a recent study has proposed four main reasons for the 90% failure rate of drug development, one being related to drug toxicity, which accounts for 30% of the attrition of drug candidates (Sun et al, 2022). Given the deleterious impact of ADRs, collectively, on healthcare and drug development processes, comprehensive toxicological-based studies are urgently needed to screen and further elucidate the toxicity mechanisms implicated in medication ADRs.

Conventional *in vivo* and cellular systems toxicological-based approaches have been principally adopted to investigate the ADRs-induced drug development failure of medications, mainly through observing targeted toxicological endpoints. Although these conventional methods have yielded crucial outcomes, they have several drawbacks. They are time-consuming, and their primary focus, namely, on identifying and testing limited molecular targets, is often unlikely to fully characterise the safety profile of a drug. A growing body of single- and multi-omics-based approaches has therefore emerged as powerful tools in toxicological research, providing comprehensive and unprecedented mechanistic insights capable of filling the existing data gaps and hence improving our understanding of drug toxicity (Hu & Jia, 2021; Li et al, 2021; Marx-Stoelting et al, 2015; Nguyen et al, 2022). Notably, it is evident that most of the toxicological studies performed thus far have adopted single-omics-based approaches (Hu & Jia, 2021; Li et al, 2022; Nury et al, 2023; Olesti et al, 2021; Zaitsu et al, 2016). Despite the extensive findings of these studies, the single-omics-derived data are mainly associative and lack the resolving power required to establish

causality between observed molecular perturbations and phenotypic manifestations. These concerns about the single-omics approach have led to a revolution in omics study design and a paradigm shift toward integrating a multi-omics-based approach (Hu & Jia, 2021; Li et al, 2021). Recent papers have implied that the application of the multi-omics approach has provided novel and compelling opportunities to establish causality across different cellular function levels; thus, it has become the cutting edge of ADR research (Chen et al, 2020; Hu & Jia, 2021; Nguyen et al, 2022; Xie et al, 2020).

Recognising the transformative power of multi-omics integration in toxicology research, and with the aim of expanding upon our prior solo-omics investigation (Al Sultan et al, 2024a; b), this study was designed to integrate our toxicometabolomics and toxicoproteomics analyses of human adult cardiomyocytes AC16 treated with a class of anti-diabetic agents named thiazolidinedione (TZD). The current study introduced a novel liquid chromatography–mass spectrometry (LC–MS)-based multi-omics pipeline designed to (i) integrate potential relationships among the key identified metabolites and proteins and (ii) identify novel protein-metabolite modules capable of elucidating previously undiscovered biochemical pathways perturbed in TZD toxicity.

5.2 Methods

5.2.1 Reagents and Chemicals

TZDs, PGZ and ROSI, were obtained from Sigma-Aldrich (St. Louis, MO, USA). The LC–MS analysis used reagents purchased from Fisher Scientific (Loughborough, Leicestershire, UK): high-performance liquid chromatography (HPLC)-grade acetonitrile, methanol, analytical-grade formic acid, and ultrapure water.

5.2.2 Cells and Cell Culture

The AC16 cell line was purchased from Sigma-Aldrich (Product. No. SCC109; St Louis, MO, USA) and cultured in Dulbecco's Modified Eagle's Medium (DMEM/F-12, Product. No. D6434; Sigma-Aldrich, St Louis, MO, USA) supplemented with 12.5% foetal bovine serum (FBS), 1% antibiotics (streptomycin and penicillin) and 2 mM L-glutamine at 37°C in a humid atmosphere of 5% CO_2 and 95% air.

5.2.3 LC–MS-based Toxicometabolomics Analysis

A comprehensive description of the methodologies used for sample preparation, metabolite extraction, and LC–MS data acquisition and processing is described in Chapter 3, Sections (3.2.3–3.2.5).

5.2.4 LC–MS-based Toxicoproteomics Analysis

The specific methodologies employed for each stage of the proteomic analysis are documented in Chapter 4. Chapter 4, Sections 4.2.3 and 4.2.4, detail the sample preparation procedures for proteomic profiling, including protein extraction, trypsin digestion, and peptide clean-up. Furthermore, Section 4.2.5 outlines the microflow LC–MS data acquisition and processing protocols.

5.2.5 Integration Paradigms and Bioinformatic Analyses

5.2.5.1 Data-Driven Analysis

To integrate the shotgun toxicoproteomics and toxicometabolomics data, an *N-integration* framework, namely the Data Integration Analysis for Biomarker Discovery using Latent cOmponents (DIABLO) impeded in the *mixOmics* R package, was employed (Rohart et al, 2017). The applied DIABLO model, also referred as multiblock sparse partial least squares discriminant analysis (MB-sPLS-DA), imposes sparseness within the latent components and hence was utilised to dissect discriminative omics features across omics datasets while concurrently performing simultaneous dimension reduction (Rohart et al, 2017). Regarding MB-sPLS-DA parameter selection and performance evaluation, a design matrix tuned to 0.1 was used to accentuate the discrimination between genotype groups during analysis. The classification performance was evaluated using the repeated cross-validation through the *perf* function (Rohart et al, 2017). Five-fold cross-validation repeated 50 times was used, and the classification error rate (overall and balanced error rate [BER]) resulting from the cross-validation process across different numbers of components was then recorded for each type of prediction distance. The model with the lowest error rate was subsequently chosen to define the optimal number of components for the MB-sPLS-DA model. Lastly, with respect to feature selection, the *tune.block.splsda* function (Rohart et al, 2017) was run with five-fold cross-validation repeated 50 times to determine the suitable number of molecular signatures on each component.

Through analysis of the PGZ datasets using the outlined parameters, the MB-sPLS-DA model constructed with two components yielded the most favourable outcome, namely, the lowest overall estimation error rate (**Figure 5.1A**). This, coupled with its excellent discriminatory power, designated it as the optimal model for further investigation. Regarding the supervised integrative analysis of ROSI multi-omics datasets, the optimal number of components on the basis of the performance plot shown in **Figure 5.1B** was four; hence, this value was chosen for all downstream analyses.

The MB-sPLS-DA results were primarily visualised using the *mixOmics* R package (Rohart et al, 2017) and the Cytoscape software platform (Cytoscape; https://cytoscape.org; v3.10.1).

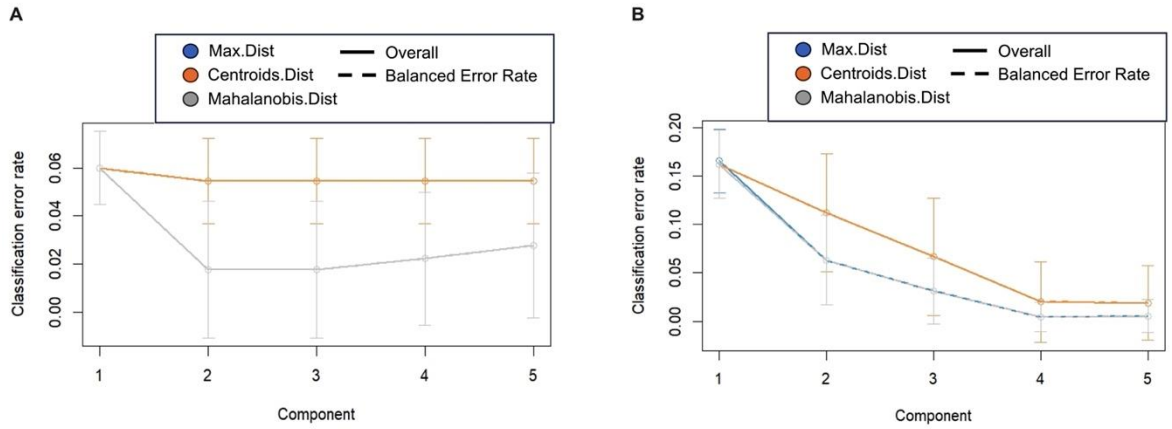

Figure 5.1 Evaluation of MB-sPLS-DA model performance via repeated cross-validation. MB-sPLS-DA classification performance was evaluated using repeated cross-validation (50 × 5-fold) for each component, considering both overall and balanced error rate across different prediction distances (max.dist, centroids.dist, mahalanobis.dist) in the PGZ (A) and ROSI (B) studies. The bars show the standard deviation across the repeated folds. The plots in (A and B) show that the error rate reaches a minimum of two and four components, respectively.

MB-sPLS-DA: Multiblock sparse partial least squares discriminant analysis; PGZ: Pioglitazone; ROSI: Rosiglitazone; BER: Balanced error rate

5.2.5.2 Knowledge-Driven Analysis

To gain a holistic understanding of perturbed pathways and their complex interactions across omics levels, a joint pathway analysis of the toxicoproteomics and toxicometabolomics data was performed via the joint-pathway analysis functionality of MetaboAnalyst v6.0 (https://www.metaboanalyst.ca) webserver. First, significance

testing was carried out to capture the significant features within each omics dataset. Accordingly, joint pathway analysis of the differential expressed proteins (DEPs) and metabolites/features (DEFs) was configured with the following parameters: a hypergeometric test for enrichment analysis, degree centrality as the topology measure, and a query combination approach for data integration. The KEGG enrichment terms that had a *p*-value < 0.05 were considered to be statistically significant.

5.2.6 Statistical Analysis

Statistical analyses were performed using R software version 4.3.0. All toxicometabolomics and toxicoproteomics data comprised three independent experiments, each run in triplicate (biological replicates), leading to nine samples per group. Student's t-tests or Welch's t-tests, dependent on data distribution and variance, were applied to assess statistical significance in pairwise comparisons between the two groups. To compare multiple variables within a single group, a one-way non-repeated ANOVA was followed by Dunnett's post hoc test for multiple comparisons. The correlation coefficient was assessed using Pearson's and distance correlation analyses. A *p*-value ≤ 0.05 was defined as the threshold for statistical significance. A visual summary of the analytical framework, incorporating both data-driven and knowledge-driven components, is presented as a schematic flowchart in **Figure 5.2.**

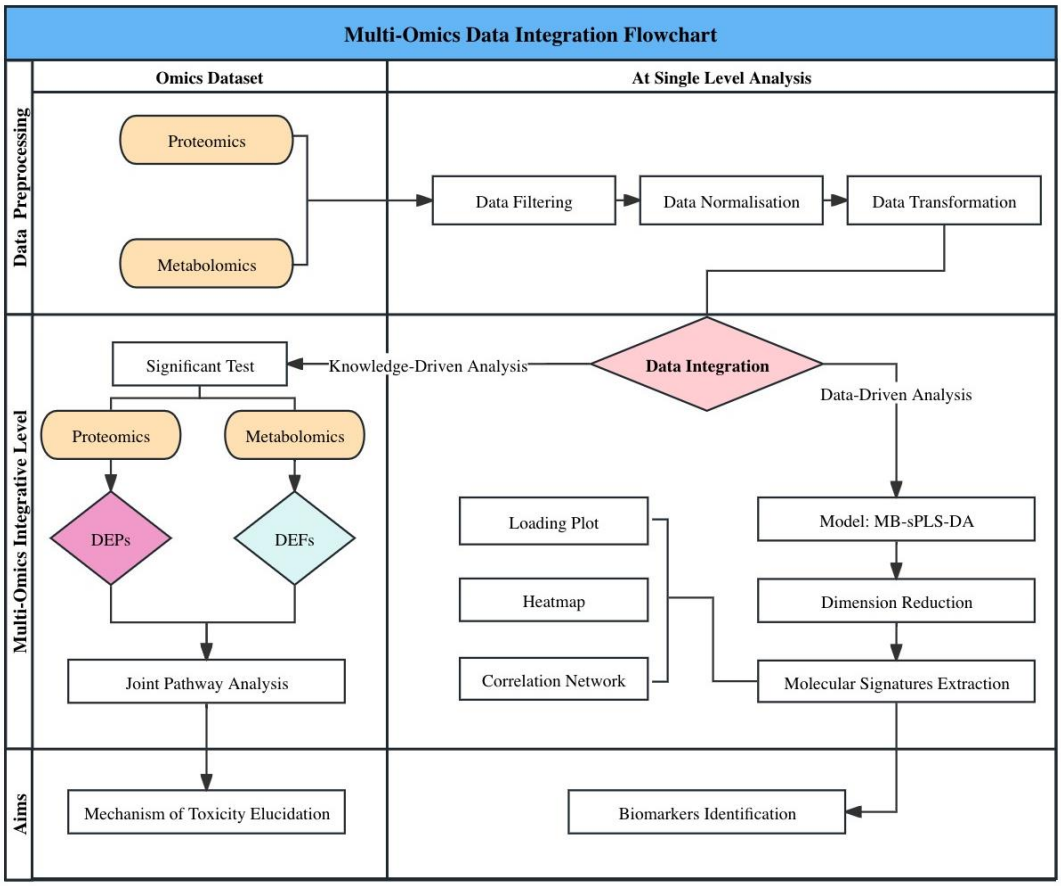

Figure 5.2 A schematic flow chart of the multi-omics integrative paradigm applied for downstream analyses. Prior to data merging, each omics dataset was subjected to data filtering, normalisation and transformation. Following these pre-processing steps, multi-omics data integration was performed, encompassing both data-driven and knowledge-based analyses (joint pathway analysis). The data-driven analysis utilised an MB-sPLS-DA model to assess inter-omics and intra-omics heterogeneity across the sample groups. Subsequently, the model was trained to identify key molecular signatures within the omics datasets, serving as potential biomarkers for TZD-induced cardiotoxicity. Furthermore, a significance test was employed within each omics dataset to capture significant features, followed by a joint pathway analysis using MetaboAnalyst v6.0 (https://www.metaboanalyst.ca) to holistically comprehend the perturbed pathways underpinning TZD's adverse effects.

MB-sPLS-DA: Multiblock sparse partial least squares discriminant analysis; DEPs: Differential expressed proteins; DEFs: Differential expressed features; TZD: Thiazolidinedione

5.3 Integrative Analysis Findings of Untargeted Toxicometabolomics and Toxicoproteomics Data

To comprehensively landscape the heterogeneity among sample groups and unveil a detailed molecular profile of TZD-induced changes in AC16-cardiomyocytes,

multivariate analysis integrating proteomics and metabolomics data was employed using the DIABLO framework.

5.3.1 Multivariate Model-Driven Analysis of AC16 Cell Proteo-metabolomic Response to PGZ Exposure

With regard to the PGZ datasets, visual inspection of the sample plots generated by the DIABLO model revealed a distinct separation between the treated and control groups across all omics datasets (**Figure 5.3A**). Furthermore, interrogation of the two omics datasets, as presented in **Figure 5.3B**, yielded a highly significant correlation between their corresponding latent components, indicating a striking level of inter-dataset concordance across heterogeneous data types.

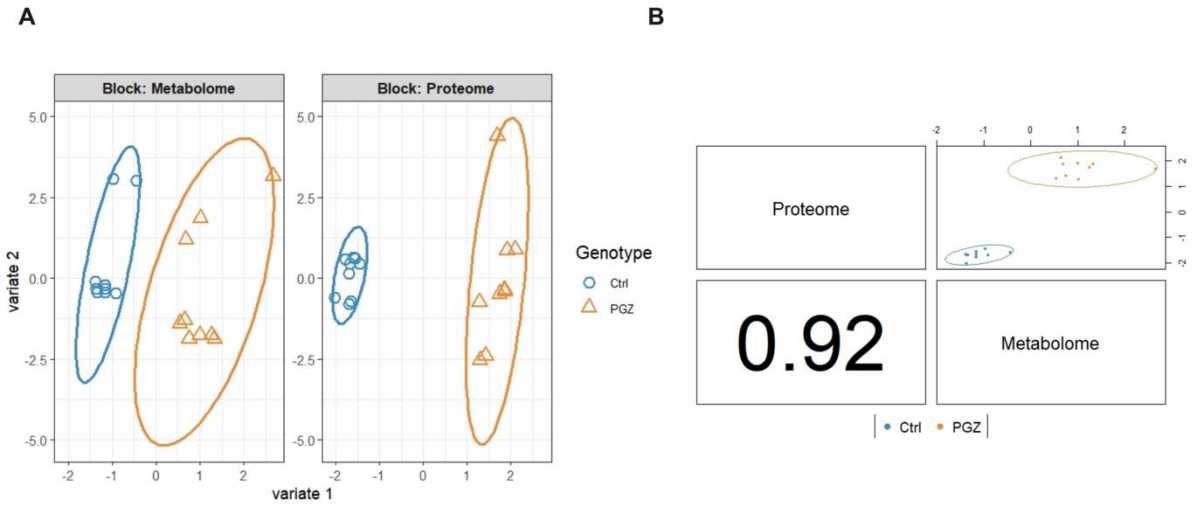

Figure 5.3 Multiblock supervised partial least squares discriminant analysis (MB-sPLS-DA) model of multi-omics data following PGZ treatment. (A) Individual omics dataset contributions to the MB-sPLS-DA model. Score plots revealed distinct separation of control and treated samples at both the metabolome and proteome levels. (B) Inter-omics correlations from plotDIABLO displaying the first component in each dataset (upper diagonal plot) and the Pearson correlation between each component (lower diagonal plot), showcasing high correlation between proteomics and metabolomics data.

MB-sPLS-DA: Multiblock sparse partial least squares discriminant analysis; PGZ: Pioglitazone

To ensure optimal feature selection for maximal discrimination, a threshold of ± 0.15 was imposed on the loading coefficients of the first and second sPLS-DA components for each data block. This applied criterion for MB-sPLS-DA feature selection (fold = 5, nrepeat = 50, using Mahalanobis as a distance measure) resulted in the identification of five proteins (**Table 5.1**) and five metabolites in each component. The multi-omics

signature extracted from component 1 included mitochondrial carnitines (tiglylcarnitine, crotonylcarnitine), L-glutamine, oleic acid, and D-pantothenic acid. Prominent protein signatures within this component comprised P52209, Q07955, P31942, P62280, and P49327. In contrast to component 1, component 2 exhibited a unique signature comprising metabolites such as spermidine, L-tyrosine, L-proline, and L-ornithine, alongside protein identifications Q56UQ5, Q16795, Q5TEC6, O75083, and Q01995 (**Table 5.1**).

Table 5.1 List of signature proteins identified by the DIABLO model in the PGZ study.

Accession	Protein Name	Gene Symbol	*p*-value
Q56UQ5	TPT1-like protein	*TPT1*	3E-10
Q16795	NADH dehydrogenase [ubiquinone] 1 alpha subcomplex subunit 9, mitochondrial	*NDUFA9*	3E-09
Q5TEC6	Histone H3-7	*H3-7*	8E-08
O75083	WD repeat-containing protein 1	*WDR1*	1E-06
P62280	Small ribosomal subunit protein uS17	*RPS11*	4E-01
Q01995	Transgelin	*TAGLN*	5E-07
P49327	Fatty acid synthase	*FASN*	4E-01
Q07955	Serine/arginine-rich splicing factor 1	*SRSF1*	2E-01
P31942	Heterogeneous nuclear ribonucleoprotein H3	*HNRNPH3*	3E-02
P52209	6-phosphogluconate dehydrogenase, decarboxylating	*PGD*	3E-01

The contribution of each selected variable to each component across all blocks is illustrated in **Figure 5.4**. The expression of each multi-omics molecular signature for each included sample is illustrated in **Figure 5.5**.

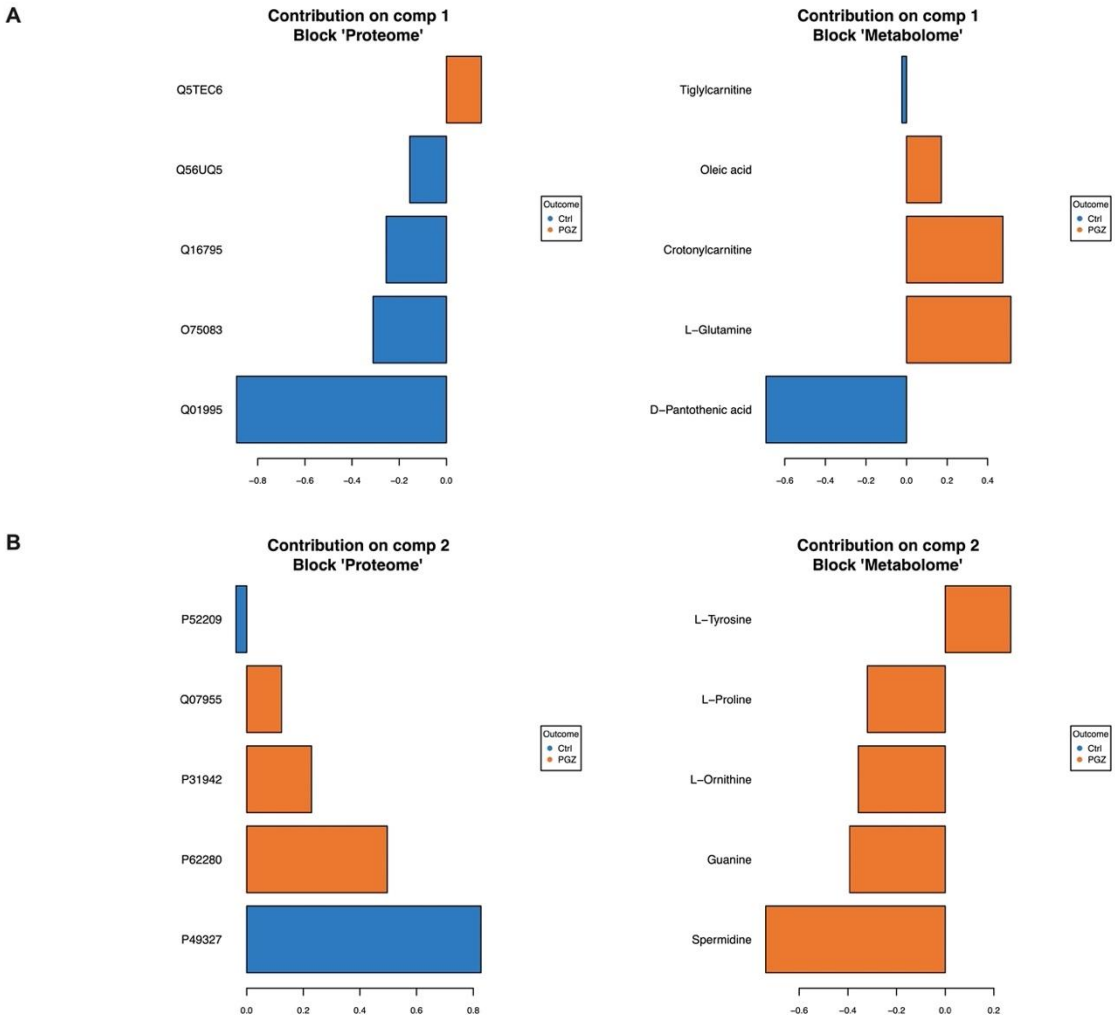

Figure 5.4 Loading plot for the molecular signatures selected by MB-sPLS-DA performed in the PGZ study. The plots (A and B) display the most important variables, ranked by the magnitude of their coefficients from bottom to top. Each variable's colour denotes the class with the highest median expression level.

MB-sPLS-DA: Multiblock sparse partial least squares discriminant analysis; PGZ: Pioglitazone

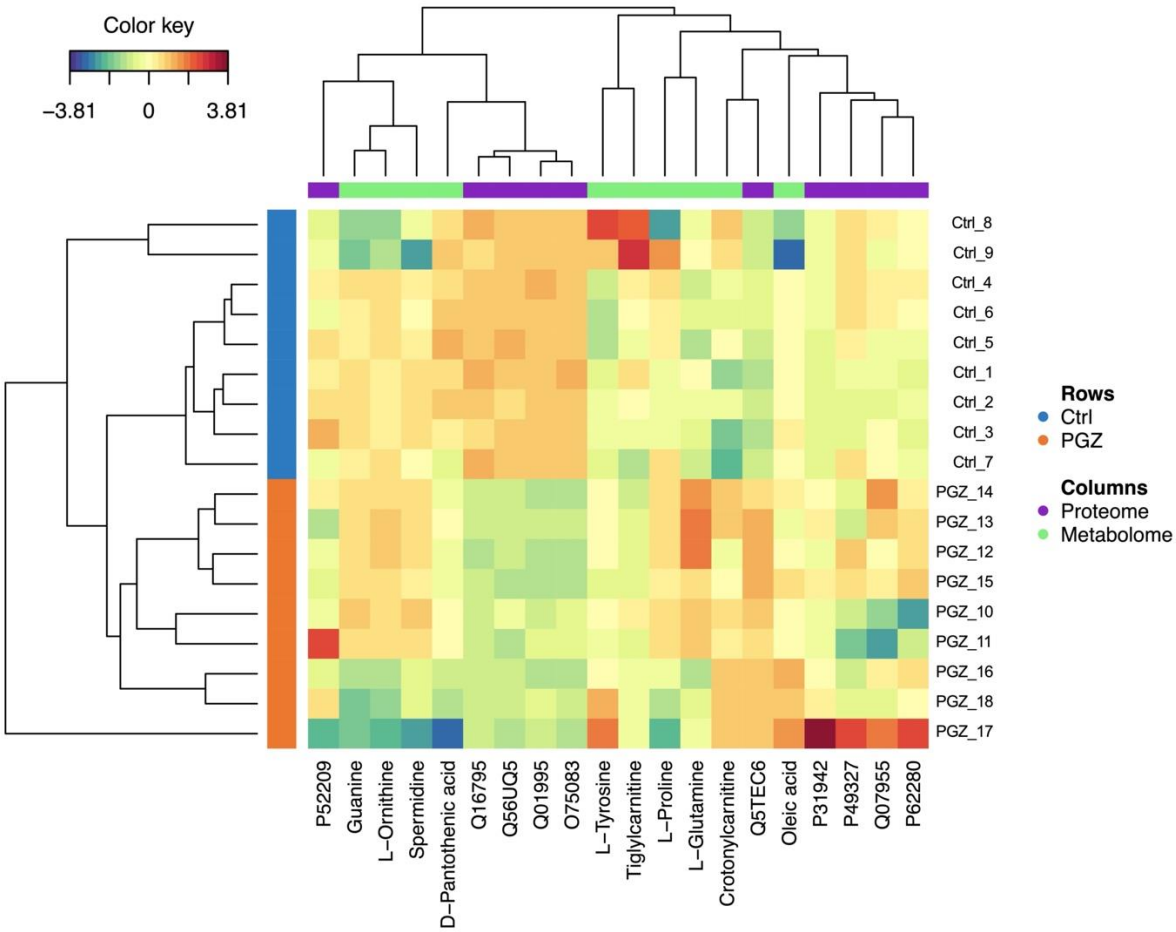

Figure 5.5 Circos plot generated from MB-sPLS-DA applied to the PGZ study data. Clustered Image Map (Euclidean distance, complete linkage) for the molecular signatures extracted by MB-sPLS-DA performed on the PGZ study.

MB-sPLS-DA: Multiblock sparse partial least squares discriminant analysis; PGZ: Pioglitazone

To visually depict the inter-molecular signature correlations, a circus plot (**Figure 5.6A**) was constructed. The plot revealed dense positive interactions between the following: L-tyrosine and P31942/P62280; L-ornithine/guanine and P52209; and D-pantothenic acid with the proteins Q56UQ5, Q16795, Q01995, and O75083. Further investigation identified robust repulsive/negative interactions involving D-pantothenic acid and Q5TEC6; guanine/L-ornithine and the P62280/P49327/P31942/Q07955 proteins; and spermidine with P62280, P49327, and P31942.

Lastly, a network of the proteomics and metabolomics key features was constructed based on the similarity matrix (**Figure 5.6B**). Analysis of this proteo-metabolomic network identified a tightly knit cluster of co-regulated features, with tiglylcarnitine, spermidine, L-tyrosine, L-ornithine, and guanine (metabolome block), and O75083 and Q5TEC6 (proteome block) serving as the prominent hub features that drive this module.

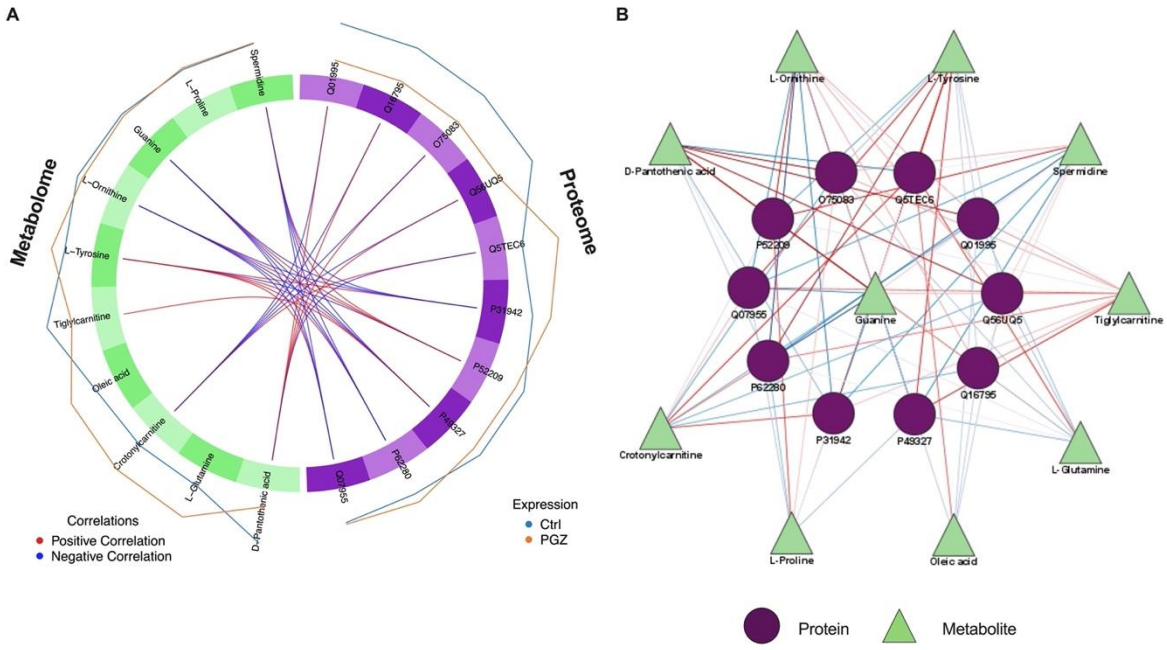

Figure 5.6 Correlation network analysis of the multi-omics signatures derived by the DIABLO framework. Plot (A) displays a circos plot depicting correlations between selected features (cut-off: 0.6), illustrating positive associations in red and negative associations in blue. Plot (B) showcases a protein-metabolite interaction network, where circular and triangle shapes represent protein and metabolite features, respectively, and edge colours red and blue represent positive and negative correlations, respectively. The width of the edges represents the strength of correlation. The protein-metabolite network was generated using (Cytoscape; https://cytoscape.org; v3.10.1).

5.3.2 Multivariate Model-Driven Analysis of AC16 Cell Proteo-metabolomic Response to ROSI Exposure

With respect to the ROSI datasets, the DIABLO method, through integrative analysis of inter-omics correlations, pinpointed several crucial features that differentiate ROSI-treated samples from the control group. Visualisation of the sample distribution after projection onto the subspace spanned by components 1 and 2 in **Figure 5.7A** reveals a distinct separation between treated and control groups. Furthermore, and similarly to the PGZ findings, the interrogation of both proteomics and metabolomics datasets, as visually depicted in **Figure 5.7B**, unveiled a highly significant correlation between their respective latent components, signifying a remarkable degree of coherence and agreement between these divergent data modalities.

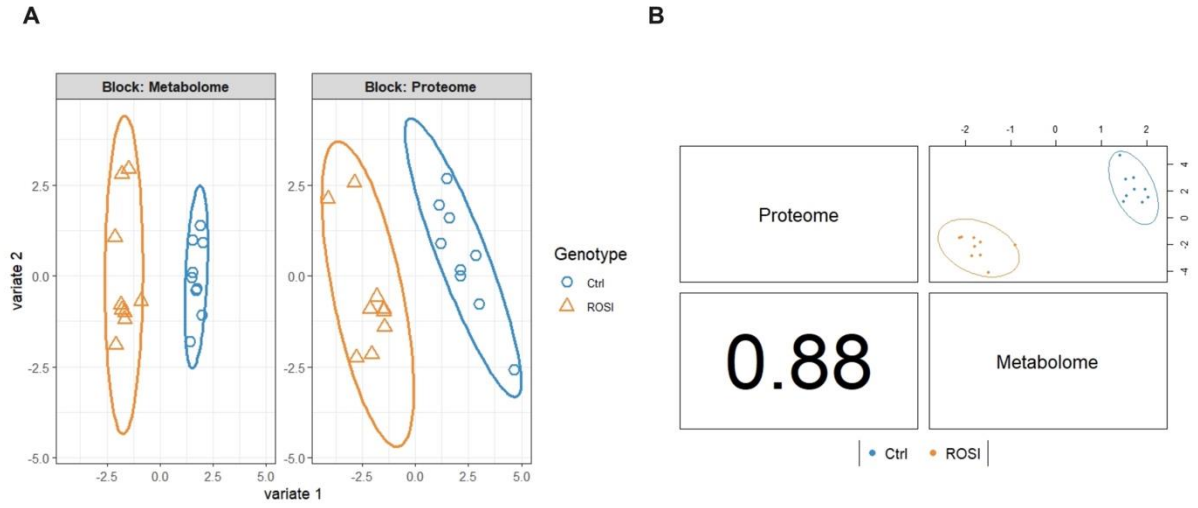

Figure 5.7 Multi-omics integration of ROSI datasets via the DIABLO mixOmics framework. (A) The individual contribution of each dataset to the MB-sPLS-DA final model, demonstrating distinct intra-omics separation between ROSI-treated samples and control groups. (B) Component correlation of each of the two datasets determined by DIABLO analysis, demonstrating a high correlation between the proteomics and metabolomics data.

MB-sPLS-DA: Multiblock sparse partial least squares discriminant analysis; ROSI: Rosiglitazone

In terms of feature selection, integrative analysis with DIABLO (fold = 5, nrepeat = 50, using Mahalanobis as a distance measure) identified a signature of 20 proteins (**Table 5.2**) and 20 metabolites across all the selected components. The identity of each

molecular signature along with its contribution to its perspective component, as well as its expression over the included samples, are illustrated in **Figures 5.8 and 5.9**.

Table 5.2 List of signature proteins identified by the DIABLO model in the ROSI study.

Accession	Protein Name	Gene Symbol	*p*-value
P67936	Tropomyosin alpha-4 chain	*TPM4*	4E-01
Q9UQE7	Structural maintenance of chromosomes protein 3	*SMC3*	4E-01
O95347	Structural maintenance of chromosomes protein 2	*SMC2*	5E-01
Q8N357	Solute carrier family 35 member F6	*SLC35F6*	3E-01
Q16181	Septin-7	*SEPTIN7*	3E-01
P62917	Large ribosomal subunit protein uL2	*RPL8*	4E-01
Q96D15	Reticulocalbin-3	*RCN3*	3E-01
A0A075B767	Peptidyl-prolyl cis-trans isomerase A-like 4H	*PPIAL4H*	5E-05
P0DN37	Peptidyl-prolyl cis-trans isomerase A-like 4G	*PPIAL4G*	5E-05
P0DN26	Peptidyl-prolyl cis-trans isomerase A-like 4F	*PPIAL4F*	5E-05
F5H284	Peptidyl-prolyl cis-trans isomerase A-like 4D	*PPIAL4D*	5E-05
A0A0B4J2A2	Peptidyl-prolyl cis-trans isomerase A-like 4C	*PPIAL4C*	5E-05
Q9Y536	Peptidyl-prolyl cis-trans isomerase A-like 4A	*PPIAL4A*	5E-05
P12268	Inosine-5'-monophosphate dehydrogenase 2	*IMPDH2*	9E-05
P50395	Rab GDP dissociation inhibitor beta	*GDI2*	7E-02
P31150	Rab GDP dissociation inhibitor alpha	*GDI1*	7E-02
P22102	Trifunctional purine biosynthetic protein adenosine-3	*GART*	5E-01
P24534	Elongation factor 1-beta	*EEF1B2*	4E-01
P0DP23	Calmodulin-1	*CALM1*	5E-01
O75947	ATP synthase subunit d, mitochondrial	*ATP5PD*	7E-02
P04083	Annexin A1	*ANXA1*	2E-01

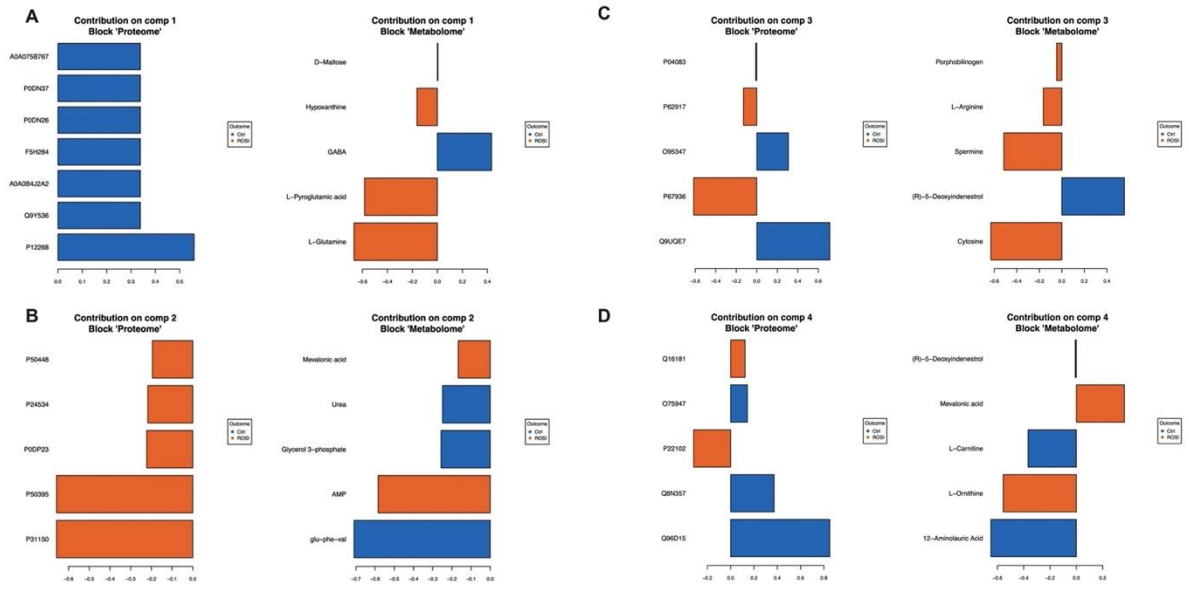

Figure 5.8 Loading plot for the molecular signatures selected by MB-sPLS-DA performed in the ROSI study. The plots (A-D) display the most important variables, ranked by the magnitude of their coefficients from bottom to top. Each variable's colour denotes the class with the highest median expression level.
MB-sPLS-DA: Multiblock sparse partial least squares discriminant analysis; ROSI: Rosiglitazone

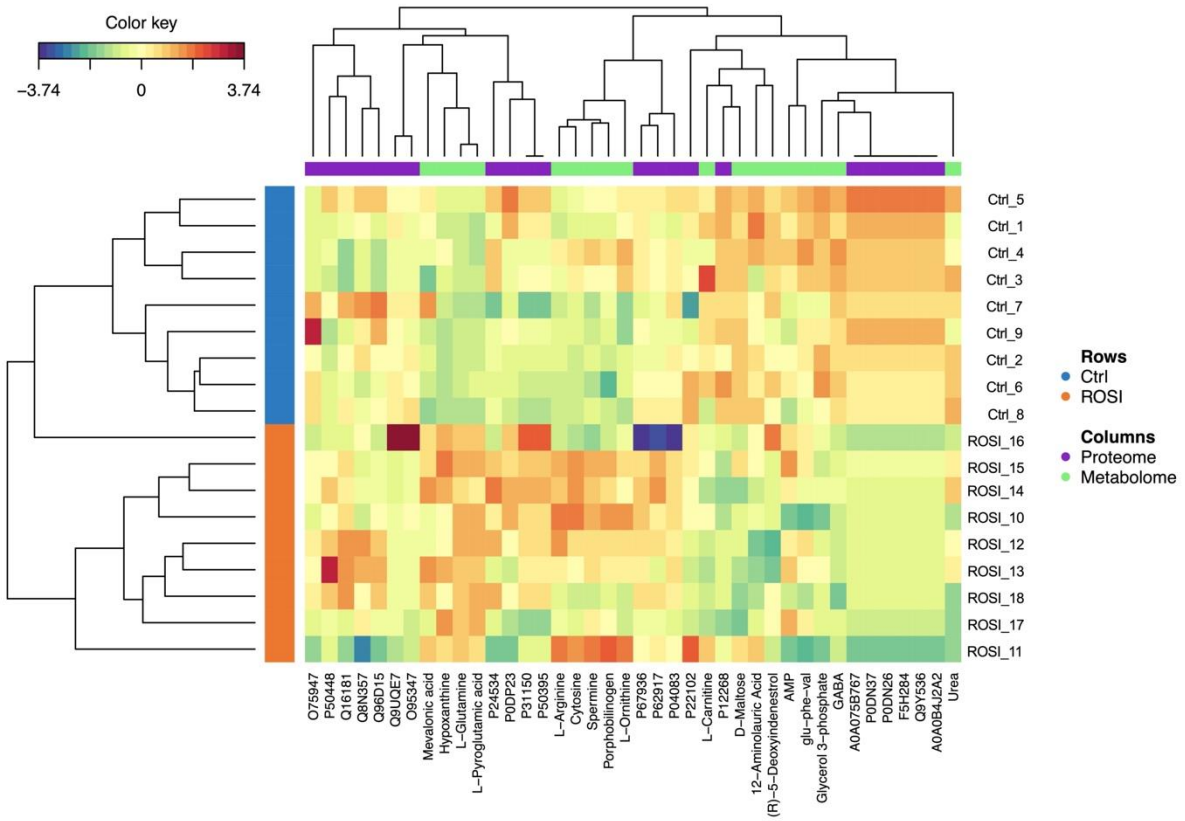

Figure 5.9 Circos plot generated from MB-sPLS-DA applied to the ROSI study data. Clustered Image Map (Euclidean distance, complete linkage) for the molecular signatures extracted by MB-sPLS-DA performed on the ROSI study.

MB-sPLS-DA: Multiblock sparse partial least squares discriminant analysis; ROSI: Rosiglitazone

For post-feature selection analysis, a comprehensive correlation analysis unveiled a rich network of positive associations among the extracted features (**Figure 5.10A**). Within this network, GABA and D-maltose emerged as key players, exhibiting synergistic interactions with the following proteins: P12268, A0A075B767, P0DN37, P0DN26, F5H284, A0A0B4J2A2, and Q9Y536. Interestingly, urea and glycerol 3-phosphate displayed independent positive correlations with a subset of this list, including A0A075B767, P0DN37, P0DN26, F5H284, A0A0B4J2A2, and Q9Y536. Spermine, on the other hand, adopted a targeted approach, demonstrating direct positive interactions with individual proteins P67936 and P62917. Notably, AMP engaged in a distinct network of positive associations with a separate subset of proteins formed by P0DP23, P50395, and P31150. Beyond the identified positive associations, a nuanced picture of negative interactions emerged. Notably, L-glutamine, L-pyroglutamic acid, and hypoxanthine exhibited negative correlations with a same profile of protein members, comprising A0A075B767, P0DN37, P0DN26, F5H284, A0A0B4J2A2, Q9Y536, and P12268. Additionally, spermine and cytosine demonstrated strong negative associations with Q9UQE7 and O95347, respectively.

Delving deeper into the interplay between the identified proteomics and metabolomics signatures, a network analysis was conducted (**Figure 5.10B**). As shown in **Figure 5.10B**, a crucial group of hub features, spanning both proteome and metabolome, that serve as key orchestrators within the network were identified. From block one, spermine and L-ornithine were identified as prominent hubs, while block two contributed a distinct set of hub proteins, including A0A075B767, A0A0B4J2A2, F5H284, P0DN26, P0DN37, P12268, and Q9Y536.

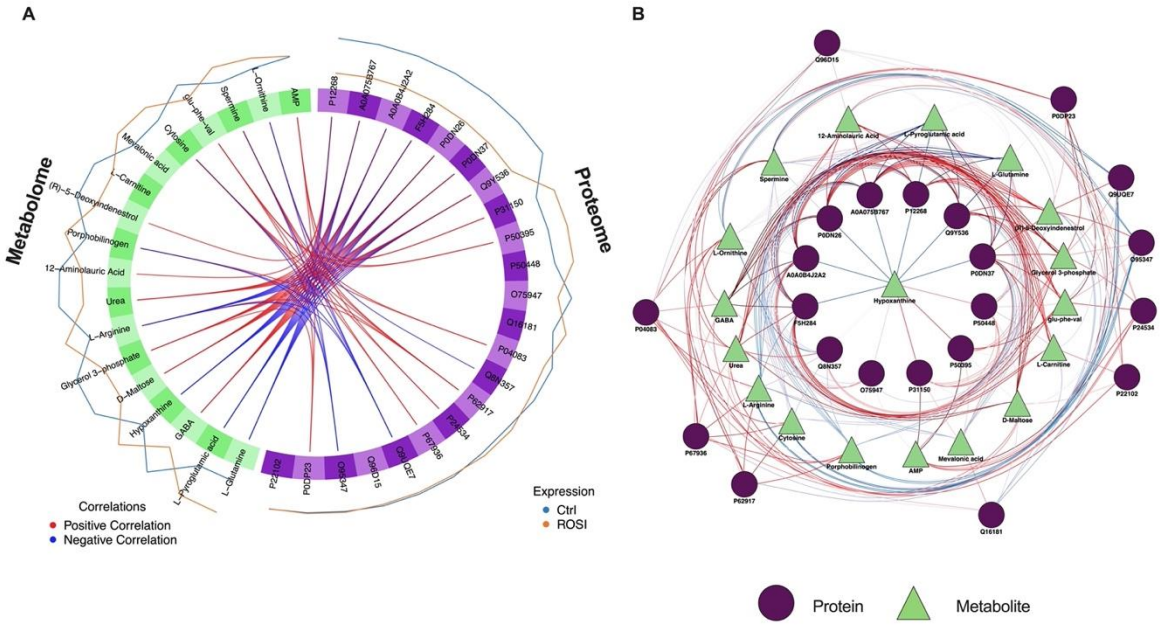

Figure 5.10 Correlation network analysis of the multi-omics signatures derived by the DIABLO framework. Plot (A) displays a circos plot depicting correlations between selected features (cut-off: 0.6), illustrating positive associations in red and negative associations in blue. Plot (B) showcases a protein-metabolite interaction network, where circular and triangle shapes represent protein and metabolite features, respectively, and edge colours red and blue represent positive and negative correlations, respectively. The width of the edges represents the strength of correlation. The protein-metabolite network was generated using (Cytoscape; https://cytoscape.org; v3.10.1).

5.3.3 Joint Pathway Analysis of the Toxicoproteo-metabolomic Data

To elucidate the biological drivers of TZD-mediated cardiotoxic effects and unveil the interconnected pathways governing these alterations at the metabolomic and proteomic levels, a comprehensive joint pathway analysis was conducted.

Analysis of PGZ-treated proteo-metabolomic datasets **(Figure 5.11A, [Table S12, Appendix Section 7.4])** revealed a pronounced enrichment in pathways related to amino acid metabolism. Notably, pathways associated with phenylalanine metabolism, phenylalanine, tyrosine and tryptophan biosynthesis, glutathione metabolism, beta-alanine metabolism, and lysine degradation exhibited significant enrichment. Additionally, pathways involved in aminoacyl-tRNA biosynthesis and pantothenate and CoA biosynthesis were identified as significantly perturbed in response to PGZ.

Complementary pathway analysis of the ROSI datasets **(Figure 5.11B, [Table S13, Appendix Section 7.4])** revealed a multifaceted metabolic rewiring encompassing several key functional domains. Pathways involved in core energy production, such as the citrate cycle, pyruvate metabolism, glycolysis/gluconeogenesis, and nitrogen metabolism, showed marked alterations. Strikingly, amino acid metabolism was extensively modulated, with enrichments noted in pathways associated with phenylalanine, tyrosine, and tryptophan biosynthesis; phenylalanine metabolism; arginine and proline metabolism; glutathione metabolism; and lysine degradation. Additionally, perturbations in aminoacyl-tRNA biosynthesis were also observed.

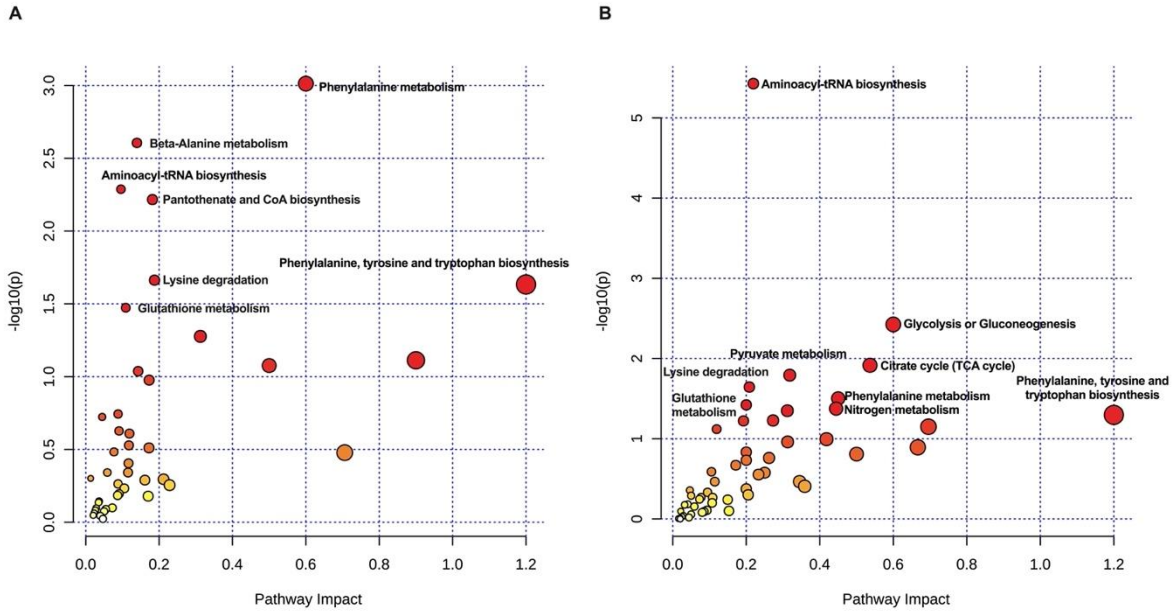

Figure 5.11 Joint pathway analysis of the proteo-metabolomic data. Dot plots in (A and B) illustrated the metabolic pathway enrichment in a joint analysis of significantly differentially expressed metabolites and proteins of PGZ and ROSI, respectively. The size and colour of each circle in (A) and (B) reflect the pathway impact value and the *p*-value, respectively. The figure was generated using MetaboAnalyst v6.0 (https://www.metaboanalyst.ca)

PGZ: Pioglitazone; ROSI: Rosiglitazone

5.4 Discussion

While ensuring the effectiveness of medication in chronic disease is paramount, recognising the importance of managing both safety and cost through a holistic approach, as encapsulated by the medication triangle, contributes to optimal and enduring treatment outcomes. Within the context of T2DM management, TZDs serve as a prime example of how the medication triangle plays out in practice. Despite showcasing efficacy in maintaining glycaemic control and offering affordability, TZDs fall short in the medication triangle, primarily due to concerns surrounding their safety profile (ADA, 2023). The emergence of clinical evidence demonstrating a link between TZD usage and HF has fundamentally reshaped the risk–benefit profile of these medications, leading to marked restrictions in their clinical use (Administration, 2010; 2012; De Flines & Scheen, 2007). Nevertheless, the exact mechanisms responsible for triggering or aggravating cardiac events in response to TZD usage are still unclear, impeding a holistic understanding of this complex interplay. Motivated by the obscurity surrounding the mechanistic nature of TZD cardiotoxicity, this study introduced a comprehensive multi-omics approach to unravel the hitherto undeciphered pathomechanisms driving this adverse effect.

Employing the integrated pipeline detailed in Figure 5.2, a joint data and pathway analysis limited to co-acquired, filtered and known annotated metabolomics and proteomics data from the same biological AC16 samples was performed. The inclusion of unannotated features in data-driven analyses remains a subject of debate. Proponents argue that incorporating such features could uncover novel biological processes or subtle phenomena missed by traditional methods. Additionally, hidden correlations with other molecular features might be revealed. Conversely, our analysis opted for a conservative approach, exclusively considering features with high-confidence annotations. This decision was underpinned by the potential for uncharacterised features to introduce noise, redundancy, and complexity, hindering data interpretation. Moreover, the absence of validation and characterisation for these features limits their biological interpretability and increases the risk of erroneous conclusions. A summary of the advantages and disadvantages of including unknown features in statistical analysis, particularly when integrating multiple omics data, is presented in **Table 5.3**.

Table 5.3 Advantages and disadvantages of including unknown features in statistical analysis

Aspect	Advantages	Disadvantages
Novel biomarker discovery	Potential to discover novel biomarkers or unannotated molecules.	Unclear biological relevance without proper annotation, limiting insights.
Comprehensive data exploration	Allows a more thorough exploration of the dataset, capturing all detected signals.	Increases dataset complexity, leading to potentially overwhelming data that may complicate analysis.
Unbiased analysis	Ensures unbiased statistical analysis by considering all features, even unknown ones.	Risk of including irrelevant or noise-derived features, leading to false positives.
Cross-omics correlations	Can identify novel, unexpected relationships across different omics layers.	Difficult to establish meaningful connections between unknown features across omics layers.
Discovery potential	May reveal new pathways or mechanisms that were previously unknown.	Unannotated features cannot be linked to existing biological knowledge, limiting interpretability.
Noise and artifacts	Could represent biologically relevant but novel signals.	May include technical artifacts or noise, reducing the reliability of the dataset.
Data integration	Provides a more comprehensive integration across multiple omics layers.	Integrating unknown features across datasets is challenging without clear identification.
Computational complexity	Provides a rich dataset for advanced modeling and machine learning approaches.	Increased computational complexity and processing time due to the larger, unfiltered dataset.
Validation	Opportunity to explore novel hypotheses for further validation.	Lack of validation methods for unknown features makes it hard to assess their biological significance.
Quality control	Can be informative if unknowns are systematically related to technical or biological variations.	Increases the difficulty of quality control, as unknowns are harder to filter for reliability.
Interpretation	Allows for more exploratory analyses, potentially leading to novel insights.	Interpretation is challenging without a functional or structural context for unknowns.

Through the introduction of the DIABLO framework, an evaluation of both intra- and inter-omics heterogeneity was performed, revealing subtle yet distinct separation patterns between the predefined groups (control samples and TZD-treated AC16 cells). Furthermore, interrogation of the correlation between the proteomics and

metabolomics datasets revealed a robust positive association. This finding indicates robust agreement within the DIABLO model and justifies its suitability for further investigations aimed at (i) elucidating the system biology of TZD-induced cardiotoxicity (joint pathway analysis), from protein to the final metabolic product, and (ii) identifying the unique molecular signatures associated with different characteristics of cardiotoxicity as reflected by changes in both protein and metabolite levels.

5.4.1 Decoding the Metabolic Remodeling of AC16 Cardiomyocytes Following TZD Exposure

HF is demonstrably characterised by early disruptions in cardiac energy metabolism, preceding discernible structural alterations. Our multi-level molecular profiling corroborates this notion, uncovering distinct patterns of metabolic reprogramming across multiple pathways, culminating in perturbed cardiac energetics. Our analysis revealed a coordinated downregulation of crucial pathways involving oxidative phosphorylation (OXPHOS), the citric acid cycle (TCA), pyruvate metabolism, and fatty acid synthesis in response to TZD treatment. Conversely, increased activity was observed in glycolysis, the pentose phosphate pathway, and amino and purine metabolism. This coordinated pattern strongly suggests a marked switch in AC16 metabolic fate manifested as metabolic shift from fatty acid oxidation towards anaerobic glycolysis, potentially contributing to cardiotoxicity progression.

In the context of TCA and OXPHOS, a marked downregulation in mitochondrial $NAD(P)^+$-dependent malic enzyme (m-NAD(P)-ME), a protein with a prominent role in catalysing the oxidative decarboxylation of malate to pyruvate, feeding into the TCA cycle (Hsieh et al, 2019) was noted following PGZ treatment. However, ROSI treatment induced substantial downregulation of fumarate hydratase (FH), a homotetrameric mitochondrial enzyme catalysing the reversible hydration of fumarate to malate within the TCA (Valcarcel-Jimenez & Frezza, 2023). This downregulation led to a marked accumulation of fumarate, mirroring its observed abundance in TZD-treated cells. Another crucial protein perturbed by ROSI treatment is malate dehydrogenase, a key enzyme in the oxidation of pyruvate and TCA and a member of the malate-aspartate shuttle (Ahn et al, 2020). This metabolic pathway functions as a conduit for electrons generated during glycolysis, facilitating their transfer from the cytosol to mitochondria for OXPHOS (Ahn et al, 2020). Malate dehydrogenase

catalyses the reversible conversion of malate to oxaloacetate, enabling NADH transfer from the cytoplasm to mitochondria (Ahn et al, 2020). Therefore, given its established role, disruption of malate dehydrogenase by ROSI critically impairs the malate-aspartate shuttle, leading to reduced NADH transfer to mitochondria and compromising OXPHOS. Furthermore, ROSI treatment induced a striking enrichment in the nitrogen metabolism pathway. Notably, the glutamate dehydrogenases (GLUD1), key enzymes converting glutamate to α-ketoglutarate (α-KG), exhibited significant downregulation (Craze et al, 2019). This resulted in a marked accumulation of glutamate, as confirmed via our analysis, and compromised aerobic energy output, as α-KG serves as a crucial intermediate in the TCA cycle.

Essential for normal cardiac function, long-chain fatty acids serve as the preferred energy source for the heart, enabling efficient ATP production through mitochondrial β-oxidation while simultaneously contributing to the structural integrity and function of cellular membranes by replenishing their lipid composition (Yamamoto & Sano, 2022). Our complementary analysis revealed a compelling downregulation of the fatty acid synthesis pathway, evidenced by the marked decrease in acyl-CoA synthetase long chain family member 1 (ACSL1) expression in both PGZ- and ROSI-treated cells. This significant ACSL1 downregulation, a key enzyme responsible for long-chain fatty acid activation and β-oxidation initiation (Roelands et al, 2019), aligns with the observed reduction in cellular fatty acid levels, including palmitic and stearic acids, following TZD treatment, which together shed light on potential impairment in fatty acid oxidation that underlined the observed changes in cellular energy metabolism following PGZ and ROSI treatment. The present data support the observations of Shekar et al., who reported increased degradation of proteins essential for mitochondrial fatty acid metabolism resulting in deficits in fatty acid oxidation in a Sprague Dawley rat model of transverse aortic constriction-induced moderate HF (Shekar et al, 2014).

Beyond directly impacting fatty acid synthesis and β-oxidation, TZDs orchestrate a broader metabolic reprogramming reverberating through amino acid metabolism pathways markedly linked to fatty acid oxidation. This multifaceted effect, revealed by our integrated pathway analysis, manifests as a significant downregulation of lysine degradation in cardiac cells. This combined pathway analysis unveils an accumulation of lysine and its precursor, L-α-aminoadipate, coupled with a significant suppression

of dihydrolipoamide dehydrogenase, a critical pyruvate dehydrogenase complex subunit vital for β-oxidation and pyruvate-to-acetyl-CoA conversion feeding the TCA cycle (Duarte et al, 2021). Additionally, consistent with the lysine degradation pathway, TZD treatment associates with depleted carnitine and its precursor, γ-butyrobetaine. Given carnitine's central role in transporting long-chain fatty acids into mitochondria for β-oxidation (carnitine shuttle), this reduced carnitine pool provides a novel mechanistic explanation for the observed perturbation in cardiac energetics following TZD administration, as we described in our previous paper/ Chapter 3 (Al Sultan et al, 2024b). While both medications elicited significant effects on branched-chain amino acid metabolism, our study additionally highlights pronounced modulations in the aromatic amino acid pool, particularly L-phenylalanine and L-tyrosine. Despite their marginal contribution as energy substrates, these observations echo prior reports linking such alterations to cardiac remodelling (Geng et al, 2020; Karwi & Lopaschuk, 2023). Nevertheless, the ability of these amino acid fingerprint changes to serve as early biomarkers for subclinical cardiac hypertrophy in the context of acute TZD administration remains elusive and necessitates further research.

TZD treatment of AC16 cells triggered a metabolic shift towards anaerobic glycolysis, orchestrated by the upregulation of key glycolytic enzymes and glucose transporters, such as aldolase A and lactate dehydrogenase A noted in TZD-treated cells. Additionally, overexpression of pyruvate dehydrogenase suggested a compensatory mechanism to decrease mitochondrial oxygen consumption and potentially suppress the TCA cycle. These observations collectively indicate TZD-induced cellular hypoxia, which, along with potential cardiac energy deficits, may drive the observed upregulation of purine metabolism in both drug-treated groups (Doigneaux et al, 2020). The altered expression of Inosine-5'-monophosphate dehydrogenase 1, a key enzyme in de novo guanine nucleotide synthesis (Liu et al, 2023), could explain elevated guanine metabolite levels. Furthermore, upregulation of the purine salvage pathway, as indicated by increased inosine and hypoxanthine, suggests a cellular response to mitigate energy deficits by recovering nucleotides from RNA and DNA degradation (Johnson et al, 2019). Finally, modulated expression of adenylate kinase 6, an enzyme involved in maintaining the nuclear adenine nucleotide pool (Deline et al, 2021), further supports the notion of increased cellular demand for nucleotides under hypoxic and glucose-deprived conditions. Notably, the aforementioned

observations regarding perturbations in mitochondrial energetics align with our previously reported *in vitro* cytotoxicity finding (Chapter 2) of a significant depletion in mitochondrial ATP upon TZD exposure, underscoring the consistency of these observations and highlighting the potential impact of TZDs on cellular energy production.

TZD-induced alterations in cardiomyocyte fatty acid synthesis, β-oxidation, and amino acid and purine metabolism, as previously described, further translate to modulations in cellular redox status, highlighting the multifaceted impact of TZD on energy metabolism. Our analysis revealed a disrupted glutathione (GSH) system upon TZD administration, evidenced by a significant decrease in GSH content. This depletion could potentially stem from elevated reactive oxygen species (ROS) generated due to TZD-induced mitochondrial damage. Further proteomic investigation of TZD-treated cells unveiled perturbations in GSH anabolism, contributing to the diminished intracellular GSH pool. Specifically, downregulation of key enzymes was observed: (i) glutathione synthetase, responsible for the rate-limiting step of GSH synthesis (Tan et al, 2023), and (ii) glutathione disulfide (GSSG) reduction-related enzymes, such as glutathione reductase and glucose-6-phosphate dehydrogenase, crucial for recycling oxidised glutathione (GSSG) back to GSH (Tan et al, 2023). These findings collectively suggest a TZD-induced imbalance in the cellular redox state, rendering AC16 cells more susceptible to ROS damage.

Building upon established biomarkers and leveraging the power of data-driven-based analysis, this study successfully identified key molecular signatures associated with TZD-induced cardiotoxicity across diverse omics datasets using the DIABLO model and the *tune.block.splsda* function. Prominent among these were signatures of amino acids such as L-ornithine, L-tyrosine, and glutamine, known HF biomarkers, further solidifying their potential utility in clinical settings (Geng et al, 2020; Karwi & Lopaschuk, 2023). Similarly, proteomic signatures revealed alterations in energy metabolism pathways (OXPHOS, pentose phosphate pathway, fatty acid synthesis) reflected by proteins such as Q16795, P52209, and P49327, respectively. Interestingly, ROSI datasets yielded distinct protein signatures enriched in energy metabolism (e.g. ATP synthase) but additionally highlighted disruption of protein synthesis machinery (P0DN37, P0DN26, Q9Y536), suggesting potential endoplasmic

reticulum stress and impaired protein export. Notably, these DIABLO-derived signatures align well with the observed metabolic shifts in AC16 cells upon TZD treatment. However, for their translation into clinically relevant prognostic tools for TZD cardiotoxicity and early detection of subclinical hypertrophy, rigorous validation and further investigation are warranted.

Biological data driven independently by metabolomics and proteomics analyses, including functional assay findings (chapter 2), as well as following integration of both datasets, is comprehensively presented in **Table 5.4**.

Table 5.4 Summary of functional assay observations, solo-omics findings and integrated insights

Biological Process	*In vitro* endpoint	Metabolome Level	Proteome Level	Integration Level
		A marked accumulation of fumarate	A marked downregulation of mitochondrial NAD(P)+-dependent malic enzyme (m-NAD(P)-ME).	A marked downregulation of mitochondrial NAD(P)+-dependent malic enzyme (m-NAD(P)-ME) coupled with a marked accumulation of fumarate suggests a disruption in the TCA cycle.
Disruption in pyruvate metabolism and TCA cycle	Significant ATP Depletion following TZD treatment, measured using the CellTiter-Glo® assay.	A marked accumulation of fumarate	A downregulation of fumarate hydratase	A downregulation of fumarate hydratase and a marked accumulation of fumarate reflect a disruption in the TCA cycle, leading to altered cellular metabolism.
		Marked accumulation of glutamate	A significant downregulation in glutamate dehydrogenases	A marked accumulation of glutamate coupled with a significant downregulation of glutamate dehydrogenases likely indicates a disruption in the conversion of glutamate to α-ketoglutarate, hence compromising an aerobic energy output.
Downregulation of the fatty acid synthesis pathway	Significant ATP Depletion following TZD treatment, measured using the CellTiter-Glo® assay.	Reduction in cellular fatty acid levels, including palmitic and stearic acids	Marked decrease in acyl-CoA synthetase long chain family member 1	The significant downregulation of ACSL1, a critical enzyme initiating long-chain fatty acid activation and β-oxidation, coupled with decreased levels of cellular fatty acids such as palmitic and stearic acid following TZD treatment, suggests a potential impairment in fatty acid oxidation underlying the observed alterations in cellular energy metabolism.

Disrupted glutathione (GSH) system	Induction of oxidative stress noted in AC16 cells following TZD treatment	Significant decrease in GSH content	Downregulation of key enzymes was observed: (i) glutathione synthetase, (ii) glutathione reductase and (iii) glucose-6-phosphate dehydrogenase	The findings suggest that TZD treatment induces oxidative stress by impairing the cell's antioxidant defence mechanisms.
Alteration in purine metabolism		Elevated guanine metabolite levels	Altered expression of Inosine-5'-monophosphate dehydrogenase	Elevated guanine metabolite levels in conjunction with altered expression of inosine-5'-monophosphate dehydrogenase (IMPDH) suggest potential increase in the de novo purine synthesis to meet energy demand.
		Increased levels of inosine and hypoxanthine	Modulated expression of adenylate kinase 6	The accumulation of inosine and hypoxanthine indicates an activation of the purine salvage pathway, reflecting a metabolic shift likely occurring as a compensatory response to cellular stress.

Reflecting on the key findings noted in **Table 5.4**, the synergy between toxicometabolomics and toxicoproteomics within a multi-omics approach offers significant advantages in elucidating the mechanisms of TZD cardiotoxicity, providing a more holistic understanding of biological systems. The added values of integrating these approaches can be summarised as follows:

(i) Toxicoproteomics and toxicometabolomics complement each other in understanding molecular changes. Proteomics analyses the proteins involved in cellular processes, while metabolomics examines the small molecules that are produced or consumed by these proteins. This combined approach allows for a connection between early protein-level events and downstream metabolic perturbations, linking molecular changes to functional outcomes. For instance, a decrease in a specific metabolite might correlate with the downregulation of an enzyme involved in its synthesis. This correlation not only clarifies the molecular interactions driving toxic responses but also helps in pinpointing key regulatory nodes affected by the drug. For example, in our analysis, a significant downregulation of glutamate dehydrogenases was coupled with a marked accumulation of glutamate likely indicates a disruption in the conversion of glutamate to α-ketoglutarate, hence compromising an aerobic energy output, as illustrated in **Table 5.4**. Similarly, our toxicoproteomics analysis demonstrated a downregulation of enzymes involved in initiating long-chain fatty acid activation and β-oxidation. Concurrently, toxicometabolomics findings revealed decreased levels of cellular fatty acids like palmitic and stearic acid following TZD treatment, reinforcing a disruption in energy production pathways.

(ii) Drugs can induce toxicity by disrupting various biochemical pathways. Proteomics offers insights into the enzymes and regulatory proteins affected by the drug, while metabolomics reveals the specific metabolic pathways impacted. Our toxicoproteomics analysis demonstrated a downregulation of enzymes involved in the glutathione (GSH) system. Concurrently, toxicometabolomics findings revealed decreased levels of cellular fatty acids like palmitic and stearic acid and a marked accumulation

of fumarate, suggesting a disruption in the TCA cycle following TZD treatment. These findings suggest a possible cross-link between two biological processes, energy production and oxidative stress, indicating a strong connection between TZD treatment and mitochondrial dysfunction. This combined approach provides a more comprehensive understanding of the multi-layered biochemical disruptions caused by the drug.

(iii) A multi-omics approach offers a comprehensive understanding of the temporal dynamics of toxicity, providing a detailed view of the progression of TZD-induced cardiotoxic effects. Our study suggests a potential metabolic shift from fatty acid oxidation towards anaerobic glycolysis in AC16 cells, observed at both the proteome and metabolome levels. This temporal mapping offers a more detailed understanding of how drug toxicity evolves over time, potentially contributing to the observed acute nature of cardiotoxicity and providing insights into critical windows for intervention.

(iv) Furthermore, this approach reveals adaptive or compensatory responses, distinguishing between protective mechanisms and toxic insults by correlating protein-level stress responses with functional metabolic outcomes. In our analysis, elevated guanine metabolite levels in conjunction with altered expression of inosine-5'-monophosphate dehydrogenase (IMPDH) suggest a potential increase in de novo purine synthesis to meet energy demand. Additionally, the accumulation of inosine and hypoxanthine indicates an activation of the purine salvage pathway, reflecting a metabolic shift likely occurring as a compensatory response to cellular stress.

(v) Lastly, the integration of toxicoproteomics and toxicometabolomics approaches not only elucidates the mechanisms of toxicity but also identifies key features implicated in each perturbed pathway. These features can be selected as early biomarkers, which can be used clinically for screening and progression monitoring. This can potentially improve the detection and management of adverse drug reactions, leading to safer and more effective drug development.

5.4.2 Limitations and Future Research Directions

While the present investigation has yielded valuable insights into our understanding of TZD cardiotoxicity, it is prudent to acknowledge several limitations before drawing definitive conclusions. Motivated by the National Research Council's (NRC) emphasis on minimising animal experimentation, this study embraced the growing trend of utilising *in vitro*-to-*in vivo* extrapolation methodologies in mechanistic toxicology research (Krewski et al, 2020). Accordingly, AC16 cells were chosen as a relevant cell model for investigation. Recognising the AC16 model's prominent position within the field of cardiac research and its inherent advantages in terms of growth rate and cost-efficiency relative to other models, this study employed this cell line for its investigations. Despite the strengths of the AC16 model, certain limitations warrant consideration. Namely, its dependence on glycolysis, fibroblast-like morphology, and potential for dedifferentiation, along with the complexities of maintaining differentiated cultures (Davidson et al, 2005), restricted our investigation to proliferative cells, as we previously described in chapters 3 and 4/ papers (Al Sultan et al, 2024a; b).

The present study utilises a multi-omics framework, integrating toxicoproteomics and toxicometabolomics analyses, to establish novel causal relationships spanning various molecular levels with unprecedented precision. This comprehensive approach offers significant advantages over single-omics analyses in elucidating the complex interplay between molecular alterations and phenotypic manifestations. However, inherent challenges associated with multi-omics studies, such as variations in technology sensitivity across different investigations and the lack of standardised protocols for sample preparation and data acquisition, can hinder the comparability and reproducibility of findings. Addressing these fundamental limitations is crucial to maximising the advancement and fruitful progress within omics research.

In conclusion, this study pioneers the integration of LC–MS-based toxicoproteomics and toxicometabolomics data to unravel the mechanistic underpinnings of TZD-induced cardiotoxicity. The network analysis of proteo-metabolomic data revealed a distinct fingerprint of perturbed biochemical pathways, primarily involving energy metabolism. Downregulation of OXPHOS and fatty acid synthesis was coupled with increased activity in glycolysis, the pentose phosphate pathway, and amino acid and purine metabolism, suggesting a potential metabolic shift in AC16 cells from fatty acid

oxidation towards anaerobic glycolysis, potentially contributing to cardiotoxicity. Additionally, the study identified a marked disruption in the GSH system, indicating an imbalanced redox state triggered by TZD administration. These findings collectively illuminate promising therapeutic targets, paving the way for future research to improve the safety profile of TZD agents.

Chapter 6. General Discussion and Closing Remarks

6.1 Connecting the Dots: A Holistic View of Chapter Insights

Type II diabetes mellitus (T2DM) represents a burgeoning global pandemic, currently afflicting nearly half a billion individuals (ADA, 2023), and this alarming escalation in T2DM prevalence, incidence and associated complications has imposed a significant financial strain on healthcare systems and a cumulatively negative impact on public health outcomes (ADA, 2023). Given the current limitations in understanding the full spectrum of the pathogenesis and progressive trajectory of T2DM, lifelong medication adherence remains the central cornerstone of comprehensive disease management. The achievement of ideal adherence to medication regimes necessitates a collaborative interplay among the fundamental pillars of efficacy, cost and safety/toxicity, into the latter of which this thesis delves deeply.

The past decade has witnessed remarkable progress in T2DM management with the introduction of new drug classes. However, a critical gap exists in our understanding of their safety profiles and the mechanisms underlying their adverse effects. Traditional mechanistic studies investigating these mechanisms for anti-diabetic drugs remain scarce in the literature. Despite the recent surge in single- and multi-omics investigations to understand T2DM pathogenesis (Gan et al, 2019; Kupai et al, 2022; Liu et al, 2022; Passaro et al, 2021; Tayanloo-Beik et al, 2021; Tiwari et al, 2023; Wang et al, 2021), the safety perspective of these new drugs remains underexplored, which exacerbates this gap. This is further evidenced by the few omics-based studies. Most of these studies were toxicogenomic in nature, primarily focused on identifying potential associations between genotypes and the adverse effects caused by oral antidiabetic drugs (Baye et al, 2021; Dawed et al, 2016).

In these studies, various SNPs in *SLC22A1*, *SLC29A4* and *SLC6A4*, which encode drug transporters and metabolising enzymes, were found to be associated with the GI intolerance attributed to metformin use (Baye et al, 2021; Dawed et al, 2019). These adverse effects were further shown to worsen with concomitant treatment with transporter-inhibiting drugs (Baye et al, 2021). Regarding sulfonylureas, *CYP2C9* genetic variants were associated with a higher risk of sulfonylurea-induced hypoglycaemia (Baye et al, 2021; Gökalp et al, 2011). Furthermore, the *CYP2C8*3* variant was associated with less weight gain in cases of rosiglitazone treatment (Baye et al, 2021; Dawed et al, 2019). The C allele of rs6123045 (an intronic SNP in

NFATC2) was markedly associated with a higher rate of rosiglitazone (ROSI)-induced oedema (Baye et al, 2021; Dawed et al, 2016).

To the best of our knowledge, no other omics-based studies have been conducted to assess the effect of genetic polymorphisms on the incidence of the adverse effects associated with other antidiabetic agents or to elucidate the mechanism of action of such adverse effects. This highlights a gap in omics-based investigations of the pharmacological landscape of T2DM, particularly regarding predicting and elucidating the potential mechanisms underlying drug toxicities.

Driven by the alarming rise in T2DM diagnoses globally and, particularly, in my own country of Kuwait, coupled with the need for cost-effective and safe medications, this research aims to embrace the power of omics-based technologies from a toxicological perspective. Recognising the limited application of omics in understanding drug toxicity, this study strives to bridge this gap by establishing an adverse outcome pathway (AOP) framework, the basis of which comprises two distinct disciplines: *in vitro* cytotoxicity testing and multi-omics strategies coupled with bioinformatics data modelling, with the ultimate aim of illuminating the potential molecular mechanisms responsible for drug-induced toxicities, initially focusing on a specific class of T2DM agents, namely thiazolidinediones (TZDs). TZDs represent a prime example of the dynamic interplay among efficacy, cost and safety within the clinical framework of medication management. Despite demonstrating an established efficacy in maintaining the glycaemic control and offering affordability, TZDs encounter limitations, primarily due to cardiotoxicity cases associated with their usage (ADA, 2023). The emergence of these case reports has profoundly reshaped the risk–benefit profile of these medications, leading to marked restrictions on their clinical use (Administration, 2010; 2012; De Flines & Scheen, 2007). Nonetheless, the exact mechanisms responsible for TZD-induced cardiotoxicity remain unravelled, impeding a holistic understanding of this complex interplay. Hence, by integrating our proposed AOP framework and delving into the implicated pathways leading to adverse effects, this research proposes therapeutic strategies that have the potential to improve pharmaceutical safety profiles, promoting patient protections and support and enabling the selection of cost-effective medications.

In Chapter 2, the first component of the AOP framework, traditional toxicity testing, was introduced. Guided by the National Research Council's emphasis on reducing animal experimentation (Yu et al, 2020), the cellular model for the *in vitro* toxicity testing of TZDs was developed. The model employed both human adult cardiomyocytes and human cardiac fibroblasts to enhance *in vitro–in vivo* translation, acknowledging the fact that the application of human cardiac cell lines to the study of TZD cardiotoxicity is limited. Recognising the extent of the assays encompassed within established traditional toxicity testing methodologies, our framework was directed towards the specific domain of mitochondrial assays, motivated by two distinct rationales, as follows. First, the well-documented evidence linking mitochondrial dysfunction to troglitazone, the oldest member of the TZD family, as an off-target organelle responsible for troglitazone-induced liver failure (Julie et al, 2008), prompted us to explore whether this phenomenon is drug-specific or observable among the entire TZD class. Second, a previous paper finding interestingly suggested mitochondrial dysfunction as a potential contributor to pioglitazone (PGZ) cardiotoxic effects (Zhong et al, 2018). These two factors were the determinants behind the workflow designated in Chapter 2, which comprises five mitochondrial assays, each of which carries a different endpoint: (MTT assay: implication of mitochondrial dehydrogenases; mitochondrial adenosine triphosphate [ATP] assay: measurement of OXPHOS; caspase 3/7 assay: activity of caspase 3/7 in cellular apoptosis; mitochondrial membrane potential [MMP]: reflection of membrane depolarisation [ΔΨm], electron transfer and OXPHOS; and ROS: measurement of oxidative stress). The key insights driven by this chapter can be summarised as follows:

- The concentration-response modelling of TZD agents against the developed cellular models demonstrated a concentration-dependent loss of cell viability with a high potency, reflected by the half-maximal inhibitory concentration (IC_{50}) measure.
- Treatment with TZDs resulted in a significant decline in ATP production in both human cardiomyocytes and fibroblasts. Notably, this reduction remained evident following the introduction of the PPAR-γ antagonist GW9662, implying the existence of PPAR-γ-independent mechanisms governing TZD-mediated perturbations in mitochondrial energy production.

- The decline in ATP production prompted the investigation of the MMP (ΔΨm), the key hallmark of the mitochondrial bioenergetic state. Notably, both cardiac cells displayed impaired ΔΨm upon TZD exposure. Acknowledging the prominent role of ΔΨm in ATP production, it has been postulated that TZD treatment induces mitochondrial uncoupling, potentially initiating a series of events stemming from the disruption of the proton motive force, a central driver of ΔΨm, ultimately culminating in compromised ATP production.
- Through the application of H_2DCFDA, a fluorescent dye sensitive to ROS, the effect of TZDs on ROS generation was investigated. Our results revealed the induction of oxidative stress in response to TZD exposure, suggesting a possible additional mechanism involved in TZD-induced cardiotoxicity.
- An investigation of cell death mechanisms through a caspase 3/7 activity assessment demonstrated a high degree of specificity to the modality of cell death, depending on the specific drug and cell line employed.

Collectively, this chapter underlines the anticipated class specificity of mitochondrial dysfunction and its prominent involvement in TZD cytotoxicity, with three distinct potential mechanisms implicated: disturbances in mitochondrial energetics, ΔΨm dysregulation and oxidative stress induction.

Capitalising on recent breakthroughs in omics technologies and the concomitant advancements in bioinformatics tools, single- and multi-omics studies were conducted, forming the second and principal component of our AOP framework.

In Chapter 3, an untargeted liquid chromatography–mass spectrometry (LC–MS)-based approach was introduced, followed by multivariate statistics. Owing to the progressive establishment of toxicometabolomics as a powerful tool in toxicological research over the past few decades (Olesti et al, 2021), this approach was adopted herein to (i) profile the biochemical pathways perturbed in TZD-treated AC16 human cardiomyocytes and (ii) identify biomarker candidates associated with such an effect that could serve as potential therapeutic targets for TZDs' undesirable effects.

The principal findings presented in this chapter can be summarised as follows:

- The acute administration of either TZD agent resulted in a significant modulation in carnitine content, reflecting a potential disruption to the mitochondrial carnitine shuttle and mitochondrial energetics.
- Over-expression was noted in purine metabolites, including inosine, hypoxanthine, adenosine and adenosine monophosphate/diphosphate (AMP/ADP), suggesting a modulation in purine metabolism accompanying TZD treatment.
- TZD treatment resulted in marked modulations in amino acids fingerprints, characterised by high levels of branched-chain amino acids (BCAAs), such as L-leucine, L-isoleucine and valine, which are well-established markers of cardiovascular disease (Xiong et al, 2022).
- Beyond the observed modulations in BCAAs, alterations in L-tyrosine and γ-aminobutyric acid were identified, evidently established as early biomarkers of cardiac hypertrophy (Zhao et al, 2023). These observations imply the potential of TZD-induced cardiac tissue remodelling, another hallmark of cardiotoxicity.

In summary, the findings in Chapter 3 shed light on the alterations in biochemical pathways primarily attributed to cardiac energetics. Furthermore, the profiling of the AC16 metabolome in response to TZD revealed characteristic features of cardiac hypertrophy, suggesting the potential discovery of early biomarkers of TZD-related cardiotoxic effects.

Proceeding with the single-omics based approach, a novel microflow LC–MS-based toxicoproteomics pipeline (Chapter 4) was implemented to characterise comprehensively the protein-level molecular alterations and profile the perturbed pathways triggered by TZD exposure.

As such, the central findings presented in this chapter can be summarised as follows:

- The in-depth differential and weighted correlation network analyses showed that the cardiotoxicity of TZDs primarily stemmed from mitochondrial OXPHOS impairment, with distinct signalling mechanisms observed for PGZ and ROSI.
- The type of cell death was also found related to the mitochondria—protein upregulation in the PGAM5–Drp1 axis, as noted in PGZ-treated cells,

suggested mitochondrial-mediated necroptosis. However, caspase-mediated apoptosis was the distinct form of cell death characterising ROSI-treated cells.

- Our toxicoproteomics findings revealed additional mechanistic aspects of cardiotoxicity; however, these findings highlight drug specificity, as follows:
    - Both dysregulation and regulation in cardiomyocyte contractility were noted in the ROSI-treated cells, with potential mechanisms related to perturbation in mitochondrial complex expressions (MT-CO1 and UQCRC1) and cardiac sodium pump (Na^+/K^+ ATPase) function, impeding cytosolic calcium homeostasis.
    - Impairments in protein homeostasis, or proteostasis, were detected in ROSI-treated cells, potentially contributing to defects in protein maturation, the accumulation of unfolded or misfolded proteins and disruption of endoplasmic reticulum homeostasis.
    - A disruption in the cytoskeletal architecture, primarily driven by integrin-signalling pathways (namely the talin–vinculin axis and the Rho/ROCK pathway), was noted in PGZ-treated cells, suggesting a potential mechanism implicated in myocardial contractile failure.
    - An investigation of PGZ-treated cells demonstrated a synergistic interplay between the complement and coagulation systems, manifested by an upregulation of proteins involved in immunothrombosis. This observation proposes a potential mechanism for the cardiotoxic effects of PGZ.

In summary, insightful data were extracted from the toxicoproteomics approach, further solidifying the implication of mitochondrial dysfunction as the primary off-target organelle that characterised TZD cytotoxicity. While focusing on alterations in cardiac energetics, the analyses additionally revealed previously unknown, drug-specific mitochondrial-independent contributions to TZD cardiotoxicity, enriching our understanding of TZD's adverse effects.

To elucidate comprehensively the underlying mechanisms of TZD's cardiotoxicity and to explore the multifaceted interactions among diverse molecular levels, a multi-omics integration approach was employed, transitioning the investigative paradigm from associative to causative. In the multi-omics integration chapter (Chapter 5), a

combined data- and knowledge-driven analysis of co-acquired toxicometabolomics and toxicoproteomics data from the same biological AC16 samples was performed.

The key findings extracted from the integrative approach can be summarised as follows:

- The investigation of intra-omics heterogeneity within the sample groups revealed a clear separation at each investigated molecular layer.
- An evaluation of the inter-omics heterogeneity demonstrated a similar pattern of distinct separation between the control and TZD-treated cells, reflecting differentiable molecular profiles among sample groups.
- The interrogation of the correlation between the toxicoproteomics and toxicometabolomics datasets revealed a robust positive association, implying internal coherence within the DIABLO model and supporting its applicability for further exploration.
- The joint pathway analysis revealed alterations in the metabolic fate of AC16 cells triggered by TZD exposure, with changes evident at both the metabolite and protein expression levels.
- The joint analysis findings strongly re-enforced the marked switch in AC16 metabolic fate, manifested as a metabolic shift from fatty acid oxidation towards anaerobic glycolysis, potentially contributing to cardiotoxicity progression.
- An analysis of TZD-treated cells revealed a substantial downregulation of the fatty acid synthesis pathway, manifested by a marked decrease in the ACSL1 expression. This finding aligns with the observed reduction in cellular fatty acid levels, most notably palmitic acid and stearic acid, suggesting the potential impairment of fatty acid oxidation and contributing to the altered cellular energy metabolism observed upon PGZ and ROSI treatment.
- An investigation of TZD-treated cells revealed alterations in amino acid metabolism, specifically the marked downregulation in lysine degradation, known to be linked to fatty acid oxidation, suggesting an additional mechanism is implicated in TZD-induced perturbation in fatty acid oxidation. Through the combined pathway analysis, the study unveiled an accumulation of lysine and its precursor, L-α-aminoadipate, coupled with the significant suppression of dihydrolipoamide dehydrogenase, a critical pyruvate dehydrogenase complex

subunit vital for β-oxidation and pyruvate-to-acetyl-CoA conversion, feeding the TCA cycle (Duarte et al, 2021) and suggesting a collectively marked downregulation in lysine degradation, potentially contributing to the observed disruptions in fatty acid oxidation.

- The integrated analysis shed light on potential mechanisms contributing to the increased purine metabolism detected in the toxicometabolomics data. Proteomic profiling revealed the activation of a hypoxia-related pathway, a well-established inducer of purine metabolism (Doigneaux et al, 2020). Moreover, the altered expression of Inosine-5'-monophosphate dehydrogenase 1, a key enzyme in de novo guanine nucleotide synthesis (Liu et al, 2023), provides a potential explanation for the observed elevation in guanine metabolite levels in TZD-treated cells. Lastly, the perturbed expression of adenylate kinase 6, an enzyme crucial to maintaining the nuclear adenine nucleotide pool (Deline et al, 2021), further supports the hypothesis of an increased cellular demand among nucleotides under the conditions of hypoxia and glucose deprivation.
- Our comprehensive analysis highlighted the induction of oxidative stress, triggered upon TZD exposure, and it also revealed a disrupted glutathione (GSH) system upon TZD administration, evidenced by a significant decrease in GSH content. This disruption is explained to be secondary for elevated reactive oxygen species (ROS), generated due to TZD-induced mitochondrial damage or perturbations in GSH anabolism and characterised by the downregulation of crucial enzymes, including glutathione synthetase and glucose-6-phosphate dehydrogenase, contributing to the diminished intracellular GSH pool.
- Capitalising on the power of the DIABLO model in extracting potential biomarkers from diverse omics datasets, the data-driven analysis identified amino acids, including L-ornithine, L-tyrosine and glutamine, known HF biomarkers (Xiong et al, 2022; Zhao et al, 2023), as candidate biomarkers, opening novel avenues for profiling TZD cardiotoxicity progression.

In summary, the integration of multi-omics datasets yielded valuable insights into the molecular mechanisms underlying the key findings previously observed in single-omics analyses, thereby enriching our understanding of the potential molecular pathways involved in TZD-induced cardiotoxicity. Furthermore, the integration model

revealed key molecular signatures across omics datasets, potentially serving as valuable biomarkers for the early detection of TZD-induced cardiotoxicity.

6.2 Unveiling the Horizon: Directions for Continued Research

Considering the progressive nature of TZD-induced cardiotoxicity, that is transitioning from an acute to a potential chronic phase, a comprehensive understanding of each pathophysiological stage is crucial. While acknowledging the limitations of research timeframes and initial laboratory access restrictions due to the COVID-19 pandemic, this thesis aimed to develop a reproducible framework, incorporating analytical tools designed to expedite the acquisition of key insights into the molecular mechanisms governing the acute stage of cardiotoxicity and striving to identify early biomarkers for predicting the onset and progression of this adverse effect.

Extending the present investigation, our future research plans will prioritise further clarification of the aetiological underpinnings of the acute manifestation of TZD-induced cardiotoxicity. Following the successful elucidation of key molecular mechanisms underlying TZD-mediated cardiotoxicity through a comprehensive combination of *in vitro* cytotoxicity testing and omics-based analyses, coupled with the identification of potential early-stage biomarkers, the next crucial step is validation of the observed molecular perturbations. This validation will be crucial to translating these findings into clinically actionable prognostic biomarkers and therapeutic targets for mitigating TZD-associated side effects. Therapeutic targets identified in this study require additional validation and are as follows:

6.2.1 Uncovering New Therapeutic Opportunities: The Path to Validation

6.2.1.1 Mitophagy: A New Potential Target for Preventing TZD-Induced HF

Expanding upon the *in vitro* findings, our analyses revealed an upregulation of oxidative stress and a decline in MMP following TZD treatment. These molecular alterations are recognised as potent inducers of PINK1/Parkin-mediated mitophagy (Lee et al, 2017). Mitophagy is indispensable for maintaining cardiac health (Wang et al, 2023). Given the heart's heavy reliance on mitochondrial function, the timely removal of damaged mitochondria through this process is crucial. HF is often characterised by impaired mitophagy, resulting in the accumulation of dysfunctional mitochondria (Onishi et al, 2021; Wang et al, 2023). Inefficient mitophagy in clearing

these damaged organelles can precipitate cardiomyocyte apoptosis and ultimately, HF (Onishi et al, 2021; Wang et al, 2023). At the molecular level and under stress, the mitochondrial protease OMA1 cleaves Opa1 into a short form, inhibiting mitochondrial fusion and promoting fragmentation, culminating in necrotic cell death, fibrosis, and ventricular remodeling (Wai et al, 2015). Interestingly, Wang et al. reported that AMPKα2-mediated phosphorylation of PINK1 activates the PINK1-Parkin pathway, enhancing mitophagy and safeguarding myocardial cells from stress-induced damage, thereby mitigating HF progression (Wang et al, 2018). Therefore, assessing the expression of the mitophagy pathway is crucial as it represents a potential therapeutic target for TZD-induced cardiotoxicity. Our future research will characterise the mRNA and protein expression levels of PINK1 and Parkin using RT-qPCR and Western blotting, respectively, to evaluate their potential involvement in this condition.

6.2.1.2 **Necroptosis: A Novel Pathway in TZD-Induced Cardiotoxicity**

Diverse forms of heart disease, including MI, HF, cardiomyopathies, and myocarditis, involve multiple cell death pathways. Recent research highlights the significant contribution of necroptosis to the pathogenesis of major cardiac events like HF (Guo et al, 2022). Key necroptotic mediators, including RIPK1, RIPK3, and MLKL, and their phosphorylated forms, exhibited elevated levels in failing human hearts compared to healthy controls (Guo et al, 2022). A parallel increase in these proteins was observed in mice subjected to transverse aortic constriction (TAC) (Marunouchi et al, 2021). Notably, the administration of Hsp90 inhibitor 17-AAG reversed the upregulation of RIPK1, RIPK3, and MLKL following TAC (Marunouchi et al, 2021). Furthermore, doxorubicin, a chemotherapeutic agent, induces cardiomyopathy in approximately 10% of patients (Zhang et al, 2016). Although the underlying mechanisms remain elusive, multiple cell death pathways, including necroptosis, have been implicated (Zhang et al, 2016). RIPK3 upregulation in cardiomyocytes following doxorubicin treatment was reported supporting the involvement of necroptosis (Zhang et al, 2016). Of importance, global deletion of RIPK3 mitigated doxorubicin-induced cardiac dysfunction, further confirming this pathway's role (Zhang et al, 2016). Given the consistency between the current findings and previous research implicating RIPK3 in doxorubicin-induced cardiomyopathy, further investigation into RIPK3's role in TZD-induced cardiac dysfunction is warranted. To this end, an *in vivo* model utilising adult

RIPK3 knockout and wild-type C57BL/6 mice will be developed to examine RIPK3's involvement in TZD-induced necroptosis and HF.

6.2.1.3 Mitochondrial Dysfunction in TZD Therapy: Drug-Specific or Class-Wide Phenomenon?

Results presented herein reinforce the established link between TZDs and mitochondrial dysfunction, consistent with previous findings on troglitazone and the prototypical compound of TZD class ciglitazone (Julie et al, 2008). This suggests a strong potential interaction between the TZD core structure and mitochondrial proteins. To explore this further, *in silico* docking studies using GOLD software, as described by (Zhong et al, 2018), will be conducted. To elucidate potential binding partners, mitochondrial proteins identified in our analysis will be subjected to docking simulations with both TZD agents to identify the specific pharmacophore responsible for the toxic effect. Proteins with the highest docking scores will undergo further investigation to assess their biological significance (i.e., map the protein against our KEGG pathway analysis) and Western blotting to validate protein expression. Subsequently, structure-activity relationship (SAR) studies will be performed by docking drug analogs to understand how structural modifications influence binding affinity and toxicity. Ultimately, these findings will inform the design of modified drug structures with reduced affinity for the toxic target protein while preserving therapeutic efficacy.

6.2.2 AC16 and Beyond: Advancing Model Capabilities

6.2.2.1 The Transition from Proliferative to Differentiated state

The current study primarily employed an *in vitro* model utilizing proliferative human cardiac cells. Given the substantial alterations in gene expression, cellular architecture, and function associated with the transition from a proliferative to a differentiated cardiomyocyte state, which significantly influence cardiac physiology and development, future research will be directed towards re-evaluating these findings using differentiated cell models. Human induced pluripotent stem cell-derived cardiomyocytes (iPSC-cardiomyocytes) currently represent one of the most advanced and well-characterised model systems (Burnett et al, 2021). The accessibility of high-quality iPSC- cardiomyocytes encourages its application in toxicological research

(Burnett et al, 2021). Future research will focus on investigating TZD cardiotoxicity using iPSC-differentiated cardiomyocytes. To further elucidate the complex effects of TZDs, a co-culture system incorporating these cells with other cardiac cell types, such as fibroblasts, will be developed (Giacomelli et al, 2020; Groen et al, 2024). This approach will enable the examination of cell-cell interactions following TZD administration and facilitate a more comprehensive assessment of toxicological impacts in a more integrated system.

6.2.2.2 **Expanding the Cellular Landscape: Beyond Heart Cells**

To unravel comprehensively the complexity of TZD-induced cardiotoxicity, a systematic evaluation of their cytotoxic effects on diverse cell lines, including kidney, liver and brain cells, is imperative. Such a multi-organ approach holds the potential to reveal the multifaceted nature of TZD action and uncover crosstalk mechanisms between different organ systems contributing to TZD's adverse effect. This multi-organ cytotoxicity evaluation is designated as a key component of our future research agenda, aiming to provide a more holistic understanding of TZD-induced adverse effects and to identify potential therapeutic targets.

6.2.3 **Omics to Outcomes: A Path to Targeted Approaches**

Building upon the untargeted omics analysis conducted on the AC16 model, the subsequent phase will employ targeted omics approaches. A targeted metabolomics strategy, centered on characteristic features identified in the untargeted study, will be implemented to precisely quantify and track metabolite fluctuations in response to TZD exposure. This focused approach will facilitate a more in-depth examination of specific metabolic pathways or processes, mitigating the complexity inherent to untargeted analyses and enhancing reproducibility and reliability through the prioritisation of predefined metabolites. Furthermore, to investigate the metabolism of TZDs and assess their toxicological potential, a comprehensive *in vitro* model utilising liver microsomes will be employed. This model aims to characterise the biotransformation products of TZDs by exposing them to liver microsomes, which replicate the enzymatic environment of the endoplasmic reticulum involved in drug metabolism (Sun et al, 2024). Following incubation, the metabolites will be analysed using advanced analytical techniques such as mass spectrometry to identify and quantify biotransformation products. To further evaluate the potential toxicity of these

metabolites, functional assays similar to those described in Chapter 2 will be utilised. These assays will include cellular viability tests, oxidative stress assessments, and assays for apoptosis and necrosis. This approach will provide a detailed understanding of the metabolic pathways of TZDs and their potential toxic effects, offering insights into their safety profiles and mechanisms of toxicity.

At the proteome level, following the successful implementation of a label-free approach, the next step is to transition towards a targeted approach. Given the suggestive role of OXPHOS in thiazolidinedione (TZD) cardiotoxicity, the targeted approach will be designed to specifically investigate the proteins involved in this pathway. This will involve quantifying key components of the OXPHOS machinery to better understand their alterations in response to TZD exposure, thereby providing more detailed insights into the mechanistic underpinnings of TZD-induced cardiotoxicity. To achieve this objective, a recently applied method by (Imami et al, 2023) will be utilised to uncover the comprehensive picture of (post-)translational regulation of both mitochondrial- and nuclear-encoded subunits of OXPHOS complexes. This approach involves an MS-based proteomic technique that integrates biochemical isolation of mitochondria with pulse stable isotope labeling by amino acids in cell culture (pSILAC). pSILAC, an advanced variation of the standard SILAC technique, is specifically designed to measure the rate of protein synthesis rather than merely comparing protein abundance across different samples (Imami et al, 2023). By combining pSILAC with mitochondrial isolation, this method will enable the quantification of mitochondrial-encoded proteins and facilitate the monitoring of mitochondrial translation. This will provide insights into how OXPHOS is perturbed following exposure to TZDs, thereby elucidating the mechanisms underlying TZD-induced cardiotoxicity.

The integrated analysis of toxicometabolomics and toxicoproteomics provided a comprehensive understanding of the observed effects identified in individual omics studies, deepening insights into TZD-induced cardiotoxicity. Given the established correlation between the proteome and genome, incorporating transcriptomics into the analysis is expected to enhance data flow and provide a more holistic perspective on the underlying mechanisms of TZD cardiotoxicity. Single-cell RNA sequencing (scRNA-seq) represents a transformative advancement in toxicology, enabling

unprecedented insights into cellular heterogeneity and the molecular basis of toxicity (Kim & Cho, 2023). By profiling gene expression at the individual cell level, rather than relying on bulk tissue analysis, scRNA-seq unveils the diverse cellular responses within a tissue, providing a more comprehensive understanding of toxicological effects. The primary objectives of employing single-cell transcriptomics are to enhance spatial resolution and contextual understanding of gene expression within tissue architecture, as well as to investigate the impact of cellular interactions on toxicity (Kim & Cho, 2023). Furthermore, integrating single-cell transcriptomics with existing toxicoproteomics and toxicometabolomics approaches will provide a more comprehensive overview of cellular responses to TZDs, facilitating a deeper understanding of intricate biological processes and interactions.

6.3 **Concluding Remarks**

The concluding remarks of this thesis highlight the development of a putative AOP framework devised to elucidate the molecular mechanisms driving the manifestation of TZD-induced cardiotoxicity. Given the growing body of literature on drug-induced cardiotoxicity, such as those related to doxorubicin (Geng et al, 2020) and cyclophosphamide (Dionísio et al, 2022), the current AOP can be integrated with existing models to construct a more comprehensive AOP network. AOP networks offer several advantages. They provide a comprehensive overview of interconnected molecular mechanisms and biological pathways, revealing how diverse mechanisms converge to produce similar adverse outcomes. Additionally, AOP networks capture intricate interactions between pathways and endpoints, facilitating the identification of how different stressors or chemicals impact multiple pathways simultaneously. This holistic approach enhances predictive toxicity assessment by enabling extrapolation across species and chemicals with similar mechanisms, even in the absence of direct data. Ultimately, AOP networks contribute to more informed regulatory decisions by providing a structured framework for integrating diverse evidence, thereby enhancing assessment transparency and reliability.

The findings of our framework collectively shed light onto novel molecular mechanisms, potentially resolving decades-old contradictory data surrounding TZD agents. Key molecular targets identified include impaired OXPHOS, carnitine shuttle dysfunction, and multiple cell death pathways. Potential interventions include carnitine

supplementation, as employed in valproic acid therapy (Okumura et al, 2021), or drug redesign to inhibit interactions with deleterious protein targets. These strategies aim to mitigate TZD toxicity, thereby re-establishing their viability as a first-line treatment for T2DM. The affordability and convenience of oral TZD administration are particularly advantageous for middle- and low-income populations, such as those in the MENA region with high T2DM prevalence (Khalil et al, 2024). Improved glycemic control, delayed disease progression, reduced micro- and macrovascular complications, and enhanced patient productivity are anticipated outcomes, ultimately alleviating the substantial healthcare burden associated with T2DM and its complications.

Lastly, this research highlights the transformative power of integrating traditional and omics-based methodologies, and its comprehensive approach expedites the acquisition of toxicology-driven insights, offering renewed hope for revisiting the safety of long-forgotten medications and forging a crucial pathway towards safer medications and improved patient compliance.

7 Appendices

7.1 Supplementary Table for Chapter 2

Table S1. Summary of utilized assays and their operational principles.

Assay Name	Cell-Based Assay Mechanism	Reference
MTT	The MTT colorimetric method relies on the reduction of a yellow tetrazolium salt, referred as MTT (3-(4,5-dimethylthiazol-2-yl)-2,5-diphenyltetrazolium bromide), to form purple formazan crystals by metabolically active cells. These viable cells contain NAD(P)H-dependent oxidoreductase enzymes that facilitate the reduction of MTT to formazan. Subsequently, the insoluble formazan crystals are dissolved using a solubilization solution, and the resulting colored solution's absorbance is measured at 500-600 nanometers using a multi-well spectrophotometer.	(Ghasemi et al, 2023)
Caspase-Glo 3/7	The Caspase-Glo 3/7 assay consists of a proluminescent caspase-3/7 DEVD-aminoluciferin substrate and a proprietary thermostable luciferase within a reagent designed to optimize caspase-3/7 activity, luciferase activity, and cell lysis. Upon adding the single Caspase-Glo 3/7 reagent in an "add-mix-measure" format, the cells undergo lysis, leading to caspase cleavage of the substrate. This process releases free aminoluciferin, which is then consumed by the luciferase, producing a luminescent signal proportional to caspase-3/7 activity.	(Niles et al, 2008)
CellTiter-Glo	The CellTiter-Glo luminescent cell viability assay relies on luciferase to measure the amount of ATP present in metabolically active cells. Upon addition to the cell culture, the CellTiter-Glo reagent performs three key functions: lysing cells to release ATP, inhibiting endogenous ATPases to prevent ATP degradation, and providing the necessary luciferin and luciferase for an ATP-dependent luminescent signal. The intensity of the light output directly correlates with the number of viable cells.	(Hannah et al, 2001)
JC-1	This assay utilizes the JC-1 dye, a membrane-permeant fluorescent probe commonly employed in apoptosis investigations for assessing mitochondrial health. JC-1 dye accumulates in mitochondria in a potential-dependent manner, initially emitting a green fluorescence at approximately 529 nm for its monomeric form. As the dye concentration increases, it transitions to a red fluorescence at around 590 nm, indicative of the formation of red fluorescent J-aggregates. Thus, mitochondrial depolarization is characterised by a reduction in the ratio of red to green fluorescence intensity.	(Sivandzade et al, 2019)
H_2DCFDA	This assay relies on the cell-permeant compound 2',7'-dichlorodihydrofluorescein diacetate (H_2DCFDA), also known as dichlorofluorescein diacetate, which serves as a chemically reduced form of fluorescein and functions as an indicator for reactive oxygen species (ROS) within cells. Upon intracellular esterase cleavage of the acetate groups and subsequent oxidation, the initially nonfluorescent H_2DCFDA is converted into the highly fluorescent 2',7'-dichlorofluorescein (DCF).	(Wu & Yotnda, 2011)

References

Ghasemi, M., Liang, S., Luu, Q. M. & Kempson, I. (2023) The MTT Assay: A Method for Error Minimization and Interpretation in Measuring Cytotoxicity and Estimating Cell Viability, *Cell Viability Assays: Methods and Protocols*Springer, 15-33.

Hannah, R., Beck, M., Moravec, R. & Riss, T. (2001) CellTiter-Glo™ Luminescent cell viability assay: a sensitive and rapid method for determining cell viability. *Promega Cell Notes*, 2(11).

Niles, A. L., Moravec, R. A. & Riss, T. L. (2008) Caspase activity assays. *Apoptosis and Cancer: Methods and Protocols*, 137-150.

Sivandzade, F., Bhalerao, A. & Cucullo, L. (2019) Analysis of the mitochondrial membrane potential using the cationic JC-1 dye as a sensitive fluorescent probe. *Bio-protocol*, 9(1), e3128-e3128.

Wu, D. & Yotnda, P. (2011) Production and detection of reactive oxygen species (ROS) in cancers. *JoVE (Journal of Visualized Experiments)*(57), e3357.

7.2 Supplementary Tables for Chapter 3

Table S2. Findings of metabolite set enrichment analysis on characteristic features identified in the PGZ study.

Pathway Term	Total	Expected	Hits	Raw *p*	Holm *p*	FDR
Spermidine and Spermine Biosynthesis	18	0.251	3	0.00157	0.154	0.154
Urea Cycle	28	0.391	3	0.00579	0.562	0.228
Glycine and Serine Metabolism	59	0.824	4	0.00697	0.669	0.228
Beta Oxidation of Very Long Chain Fatty Acids	17	0.238	2	0.0219	1	0.401
Alanine Metabolism	17	0.238	2	0.0219	1	0.401
Glutathione Metabolism	20	0.279	2	0.0298	1	0.401
Arginine and Proline Metabolism	52	0.727	3	0.032	1	0.401
Pantothenate and CoA Biosynthesis	21	0.293	2	0.0327	1	0.401
Oxidation of Branched Chain Fatty Acids	26	0.363	2	0.0487	1	0.448
Phenylalanine and Tyrosine Metabolism	27	0.377	2	0.0521	1	0.448
Selenoamino Acid Metabolism	27	0.377	2	0.0521	1	0.448
Methylhistidine Metabolism	4	0.0559	1	0.0548	1	0.448
Ammonia Recycling	31	0.433	2	0.0669	1	0.504
Beta-Alanine Metabolism	34	0.475	2	0.0788	1	0.552
Propanoate Metabolism	42	0.587	2	0.114	1	0.65
Histidine Metabolism	42	0.587	2	0.114	1	0.65
Thiamine Metabolism	9	0.126	1	0.119	1	0.65
Lactose Degradation	9	0.126	1	0.119	1	0.65
Glutamate Metabolism	48	0.671	2	0.142	1	0.706
Trehalose Degradation	11	0.154	1	0.144	1	0.706
Phosphatidylethanolamine Biosynthesis	12	0.168	1	0.156	1	0.709
Glucose-Alanine Cycle	13	0.182	1	0.168	1	0.709
Thyroid hormone synthesis	13	0.182	1	0.168	1	0.709
Phosphatidylcholine Biosynthesis	14	0.196	1	0.18	1	0.709
Valine, Leucine and Isoleucine Degradation	59	0.824	2	0.197	1	0.709
Phosphatidylinositol Phosphate Metabolism	17	0.238	1	0.214	1	0.709
Mitochondrial Electron Transport Chain	19	0.265	1	0.236	1	0.709
Lactose Synthesis	19	0.265	1	0.236	1	0.709
Nucleotide Sugars Metabolism	20	0.279	1	0.247	1	0.709
Catecholamine Biosynthesis	20	0.279	1	0.247	1	0.709
Riboflavin Metabolism	20	0.279	1	0.247	1	0.709
Threonine and 2-Oxobutanoate Degradation	20	0.279	1	0.247	1	0.709
Tyrosine Metabolism	70	0.978	2	0.255	1	0.709
Sulfate/Sulfite Metabolism	22	0.307	1	0.269	1	0.709

Carnitine Synthesis	22	0.307	1	0.269	1	0.709
Transfer of Acetyl Groups into Mitochondria	22	0.307	1	0.269	1	0.709
Purine Metabolism	73	1.02	2	0.272	1	0.709
Glycolysis	23	0.321	1	0.279	1	0.709
Inositol Phosphate Metabolism	24	0.335	1	0.289	1	0.709
Glycerolipid Metabolism	25	0.349	1	0.3	1	0.709
Cysteine Metabolism	26	0.363	1	0.31	1	0.709
Phytanic Acid Peroxisomal Oxidation	26	0.363	1	0.31	1	0.709
Mitochondrial Beta-Oxidation of Short Chain Saturated Fatty Acids	27	0.377	1	0.32	1	0.709
Mitochondrial Beta-Oxidation of Long Chain Saturated Fatty Acids	28	0.391	1	0.329	1	0.709
Pentose Phosphate Pathway	29	0.405	1	0.339	1	0.709
Folate Metabolism	29	0.405	1	0.339	1	0.709
Inositol Metabolism	30	0.419	1	0.348	1	0.709
Starch and Sucrose Metabolism	31	0.433	1	0.358	1	0.709
Fructose and Mannose Degradation	31	0.433	1	0.358	1	0.709
Citric Acid Cycle	32	0.447	1	0.367	1	0.709
Amino Sugar Metabolism	33	0.461	1	0.376	1	0.709
Gluconeogenesis	33	0.461	1	0.376	1	0.709
Nicotinate and Nicotinamide Metabolism	35	0.489	1	0.394	1	0.729
Galactose Metabolism	38	0.531	1	0.42	1	0.762
Sphingolipid Metabolism	40	0.559	1	0.437	1	0.778
Methionine Metabolism	42	0.587	1	0.453	1	0.793
Fatty acid Metabolism	43	0.601	1	0.461	1	0.793
Pyruvate Metabolism	47	0.657	1	0.492	1	0.829
Steroid Biosynthesis	48	0.671	1	0.499	1	0.829
Pyrimidine Metabolism	57	0.796	1	0.562	1	0.903
Warburg Effect	57	0.796	1	0.562	1	0.903
Tryptophan Metabolism	59	0.824	1	0.575	1	0.909
Bile Acid Biosynthesis	65	0.908	1	0.611	1	0.951

Table S3. Findings of pathway enrichment analysis on characteristic features identified in the PGZ study.

Pathway Term	Total	Expected	Hits	Raw *p*	Enrichment	Holm adjust	FDR	Impact
Arginine and proline metabolism	36	0.32	4	0.0001959	3.708	0.015672	0.015672	0.25465
Phenylalanine, tyrosine and tryptophan biosynthesis	4	0.035556	2	0.000436	3.3605	0.034446	0.017441	1
beta-Alanine metabolism	21	0.18667	3	0.0006774	3.1691	0.052844	0.018066	0.05597
Glutathione metabolism	28	0.24889	3	0.0016082	2.7937	0.12383	0.031899	0.00719
Phenylalanine metabolism	8	0.071111	2	0.0019937	2.7003	0.15152	0.031899	0.35714
Pantothenate and CoA biosynthesis	20	0.17778	2	0.012727	1.8953	0.95455	0.1697	0.0068
Valine, leucine and isoleucine biosynthesis	8	0.071111	1	0.069087	1.1606	1	0.78956	0
Arginine biosynthesis	14	0.12444	1	0.11796	0.92825	1	1	0.06091
Purine metabolism	70	0.62222	2	0.12564	0.90086	1	1	0.03301
Histidine metabolism	16	0.14222	1	0.13372	0.87381	1	1	0.22131
Ubiquinone and other terpenoid-quinone biosynthesis	18	0.16	1	0.14921	0.82619	1	1	0
Selenocompound metabolism	20	0.17778	1	0.16445	0.78397	1	1	0
Alanine, aspartate and glutamate metabolism	28	0.24889	1	0.22289	0.6519	1	1	0
Lysine degradation	30	0.26667	1	0.2369	0.62543	1	1	0
Glycine, serine and threonine metabolism	33	0.29333	1	0.25747	0.58927	1	1	0
Biosynthesis of unsaturated fatty acids	36	0.32	1	0.27753	0.5567	1	1	0
Valine, leucine and isoleucine degradation	40	0.35556	1	0.30348	0.51787	1	1	0
Tyrosine metabolism	42	0.37333	1	0.31613	0.50013	1	1	0.13972

Table S4. Findings of metabolite set enrichment analysis on characteristic features identified in the ROSI study.

Pathway Term	Total	Expected	Hits	Raw *p*	Holm *p*	FDR
Betaine Metabolism	21	0.923	4	0.0113	1	1
Methionine Metabolism	43	1.89	5	0.036	1	1
Spermidine and Spermine Biosynthesis	18	0.791	3	0.0408	1	1
Carnitine Synthesis	22	0.967	3	0.0681	1	1
D-Arginine and D-Ornithine Metabolism	11	0.483	2	0.0807	1	1
Glycerolipid Metabolism	25	1.1	3	0.0928	1	1
Phosphatidylethanolamine Biosynthesis	12	0.527	2	0.0942	1	1
Purine Metabolism	74	3.25	6	0.0989	1	1
Oxidation of Branched Chain Fatty Acids	26	1.14	3	0.102	1	1
Glycine and Serine Metabolism	59	2.59	5	0.111	1	1
Phosphatidylcholine Biosynthesis	14	0.615	2	0.123	1	1
Methylhistidine Metabolism	4	0.176	1	0.165	1	1
Beta Oxidation of Very Long Chain Fatty Acids	17	0.747	2	0.169	1	1
Arginine and Proline Metabolism	53	2.33	4	0.199	1	1
Mitochondrial Electron Transport Chain	19	0.835	2	0.202	1	1
Catecholamine Biosynthesis	20	0.879	2	0.218	1	1
Glutathione Metabolism	21	0.923	2	0.235	1	1
Biotin Metabolism	8	0.352	1	0.303	1	1
Thiamine Metabolism	9	0.396	1	0.334	1	1
Lactose Degradation	9	0.396	1	0.334	1	1
De Novo Triacylglycerol Biosynthesis	9	0.396	1	0.334	1	1
Phenylalanine and Tyrosine Metabolism	28	1.23	2	0.351	1	1
Selenoamino Acid Metabolism	28	1.23	2	0.351	1	1
Steroid Biosynthesis	48	2.11	3	0.354	1	1
Phospholipid Biosynthesis	29	1.27	2	0.367	1	1
Folate Metabolism	29	1.27	2	0.367	1	1
Urea Cycle	29	1.27	2	0.367	1	1
Lysine Degradation	30	1.32	2	0.384	1	1
Tyrosine Metabolism	72	3.16	4	0.391	1	1
Glycerol Phosphate Shuttle	11	0.483	1	0.392	1	1
Trehalose Degradation	11	0.483	1	0.392	1	1
Cardiolipin Biosynthesis	11	0.483	1	0.392	1	1
Starch and Sucrose Metabolism	31	1.36	2	0.4	1	1
Ammonia Recycling	32	1.41	2	0.415	1	1
Taurine and Hypotaurine Metabolism	12	0.527	1	0.419	1	1
Ketone Body Metabolism	13	0.571	1	0.444	1	1
Thyroid hormone synthesis	13	0.571	1	0.444	1	1
Pyrimidine Metabolism	59	2.59	3	0.487	1	1
Valine, Leucine and Isoleucine Degradation	60	2.64	3	0.499	1	1

Tryptophan Metabolism	60	2.64	3	0.499	1	1
Alanine Metabolism	17	0.747	1	0.537	1	1
Phosphatidylinositol Phosphate Metabolism	17	0.747	1	0.537	1	1
Bile Acid Biosynthesis	65	2.86	3	0.555	1	1
Histidine Metabolism	43	1.89	2	0.574	1	1
Fatty acid Metabolism	43	1.89	2	0.574	1	1
Nucleotide Sugars Metabolism	20	0.879	1	0.596	1	1
Vitamin B6 Metabolism	20	0.879	1	0.596	1	1
Riboflavin Metabolism	20	0.879	1	0.596	1	1
Lactose Synthesis	20	0.879	1	0.596	1	1
Threonine and 2-Oxobutanoate Degradation	20	0.879	1	0.596	1	1
Pantothenate and CoA Biosynthesis	21	0.923	1	0.615	1	1
Sulfate/Sulfite Metabolism	22	0.967	1	0.632	1	1
Transfer of Acetyl Groups into Mitochondria	22	0.967	1	0.632	1	1
Glutamate Metabolism	49	2.15	2	0.647	1	1
Glycolysis	25	1.1	1	0.679	1	1
Cysteine Metabolism	26	1.14	1	0.694	1	1
Phytanic Acid Peroxisomal Oxidation	26	1.14	1	0.694	1	1
Inositol Phosphate Metabolism	26	1.14	1	0.694	1	1
Mitochondrial Beta-Oxidation of Short Chain Saturated Fatty Acids	27	1.19	1	0.708	1	1
Mitochondrial Beta-Oxidation of Long Chain Saturated Fatty Acids	28	1.23	1	0.721	1	1
Pterine Biosynthesis	29	1.27	1	0.733	1	1
Pentose Phosphate Pathway	29	1.27	1	0.733	1	1
Citric Acid Cycle	32	1.41	1	0.768	1	1
Fructose and Mannose Degradation	32	1.41	1	0.768	1	1
Inositol Metabolism	33	1.45	1	0.778	1	1
Amino Sugar Metabolism	33	1.45	1	0.778	1	1
Beta-Alanine Metabolism	34	1.49	1	0.789	1	1
Fatty Acid Elongation In Mitochondria	35	1.54	1	0.798	1	1
Aspartate Metabolism	35	1.54	1	0.798	1	1
Gluconeogenesis	35	1.54	1	0.798	1	1
Fatty Acid Biosynthesis	35	1.54	1	0.798	1	1
Nicotinate and Nicotinamide Metabolism	37	1.63	1	0.816	1	1
Galactose Metabolism	38	1.67	1	0.824	1	1
Porphyrin Metabolism	40	1.76	1	0.84	1	1
Sphingolipid Metabolism	40	1.76	1	0.84	1	1
Propanoate Metabolism	42	1.85	1	0.854	1	1
Pyruvate Metabolism	48	2.11	1	0.89	1	1
Warburg Effect	58	2.55	1	0.932	1	1

Table S5. Findings of pathway enrichment analysis on characteristic features identified in the ROSI study.

Pathway Term	Total	Expected	Hits	Raw *p*	Enrichment	Holm adjust	FDR	Impact
Aminoacyl-tRNA biosynthesis	48	1.3006	8	2.47E-05	4.6066	0.0020783	0.002078	0
Purine metabolism	65	1.7613	7	0.001385	2.8585	0.11498	0.054499	0.06812
Phenylalanine metabolism	10	0.27097	3	0.001946	2.7108	0.1596	0.054499	0.35714
Arginine and proline metabolism	38	1.0297	5	0.002965	2.5279	0.24023	0.062282	0.14778
Phenylalanine, tyrosine and tryptophan biosynthesis	4	0.10839	2	0.004156	2.3813	0.33251	0.069828	1
Glycine, serine and threonine metabolism	33	0.89419	4	0.010779	1.9674	0.85151	0.1509	0.05034
Valine, leucine and isoleucine biosynthesis	8	0.21677	2	0.018102	1.7423	1	0.21722	0
Lysine degradation	25	0.67742	3	0.028111	1.5511	1	0.29517	0.14554
Glutathione metabolism	28	0.75871	3	0.037855	1.4219	1	0.35332	0.01428
Terpenoid backbone biosynthesis	18	0.48774	2	0.083408	1.0788	1	0.70063	0.11429
Tyrosine metabolism	42	1.1381	3	0.10233	0.99	1	0.70329	0.15223
D-Arginine and D-ornithine metabolism	4	0.10839	1	0.10416	0.98231	1	0.70329	0
beta-Alanine metabolism	21	0.56903	2	0.10884	0.9632	1	0.70329	0.05597
D-Glutamine and D-glutamate metabolism	6	0.16258	1	0.15219	0.81762	1	0.91312	0
Alanine, aspartate and glutamate metabolism	28	0.75871	2	0.17434	0.7586	1	0.97064	0.08654
Taurine and hypotaurine metabolism	8	0.21677	1	0.1977	0.704	1	0.97064	0.28571
Ubiquinone and other terpenoid-quinone biosynthesis	9	0.24387	1	0.21955	0.65847	1	0.97064	0
One carbon pool by folate	9	0.24387	1	0.21955	0.65847	1	0.97064	0
Vitamin B6 metabolism	9	0.24387	1	0.21955	0.65847	1	0.97064	0.07843
Biotin metabolism	10	0.27097	1	0.24082	0.6183	1	1	0
Glycerophospholipid metabolism	36	0.97548	2	0.25483	0.59375	1	1	0.10675
Valine, leucine and isoleucine degradation	40	1.0839	2	0.29572	0.52911	1	1	0
Tryptophan metabolism	41	1.111	2	0.30593	0.51438	1	1	0.23655
Arginine biosynthesis	14	0.37935	1	0.32039	0.49432	1	1	0
Butanoate metabolism	15	0.40645	1	0.33897	0.46984	1	1	0.03175
Histidine metabolism	16	0.43355	1	0.35706	0.44726	1	1	0
Glycerolipid metabolism	16	0.43355	1	0.35706	0.44726	1	1	0.04361
Starch and sucrose metabolism	18	0.48774	1	0.39179	0.40694	1	1	0.07306
Folate biosynthesis	27	0.73161	1	0.52673	0.27841	1	1	0
Porphyrin and chlorophyll metabolism	30	0.8129	1	0.56484	0.24808	1	1	0.05288
Cysteine and methionine metabolism	33	0.89419	1	0.59995	0.22189	1	1	0.10446
Biosynthesis of unsaturated fatty acids	36	0.97548	1	0.63228	0.19909	1	1	0
Fatty acid elongation	39	1.0568	1	0.66206	0.1791	1	1	0
Fatty acid degradation	39	1.0568	1	0.66206	0.1791	1	1	0
Fatty acid biosynthesis	47	1.2735	1	0.73044	0.13642	1	1	0.01473

7.3 Supplementary Tables for Chapter 4

Table S6. Processing step workflow nodes followed for protein analysis using Proteome Discoverer.

Processing Workflow	Workflow Node	Parameter	Value
Processing node 0: Spectrum Files RC	Search Settings	File Name(s)	AS_Raw
		Protein Database	Homo sapiens (sp_canonical TaxID=9606)
		Enzyme Name	Trypsin (Full)
		Precursor Mass Tolerance	20 ppm
		Fragment Mass Tolerance	0.5 Da
		Static Modification	Carbamidomethyl / +57.021 Da (C)
	Regression Settings	Regression Model	Non-linear Regression
		Parameter Tuning	Coarse
Processing node 4: Minora Feature Detector	Storage Settings	Feature Traces to Store	All
	Peak & Feature Detection	Min. Trace Length	5
		S/N Threshold	1
		Max. ΔRT of Isotope Pattern Multiplets [min]	0.2
	Feature to ID Linking	PSM Confidence At Least	High
Processing node 1: Spectrum Selector	General Settings	Precursor Selection	Use MS1 Precursor
		Use Isotope Pattern in Precursor Reevaluation	TRUE
		Provide Profile Spectra	Automatic
		Spectra to Store	All
	Spectrum Properties Filter	Lower RT Limit	0
		Upper RT Limit	0
		First Scan	0
		Last Scan	0
		Total Intensity Threshold	0
		Minimum Peak Count	1
	Spectrum Properties Filter for DDA Spectra	Lowest Charge State	0
		Highest Charge State	0
		Min. Precursor Mass	350 Da
		Max. Precursor Mass	5000 Da
	Scan Event Filters	MS Order	Is Not MS1
		Min. Collision Energy	0
		Max. Collision Energy	1000

		Scan Type	Is Full
	Peak Filters	S/N Threshold (FT-only)	1.5
	Replacements for Unrecognized Properties	Unrecognized Charge Replacements	Automatic
		Unrecognized Mass Analyzer Replacements	ITMS
		Unrecognized MS Order Replacements	MS2
		Unrecognized Activation Type Replacements	CID
		Unrecognized Polarity Replacements	+
		Unrecognized MS Resolution@200 Replacements	60000
		Unrecognized MSn Resolution@200 Replacements	30000
	Precursor Pattern Extraction	Precursor Clipping Range Before	2.5 Da
		Precursor Clipping Range After	5.5 Da
Processing node 2: Sequest HT	Input Data	Protein Database	Homo sapiens (sp_canonical TaxID=9606)
		Enzyme Name	Trypsin (Full)
		Max. Missed Cleavage Sites	2
		Min. Peptide Length	6
		Max. Peptide Length	144
		Max. Number of Peptides Reported	10
	Tolerances	Precursor Mass Tolerance	10 ppm
		Fragment Mass Tolerance	0.02 Da
		Use Average Precursor Mass	FALSE
		Use Average Fragment Mass	FALSE
	Spectrum Matching	Use Neutral Loss a Ions	TRUE
		Use Neutral Loss b Ions	TRUE
		Use Neutral Loss y Ions	TRUE
		Use Flanking Ions	TRUE
		Weight of a Ions	0
		Weight of b Ions	1
		Weight of c Ions	0
		Weight of x Ions	0
		Weight of y Ions	1
		Weight of z Ions	0
	Dynamic Modifications	Max. Equal Modifications Per Peptide	3
		Max. Dynamic Modifications Per Peptide	4
		Dynamic Modification	Oxidation / +15.995 Da (M)

	Dynamic Modifications (protein terminus)	N-Terminal Modification	Acetyl / +42.011 Da (N-Terminus)
		N-Terminal Modification	Met-loss / -131.040 Da (M)
		N-Terminal Modification	Met-loss+Acetyl / -89.030 Da (M)
	Static Modifications	Static Modification	Carbamidomethyl / +57.021 Da (C)
Processing node 3: Percolator	Target/Decoy Strategy	Target/Decoy Selection	Concatenated
		Validation Based on	q-Value
	Input Data	Maximum Delta Cn	0.05
		Maximum Rank	0
	FDR Targets	Target FDR (Strict)	0.01
		Target FDR (Relaxed)	0.05

Table S7. Consensus Step Workflow nodes followed for protein analysis using Proteome Discoverer.

Consensus Step	Workflow Node	Parameter	Value
Processing node 0: MSF Files	Storage Settings	Spectra to Store	Identified or Quantified
		Feature Traces to Store	All
	Merging of Identified Peptide and Proteins	Merge Mode	Globally by Search Engine Type
	FASTA Title Line Display	Reported FASTA Title Lines	Best match
		Title Line Rule	standard
	PSM Filters	Maximum Delta Cn	0.05
		Maximum Rank	0
		Maximum Delta Mass	0 ppm
Processing node 10: Feature Mapper	Chromatographic Alignment	Perform RT Alignment	TRUE
		Parameter Tuning	Coarse
		Maximum RT Shift [min]	10
		Mass Tolerance	10 ppm
	Feature Linking and Mapping	RT Tolerance [min]	0
		Mass Tolerance	0 ppm
		Min. S/N Threshold	5
		Map single PSMs	TRUE
Processing node 11: Precursor Ions Quantifier	General Quantification Settings	Peptides to Use	Unique + Razor
		Consider Protein Groups for Peptide Uniqueness	TRUE
		Use Shared Quan Results	FALSE
		Reject Quan Results with Missing Channels	FALSE
	Precursor Quantification	Precursor Abundance Based On	Intensity
		Min. # Replicate Features [%]	0
	Normalization and Scaling	Normalization Mode	Total Peptide Amount
		Scaling Mode	On All Average
	Exclude Peptides from Protein Quantification	For Normalization	Use All Peptides
		For Protein Roll-Up	Use All Peptides
		For Pairwise Ratios	Exclude Modified
	Quan Rollup and Hypothesis Testing	Protein Abundance Calculation	Summed Abundances
		N for Top N	3
		Protein Ratio Calculation	Pairwise Ratio Based
		Maximum Allowed Fold Change	100
		Imputation Mode	None

		Hypothesis Test	t-test (Background Based)
		Calculate Hypothesis Test for Peptides	FALSE
	Quan Ratio Distributions	1st Fold Change Threshold	2
		2nd Fold Change Threshold	4
		3rd Fold Change Threshold	6
		4th Fold Change Threshold	8
		5th Fold Change Threshold	10
Processing node 1: PSM Grouper	Peptide Group Modifications	Site Probability Threshold	75
Processing node 2: Peptide Validator	General Validation Settings	Validation Mode	Automatic (Control peptide level error rate if possible)
		Target FDR (Strict) for PSMs	0.01
		Target FDR (Relaxed) for PSMs	0.05
		Target FDR (Strict) for Peptides	0.01
		Target FDR (Relaxed) for Peptides	0.05
	Specific Validation Settings	Validation Based on	q-Value
		Target/Decoy Selection for PSM Level FDR Calculation Based on Score	Automatic
		Reset Confidences for Nodes without Decoy Search (Fixed score thresholds)	FALSE
Processing node 3: Peptide and Protein Filter	Peptide Filters	Peptide Confidence At Least	High
		Keep Lower Confident PSMs	FALSE
		Minimum Peptide Length	6
		Remove Peptides Without Protein Reference	FALSE
	Protein Filters	Minimum Number of Peptide Sequences	1
		Count Only Rank 1 Peptides	FALSE
		Count Peptides Only for Top Scored Protein	FALSE
Processing node 4: Protein Marker	Annotate Species	As Species Map	FALSE
		As Species Names	FALSE
	Mark Additional Entities	Annotation Groups	FALSE
		Pathway Groups	FALSE
		Modification Sites	TRUE
		Peptide Isoform Groups	TRUE
Processing node 5: Protein Annotation	Annotation Aspects	1. Aspect	Biological Process
			Cellular Component
			Molecular Function
	Annotation/Pathway Groups	Protein Database	Homo sapiens (sp_canonical TaxID=9606)
Processing node 6: Protein Scorer	No parameters	No parameters	No parameters

Processing node 7: Protein FDR Validator	Confidence Thresholds	Target FDR (Strict)	0.01
		Target FDR (Relaxed)	0.05
Processing node 8: Protein Grouping	Protein Grouping	Apply strict parsimony principle	TRUE
Processing node 9: Peptide in Protein Annotation	Flanking Residues	Annotate Flanking Residues of the Peptide	TRUE
		Number Flanking Residues in Connection Tables	1
	Modifications in Peptide	Protein Modifications Reported	Only for Master Proteins
	Modifications in Protein	Modification Sites Reported	All And Specific
		Minimum PSM Confidence	High
		Report Only PTMs	TRUE
	Positions in Protein	Protein Positions for Peptides	Only for Master Proteins
Processing node 13: Data Distributions	ID Distributions (Bottom-up)	Peptides to Use	Only unique peptides based on protein groups

Table S8. List of significantly enriched pathways of the differential expressed proteins identified in the PGZ study, as analysed by KEGG pathway analysis.

Category	Term	Count	%	*P*-Value	Fold Enrichment	FDR
KEGG_PATHWAY	Staphylococcus aureus infection	25	3.9	2.20E-14	7.2	5.60E-12
KEGG_PATHWAY	Complement and coagulation cascades	22	3.5	1.60E-12	7.1	2.10E-10
KEGG_PATHWAY	Estrogen signaling pathway	23	3.6	3.20E-09	4.6	2.80E-07
KEGG_PATHWAY	Focal adhesion	26	4.1	4.90E-08	3.6	3.10E-06
KEGG_PATHWAY	ECM-receptor interaction	16	2.5	4.50E-07	5	2.30E-05
KEGG_PATHWAY	Human papillomavirus infection	31	4.9	2.50E-06	2.6	1.10E-04
KEGG_PATHWAY	Proteoglycans in cancer	19	3	4.00E-04	2.6	1.30E-02
KEGG_PATHWAY	Cholesterol metabolism	9	1.4	4.20E-04	4.9	1.30E-02
KEGG_PATHWAY	Shigellosis	20	3.2	1.40E-03	2.2	3.80E-02
KEGG_PATHWAY	Regulation of actin cytoskeleton	19	3	1.50E-03	2.3	3.80E-02
KEGG_PATHWAY	Malaria	8	1.3	1.90E-03	4.4	4.50E-02
KEGG_PATHWAY	Melanogenesis	11	1.7	3.30E-03	3	6.90E-02
KEGG_PATHWAY	Systemic lupus erythematosus	13	2.1	3.50E-03	2.6	6.90E-02
KEGG_PATHWAY	Adherens junction	9	1.4	3.80E-03	3.5	6.90E-02
KEGG_PATHWAY	PI3K-Akt signaling pathway	24	3.8	4.30E-03	1.9	7.30E-02
KEGG_PATHWAY	Platelet activation	12	1.9	4.90E-03	2.7	7.60E-02
KEGG_PATHWAY	Steroid biosynthesis	5	0.8	5.00E-03	6.9	7.60E-02
KEGG_PATHWAY	Hepatocellular carcinoma	14	2.2	7.40E-03	2.3	1.10E-01
KEGG_PATHWAY	Wnt signaling pathway	14	2.2	8.20E-03	2.3	1.10E-01
KEGG_PATHWAY	Thyroid cancer	6	0.9	9.90E-03	4.5	1.20E-01
KEGG_PATHWAY	Cushing syndrome	13	2.1	9.90E-03	2.3	1.20E-01
KEGG_PATHWAY	Protein digestion and absorption	10	1.6	1.20E-02	2.7	1.30E-01
KEGG_PATHWAY	Colorectal cancer	9	1.4	1.20E-02	2.9	1.30E-01
KEGG_PATHWAY	Ferroptosis	6	0.9	1.50E-02	4.1	1.60E-01
KEGG_PATHWAY	Endometrial cancer	7	1.1	1.70E-02	3.3	1.80E-01
KEGG_PATHWAY	Mineral absorption	7	1.1	2.00E-02	3.2	2.00E-01
KEGG_PATHWAY	Basal cell carcinoma	7	1.1	2.50E-02	3.1	2.40E-01
KEGG_PATHWAY	Human cytomegalovirus infection	15	2.4	3.20E-02	1.8	2.90E-01
KEGG_PATHWAY	Salmonella infection	16	2.5	3.50E-02	1.8	3.00E-01
KEGG_PATHWAY	Prion disease	17	2.7	3.70E-02	1.7	3.00E-01
KEGG_PATHWAY	Alcoholism	13	2.1	3.70E-02	1.9	3.00E-01
KEGG_PATHWAY	Coronavirus disease - COVID-19	15	2.4	4.00E-02	1.8	3.00E-01
KEGG_PATHWAY	Neutrophil extracellular trap formation	13	2.1	4.10E-02	1.9	3.00E-01
KEGG_PATHWAY	Gastric cancer	11	1.7	4.20E-02	2	3.00E-01
KEGG_PATHWAY	Pathways in cancer	28	4.4	4.20E-02	1.5	3.00E-01
KEGG_PATHWAY	African trypanosomiasis	5	0.8	4.30E-02	3.7	3.00E-01

Table S9. List of significantly enriched pathways of the differential expressed proteins identified in the ROSI study, as analysed by KEGG pathway analysis.

Category	Term	Count	%	*P*-Value	Fold Enrichment	FDR
KEGG_PATHWAY	Neutrophil extracellular trap formation	45	10.2040816	6.78E-28	8.02729993	1.67E-25
KEGG_PATHWAY	Systemic lupus erythematosus	38	8.61678005	3.49E-26	9.45046924	4.29E-24
KEGG_PATHWAY	Alcoholism	37	8.39002268	5.06E-20	6.70554711	4.15E-18
KEGG_PATHWAY	Viral carcinogenesis	24	5.44217687	2.42E-08	4.00840336	1.49E-06
KEGG_PATHWAY	Shigellosis	26	5.89569161	5.11E-08	3.58646617	2.52E-06
KEGG_PATHWAY	Protein processing in endoplasmic reticulum	20	4.53514739	4.82E-07	4.00840336	1.98E-05
KEGG_PATHWAY	Vibrio cholerae infection	11	2.49433107	1.40E-06	7.49571429	4.91E-05
KEGG_PATHWAY	Carbon metabolism	15	3.40136054	5.92E-06	4.44409938	1.82E-04
KEGG_PATHWAY	Parkinson disease	22	4.98866213	3.20E-05	2.8179377	8.73E-04
KEGG_PATHWAY	Phagosome	16	3.62811791	3.59E-05	3.58646617	8.73E-04
KEGG_PATHWAY	Protein export	7	1.58730159	3.91E-05	10.3695652	8.73E-04
KEGG_PATHWAY	Oxidative phosphorylation	14	3.17460317	1.42E-04	3.55970149	0.00290797
KEGG_PATHWAY	Mineral absorption	9	2.04081633	3.28E-04	5.11071429	0.00619775
KEGG_PATHWAY	Transcriptional misregulation in cancer	16	3.62811791	5.17E-04	2.82457439	0.00908208
KEGG_PATHWAY	Necroptosis	14	3.17460317	7.56E-04	3	0.01240549
KEGG_PATHWAY	Prion disease	19	4.30839002	0.00100835	2.3799895	0.01550337
KEGG_PATHWAY	Coronavirus disease - COVID-19	17	3.85487528	0.00124357	2.4966133	0.01799517
KEGG_PATHWAY	Huntington disease	20	4.53514739	0.00156099	2.22689076	0.02133358
KEGG_PATHWAY	Staphylococcus aureus infection	10	2.2675737	0.00190939	3.54910714	0.02374764
KEGG_PATHWAY	Alzheimer disease	23	5.2154195	0.0019307	2.04073661	0.02374764
KEGG_PATHWAY	Diabetic cardiomyopathy	15	3.40136054	0.00246726	2.51759324	0.02890219
KEGG_PATHWAY	Proximal tubule bicarbonate reclamation	5	1.13378685	0.00407364	7.4068323	0.04482121
KEGG_PATHWAY	Central carbon metabolism in cancer	8	1.81405896	0.0041906	3.89387755	0.04482121
KEGG_PATHWAY	Amyotrophic lateral sclerosis	21	4.76190476	0.00488684	1.96565934	0.05009012
KEGG_PATHWAY	Estrogen signaling pathway	11	2.49433107	0.00676752	2.73566215	0.06659244
KEGG_PATHWAY	Citrate cycle (TCA cycle)	5	1.13378685	0.01074722	5.67857143	0.10168522
KEGG_PATHWAY	Pathways of neurodegeneration - multiple diseases	24	5.44217687	0.01200885	1.71788715	0.10941401
KEGG_PATHWAY	Glycolysis / Gluconeogenesis	7	1.58730159	0.01324569	3.55970149	0.1125288
KEGG_PATHWAY	Cardiac muscle contraction	8	1.81405896	0.01346542	3.13300493	0.1125288
KEGG_PATHWAY	Chemical carcinogenesis - reactive oxygen species	14	3.17460317	0.01372302	2.13901345	0.1125288
KEGG_PATHWAY	HIF-1 signaling pathway	9	2.04081633	0.0143243	2.81323722	0.11367025
KEGG_PATHWAY	DNA replication	5	1.13378685	0.0201652	4.73214286	0.15501997
KEGG_PATHWAY	Biosynthesis of amino acids	7	1.58730159	0.02206668	3.18	0.16449705
KEGG_PATHWAY	Ribosome	11	2.49433107	0.02450536	2.24422583	0.17249874
KEGG_PATHWAY	Spliceosome	13	2.9478458	0.0245425	2.05059524	0.17249874
KEGG_PATHWAY	Synaptic vesicle cycle	7	1.58730159	0.02620358	3.05769231	0.17905779
KEGG_PATHWAY	Viral myocarditis	6	1.36054422	0.03039695	3.40714286	0.20053976
KEGG_PATHWAY	Ferroptosis	5	1.13378685	0.03097769	4.15505226	0.20053976

KEGG_PATHWAY	Collecting duct acid secretion	4	0.90702948	0.04307116	5.04761905	0.27167963
KEGG_PATHWAY	Pyruvate metabolism	5	1.13378685	0.04770761	3.62462006	0.29340181

Table S10. List of significantly enriched pathways of the blue module members identified in the PGZ study, as analysed by KEGG pathway analysis.

Category	Term	Count	%	*P*-Value	Fold Enrichment	FDR
KEGG_PATHWAY	Neutrophil extracellular trap formation	27	5.9	1.40E-10	4.6	2.00E-08
KEGG_PATHWAY	Systemic lupus erythematosus	23	5.1	1.50E-10	5.4	2.00E-08
KEGG_PATHWAY	Prion disease	32	7	2.80E-10	3.8	2.40E-08
KEGG_PATHWAY	Complement and coagulation cascades	16	3.5	4.90E-08	6	3.20E-06
KEGG_PATHWAY	Diabetic cardiomyopathy	24	5.3	6.70E-08	3.8	3.50E-06
KEGG_PATHWAY	Parkinson disease	27	5.9	1.90E-07	3.3	8.10E-06
KEGG_PATHWAY	Alcoholism	22	4.8	3.00E-07	3.8	1.10E-05
KEGG_PATHWAY	Cholesterol metabolism	12	2.6	3.30E-07	7.5	1.10E-05
KEGG_PATHWAY	Huntington disease	28	6.2	8.40E-07	2.9	2.40E-05
KEGG_PATHWAY	Oxidative phosphorylation	17	3.7	3.60E-06	4.1	9.30E-05
KEGG_PATHWAY	Focal adhesion	21	4.6	3.90E-06	3.3	9.30E-05
KEGG_PATHWAY	Chemical carcinogenesis - reactive oxygen species	22	4.8	5.40E-06	3.2	1.20E-04
KEGG_PATHWAY	Alzheimer disease	29	6.4	2.10E-05	2.4	4.20E-04
KEGG_PATHWAY	Amyotrophic lateral sclerosis	27	5.9	6.00E-05	2.4	1.10E-03
KEGG_PATHWAY	Protein processing in endoplasmic reticulum	17	3.7	7.90E-05	3.2	1.40E-03
KEGG_PATHWAY	Platelet activation	14	3.1	1.20E-04	3.6	1.90E-03
KEGG_PATHWAY	Viral carcinogenesis	18	4	2.00E-04	2.8	3.00E-03
KEGG_PATHWAY	Thermogenesis	19	4.2	3.10E-04	2.6	4.50E-03
KEGG_PATHWAY	ECM-receptor interaction	11	2.4	3.80E-04	4	5.20E-03
KEGG_PATHWAY	Spliceosome	14	3.1	6.30E-04	3.1	8.30E-03
KEGG_PATHWAY	Pathways of neurodegeneration - multiple diseases	29	6.4	8.00E-04	2	1.00E-02
KEGG_PATHWAY	Phagosome	14	3.1	8.70E-04	3	1.00E-02
KEGG_PATHWAY	Necroptosis	13	2.9	3.90E-03	2.6	4.40E-02
KEGG_PATHWAY	Malaria	7	1.5	4.30E-03	4.5	4.70E-02
KEGG_PATHWAY	Proteoglycans in cancer	15	3.3	4.70E-03	2.3	4.90E-02
KEGG_PATHWAY	Regulation of actin cytoskeleton	16	3.5	5.10E-03	2.2	5.10E-02
KEGG_PATHWAY	Pathogenic Escherichia coli infection	14	3.1	8.30E-03	2.3	7.80E-02
KEGG_PATHWAY	Ferroptosis	6	1.3	8.40E-03	4.7	7.80E-02
KEGG_PATHWAY	Carbon metabolism	10	2.2	9.40E-03	2.8	8.50E-02
KEGG_PATHWAY	Bacterial invasion of epithelial cells	8	1.8	9.70E-03	3.3	8.50E-02
KEGG_PATHWAY	Estrogen signaling pathway	11	2.4	1.10E-02	2.6	9.00E-02
KEGG_PATHWAY	Coronavirus disease - COVID-19	15	3.3	1.30E-02	2.1	1.10E-01
KEGG_PATHWAY	Lipid and atherosclerosis	14	3.1	1.60E-02	2.1	1.30E-01
KEGG_PATHWAY	HIF-1 signaling pathway	9	2	2.00E-02	2.6	1.50E-01
KEGG_PATHWAY	Leukocyte transendothelial migration	9	2	2.50E-02	2.5	1.90E-01
KEGG_PATHWAY	Protein export	4	0.9	3.30E-02	5.6	2.40E-01
KEGG_PATHWAY	Metabolic pathways	60	13.2	4.50E-02	1.2	3.10E-01
KEGG_PATHWAY	Lysine degradation	6	1.3	4.50E-02	3.1	3.10E-01

Table S11. List of significantly enriched pathways of the brown module members identified in the ROSI study, as analysed by KEGG pathway analysis.

Category	Term	Count	%	*P*-Value	Fold Enrichment	FDR
KEGG_PATHWAY	Mineral absorption	6	5	2.34E-05	16.83529	0.001505
KEGG_PATHWAY	Ribosome	8	6.666667	4.59E-05	8.064812	0.001505
KEGG_PATHWAY	Coronavirus disease - COVID-19	9	7.5	5.07E-05	6.530933	0.001505
KEGG_PATHWAY	Complement and coagulation cascades	4	3.333333	0.013554	7.830369	0.301567
KEGG_PATHWAY	African trypanosomiasis	3	2.5	0.019441	13.65024	0.346045
KEGG_PATHWAY	Malaria	3	2.5	0.03409	10.10118	0.505668
KEGG_PATHWAY	Glycolysis / Gluconeogenesis	3	2.5	0.057825	7.538191	0.735204
KEGG_PATHWAY	Tight junction	4	3.333333	0.076071	3.961246	0.846295

7.4 Supplementary Tables for Chapter 5

Table S12. Joint pathway analysis results from proteo-metabolic data in the PGZ study.

Pathway Term	Total	Expected	Hits	Raw *p*	Enrichment	Holm adjust	FDR	Impact
Phenylalanine metabolism	21	0.46475	4	0.00097039	3.0131	0.081513	0.081513	0.6
beta-Alanine metabolism	44	0.97377	5	0.0024794	2.6056	0.20579	0.10414	0.13953
Aminoacyl-tRNA biosynthesis	74	1.6377	6	0.0051603	2.2873	0.42315	0.12758	0.09589
Pantothenate and CoA biosynthesis	34	0.75246	4	0.0060751	2.2164	0.49209	0.12758	0.18182
Lysine degradation	49	1.0844	4	0.021736	1.6628	1	0.32578	0.1875
Phenylalanine, tyrosine and tryptophan biosynthesis	11	0.24344	2	0.02327	1.6332	1	0.32578	1.2
Glutathione metabolism	56	1.2393	4	0.03364	1.4731	1	0.40368	0.10909
Ubiquinone and other terpenoid-quinone biosynthesis	17	0.37623	2	0.052883	1.2767	1	0.55527	0.3125
Vitamin B6 metabolism	21	0.46475	2	0.077226	1.1122	1	0.70063	0.9
Biosynthesis of unsaturated fatty acids	47	1.0402	3	0.08394	1.076	1	0.70063	0.5
Arginine and proline metabolism	78	1.7262	4	0.091749	1.0374	1	0.70063	0.14286
Steroid biosynthesis	82	1.8148	4	0.10556	0.97652	1	0.73889	0.17284
Selenocompound metabolism	35	0.77459	2	0.18053	0.74346	1	1	0.088235
Glycine, serine and threonine metabolism	68	1.5049	3	0.18909	0.72332	1	1	0.044776
Valine, leucine and isoleucine biosynthesis	12	0.26557	1	0.23599	0.62711	1	1	0.090909
Starch and sucrose metabolism	43	0.95164	2	0.246	0.60907	1	1	0.11905
Glycerophospholipid metabolism	86	1.9033	3	0.29624	0.52835	1	1	0.11765
Tyrosine metabolism	88	1.9475	3	0.30855	0.51068	1	1	0.17241
Porphyrin and chlorophyll metabolism	53	1.173	2	0.32887	0.48298	1	1	0.076923
Sulfur metabolism	18	0.39836	1	0.33253	0.47817	1	1	0.70588
Alanine, aspartate and glutamate metabolism	61	1.35	2	0.39362	0.40493	1	1	0.11667
Arginine biosynthesis	27	0.59754	1	0.45531	0.3417	1	1	0.11538
Inositol phosphate metabolism	69	1.527	2	0.45557	0.34144	1	1	0.058824
Fatty acid elongation	75	1.6598	2	0.49969	0.3013	1	1	0.013514
Purine metabolism	166	3.6738	4	0.50681	0.29515	1	1	0.21212
Histidine metabolism	32	0.7082	1	0.51363	0.28935	1	1	0.16129
Glycerolipid metabolism	35	0.77459	1	0.54564	0.2631	1	1	0.088235
Various types of N-glycan biosynthesis	36	0.79672	1	0.55584	0.25505	1	1	0.22857
Ether lipid metabolism	39	0.86311	1	0.58512	0.23276	1	1	0.10526
Pyruvate metabolism	45	0.9959	1	0.6381	0.19511	1	1	0.090909
Pentose phosphate pathway	47	1.0402	1	0.65424	0.18426	1	1	0.086957
Propanoate metabolism	48	1.0623	1	0.66204	0.17912	1	1	0.17021

Glyoxylate and dicarboxylate metabolism	56	1.2393	1	0.71854	0.14355	1	1	0.036364
Sphingolipid metabolism	58	1.2836	1	0.73115	0.13599	1	1	0.035088
Drug metabolism - other enzymes	70	1.5492	1	0.79596	0.099111	1	1	0.072464
Cysteine and methionine metabolism	71	1.5713	1	0.80061	0.096582	1	1	0.028571
Phosphatidylinositol signaling system	74	1.6377	1	0.81394	0.089409	1	1	0.054795
N-Glycan biosynthesis	77	1.7041	1	0.82639	0.082813	1	1	0.026316
Arachidonic acid metabolism	81	1.7926	1	0.84174	0.074824	1	1	0.05
Valine, leucine and isoleucine degradation	88	1.9475	1	0.86545	0.062759	1	1	0.022989
Pyrimidine metabolism	99	2.191	1	0.89584	0.047768	1	1	0.020408
Fatty acid degradation	102	2.2574	1	0.90289	0.044366	1	1	0.039604
Fatty acid biosynthesis	129	2.8549	1	0.94851	0.022957	1	1	0.046875

Table S13. Joint pathway analysis results from proteo-metabolic data in the ROSI study.

Pathway Term	Total	Expected	Hits	Raw *p*	Enrichment	Holm adjust	FDR	Impact
Aminoacyl-tRNA biosynthesis	74	2.4869	12	3.73E-06	5.4279	0.00031362	0.000	0.21918
Glycolysis or Gluconeogenesis	61	2.05	7	0.003759	2.4249	0.31203	0.157	0.6
Citrate cycle (TCA cycle)	42	1.4115	5	0.012145	1.9156	0.99591	0.338	0.53659
Pyruvate metabolism	45	1.5123	5	0.016127	1.7925	1	0.338	0.31818
Lysine degradation	49	1.6467	5	0.022675	1.6445	1	0.376	0.20833
Phenylalanine metabolism	21	0.70574	3	0.031442	1.5025	1	0.376	0.45
Glutathione metabolism	56	1.882	5	0.037865	1.4218	1	0.376	0.2
D-Glutamine and D-glutamate metabolism	10	0.33607	2	0.042145	1.3753	1	0.376	0.44444
Nitrogen metabolism	10	0.33607	2	0.042145	1.3753	1	0.376	0.44444
Arginine and proline metabolism	78	2.6213	6	0.044761	1.3491	1	0.376	0.31169
Phenylalanine, tyrosine and tryptophan biosynthesis	11	0.36967	2	0.050407	1.2975	1	0.384	1.2
Valine, leucine and isoleucine biosynthesis	12	0.40328	2	0.059195	1.2277	1	0.387	0.27273
Arginine biosynthesis	27	0.90738	3	0.059921	1.2224	1	0.387	0.19231
Pentose phosphate pathway	47	1.5795	4	0.070824	1.1498	1	0.424	0.69565
Glycine, serine and threonine metabolism	68	2.2852	5	0.075816	1.1202	1	0.424	0.1194
Purine metabolism	166	5.5787	9	0.10121	0.99478	1	0.531	0.41818
Ubiquinone and other terpenoid-quinone biosynthesis	17	0.57131	2	0.10959	0.96024	1	0.541	0.3125
Neomycin, kanamycin and gentamicin biosynthesis	4	0.13443	1	0.12788	0.89321	1	0.596	0.66667
Alanine, aspartate and glutamate metabolism	61	2.05	4	0.14664	0.83376	1	0.648	0.2
Vitamin B6 metabolism	21	0.70574	2	0.15548	0.80831	1	0.653	0.5
Starch and sucrose metabolism	43	1.4451	3	0.1738	0.75994	1	0.695	0.2619
D-Arginine and D-ornithine metabolism	6	0.20164	1	0.18561	0.73139	1	0.708	0.2
Cysteine and methionine metabolism	71	2.3861	4	0.2141	0.66938	1	0.781	0.17143
N-Glycan biosynthesis	77	2.5877	4	0.25815	0.58812	1	0.891	0.10526
Riboflavin metabolism	9	0.30246	1	0.26521	0.57641	1	0.891	0.25
One carbon pool by folate	31	1.0418	2	0.27986	0.55306	1	0.904	0.23333
Terpenoid backbone biosynthesis	36	1.2098	2	0.34268	0.46511	1	1	0.11429
Tyrosine metabolism	88	2.9574	4	0.34269	0.4651	1	1	0.34483
Fructose and mannose metabolism	40	1.3443	2	0.39174	0.407	1	1	0.35897
Taurine and hypotaurine metabolism	16	0.5377	1	0.42228	0.3744	1	1	0.2
beta-Alanine metabolism	44	1.4787	2	0.43916	0.35738	1	1	0.04651
Fatty acid elongation	75	2.5205	3	0.46568	0.33192	1	1	0.09459
Amino sugar and nucleotide sugar metabolism	79	2.6549	3	0.50062	0.30049	1	1	0.20513
Biotin metabolism	21	0.70574	1	0.51368	0.28931	1	1	0.05
Porphyrin and chlorophyll metabolism	53	1.7811	2	0.53805	0.26918	1	1	0.07692
Tryptophan metabolism	84	2.823	3	0.54267	0.26546	1	1	0.10843

Glyoxylate and dicarboxylate metabolism	56	1.882	2	0.5683	0.24542	1	1	0.07272
Valine, leucine and isoleucine degradation	88	2.9574	3	0.57484	0.24045	1	1	0.14943
Butanoate metabolism	29	0.97459	1	0.63108	0.19992	1	1	0.10714
Pyrimidine metabolism	99	3.327	3	0.65589	0.18317	1	1	0.04081
Histidine metabolism	32	1.0754	1	0.66747	0.17557	1	1	0.03225
Glycerolipid metabolism	35	1.1762	1	0.70031	0.15471	1	1	0.05882
Glycosaminoglycan degradation	44	1.4787	1	0.7808	0.10746	1	1	0.09302
Glycerophospholipid metabolism	86	2.8902	2	0.79436	0.099985	1	1	0.15294
Biosynthesis of unsaturated fatty acids	47	1.5795	1	0.80255	0.095528	1	1	0.02173
Propanoate metabolism	48	1.6131	1	0.80932	0.091882	1	1	0.0851
Galactose metabolism	51	1.7139	1	0.82827	0.081829	1	1	0.08
Folate biosynthesis	61	2.05	1	0.87898	0.056023	1	1	0.05
Drug metabolism - other enzymes	70	2.3525	1	0.91179	0.040107	1	1	0.02898
Arachidonic acid metabolism	81	2.7221	1	0.94016	0.026796	1	1	0.025
Primary bile acid biosynthesis	92	3.0918	1	0.95949	0.01796	1	1	0.04395
Fatty acid degradation	102	3.4279	1	0.97163	0.0125	1	1	0.0198
Fatty acid biosynthesis	129	4.3352	1	0.98924	0.0046988	1	1	0.01562
Steroid hormone biosynthesis	199	6.6877	1	0.99917	0.0003585	1	1	0.0202

8 References

Abdallah, C., Dumas-Gaudot, E., Renaut, J. & Sergeant, K. (2012) Gel-based and gel-free quantitative proteomics approaches at a glance. International journal of plant genomics, 2012.

Administration, U. F. a. D. (2010) FDA Drug Safety Communication: Ongoing review of Avandia (rosiglitazone) and cardiovascular safety. Available from: https://www.fda.gov/drugs/postmarket-drug-safety-information-patients-and-providers/fda-drug-safety-communication-ongoing-review-avandia-rosiglitazone-and-cardiovascular-safety

Administration, U. F. a. D. (2012) FDA Drug Safety Communication: Update to ongoing safety review of Actos (pioglitazone) and increased risk of bladder cancer. Available from: http://www.fda.gov/Drugs/DrugSafety/ucm259150.htm

Ahn, J. H., Seo, H., Park, W., Seok, J., Lee, J. A., Kim, W. J., Kim, G. B., Kim, K.-J. & Lee, S. Y. (2020) Enhanced succinic acid production by Mannheimia employing optimal malate dehydrogenase. Nature communications, 11(1), 1970.

Akhter, M. S. & Uppal, P. (2020) Toxicity of metformin and hypoglycemic therapies. Advances in chronic kidney disease, 27(1), 18-30.

Al Sultan, A., Rattray, Z. & Rattray, N. J. (2024a) Cytotoxicity and toxicoproteomics analysis of thiazolidinedione exposure in human-derived cardiomyocytes. Journal of Applied Toxicology.

Al Sultan, A., Rattray, Z. & Rattray, N. J. (2024b) Toxicometabolomics-based cardiotoxicity evaluation of Thiazolidinedione exposure in human-derived cardiomyocytes. Metabolomics, 20(2), 24.

Al-Amrani, S., Al-Jabri, Z., Al-Zaabi, A., Alshekaili, J. & Al-Khabori, M. (2021) Proteomics: Concepts and applications in human medicine. World Journal of Biological Chemistry, 12(5), 57.

Al-Daghri, N. M., Costa, A. S., Alokail, M. S., Zanzottera, M., Alenad, A. M., Mohammed, A. K., Clerici, M. & Guerini, F. R. (2016) Synaptosomal protein of 25 kDa (Snap25) polymorphisms associated with glycemic parameters in type 2 diabetes patients. Journal of diabetes research, 2016.

Alamri, B. N., Shin, K., Chappe, V. & Anini, Y. (2016) The role of ghrelin in the regulation of glucose homeostasis. Hormone molecular biology and clinical investigation, 26(1), 3-11.

Ali Khan, H. & Mutus, B. (2014) Protein disulfide isomerase a multifunctional protein with multiple physiological roles. Frontiers in chemistry, 2, 70.

Alshammari, T. M. (2016) Drug safety: The concept, inception and its importance in patients' health. Saudi Pharmaceutical Journal, 24(4), 405-412.

An, J., Nichols, G. A., Qian, L., Munis, M. A., Harrison, T. N., Li, Z., Wei, R., Weiss, T., Rajpathak, S. & Reynolds, K. (2021) Prevalence and incidence of microvascular and macrovascular complications over 15 years among patients with incident type 2 diabetes. BMJ Open Diabetes Research and Care, 9(1), e001847.

Anand, S., Samuel, M., Ang, C.-S., Keerthikumar, S. & Mathivanan, S. (2017) Label-based and label-free strategies for protein quantitation. Proteome bioinformatics, 31-43.

Ankley, G. T. & Edwards, S. W. (2018) The adverse outcome pathway: a multifaceted framework supporting 21st century toxicology. Current opinion in toxicology, 9, 1-7.

Antczak, P., White, T. A., Giri, A., Michelangeli, F., Viant, M. R., Cronin, M. T., Vulpe, C. & Falciani, F. (2015) Systems biology approach reveals a calcium-dependent mechanism for basal toxicity in Daphnia magna. Environmental science & technology, 49(18), 11132-11140.

Araújo, A. M., Carvalho, F., Guedes de Pinho, P. & Carvalho, M. (2021) Toxicometabolomics: small molecules to answer big toxicological questions. Metabolites, 11(10), 692.

Asakawa, M., Takano, H., Nagai, T., Uozumi, H., Hasegawa, H., Kubota, N., Saito, T., Masuda, Y., Kadowaki, T. & Komuro, I. (2002) Peroxisome proliferator-activated receptor γ plays a critical role in inhibition of cardiac hypertrophy in vitro and in vivo. Circulation, 105(10), 1240-1246.

Aschenbrenner, D. S. (2020) Boxed Warning Removed from Canagliflozin Labeling. AJN The American Journal of Nursing, 120(12), 22.

Aslam, B., Basit, M., Nisar, M. A., Khurshid, M. & Rasool, M. H. (2016) Proteomics: technologies and their applications. Journal of chromatographic science, 1-15.

Association, A. D. (2023) Standards of care in diabetes—2023 abridged for primary care providers. Clinical Diabetes, 41(1), 4-31.

Aukrust, P. l., Gullestad, L., Lappegård, K. T., Ueland, T., Aass, H., Wikeby, L., Simonsen, S., Frøland, S. S. & Mollnes, T. E. (2001) Complement activation in patients with congestive heart failure: effect of high-dose intravenous immunoglobulin treatment. Circulation, 104(13), 1494-1500.

Bailey, C. J., Gross, J. L., Hennicken, D., Iqbal, N., Mansfield, T. A. & List, J. F. (2013) Dapagliflozin add-on to metformin in type 2 diabetes inadequately controlled with metformin: a randomized, double-blind, placebo-controlled 102-week trial. BMC medicine, 11(1), 43.

Bajal, E., Katara, V., Bhatia, M. & Hooda, M. (2022) A review of clustering algorithms: comparison of DBSCAN and K-mean with oversampling and t-SNE. Recent Patents on Engineering, 16(2), 17-31.

Bakhti, M., Böttcher, A. & Lickert, H. (2019) Modelling the endocrine pancreas in health and disease. Nature Reviews Endocrinology, 15(3), 155-171.

Banerjee, S. & Mazumdar, S. (2012) Electrospray ionization mass spectrometry: a technique to access the information beyond the molecular weight of the analyte. International journal of analytical chemistry, 2012.

Barnes, D. A., Firman, J., Belfield, S., Cronin, M., Vinken, M., Janssen, M. & Masereeuw, R. (2024) Development of an adverse outcome pathway network for nephrotoxicity. Archives of Toxicology, 98(3), 929-942.

Baye, A. M., Fanta, T. G., Siddiqui, M. K. & Dawed, A. Y. (2021) The genetics of adverse drug outcomes in type 2 diabetes: A systematic review. Frontiers in Genetics, 12, 675053.

Bersoff-Matcha, S. J., Chamberlain, C., Cao, C., Kortepeter, C. & Chong, W. H. (2019) Fournier gangrene associated with sodium–glucose cotransporter-2 inhibitors: a review of spontaneous postmarketing cases. Annals of Internal Medicine, 170(11), 764-769.

Betancourt, A., Mobley, J. A., Wang, J., Jenkins, S., Chen, D., Kojima, K., Russo, J. & Lamartiniere, C. A. (2014) Alterations in the rat serum proteome induced by prepubertal exposure to bisphenol a and genistein. Journal of proteome research, 13(3), 1502-1514.

Biswas, A., Rabbani, S. I. & Devi, K. (2012) Influence of pioglitazone on experimental heart failure and hyperlipidemia in rats. Indian journal of pharmacology, 44(3), 333.

Bodhini, D. & Mohan, V. (2022) Diabetes burden in the IDF-MENA region. Medknow.

Bonaventura, A., Montecucco, F. & Dallegri, F. (2015) Update on strategies limiting iatrogenic hypoglycemia. Endocrine connections, 4(3), R37-R45.

Bonnefond, A., Unnikrishnan, R., Doria, A., Vaxillaire, M., Kulkarni, R. N., Mohan, V., Trischitta, V. & Froguel, P. (2023) Monogenic diabetes. Nature Reviews Disease Primers, 9(1), 12.

Borts, D. J. (2019) Biomarkers detection for toxicity testing using metabolomics, Biomarkers in ToxicologyElsevier, 1111-1124.

Boucher, J., Kleinridders, A. & Kahn, C. R. (2014) Insulin receptor signaling in normal and insulin-resistant states. Cold Spring Harb Perspect Biol, 6(1).

Brewer, C. T., Kodali, K., Wu, J., Shaw, T. I., Peng, J. & Chen, T. (2020) Toxicoproteomic profiling of hPXR transgenic mice treated with rifampicin and isoniazid. Cells, 9(7), 1654.

Brewitz, L., Tumber, A., Pfeffer, I., McDonough, M. A. & Schofield, C. J. (2020) Aspartate/asparagine-β-hydroxylase: a high-throughput mass spectrometric assay for discovery of small molecule inhibitors. Scientific Reports, 10(1), 8650.

Brockmeier, E. K., Hodges, G., Hutchinson, T. H., Butler, E., Hecker, M., Tollefsen, K. E., Garcia-Reyero, N., Kille, P., Becker, D. & Chipman, K. (2017) The role of omics in the application of adverse outcome pathways for chemical risk assessment. Toxicological Sciences, 158(2), 252-262.

Bujak, R., Struck-Lewicka, W., Markuszewski, M. J. & Kaliszan, R. (2015) Metabolomics for laboratory diagnostics. Journal of pharmaceutical and biomedical analysis, 113, 108-120.

Burnett, S. D., Blanchette, A. D., Chiu, W. A. & Rusyn, I. (2021) Human induced pluripotent stem cell (iPSC)-derived cardiomyocytes as an in vitro model in toxicology: strengths and weaknesses for hazard identification and risk characterization. Expert opinion on drug metabolism & toxicology, 17(8), 887-902.

Buse, J. B. (2016) Liraglutide and Cardiovascular Outcomes in Type 2 Diabetes. The New England journal of medicine, 375(18), 1798-1799.

Busiello, R. A., Savarese, S. & Lombardi, A. (2015) Mitochondrial uncoupling proteins and energy metabolism. Frontiers in Physiology, 6.

Cabaton, N. J., Poupin, N., Canlet, C., Tremblay-Franco, M., Audebert, M., Cravedi, J.-P., Riu, A., Jourdan, F. & Zalko, D. (2018) An untargeted metabolomics approach to investigate the metabolic modulations of HepG2 cells exposed to low doses of bisphenol A and 17β-estradiol. Frontiers in Endocrinology, 9, 571.

Chandra, V., Huang, P., Hamuro, Y., Raghuram, S., Wang, Y., Burris, T. P. & Rastinejad, F. (2008) Structure of the intact PPAR-γ–RXR-α nuclear receptor complex on DNA. Nature, 456(7220), 350-356.

Chatzigeorgiou, A., Halapas, A., Kalafatakis, K. & Kamper, E. (2009) The use of animal models in the study of diabetes mellitus. In vivo, 23(2), 245-258.

Chaudhury, A., Duvoor, C., Reddy Dendi, V. S., Kraleti, S., Chada, A., Ravilla, R., Marco, A., Shekhawat, N. S., Montales, M. T., Kuriakose, K., Sasapu, A., Beebe, A., Patil, N., Musham, C. K., Lohani, G. P. & Mirza, W. (2017) Clinical Review of Antidiabetic Drugs: Implications for Type 2 Diabetes Mellitus Management. Front Endocrinol (Lausanne), 8, 6.

Chen, C., Cohrs, C. M., Stertmann, J., Bozsak, R. & Speier, S. (2017) Human beta cell mass and function in diabetes: Recent advances in knowledge and technologies to understand disease pathogenesis. Mol Metab, 6(9), 943-957.

Chen, X., Yu, C., Kang, R. & Tang, D. (2020) Iron metabolism in ferroptosis. Frontiers in cell and developmental biology, 8, 590226.

Chen, Y., Ni, J., Gao, Y., Zhang, J., Liu, X., Chen, Y., Chen, Z. & Wu, Y. (2020) Integrated proteomics and metabolomics reveals the comprehensive characterization of antitumor mechanism underlying Shikonin on colon cancer patient-derived xenograft model. Scientific Reports, 10(1), 14092.

Cheng, M., Lin, N., Dong, D., Ma, J., Su, J. & Sun, L. (2021) PGAM5: a crucial role in mitochondrial dynamics and programmed cell death. European journal of cell biology, 100(1), 151144.

Chetan, M. R., Thrower, S. L. & Narendran, P. (2019) What is type 1 diabetes? Medicine, 47(1), 5-9.

Chicco, D. & Agapito, G. (2022) Nine quick tips for pathway enrichment analysis. PLoS computational biology, 18(8), e1010348.

Chinnam, P., Mohsin, M. & Shafee, L. M. (2012) Evaluation of acute toxicity of pioglitazone in mice. Toxicology international, 19(3), 250.

Chu, S. H., Huang, M., Kelly, R. S., Benedetti, E., Siddiqui, J. K., Zeleznik, O. A., Pereira, A., Herrington, D., Wheelock, C. E. & Krumsiek, J. (2019) Integration of metabolomic and other omics data in population-based study designs: an epidemiological perspective. Metabolites, 9(6), 117.

Cielecka-Piontek, J., Zalewski, P., Jelińska, A. & Garbacki, P. (2013) UHPLC: the greening face of liquid chromatography. Chromatographia, 76, 1429-1437.

Ciregia, F., Bugliani, M., Ronci, M., Giusti, L., Boldrini, C., Mazzoni, M. R., Mossuto, S., Grano, F., Cnop, M., Marselli, L., Giannaccini, G., Urbani, A., Lucacchini, A. & Marchetti, P. (2017) Palmitate-induced lipotoxicity alters acetylation of multiple proteins in clonal β cells and human pancreatic islets. Sci Rep, 7(1), 13445.

Conlon, K. C. & Duggan, S. N. (2017) Pancreatogenic Type 3c Diabetes: Underestimated, underappreciated and poorly managed. Practical gastroenterology, 15.

Conolly, R. B., Ankley, G. T., Cheng, W., Mayo, M. L., Miller, D. H., Perkins, E. J., Villeneuve, D. L. & Watanabe, K. H. (2017) Quantitative adverse outcome pathways and their application to predictive toxicology. Environmental science & technology, 51(8), 4661-4672.

Coskun, O. (2016) Separation techniques: chromatography. Northern clinics of Istanbul, 3(2), 156.

Courtenay, M. & Griffiths, M. (2010) Introduction to medication errors and medication safety. Medication safety an essential guide, 1-7.

Craze, M. L., El-Ansari, R., Aleskandarany, M. A., Cheng, K. W., Alfarsi, L., Masisi, B., Diez-Rodriguez, M., Nolan, C. C., Ellis, I. O. & Rakha, E. A. (2019) Glutamate dehydrogenase (GLUD1) expression in breast cancer. Breast cancer research and treatment, 174, 79-91.

Currie, C. J., Peyrot, M., Morgan, C. L., Poole, C. D., Jenkins-Jones, S., Rubin, R. R., Burton, C. M. & Evans, M. (2012) The impact of treatment noncompliance on mortality in people with type 2 diabetes. Diabetes care, 35(6), 1279-1284.

D'souza, A. M., Johnson, J. D., Clee, S. M. & Kieffer, T. J. (2016) Suppressing hyperinsulinemia prevents obesity but causes rapid onset of diabetes in leptin-deficient Lepob/ob mice. Molecular metabolism, 5(11), 1103-1112.

Dahabiyeh, L. A., Malkawi, A. K., Wang, X., Colak, D., Mujamammi, A. H., Sabi, E. M., Li, L., Dasouki, M. & Abdel Rahman, A. M. (2020) Dexamethasone-induced perturbations in tissue metabolomics revealed by chemical isotope labeling LC-MS analysis. Metabolites, 10(2), 42.

Davidson, M. M., Nesti, C., Palenzuela, L., Walker, W. F., Hernandez, E., Protas, L., Hirano, M. & Isaac, N. D. (2005) Novel cell lines derived from adult human ventricular cardiomyocytes. Journal of molecular and cellular cardiology, 39(1), 133-147.

Dawed, A. Y., Donnelly, L., Tavendale, R., Carr, F., Leese, G., Palmer, C. N., Pearson, E. R. & Zhou, K. (2016) CYP2C8 and SLCO1B1 variants and therapeutic response to thiazolidinediones in patients with type 2 diabetes. Diabetes care, 39(11), 1902-1908.

Dawed, A. Y., Zhou, K., van Leeuwen, N., Mahajan, A., Robertson, N., Koivula, R., Elders, P. J., Rauh, S. P., Jones, A. G. & Holl, R. W. (2019) Variation in the plasma membrane monoamine transporter (PMAT)(encoded by SLC29A4) and organic cation transporter 1 (OCT1)(encoded by SLC22A1) and gastrointestinal intolerance to metformin in type 2 diabetes: an IMI DIRECT study. Diabetes Care, 42(6), 1027-1033.

Dawson, P. H. (2013) Quadrupole mass spectrometry and its applicationsElsevier.

de Bont, C. M., Boelens, W. C. & Pruijn, G. J. (2019) NETosis, complement, and coagulation: a triangular relationship. Cellular & molecular immunology, 16(1), 19-27.

De Flines, J. & Scheen, A. J. (2007) [Glitazones and congestive heart failure: update on PROactive, ADOPT, DREAM and RECORD clinical trials]. Rev Med Suisse, 3(122), 1876, 1878-83.

De Meyts, P. (2016) The insulin receptor and its signal transduction network, Endotext [Internet]MDText. com, Inc.

de Oliveira Andrade, A., Marques, L. G., Resende, O., Andrade de Oliveira, G., Rodrigues da Silva Souza, L. & Alves Pereira, A. (2022) Prediction and Visualisation of SICONV Project Profiles Using Machine Learning. Systems, 10(6), 252.

Deer, E. L., González-Hernández, J., Coursen, J. D., Shea, J. E., Ngatia, J., Scaife, C. L., Firpo, M. A. & Mulvihill, S. J. (2010) Phenotype and genotype of pancreatic cancer cell lines. Pancreas, 39(4), 425.

DeFronzo, R. A., Inzucchi, S., Abdul-Ghani, M. & Nissen, S. E. (2019) Pioglitazone: the forgotten, cost-effective cardioprotective drug for type 2 diabetes. Diabetes and Vascular Disease Research, 16(2), 133-143.

DeFronzo, R. A., Mehta, R. J. & Schnure, J. J. (2013) Pleiotropic effects of thiazolidinediones: implications for the treatment of patients with type 2 diabetes mellitus. Hospital practice, 41(2), 132-147.

DeFronzo, R., Fleming, G. A., Chen, K. & Bicsak, T. A. (2016) Metformin-associated lactic acidosis: Current perspectives on causes and risk. Metabolism, 65(2), 20-29.

Deline, M. L., Grashei, M., van Heijster, F. H., Schilling, F., Straub, J. & Fromme, T. (2021) Adenylate kinase derived ATP shapes respiration and calcium storage of isolated mitochondria. Biochimica et Biophysica Acta (BBA)-Bioenergetics, 1862(7), 148409.

Demine, S., Renard, P. & Arnould, T. (2019) Mitochondrial uncoupling: a key controller of biological processes in physiology and diseases. Cells, 8(8), 795.

Denicolo, S., Perco, P., Thoeni, S. & Mayer, G. (2021) Non-adherence to antidiabetic and cardiovascular drugs in type 2 diabetes mellitus and its association with renal and

cardiovascular outcomes: A narrative review. Journal of Diabetes and its Complications, 35(7), 107931.

Deputy, N. P., Kim, S. Y., Conrey, E. J. & Bullard, K. M. (2018) Prevalence and changes in preexisting diabetes and gestational diabetes among women who had a live birth—United States, 2012–2016. Morbidity and Mortality Weekly Report, 67(43), 1201.

Deracinois, B., Flahaut, C., Duban-Deweer, S. & Karamanos, Y. (2013) Comparative and quantitative global proteomics approaches: an overview. Proteomes, 1(3), 180-218.

Deshpande, O. A. & Mohiuddin, S. S. (2020) Biochemistry, oxidative phosphorylation.

Dhuriya, Y. K. & Sharma, D. (2018) Necroptosis: a regulated inflammatory mode of cell death. Journal of neuroinflammation, 15(1), 1-9.

Dimitriadis, G., Mitrou, P., Lambadiari, V., Maratou, E. & Raptis, S. A. (2011) Insulin effects in muscle and adipose tissue. Diabetes Research and Clinical Practice, 93, S52-S59.

Dionísio, F., Araújo, A. M., Duarte-Araújo, M., Bastos, M. d. L., Guedes de Pinho, P., Carvalho, F. & Costa, V. M. (2022) Cardiotoxicity of cyclophosphamide's metabolites: An in vitro metabolomics approach in AC16 human cardiomyocytes. Archives of toxicology, 96(2), 653-671.

Doigneaux, C., Pedley, A. M., Mistry, I. N., Papayova, M., Benkovic, S. J. & Tavassoli, A. (2020) Hypoxia drives the assembly of the multienzyme purinosome complex. Journal of Biological Chemistry, 295(28), 9551-9566.

Draznin, B. (2011) Mechanism of the mitogenic influence of hyperinsulinemia. Diabetology & metabolic syndrome, 3(1), 1-3 %@ 1758-5996.

Drucker, D. J. (2007) Dipeptidyl peptidase-4 inhibition and the treatment of type 2 diabetes: preclinical biology and mechanisms of action. Diabetes care, 30(6), 1335-1343.

Duan, S. Z., Ivashchenko, C. Y., Russell, M. W., Milstone, D. S. & Mortensen, R. M. (2005) Cardiomyocyte-specific knockout and agonist of peroxisome proliferator–activated receptor-γ both induce cardiac hypertrophy in mice. Circulation research, 97(4), 372-379.

Duarte, I., Caio, J., Moedas, M., Rodrigues, L., Leandro, A., Rivera, I. & Silva, M. (2021) Dihydrolipoamide dehydrogenase, pyruvate oxidation, and acetylation-dependent mechanisms intersecting drug iatrogenesis. Cellular and Molecular Life Sciences, 1-18.

Eckerle, I., Lenk, M. & Ulrich, R. G. (2014) More novel hantaviruses and diversifying reservoir hosts—time for development of reservoir-derived cell culture models? Viruses, 6(3), 951-967.

Edgerton, D. S., Kraft, G., Smith, M., Farmer, B., Williams, P. E., Coate, K. C., Printz, R. L., O'Brien, R. M. & Cherrington, A. D. (2017) Insulin's direct hepatic effect explains the inhibition of glucose production caused by insulin secretion. JCI insight, 2(6).

Egan, A. M. & Dinneen, S. F. (2019) What is diabetes? Medicine, 47(1), 1-4.

Elashoff, M., Matveyenko, A. V., Gier, B., Elashoff, R. & Butler, P. C. (2011) Pancreatitis, pancreatic, and thyroid cancer with glucagon-like peptide-1–based therapies. Gastroenterology, 141(1), 150-156.

Erdmann, E., Dormandy, J., Wilcox, R., Massi-Benedetti, M. & Charbonnel, B. (2007) PROactive 07: pioglitazone in the treatment of type 2 diabetes: results of the PROactive study. Vascular Health and Risk Management, 3(4), 355-370.

Festuccia, W. T., Laplante, M., Brûlé, S., Houde, V. P., Achouba, A., Lachance, D., Pedrosa, M. L., Silva, M. E., Guerra-Sá, R. & Couet, J. (2009) Rosiglitazone-induced heart remodelling is associated with enhanced turnover of myofibrillar protein and mTOR activation. Journal of molecular and cellular cardiology, 47(1), 85-95.

Forouhi, N. G. & Wareham, N. J. (2022) Epidemiology of diabetes. Medicine.

Fraga-Corral, M., Carpena, M., Garcia-Oliveira, P., Pereira, A., Prieto, M. & Simal-Gandara, J. (2022) Analytical metabolomics and applications in health, environmental and food science. Critical Reviews in Analytical Chemistry, 52(4), 712-734.

Frangogiannis, N. G. (2019) The extracellular matrix in ischemic and nonischemic heart failure. Circulation research, 125(1), 117-146.

Frantz, C., Stewart, K. M. & Weaver, V. M. (2010) The extracellular matrix at a glance. Journal of cell science, 123(24), 4195-4200.

Gan, W. Z., Ramachandran, V., Lim, C. S. Y. & Koh, R. Y. (2019) Omics-based biomarkers in the diagnosis of diabetes. Journal of Basic and Clinical Physiology and Pharmacology, 31(2), 20190120.

García-Cañaveras, J., Castell, J., Donato, M. & Lahoz, A. (2016) A metabolomics cell-based approach for anticipating and investigating drug-induced liver injury. Sci Rep 6: 27239.

Gauthier, B. R. & Wollheim, C. B. (2008) Synaptotagmins bind calcium to release insulin. American Journal of Physiology-Endocrinology and Metabolism, 295(6), E1279-E1286.

Geng, C., Cui, C., Wang, C., Lu, S., Zhang, M., Chen, D. & Jiang, P. (2020) Systematic evaluations of doxorubicin-induced toxicity in rats based on metabolomics. ACS omega, 6(1), 358-366.

Ghasemi, M., Liang, S., Luu, Q. M. & Kempson, I. (2023) The MTT Assay: A Method for Error Minimization and Interpretation in Measuring Cytotoxicity and Estimating Cell Viability, Cell Viability Assays: Methods and ProtocolsSpringer, 15-33.

Giacomelli, E., Meraviglia, V., Campostrini, G., Cochrane, A., Cao, X., Van Helden, R. W., Garcia, A. K., Mircea, M., Kostidis, S. & Davis, R. P. (2020) Human-iPSC-derived cardiac stromal cells enhance maturation in 3D cardiac microtissues and reveal non-cardiomyocyte contributions to heart disease. Cell stem cell, 26(6), 862-879. e11.

Gill, J. S., Bansal, B., Singhal, S., Schaefer, K. & Singhal, S. (2023) Integrated approaches to testing and assessment during the development of arsenic toxicology, Handbook of Arsenic ToxicologyElsevier, 871-882.

Giordano, E., Flamigni, F., Guarnieri, C., Muscari, C., Pignatti, C., Stefanelli, C., Tantini, B. & Caldarera, C. M. (2010) Polyamines in cardiac physiology and disease. Open Heart Failure Journal, 3(1).

Gökalp, O., Gunes, A., Çam, H., Cure, E., Aydın, O., Tamer, M. N., Scordo, M. G. & Dahl, M.-L. (2011) Mild hypoglycaemic attacks induced by sulphonylureas related to CYP2C9, CYP2C19 and CYP2C8 polymorphisms in routine clinical setting. European journal of clinical pharmacology, 67, 1223-1229.

Gouni-Berthold, I., Berthold, H. K., Weber, A.-A., Ko, Y., Seul, C., Vetter, H. & Sachinidis, A. (2001) Troglitazone and rosiglitazone induce apoptosis of vascular smooth muscle cells through an extracellular signal-regulated kinase-independent pathway. Naunyn-Schmiedeberg's archives of pharmacology, 363, 215-221.

Goutelle, S., Maurin, M., Rougier, F., Barbaut, X., Bourguignon, L., Ducher, M. & Maire, P. (2008) The Hill equation: a review of its capabilities in pharmacological modelling. Fundamental & clinical pharmacology, 22(6), 633-648.

Graudejus, O., Ponce Wong, R., Varghese, N., Wagner, S. & Morrison, B. (2018) Bridging the gap between in vivo and in vitro research: Reproducing in vitro the mechanical and electrical environment of cells in vivo. Frontiers in Cellular Neuroscience, 12.

Greggio, C., De Franceschi, F. & Grapin-Botton, A. (2015) Concise Reviews: In Vitro-Produced Pancreas Organogenesis Models in Three Dimensions: Self-Organization From Few Stem Cells or Progenitors. Stem Cells, 33(1), 8-14.

Groen, E., Mummery, C. L., Yiangou, L. & Davis, R. P. (2024) Three-dimensional cardiac models: a pre-clinical testing platform. Biochemical Society Transactions, BST20230444.

Group, A. t. C. C. R. i. D. S. (2008) Effects of intensive glucose lowering in type 2 diabetes. New England journal of medicine, 358(24), 2545-2559.

Guo, X., Chen, Y. & Liu, Q. (2022) Necroptosis in heart disease: Molecular mechanisms and therapeutic implications. Journal of molecular and cellular cardiology, 169, 74-83.

Guthrie, R. (2018) Canagliflozin and cardiovascular and renal events in type 2 diabetes. Postgraduate Medicine, 130(2), 149-153.

Haag, A. M. (2016) Mass analyzers and mass spectrometers. Modern proteomics–Sample preparation, analysis and practical applications, 157-169.

Haimbaugh, A., Meyer, D., Akemann, C., Gurdziel, K. & Baker, T. R. (2022) Comparative toxicotranscriptomics of single cell RNA-Seq and conventional RNA-Seq in TCDD-exposed testicular tissue. Frontiers in Toxicology, 4, 821116.

Halappanavar, S., Van Den Brule, S., Nymark, P., Gaté, L., Seidel, C., Valentino, S., Zhernovkov, V., Høgh Danielsen, P., De Vizcaya, A. & Wolff, H. (2020) Adverse outcome pathways as a tool for the design of testing strategies to support the safety assessment of emerging advanced materials at the nanoscale. Particle and Fibre Toxicology, 17, 1-24.

Hartmann, S., Ridley, A. J. & Lutz, S. (2015) The function of Rho-associated kinases ROCK1 and ROCK2 in the pathogenesis of cardiovascular disease. Frontiers in pharmacology, 6, 276.

He, G.-W., Günther, C., Kremer, A. E., Thonn, V., Amann, K., Poremba, C., Neurath, M. F., Wirtz, S. & Becker, C. (2017) PGAM5-mediated programmed necrosis of hepatocytes drives acute liver injury. Gut, 66(4), 716-723.

He, H., Tao, H., Xiong, H., Duan, S. Z., McGowan Jr, F. X., Mortensen, R. M. & Balschi, J. A. (2014) Rosiglitazone causes cardiotoxicity via peroxisome proliferator-activated receptor γ-independent mitochondrial oxidative stress in mouse hearts. Toxicological Sciences, 138(2), 468-481.

Hemmerich, J. & Ecker, G. F. (2020) In silico toxicology: From structure–activity relationships towards deep learning and adverse outcome pathways. Wiley Interdisciplinary Reviews: Computational Molecular Science, 10(4), e1475.

Herman, W. H., Schillinger, D., Bolen, S., Boltri, J. M., Bullock, A., Chong, W., Conlin, P. R., Cook IV, J. W., Dokun, A. & Fukagawa, N. (2023) The National Clinical Care Commission report to Congress: recommendations to better leverage federal policies and programs to prevent and control diabetes. Diabetes Care, 46(2), 255-261.

Herrer, I., Roselló-Lletí, E., Rivera, M., Molina-Navarro, M. M., Tarazón, E., Ortega, A., Martínez-Dolz, L., Triviño, J. C., Lago, F. & González-Juanatey, J. R. (2014) RNA-sequencing analysis reveals new alterations in cardiomyocyte cytoskeletal genes in patients with heart failure. Laboratory investigation, 94(6), 645-653.

Hiram-Bab, S., Shapira, Y., Gershengorn, M. C. & Oron, Y. (2012) Serum deprivation induces glucose response and intercellular coupling in human pancreatic adenocarcinoma PANC-1 cells. Pancreas, 41(2), 238.

Holman, R. R., Bethel, M. A., Mentz, R. J., Thompson, V. P., Lokhnygina, Y., Buse, J. B., Chan, J. C., Choi, J., Gustavson, S. M. & Iqbal, N. (2017) Effects of once-weekly exenatide on cardiovascular outcomes in type 2 diabetes. New England Journal of Medicine, 377(13), 1228-1239.

Holman, R. R., Paul, S. K., Bethel, M. A., Matthews, D. R. & Neil, H. A. W. (2008) 10-year follow-up of intensive glucose control in type 2 diabetes. New England journal of medicine, 359(15), 1577-1589.

Home, P. D., Pocock, S. J., Beck-Nielsen, H., Gomis, R., Hanefeld, M., Jones, N. P., Komajda, M. & McMurray, J. J. (2007) Rosiglitazone evaluated for cardiovascular outcomes—an interim analysis. New England Journal of Medicine, 357(1), 28-38.

Horita, S., Nakamura, M., Satoh, N., Suzuki, M. & Seki, G. (2015) Thiazolidinediones and edema: recent advances in the pathogenesis of thiazolidinediones-induced renal sodium retention. PPAR research, 2015.

Hsieh, J.-Y., Shih, W.-T., Kuo, Y.-H., Liu, G.-Y. & Hung, H.-C. (2019) Functional roles of metabolic intermediates in regulating the human mitochondrial NAD (P)+-dependent malic enzyme. Scientific Reports, 9(1), 9081.

Hu, C. & Jia, W. (2021) Multi-omics profiling: the way toward precision medicine in metabolic diseases. Journal of molecular cell biology, 13(8), 576-593.

Hu, P., Miller, A. E., Yeh, C.-R., Bingham, G. C., Civelek, M. & Barker, T. H. (2023) SEMA7a primes integrin α5β1 engagement instructing fibroblast mechanotransduction, phenotype and transcriptional programming. Matrix Biology, 121, 179-193.

Hu, W., Liang, K., Zhu, H., Zhao, C., Hu, H. & Yin, S. (2022) Ferroptosis and its role in chronic diseases. Cells, 11(13), 2040.

Hubbard, S. R. (1997) Crystal structure of the activated insulin receptor tyrosine kinase in complex with peptide substrate and ATP analog. The EMBO journal.

Hubbard, S. R., Wei, L. & Hendrickson, W. A. (1994) Crystal structure of the tyrosine kinase domain of the human insulin receptor. Nature, 372(6508), 746-754.

Hughes, G., Cruickshank-Quinn, C., Reisdorph, R., Lutz, S., Petrache, I., Reisdorph, N., Bowler, R. & Kechris, K. (2014) MSPrep—Summarization, normalization and diagnostics for processing of mass spectrometry–based metabolomic data. Bioinformatics, 30(1), 133-134.

Hui, H., Wright, C. & Perfetti, R. (2001) Glucagon-like peptide 1 induces differentiation of islet duodenal homeobox-1–positive pancreatic ductal cells into insulin-secreting cells. Diabetes, 50(4), 785-796.

Huveneers, S. & Danen, E. H. (2009) Adhesion signaling–crosstalk between integrins, Src and Rho. Journal of cell science, 122(8), 1059-1069.

Imami, K., Selbach, M. & Ishihama, Y. (2023) Monitoring mitochondrial translation by pulse SILAC. Journal of Biological Chemistry, 299(2).

Irfan Maqsood, M., Matin, M. M., Bahrami, A. R. & Ghasroldasht, M. M. (2013) Immortality of cell lines: challenges and advantages of establishment. Cell biology international, 37(10), 1038-1045.

Jarrar, Y. B., Jarrar, Q., Abaalkhail, S. J., Moh'd Kalloush, H., Naser, W., Zihlif, M., Al Shhab, M., El Madani, A., Jamous, Y. & Lee, S. J. (2022) Molecular toxicological alterations in the mouse hearts induced by sub-chronic thiazolidinedione drugs administration. Fundamental & Clinical Pharmacology, 36(1), 143-149.

Jennings, P. (2015) The future of in vitro toxicology. Toxicology in Vitro, 29(6), 1217-1221.

Johnson, T. A., Jinnah, H. & Kamatani, N. (2019) Shortage of cellular ATP as a cause of diseases and strategies to enhance ATP. Frontiers in pharmacology, 10, 98.

Jonsson, M. K., Hartman, R. J., Ackers-Johnson, M., Tan, W. L., Lim, B., van Veen, T. A. & Foo, R. S. (2016) A transcriptomic and epigenomic comparison of fetal and adult human cardiac fibroblasts reveals novel key transcription factors in adult cardiac fibroblasts. JACC: Basic to Translational Science, 1(7), 590-602.

Joon, H. K., Thalor, A. & Gupta, D. (2023) Machine learning analysis of lung squamous cell carcinoma gene expression datasets reveals novel prognostic signatures. Computers in Biology and Medicine, 107430.

Joseph, P. (2017) Transcriptomics in toxicology. Food and Chemical Toxicology, 109, 650-662.

Julie, N., Julie, I., Kende, A. & Wilson, G. (2008) Mitochondrial dysfunction and delayed hepatotoxicity: another lesson from troglitazone. Diabetologia, 51, 2108-2116.

Kahn, S. E., Haffner, S. M., Heise, M. A., Herman, W. H., Holman, R. R., Jones, N. P., Kravitz, B. G., Lachin, J. M., O'Neill, M. C. & Zinman, B. (2006) Glycemic durability of rosiglitazone, metformin, or glyburide monotherapy. New England Journal of Medicine, 355(23), 2427-2443.

Karahalil, B. (2016) Overview of systems biology and omics technologies. Current medicinal chemistry, 23(37), 4221-4230.

Karugu, C. H., Ilboudo, P. G., Boachie, M. K., Mburu, L., Sanya, R., Moolla, A., Ojiambo, V., Kruger, P., Vandevijvere, S. & Agyemang, C. (2023) The Economic Burden of Type 2 Diabetes on the Public Healthcare System in Kenya: A Cost of Illness Study.

Karwi, Q. G. & Lopaschuk, G. D. (2023) Branched-chain amino acid metabolism in the failing heart. Cardiovascular Drugs and Therapy, 37(2), 413-420.

Kennel, P. J., Liao, X., Saha, A., Ji, R., Zhang, X., Castillero, E., Brunjes, D., Takayama, H., Naka, Y. & Thomas, T. (2019) Impairment of myocardial glutamine homeostasis induced by suppression of the amino acid carrier SLC1A5 in failing myocardium. Circulation: Heart Failure, 12(12), e006336.

Khalil, S. A., Azar, S., Hafidh, K., Ayad, G. & Safwat, M. (2024) Prevalence and Co-prevalence of Comorbidities among Patients with Type 2 Diabetes Mellitus in the MENA Region: A Systematic Review. Current Diabetes Reviews, 20(7).

Khan, S., Beigh, S., Chaudhari, B. P., Sharma, S., Aliul Hasan Abdi, S., Ahmad, S., Ahmad, F., Parvez, S. & Raisuddin, S. (2016) Mitochondrial dysfunction induced by Bisphenol A is a factor of its hepatotoxicity in rats. Environmental toxicology, 31(12), 1922-1934.

Kharechkina, E. S., Nikiforova, A. B., Belosludtsev, K. N., Rokitskaya, T. I., Antonenko, Y. N. & Kruglov, A. G. (2021) Pioglitazone is a mild carrier-dependent uncoupler of oxidative phosphorylation and a modulator of mitochondrial permeability transition. Pharmaceuticals, 14(10), 1045.

Kim, J.-H., Nam, W. S., Kim, S. J., Kwon, O. K., Seung, E. J., Jo, J. J., Shresha, R., Lee, T. H., Jeon, T. W. & Ki, S. H. (2017) Mechanism investigation of rifampicin-induced liver injury using comparative toxicoproteomics in mice. International journal of molecular sciences, 18(7), 1417.

Kim, S. H. & Cho, S. Y. (2023) Single-cell transcriptomics to understand the cellular heterogeneity in toxicology. Molecular & Cellular Toxicology, 19(2), 223-228.

Kirkland, J. & DeStefano, J. (2006) The art and science of forming packed analytical high-performance liquid chromatography columns. Journal of Chromatography A, 1126(1-2), 50-57.

Kirkman, M. S., Mahmud, H. & Korytkowski, M. T. (2018) Intensive blood glucose control and vascular outcomes in patients with type 2 diabetes mellitus. Endocrinology and Metabolism Clinics, 47(1), 81-96.

Kirschstein, T., Sahre, T., Kernig, K., Protzel, C., Porath, K., Köhling, R. & Hakenberg, O. W. (2015) Inverse relationship of Rho kinase and myosin-light chain kinase expression in the aging human detrusor smooth muscle. BMC urology, 15(1), 1-9.

Kisly, I., Remme, J. & Tamm, T. (2019) Ribosomal protein eL24, involved in two intersubunit bridges, stimulates translation initiation and elongation. Nucleic acids research, 47(1), 406-420.

Kojima, N. (2014) In vitro reconstitution of pancreatic islets. Organogenesis, 10(2), 225-230.

Kolde, R. & Kolde, M. R. (2015) Package 'pheatmap'. R package, 1(7), 790.

Korkmaz, H. A. & Ermiş, Ç. (2019) A case of immune-mediated type 1 diabetes mellitus due to congenital rubella ınfection. Annals of Pediatric Endocrinology & Metabolism, 24(1), 68.

Krewski, D., Acosta Jr, D., Andersen, M., Anderson, H., Bailar III, J. C., Boekelheide, K., Brent, R., Charnley, G., Cheung, V. G. & Green Jr, S. (2010) Toxicity testing in the 21st century: a vision and a strategy. Journal of Toxicology and Environmental Health, Part B, 13(2-4), 51-138.

Krewski, D., Andersen, M. E., Tyshenko, M. G., Krishnan, K., Hartung, T., Boekelheide, K., Wambaugh, J. F., Jones, D., Whelan, M. & Thomas, R. (2020) Toxicity testing in the 21st century: progress in the past decade and future perspectives. Archives of toxicology, 94, 1-58.

Krijthe, J., van der Maaten, L. & Krijthe, M. J. (2018) Package 'Rtsne'. R package version 0.13.

Kumar, U. & Singh, S. (2020) Role of Somatostatin in the Regulation of Central and Peripheral Factors of Satiety and Obesity. International Journal of Molecular Sciences, 21(7), 2568.

Kupai, K., Várkonyi, T., Török, S., Gáti, V., Czimmerer, Z., Puskás, L. G. & Szebeni, G. J. (2022) Recent Progress in the Diagnosis and Management of Type 2 Diabetes Mellitus in the Era of COVID-19 and Single Cell Multi-Omics Technologies. Life, 12(8), 1205.

Lai, L., Leone, T. C., Keller, M. P., Martin, O. J., Broman, A. T., Nigro, J., Kapoor, K., Koves, T. R., Stevens, R. & Ilkayeva, O. R. (2014) Energy metabolic reprogramming in the hypertrophied and early stage failing heart: a multisystems approach. Circulation: Heart Failure, 7(6), 1022-1031.

Lane, A. N. & Fan, T. W. (2015) Regulation of mammalian nucleotide metabolism and biosynthesis. Nucleic acids research, 43(4), 2466-2485.

Lang, S., Pfeffer, S., Lee, P.-H., Cavalié, A., Helms, V., Förster, F. & Zimmermann, R. (2017) An update on Sec61 channel functions, mechanisms, and related diseases. Frontiers in physiology, 887.

Langfelder, P. & Horvath, S. (2008) WGCNA: an R package for weighted correlation network analysis. BMC bioinformatics, 9(1), 1-13.

Langfelder, P. & Horvath, S. (2012) Fast R functions for robust correlations and hierarchical clustering. Journal of statistical software, 46(11).

Langhans, S. A. (2018) Three-dimensional in vitro cell culture models in drug discovery and drug repositioning. Frontiers in pharmacology, 9, 6.

Lankatillake, C., Huynh, T. & Dias, D. A. (2019) Understanding glycaemic control and current approaches for screening antidiabetic natural products from evidence-based medicinal plants. Plant methods, 15(1), 105.

Lee, A. Y., Jang, Y., Hong, S.-H., Chang, S.-H., Park, S., Kim, S., Kang, K.-S., Kim, J.-E. & Cho, M.-H. (2017) Ephedrine-induced mitophagy via oxidative stress in human hepatic stellate cells. The Journal of Toxicological Sciences, 42(4), 461-473.

Lee, L. C., Liong, C.-Y. & Jemain, A. A. (2018) Partial least squares-discriminant analysis (PLS-DA) for classification of high-dimensional (HD) data: a review of contemporary practice strategies and knowledge gaps. Analyst, 143(15), 3526-3539.

Lemelman, M. B., Letourneau, L. & Greeley, S. A. W. (2018) Neonatal diabetes mellitus: an update on diagnosis and management. Clinics in perinatology, 45(1), 41-59 %@ 0095-5108.

Lheureux, P. E. & Hantson, P. (2009) Carnitine in the treatment of valproic acid-induced toxicity. Clinical Toxicology, 47(2), 101-111.

Li, H. H., Hyduke, D. R., Chen, R., Heard, P., Yauk, C. L., Aubrecht, J. & Fornace Jr, A. J. (2015) Development of a toxicogenomics signature for genotoxicity using a dose-

optimization and informatics strategy in human cells. Environmental and molecular mutagenesis, 56(6), 505-519.

Li, J., Lang, M.-J., Mao, X.-B., Tian, L. & Feng, Y.-B. (2008a) Antiapoptosis and mitochondrial effect of pioglitazone preconditioning in the ischemic/reperfused heart of rat. Cardiovascular drugs and therapy, 22, 283-291.

Li, J., Liu, N. & Wei, Q. (2008b) Effect of rosiglitazone on cardiac fibroblast proliferation, nitric oxide production and connective tissue growth factor expression induced by advanced glycation end-products. Journal of International Medical Research, 36(2), 329-335.

Li, L., Shen, J., Bala, M. M., Busse, J. W., Ebrahim, S., Vandvik, P. O., Rios, L. P., Malaga, G., Wong, E. & Sohani, Z. (2014) Incretin treatment and risk of pancreatitis in patients with type 2 diabetes mellitus: systematic review and meta-analysis of randomised and non-randomised studies. Bmj, 348, g2366.

Li, W., Li, S., Cao, Z., Sun, Y., Qiu, W., Jia, M. & Su, M. (2022) Exploration of the amino acid metabolic signature in anthracycline-induced cardiotoxicity using an optimized targeted metabolomics approach based on UPLC-MS/MS. Naunyn-Schmiedeberg's Archives of Pharmacology, 395(10), 1209-1224.

Li, Y.-Y., Ghanbari, R., Pathmasiri, W., McRitchie, S., Poustchi, H., Shayanrad, A., Roshandel, G., Etemadi, A., Pollock, J. D. & Malekzadeh, R. (2020) Untargeted metabolomics: biochemical perturbations in Golestan Cohort Study opium users inform intervention strategies. Frontiers in Nutrition, 7, 584585.

Li, Y., Ma, L., Wu, D. & Chen, G. (2021) Advances in bulk and single-cell multi-omics approaches for systems biology and precision medicine. Briefings in Bioinformatics, 22(5), bbab024.

Liang, H., Tang, T., Huang, H., Li, T., Gao, C., Han, Y., Yuan, B., Gao, S., Wang, H. & Zhou, M.-L. (2022) Peroxisome proliferator-activated receptor-γ ameliorates neuronal ferroptosis after traumatic brain injury in mice by inhibiting cyclooxygenase-2. Experimental Neurology, 354, 114100.

Lin, P.-P., Hsieh, Y.-M., Kuo, W.-W., Lin, C.-C., Tsai, F.-J., Tsai, C.-H., Huang, C.-Y. & Tsai, C.-C. (2012) Inhibition of cardiac hypertrophy by probiotic-fermented purple sweet potato yogurt in spontaneously hypertensive rat hearts. International journal of molecular medicine, 30(6), 1365-1375.

Lincoff, A. M., Wolski, K., Nicholls, S. J. & Nissen, S. E. (2007) Pioglitazone and risk of cardiovascular events in patients with type 2 diabetes mellitus: a meta-analysis of randomized trials. Jama, 298(10), 1180-1188.

Liu, J., Li, L., Li, S., Wang, Y., Qin, X., Deng, K., Liu, Y., Zou, K. & Sun, X. (2020) SGLT2 inhibitors and risk of diabetic ketoacidosis in patients with type 2 diabetes: systematic review and meta-analysis of randomized controlled trials. Diabetes, Obesity & Metabolism.

Liu, J., Liu, S., Yu, Z., Qiu, X., Jiang, R. & Li, W. (2022) Uncovering the gene regulatory network of type 2 diabetes through multi-omic data integration. Journal of Translational Medicine, 20(1), 604.

Liu, Q., Chen, Y., Auger-Messier, M. & Molkentin, J. D. (2012) Interaction between NFκB and NFAT coordinates cardiac hypertrophy and pathological remodeling. Circulation research, 110(8), 1077-1086.

Liu, S.-S., Li, J.-S., Xue, M., Wu, W.-J., Li, X. & Chen, W. (2023) LncRNA UCA1 Participates in De Novo Synthesis of Guanine Nucleotides in Bladder Cancer by Recruiting TWIST1 to Increase IMPDH1/2. International Journal of Biological Sciences, 19(8), 2599.

Liu, S., Zeng, F., Fan, G. & Dong, Q. (2021) Identification of hub genes and construction of a transcriptional regulatory network associated with tumor recurrence in colorectal cancer by weighted gene co-expression network analysis. Frontiers in genetics, 12, 649752.

Lygate, C. A., Hulbert, K., Monfared, M., Cole, M. A., Clarke, K. & Neubauer, S. (2003) The PPARγ-activator rosiglitazone does not alter remodeling but increases mortality in rats post-myocardial infarction. Cardiovascular Research, 58(3), 632-637.

Ma, T., Du, J., Zhang, Y., Wang, Y., Wang, B. & Zhang, T. (2022) GPX4-independent ferroptosis—a new strategy in disease's therapy. Cell death discovery, 8(1), 434.

Madeira, P. J. A., Alves, P. A. & Borges, C. M. (2012) High resolution mass spectrometry using FTICR and orbitrap instruments. Fourier Transform–Materials Analysis.

Mancioppi, V., Pozzi, E., Zanetta, S., Missineo, A., Savastio, S., Barbetti, F., Mellone, S., Giordano, M. & Rabbone, I. (2023) Case report: Better late than never, but sooner is better: switch from CSII to sulfonylureas in two patients with neonatal diabetes due to KCNJ11 variants. Frontiers in Endocrinology, 14, 1143736.

Mann, J. F., Ørsted, D. D., Brown-Frandsen, K., Marso, S. P., Poulter, N. R., Rasmussen, S., Tornøe, K., Zinman, B. & Buse, J. B. (2017) Liraglutide and renal outcomes in type 2 diabetes. New England Journal of Medicine, 377(9), 839-848.

Manso, A. M., Okada, H., Sakamoto, F. M., Moreno, E., Monkley, S. J., Li, R., Critchley, D. R. & Ross, R. S. (2017) Loss of mouse cardiomyocyte talin-1 and talin-2 leads to β-1 integrin reduction, costameric instability, and dilated cardiomyopathy. Proceedings of the National Academy of Sciences, 114(30), E6250-E6259.

Marso, S. P., Bain, S. C., Consoli, A., Eliaschewitz, F. G., Jódar, E., Leiter, L. A., Lingvay, I., Rosenstock, J., Seufert, J. & Warren, M. L. (2016) Semaglutide and cardiovascular outcomes in patients with type 2 diabetes. N Engl J Med, 375, 1834-1844.

Martin, L. D., Hoagland, M. A., Rhodes, E. T., Wolfsdorf, J. I., Hamrick, J. L., Fehr, J., Kim, E., Tommerdahl, K., Gleich, S. J. & O'Reilly-Shah, V. (2020) Perioperative Management of Pediatric Patients With Type 1 Diabetes Mellitus, Updated Recommendations for Anesthesiologists. Anesthesia & Analgesia, 130(4), 821-827.

Marunouchi, T., Nishiumi, C., Iinuma, S., Yano, E. & Tanonaka, K. (2021) Effects of Hsp90 inhibitor on the RIP1-RIP3-MLKL pathway during the development of heart failure in mice. European Journal of Pharmacology, 898, 173987.

Marx-Stoelting, P., Braeuning, A., Buhrke, T., Lampen, A., Niemann, L., Oelgeschlaeger, M., Rieke, S., Schmidt, F., Heise, T. & Pfeil, R. (2015) Application of omics data in regulatory toxicology: report of an international BfR expert workshop. Springer.

Mascolo, A., Rafaniello, C., Sportiello, L., Sessa, M., Cimmaruta, D., Rossi, F. & Capuano, A. (2016) Dipeptidyl peptidase (DPP)-4 inhibitor-induced arthritis/arthralgia: a review of clinical cases. Drug safety, 39, 401-407.

Matthiesen, R. (2020) LC-MS Spectra Processing. Mass Spectrometry Data Analysis in Proteomics, 59-77.

McCann, M. R., George De la Rosa, M. V., Rosania, G. R. & Stringer, K. A. (2021) L-carnitine and acylcarnitines: mitochondrial biomarkers for precision medicine. Metabolites, 11(1), 51.

Meagher, P. B., Lee, X. A., Lee, J., Visram, A., Friedberg, M. K. & Connelly, K. A. (2021) Cardiac fibrosis: key role of integrins in cardiac homeostasis and remodeling. Cells, 10(4), 770.

Meana, C., Rubin, J. M., Bordallo, C., Suarez, L., Bordallo, J. & Sanchez, M. (2016) Correlation between endogenous polyamines in human cardiac tissues and clinical parameters in patients with heart failure. Journal of cellular and molecular medicine, 20(2), 302-312.

Medina, D. A. V., Maciel, E. V. S. & Lanças, F. M. (2023) Mass spectrometric detection, instrumentation, and ionization methods, Liquid ChromatographyElsevier, 679-706.

Mendoza-Porras, O., Rusu, A. G., Stratford, C. & Wade, N. M. (2024) Rapid detection of heat stress biomarkers in Atlantic salmon (Salmo salar) liver using targeted proteomics. Aquaculture, Fish and Fisheries, 4(1), e147.

Minze, M. G., Will, K. J., Terrell, B. T., Black, R. L. & Irons, B. K. (2018) Benefits of SGLT2 inhibitors beyond glycemic control–a focus on metabolic, cardiovascular and renal outcomes. Current Diabetes Reviews, 14(6), 509-517.

Mishra, P., Singh, S. V., Verma, A. K., Srivastava, P., Sultana, S. & Rath, S. K. (2014) Rosiglitazone induces cardiotoxicity by accelerated apoptosis. Cardiovascular toxicology, 14, 99-119.

Morgan, M. J. & Kim, Y.-S. (2022) Roles of RIPK3 in necroptosis, cell signaling, and disease. Experimental & molecular medicine, 54(10), 1695-1704.

Mortimer, M., Fang, W., Zhou, X., Vodovnik, M. & Guo, L.-H. (2022) Omics Approaches in Toxicological Studies, Advances in Toxicology and Risk Assessment of Nanomaterials and Emerging ContaminantsSpringer, 61-94.

Moulder, R., Bhosale, S. D., Goodlett, D. R. & Lahesmaa, R. (2018) Analysis of the plasma proteome using iTRAQ and TMT-based Isobaric labeling. Mass spectrometry reviews, 37(5), 583-606.

Nahar, L., Onder, A. & Sarker, S. D. (2020) A review on the recent advances in HPLC, UHPLC and UPLC analyses of naturally occurring cannabinoids (2010–2019). Phytochemical Analysis, 31(4), 413-457.

Naim, M. J., Alam, M. J., Ahmad, S., Nawaz, F., Shrivastava, N., Sahu, M. & Alam, O. (2017) Therapeutic journey of 2, 4-thiazolidinediones as a versatile scaffold: An insight into structure activity relationship. European journal of medicinal chemistry, 129, 218-250.

Nakagawa, Y., Suzuki, T., Kamimura, H. & Nagai, F. (2005) N-Nitrosofenfluramine induces cytotoxicity via mitochondrial dysfunction and oxidative stress in isolated rat hepatocytes. Archives of toxicology, 79, 312-320.

Neal, B., Perkovic, V., de Zeeuw, D., Mahaffey, K. W., Fulcher, G., Stein, P., Desai, M., Shaw, W., Jiang, J. & Vercruysse, F. (2013) Rationale, design, and baseline characteristics of the Canagliflozin Cardiovascular Assessment Study (CANVAS)—a randomized placebo-controlled trial. American heart journal, 166(2), 217-223. e11.

Neal, B., Perkovic, V., Matthews, D. R., Mahaffey, K. W., Fulcher, G., Meininger, G., Erondu, N., Desai, M., Shaw, W. & Vercruysse, F. (2017) Rationale, design and baseline characteristics of the CANagliflozin cardioVascular Assessment Study–Renal (CANVAS-R): A randomized, placebo-controlled trial. Diabetes, Obesity and Metabolism, 19(3), 387-393.

Neidigh, J. W., Fesinmeyer, R. M., Prickett, K. S. & Andersen, N. H. (2001) Exendin-4 and glucagon-like-peptide-1: NMR structural comparisons in the solution and micelle-associated states. Biochemistry, 40(44), 13188-13200.

Neishabouri, S. H., Hutson, S. & Davoodi, J. (2015) Chronic activation of mTOR complex 1 by branched chain amino acids and organ hypertrophy. Amino acids, 47, 1167-1182.

Ng, K. W. & Schantz, J.-T. (2010) A manual for primary human cell cultureWorld Scientific.

Ng, S. M. & Soni, A. (2023) Ten-year review of trends in children with type 1 diabetes in England and Wales. World Journal of Diabetes, 14(8), 1194.

Nguyen, N., Jennen, D. & Kleinjans, J. (2022) Omics technologies to understand drug toxicity mechanisms. Drug Discovery Today, 103348.

Niles, A. L., Moravec, R. A. & Riss, T. L. (2008) Caspase activity assays. Apoptosis and Cancer: Methods and Protocols, 137-150.

Nissen, S. E. & Wolski, K. (2007) Effect of rosiglitazone on the risk of myocardial infarction and death from cardiovascular causes. New England Journal of Medicine, 356(24), 2457-2471.

Ntaios, G. & Kent, T. A. (2016) Insulin resistance intervention after stroke trial of pioglitazone: Is this perhaps the end of the beginning? Stroke, 47(7), 1962-1964.

Nury, C., Merg, C., Eb-Levadoux, Y., Bovard, D., Porchet, M., Maranzano, F., Loncarevic, I., Tavalaei, S., Lize, E. & Demenescu, R. L. (2023) Toxicoproteomics reveals an effect of clozapine on autophagy in human liver spheroids. Toxicology Mechanisms and Methods, 33(5), 401-410.

Nyirjesy, P., Zhao, Y., Ways, K. & Usiskin, K. (2012) Evaluation of vulvovaginal symptoms and Candida colonization in women with type 2 diabetes mellitus treated with canagliflozin, a sodium glucose co-transporter 2 inhibitor. Current medical research and opinion, 28(7), 1173-1178.

Nymark, P., Karlsson, H. L., Halappanavar, S. & Vogel, U. (2021) Adverse outcome pathway development for assessment of lung carcinogenicity by nanoparticles. Frontiers in Toxicology, 3, 653386.

Obradovic, M., Sudar-Milovanovic, E., Gluvic, Z., Banjac, K., Rizzo, M. & Isenovic, E. R. (2023) The Na+/K+-ATPase: A potential therapeutic target in cardiometabolic diseases. Frontiers in Endocrinology, 14, 1150171.

Okumura, A., Takagi, M., Numoto, S., Iwayama, H., Azuma, Y. & Kurahashi, H. (2021) Effects of L-carnitine supplementation in patients with childhood-onset epilepsy prescribed valproate. Epilepsy & Behavior, 122, 108220.

Okura, N., Asano, M., Uchino, J., Morimoto, Y., Iwasaku, M., Kaneko, Y., Yamada, T., Fukui, M. & Takayama, K. (2020) Endocrinopathies associated with immune checkpoint inhibitor cancer treatment: a review. Journal of Clinical Medicine, 9(7), 2033.

Olesti, E., González-Ruiz, V., Wilks, M. F., Boccard, J. & Rudaz, S. (2021) Approaches in metabolomics for regulatory toxicology applications. Analyst, 146(6), 1820-1834.

Omori, Y., Ohtani, T., Sakata, Y., Mano, T., Takeda, Y., Tamaki, S., Tsukamoto, Y., Kamimura, D., Aizawa, Y. & Miwa, T. (2012) L-Carnitine prevents the development of ventricular fibrosis and heart failure with preserved ejection fraction in hypertensive heart disease. Journal of hypertension, 30(9), 1834-1844.

Onishi, M., Yamano, K., Sato, M., Matsuda, N. & Okamoto, K. (2021) Molecular mechanisms and physiological functions of mitophagy. The EMBO journal, 40(3), e104705.

Orsburn, B. C. (2021) Proteome discoverer—a community enhanced data processing suite for protein informatics. Proteomes, 9(1), 15.

Ozdian, T., Holub, D., Maceckova, Z., Varanasi, L., Rylova, G., Rehulka, J., Vaclavkova, J., Slavik, H., Moudry, P. & Znojek, P. (2017) Proteomic profiling reveals DNA damage, nucleolar and ribosomal stress are the main responses to oxaliplatin treatment in cancer cells. Journal of proteomics, 162, 73-85.

Pan, D., Gao, J., Zeng, X., Ma, G., Li, N., Huang, X., Du, X., Miao, Q., Lian, J. & Xu, L. (2017) Quantitative proteomic Analysis Reveals up-regulation of caveolin-1 in FOXP3-overexpressed human gastric cancer cells. Scientific reports, 7(1), 14460.

Park, S., Kang, H.-J., Jeon, J.-H., Kim, M.-J. & Lee, I.-K. (2019) Recent advances in the pathogenesis of microvascular complications in diabetes. Archives of Pharmacal Research, 42(3), 252-262.

Park, T.-S. & Goldberg, I. J. (2012) Sphingolipids, lipotoxic cardiomyopathy, and cardiac failure. Heart failure clinics, 8(4), 633-641.

Passaro, A. P., Marzuillo, P., Guarino, S., Scaglione, F., Del Giudice, E. M. & Di Sessa, A. (2021) Omics era in type 2 diabetes: From childhood to adulthood. World Journal of Diabetes, 12(12), 2027.

Pedrosa, I., Cardoso, F., Martins, V. & Gama, E. (2023) Integrated care process in type 1 diabetes mellitus in children and adolescents: A quality improvement initiative. Journal of Healthcare Quality Research, 38(4), 245-249.

Pelley, J. W. (2012) 5 - Membranes and Intracellular Signal Transduction, in Pelley, J. W. (ed), Elsevier's Integrated Review Biochemistry (Second Edition). Philadelphia: W.B. Saunders, 39-48.

Penn, L., Rodrigues, A., Haste, A., Marques, M. M., Budig, K., Sainsbury, K., Bell, R., Araújo-Soares, V., White, M. & Summerbell, C. (2018) NHS Diabetes Prevention Programme in England: formative evaluation of the programme in early phase implementation. BMJ open, 8(2).

Persaud, S. J., Hauge-Evans, A. C. & Jones, P. M. (2014) Insulin-Secreting Cell Lines: Potential for Research and Diabetes Therapy, Cellular Endocrinology in Health and DiseaseElsevier, 239-256.

Petersen, M. C. & Shulman, G. I. (2018) Mechanisms of insulin action and insulin resistance. Physiological reviews, 98(4), 2133-2223 %@ 0031-9333.

Pfeffer MA, C., Diaz R, D., Gerstein, H., Køber, L., Lawson, F., Ping, L., Wei, X., Lewis, E., Maggioni, A. & McMurray, J. (2015) Lixisenatide in Patients with Type 2 Diabetes and Acute Coronary Syndrome.

Piel, S., Ehinger, J., Elmer, E. & Hansson, M. (2015) Metformin induces lactate production in peripheral blood mononuclear cells and platelets through specific mitochondrial complex I inhibition. Acta physiologica, 213(1), 171-180.

Pitt, J. J. (2009) Principles and applications of liquid chromatography-mass spectrometry in clinical biochemistry. The Clinical Biochemist Reviews, 30(1), 19.

Pizzatti, L., Kawassaki, A. C. B., Fadel, B., Nogueira, F., Evaristo, J. A., Woldmar, N., Teixeira, G. T., Silva, J. C. d., Scandolara, T. B. & Rech, D. (2020) Toxicoproteomics disclose pesticides as downregulators of TNF-a, IL-1b and estrogen receptor pathways in breast cancer women chronically exposed.

Premnath, S. M. & Zubair, M. (2024) Chromatography, StatPearls [Internet]StatPearls Publishing.

Prevention, C. f. D. C. a. (2023) QuickStats: Percentage of Mothers with Gestational Diabetes, by Maternal Age—National Vital Statistics System, United States, 2016 and 2021. MMWR. January 6, 2023. MMWR Morb Mortal Wkly Rep, 72.

Qi, H.-P., Wang, Y., Zhang, Q.-H., Guo, J., Li, L., Cao, Y.-G., Li, S.-Z., Li, X.-L., Shi, M.-M. & Xu, W. (2015) Activation of peroxisome proliferator-activated receptor γ (PPARγ) through NF-κB/Brg1 and TGF-ß1 pathways attenuates cardiac remodeling in pressure-overloaded rat hearts. Cellular Physiology and Biochemistry, 35(3), 899-912.

Qiu, S., Cai, Y., Yao, H., Lin, C., Xie, Y., Tang, S. & Zhang, A. (2023) Small molecule metabolites: discovery of biomarkers and therapeutic targets. Signal Transduction and Targeted Therapy, 8(1), 132.

Rachek, L. I., Yuzefovych, L. V., LeDoux, S. P., Julie, N. L. & Wilson, G. L. (2009) Troglitazone, but not rosiglitazone, damages mitochondrial DNA and induces mitochondrial dysfunction and cell death in human hepatocytes. Toxicology and applied pharmacology, 240(3), 348-354.

Rafail, S., Kourtzelis, I., Foukas, P. G., Markiewski, M. M., DeAngelis, R. A., Guariento, M., Ricklin, D., Grice, E. A. & Lambris, J. D. (2015) Complement deficiency promotes cutaneous wound healing in mice. The Journal of Immunology, 194(3), 1285-1291.

Ramakrishnan, N. A., Drescher, M. J. & Drescher, D. G. (2012) The SNARE complex in neuronal and sensory cells. Mol Cell Neurosci, 50(1), 58-69.

Rashmi, D., Zanan, R., John, S., Khandagale, K. & Nadaf, A. (2018) γ-aminobutyric acid (GABA): Biosynthesis, role, commercial production, and applications. Studies in natural products chemistry, 57, 413-452.

Rashmi, P., Urmila, A., Likhit, A., Subhash, B. & Shailendra, G. (2023) Rodent models for diabetes. 3 Biotech, 13(3), 80.

Richter, B., Bandeira-Echtler, E., Bergerhoff, K., Clar, C. & Ebrahim, S. H. (2007) Rosiglitazone for type 2 diabetes mellitus. Cochrane Database of Systematic Reviews(3).

Rickels, M. R. & Robertson, R. P. (2019) Pancreatic islet transplantation in humans: recent progress and future directions. Endocrine reviews, 40(2), 631-668.

Riess, M. L., Elorbany, R., Weihrauch, D., Stowe, D. F. & Camara, A. K. (2020) PPARγ-Independent side effects of thiazolidinediones on mitochondrial redox state in rat isolated hearts. Cells, 9(1), 252.

Rinschen, M. M., Ivanisevic, J., Giera, M. & Siuzdak, G. (2019) Identification of bioactive metabolites using activity metabolomics. Nature reviews Molecular cell biology, 20(6), 353-367.

Robards, K. & Ryan, D. (2021) Principles and practice of modern chromatographic methodsAcademic Press.

Robinson, J. F., Pennings, J. L. & Piersma, A. H. (2012) A review of toxicogenomic approaches in developmental toxicology. Developmental Toxicology: Methods and Protocols, 347-371.

Röder, P. V., Wu, B., Liu, Y. & Han, W. (2016) Pancreatic regulation of glucose homeostasis. Exp Mol Med, 48(3), e219.

Roelands, J., Garand, M., Hinchcliff, E., Ma, Y., Shah, P., Toufiq, M., Alfaki, M., Hendrickx, W., Boughorbel, S. & Rinchai, D. (2019) Long-chain acyl-CoA synthetase 1 role in sepsis and immunity: perspectives from a parallel review of public transcriptome datasets and of the literature. Frontiers in immunology, 10, 2410.

Rohart, F., Gautier, B., Singh, A. & Lê Cao, K.-A. (2017) mixOmics: An R package for 'omics feature selection and multiple data integration. PLoS computational biology, 13(11), e1005752.

Russom, C. L., LaLone, C. A., Villeneuve, D. L. & Ankley, G. T. (2014) Development of an adverse outcome pathway for acetylcholinesterase inhibition leading to acute mortality. Environmental toxicology and chemistry, 33(10), 2157-2169.

Ryu, H. M., Kim, Y. J., Oh, E. J., Oh, S. H., Choi, J. Y., Cho, J. H., Kim, C. D., Park, S. H. & Kim, Y. L. (2016) Hypoxanthine induces cholesterol accumulation and incites atherosclerosis in apolipoprotein E-deficient mice and cells. Journal of cellular and molecular medicine, 20(11), 2160-2172.

Sahu, S. C., Amankwa-Sakyi, M., O'Donnell Jr, M. W. & Sprando, R. L. (2012) Effects of usnic acid exposure on human hepatoblastoma HepG2 cells in culture. Journal of Applied Toxicology, 32(9), 722-730.

Schellinger, A. P. & Carr, P. W. (2006) Isocratic and gradient elution chromatography: a comparison in terms of speed, retention reproducibility and quantitation. Journal of Chromatography A, 1109(2), 253-266.

Schenkl, C., Heyne, E., Doenst, T., Schulze, P. C. & Nguyen, T. D. (2023) Targeting Mitochondrial Metabolism to Save the Failing Heart. Life, 13(4), 1027.

Schernthaner, G., Barnett, A. H., Betteridge, D., Carmena, R., Ceriello, A., Charbonnel, B., Hanefeld, M., Lehmann, R., Malecki, M. & Nesto, R. (2010) Is the ADA/EASD algorithm for the management of type 2 diabetes (January 2009) based on evidence or opinion? A critical analysis. Diabetologia, 53(7), 1258-1269.

Schultz, I. R. & Watanabe, K. H. (2018) The development of quantitative AOPs. A systems biology approach to advancing adverse outcome pathways for risk assessment, 263-280.

Serra, A., Fratello, M., Cattelani, L., Liampa, I., Melagraki, G., Kohonen, P., Nymark, P., Federico, A., Kinaret, P. A. S. & Jagiello, K. (2020) Transcriptomics in toxicogenomics, part III: data modelling for risk assessment. Nanomaterials, 10(4), 708.

Shan, W., Li, J., Xu, W., Li, H. & Zuo, Z. (2019) Critical role of UQCRC1 in embryo survival, brain ischemic tolerance and normal cognition in mice. Cellular and Molecular Life Sciences, 76, 1381-1396.

Shekar, K. C., Li, L., Dabkowski, E. R., Xu, W., Ribeiro Jr, R. F., Hecker, P. A., Recchia, F. A., Sadygov, R. G., Willard, B. & Kasumov, T. (2014) Cardiac mitochondrial proteome dynamics with heavy water reveals stable rate of mitochondrial protein synthesis in heart failure despite decline in mitochondrial oxidative capacity. Journal of molecular and cellular cardiology, 75, 88-97.

Singh, R. K., Saini, S. K., Prakasam, G., Kalairasan, P. & Bamezai, R. N. (2019) Role of ectopically expressed mtDNA encoded cytochrome c oxidase subunit I (MT-COI) in tumorigenesis. Mitochondrion, 49, 56-65.

Singh, S., Chang, H.-Y., Richards, T. M., Weiner, J. P., Clark, J. M. & Segal, J. B. (2013) Glucagonlike peptide 1–based therapies and risk of hospitalization for acute pancreatitis in type 2 diabetes mellitus: a population-based matched case-control study. JAMA internal medicine, 173(7), 534-539 %@ 2168-6106.

Sitbon, Y. H., Yadav, S., Kazmierczak, K. & Szczesna-Cordary, D. (2020) Insights into myosin regulatory and essential light chains: a focus on their roles in cardiac and skeletal muscle function, development and disease. Journal of muscle research and cell motility, 41, 313-327.

Skelin, M., Rupnik, M. & Cencič, A. (2010) Pancreatic beta cell lines and their applications in diabetes mellitus research. ALTEX-Alternatives to animal experimentation, 27(2), 105-113.

Śliwińska-Mossoń, M., Bil-Lula, I. & Marek, G. (2023) The cause and effect relationship of diabetes after acute pancreatitis. Biomedicines, 11(3), 667.

Sloan, G., Alam, U., Selvarajah, D. & Tesfaye, S. (2022) The treatment of painful diabetic neuropathy. Current diabetes reviews, 18(5), 42-96.

Snyder, L. R. & Dolan, J. W. (2007) High-performance gradient elution: the practical application of the linear-solvent-strength modelJohn Wiley & Sons.

Son, N.-H., Park, T.-S., Yamashita, H., Yokoyama, M., Huggins, L. A., Okajima, K., Homma, S., Szabolcs, M. J., Huang, L.-S. & Goldberg, I. J. (2007) Cardiomyocyte expression of PPARγ leads to cardiac dysfunction in mice. The Journal of clinical investigation, 117(10), 2791-2801.

Spiller, H. A. & Sawyer, T. S. (2006) Toxicology of oral antidiabetic medications. American journal of health-system pharmacy, 63(10), 929-938.

Starner, C. I., Schafer, J. A., Heaton, A. H. & Gleason, P. P. (2008) Rosiglitazone and pioglitazone utilization from January 2007 through May 2008 associated with five risk-warning events. Journal of Managed Care Pharmacy, 14(6), 523-531.

Stoker, M. L., Newport, E., Hulit, J. C., West, A. P. & Morten, K. J. (2019) Impact of pharmacological agents on mitochondrial function: a growing opportunity? Biochemical Society Transactions, 47(6), 1757-1772.

Subramaniam, S., Jurk, K., Hobohm, L., Jäckel, S., Saffarzadeh, M., Schwierczek, K., Wenzel, P., Langer, F., Reinhardt, C. & Ruf, W. (2017) Distinct contributions of complement factors to platelet activation and fibrin formation in venous thrombus development. Blood, The Journal of the American Society of Hematology, 129(16), 2291-2302.

Sui, X., Wu, Q., Cui, X., Wang, X., Zhang, L., Deng, N., Bian, Y., Xu, R. & Tian, R. (2022) Robust Capillary-and Micro-Flow Liquid Chromatography–Tandem Mass Spectrometry Methods for High-Throughput Proteome Profiling. Journal of Proteome Research, 21(10), 2472-2480.

Suman, S., Mishra, S. & Shukla, Y. (2016) Toxicoproteomics in human health and disease: an update. Expert review of proteomics, 13(12), 1073-1089.

Sun, D., Gao, W., Hu, H. & Zhou, S. (2022) Why 90% of clinical drug development fails and how to improve it? Acta Pharmaceutica Sinica B, 12(7), 3049-3062.

Sun, H., Olson, K. C., Gao, C., Prosdocimo, D. A., Zhou, M., Wang, Z., Jeyaraj, D., Youn, J.-Y., Ren, S. & Liu, Y. (2016) Catabolic defect of branched-chain amino acids promotes heart failure. Circulation, 133(21), 2038-2049.

Sun, X., Ye, Y., Sun, J., Tang, L., Yang, X. & Sun, X. (2024) Advances in the study of liver microsomes in the in vitro metabolism and toxicity evaluation of foodborne contaminants. Critical Reviews in Food Science and Nutrition, 64(11), 3264-3278.

Świderska, E., Strycharz, J., Wróblewski, A., Szemraj, J., Drzewoski, J. & Śliwińska, A. (2018) Role of PI3K/AKT pathway in insulin-mediated glucose uptake, Blood Glucose LevelsIntechOpen.

Syed, W., Menaka, M., Fazil, A. & Sana, S. (2019) A LITERATURE REVIEW ON ORAL HYPOGLYCEMIC DRUGS – MECHANISTIC ASPECTS. Asian Journal of Pharmaceutical and Clinical Research, 12(11), 5-10.

Szyszka, P., Jendryka, J., Sobków, J., Zychla, M., Białas, M., Knapkiewicz, P., Dziuban, J. & Grzebyk, T. (2024) Mems Quadrupole Mass Spectrometer. Sensors and Actuators B: Chemical, 135712.

Tan, M., Yin, Y., Ma, X., Zhang, J., Pan, W., Tan, M., Zhao, Y., Yang, T., Jiang, T. & Li, H. (2023) Glutathione system enhancement for cardiac protection: pharmacological options against oxidative stress and ferroptosis. Cell Death & Disease, 14(2), 131.

Tan, Y., Wang, M., Yang, K., Chi, T., Liao, Z. & Wei, P. (2021) PPAR-α modulators as current and potential cancer treatments. Frontiers in oncology, 11, 599995.

Tayanloo-Beik, A., Roudsari, P. P., Rezaei-Tavirani, M., Biglar, M., Tabatabaei-Malazy, O., Arjmand, B. & Larijani, B. (2021) Diabetes and heart failure: multi-omics approaches. Frontiers in physiology, 12, 705424.

Thacker, D. L., Savieo, J. & Hachad, H. (2020) Bringing Pharmacogenetics to Prescribers: Progress and Challenges. Advances in Molecular Pathology, 3, 117-129.

Thomas, I. & Gregg, B. (2017) Metformin; a review of its history and future: from lilac to longevity. Pediatric diabetes, 18(1), 10-16.

Thomas, S., Ricke, W. A. & Li, L. (2023) Toxicoproteomics of Mono (2-ethylhexyl) phthalate and Perfluorooctanesulfonic Acid in Models of Prostatic Diseases. Chemical Research in Toxicology, 36(2), 251-259.

Timofeev, V., Chuprov-Netochin, R., Samigina, V., Bezuglov, V., Miroshnikov, K. & Kuranova, I. (2010) X-ray investigation of gene-engineered human insulin crystallized from a solution containing polysialic acid. Acta crystallographica section F: Structural biology and crystallization communications, 66(3), 259-263.

Tiwari, A., Rathor, P., Trivedi, P. K. & Ch, R. (2023) Multi-Omics Reveal Interplay between Circadian Dysfunction and Type2 Diabetes. Biology, 12(2), 301.

Todorov, H., Searle-White, E. & Gerber, S. (2020) Applying univariate vs. multivariate statistics to investigate therapeutic efficacy in (pre) clinical trials: A Monte Carlo simulation study on the example of a controlled preclinical neurotrauma trial. PLoS One, 15(3), e0230798.

Tönnies, T., Brinks, R., Isom, S., Dabelea, D., Divers, J., Mayer-Davis, E. J., Lawrence, J. M., Pihoker, C., Dolan, L. & Liese, A. D. (2023) Projections of type 1 and type 2 diabetes burden in the US population aged< 20 years through 2060: the SEARCH for Diabetes in Youth study. Diabetes Care, 46(2), 313-320.

Turi, K. N., Romick-Rosendale, L., Ryckman, K. K. & Hartert, T. V. (2018) A review of metabolomics approaches and their application in identifying causal pathways of childhood asthma. Journal of Allergy and Clinical Immunology, 141(4), 1191-1201.

Urakami, T. (2019) Maturity-onset diabetes of the young (MODY): current perspectives on diagnosis and treatment. Diabetes, metabolic syndrome and obesity: targets and therapy, 12, 1047.

Valcarcel-Jimenez, L. & Frezza, C. (2023) Fumarate hydratase (FH) and cancer: a paradigm of oncometabolism. British Journal of Cancer, 129(10), 1546-1557.

Varga, Z. V., Ferdinandy, P., Liaudet, L. & Pacher, P. (2015) Drug-induced mitochondrial dysfunction and cardiotoxicity. American Journal of Physiology-Heart and Circulatory Physiology, 309(9), H1453-H1467.

Vargas, E., Joy, N. V. & Sepulveda, M. A. C. (2020) Biochemistry, Insulin Metabolic Effects. StatPearls [Internet].

Viigimaa, M., Sachinidis, A., Toumpourleka, M., Koutsampasopoulos, K., Alliksoo, S. & Titma, T. (2020) Macrovascular complications of type 2 diabetes mellitus. Current Vascular Pharmacology, 18(2), 110-116.

Vinaixa, M., Rodriguez, M. A., Samino, S., Díaz, M., Beltran, A., Mallol, R., Bladé, C., Ibañez, L., Correig, X. & Yanes, O. (2011) Metabolomics reveals reduction of metabolic oxidation in women with polycystic ovary syndrome after pioglitazone-flutamide-metformin polytherapy. PloS one, 6(12), e29052.

Viñuela, A., Snoek, L. B., Riksen, J. A. & Kammenga, J. E. (2010) Genome-wide gene expression analysis in response to organophosphorus pesticide chlorpyrifos and diazinon in C. elegans. PloS one, 5(8), e12145.

Vuda, M. & Kamath, A. (2016) Drug induced mitochondrial dysfunction: Mechanisms and adverse clinical consequences. Mitochondrion, 31, 63-74.

Wai, T., García-Prieto, J., Baker, M. J., Merkwirth, C., Benit, P., Rustin, P., Rupérez, F. J., Barbas, C., Ibañez, B. & Langer, T. (2015) Imbalanced OPA1 processing and mitochondrial fragmentation cause heart failure in mice. Science, 350(6265), aad0116.

Wajid, S., Menaka, M., Ahmed, F. & Samreen, S. (2019) A literature review on oral hypoglycemic drugs–mechanistic aspects. Asian Journal of Pharmaceutical and Clinical Research, 12(11), 5-10.

Wallach, J. D., Wang, K., Zhang, A. D., Cheng, D., Nardini, H. K. G., Lin, H., Bracken, M. B., Desai, M., Krumholz, H. M. & Ross, J. S. (2020) Updating insights into rosiglitazone and cardiovascular risk through shared data: individual patient and summary level meta-analyses. Bmj, 368.

Wang, B., Nie, J., Wu, L., Hu, Y., Wen, Z., Dong, L., Zou, M.-H., Chen, C. & Wang, D. W. (2018) AMPKα2 protects against the development of heart failure by enhancing mitophagy via PINK1 phosphorylation. Circulation research, 122(5), 712-729.

Wang, M., Wang, C. & Han, X. (2017) Selection of internal standards for accurate quantification of complex lipid species in biological extracts by electrospray ionization mass spectrometry—What, how and why? Mass spectrometry reviews, 36(6), 693-714.

Wang, S., Li, W., Hu, L., Cheng, J., Yang, H. & Liu, Y. (2020) NAguideR: performing and prioritizing missing value imputations for consistent bottom-up proteomic analyses. Nucleic acids research, 48(14), e83-e83.

Wang, S., Long, H., Hou, L., Feng, B., Ma, Z., Wu, Y., Zeng, Y., Cai, J., Zhang, D.-w. & Zhao, G. (2023) The mitophagy pathway and its implications in human diseases. Signal transduction and targeted therapy, 8(1), 304.

Wang, S., Yong, H. & He, X.-D. (2021) Multi-omics: Opportunities for research on mechanism of type 2 diabetes mellitus. World journal of diabetes, 12(7), 1070.

Wang, T., Shankar, K., Ronis, M. & Mehendale, H. (2007) Mechanisms and outcomes of drug-and toxicant-induced liver toxicity in diabetes. Critical reviews in toxicology, 37(5), 413-459.

Wang, Z., Jiang, H., Chen, S., Du, F. & Wang, X. (2012) The mitochondrial phosphatase PGAM5 functions at the convergence point of multiple necrotic death pathways. Cell, 148(1), 228-243.

Watanabe, K., Nagao, M., Toh, R., Irino, Y., Shinohara, M., Iino, T., Yoshikawa, S., Tanaka, H., Satomi-Kobayashi, S. & Ishida, T. (2021) Critical role of glutamine metabolism in cardiomyocytes under oxidative stress. Biochemical and Biophysical Research Communications, 534, 687-693.

Watkins, S. M., Reifsnyder, P. R., Pan, H.-j., German, J. B. & Leiter, E. H. (2002) Lipid metabolome-wide effects of the PPARγ agonist rosiglitazone. Journal of lipid research, 43(11), 1809-1817.

Watts, N. B., Bilezikian, J. P., Usiskin, K., Edwards, R., Desai, M., Law, G. & Meininger, G. (2016) Effects of canagliflozin on fracture risk in patients with type 2 diabetes mellitus. The Journal of Clinical Endocrinology, 101(1), 157-166.

Wei, X., Shi, X., Kim, S., Zhang, L., Patrick, J. S., Binkley, J., McClain, C. & Zhang, X. (2012) Data preprocessing method for liquid chromatography–mass spectrometry based metabolomics. Analytical chemistry, 84(18), 7963-7971.

Whicher, C., O'Neill, S. & Holt, R. G. (2020) Diabetes in the UK: 2019. Diabetic Medicine, 37(2), 242-247.

Wickham, H., Chang, W. & Wickham, M. H. (2016) Package 'ggplot2'. Create elegant data visualisations using the grammar of graphics. Version, 2(1), 1-189.

Willforss, J., Chawade, A. & Levander, F. (2018) NormalyzerDE: online tool for improved normalization of omics expression data and high-sensitivity differential expression analysis. Journal of proteome research, 18(2), 732-740.

Williams, A. & Halappanavar, S. (2015) Application of biclustering of gene expression data and gene set enrichment analysis methods to identify potentially disease causing nanomaterials. Beilstein journal of nanotechnology, 6(1), 2438-2448.

Wilson, C. M. & High, S. (2007) Ribophorin I acts as a substrate-specific facilitator of N-glycosylation. Journal of cell science, 120(4), 648-657.

Wu, D. & Yotnda, P. (2011) Production and detection of reactive oxygen species (ROS) in cancers. JoVE (Journal of Visualized Experiments)(57), e3357.

Wu, J. X., Pascovici, D., Wu, Y., Walker, A. K. & Mirzaei, M. (2021) Application of WGCNA and PloGO2 in the Analysis of Complex Proteomic Data, Statistical Analysis of Proteomic Data: Methods and ToolsSpringer, 375-390.

Wu, Y., Deng, M., Jin, Y., Liu, X., Mai, Z., You, H., Mu, X., He, X., Alharthi, R. & Kostyniuk, D. J. (2019) Toxicokinetics and toxic effects of a Chinese PFOS alternative F-53B in adult zebrafish. Ecotoxicology and Environmental Safety, 171, 460-466.

Wu, Y., Li, J., Saleem, S., Yee, S.-P., Hardikar, A. A. & Wang, R. (2010) c-Kit and stem cell factor regulate PANC-1 cell differentiation into insulin-and glucagon-producing cells. Laboratory investigation, 90(9), 1373-1384.

Xie, L., Zhao, Y., Duan, J., Fan, S., Shu, L., Liu, H., Wang, Y., Xu, Y. & Li, Y. (2020) Integrated proteomics and metabolomics reveal the mechanism of nephrotoxicity induced by triptolide. Chemical research in toxicology, 33(7), 1897-1906.

Xiong, Y., Jiang, L. & Li, T. (2022) Aberrant branched-chain amino acid catabolism in cardiovascular diseases. Frontiers in Cardiovascular Medicine, 9, 965899.

Xue, C., Gu, X., Li, G., Bao, Z. & Li, L. (2020) Mitochondrial mechanisms of necroptosis in liver diseases. International Journal of Molecular Sciences, 22(1), 66.

Yamamoto, T. & Sano, M. (2022) Deranged myocardial fatty acid metabolism in heart failure. International journal of molecular sciences, 23(2), 996.

Yang, H., Suh, D. H., Kim, D. H., Jung, E. S., Liu, K. H., Lee, C. H. & Park, C. Y. (2018) Metabolomic and lipidomic analysis of the effect of pioglitazone on hepatic steatosis in a rat model of obese Type 2 diabetes. British Journal of Pharmacology, 175(17), 3610-3625.

Ye, Z., Wang, S., Zhang, C. & Zhao, Y. (2020) Coordinated modulation of energy metabolism and inflammation by branched-chain amino acids and fatty acids. Frontiers in endocrinology, 11, 617.

Yen, C.-F., Wang, H.-S., Lee, C.-L. & Liao, S.-K. (2014) Roles of integrin-linked kinase in cell signaling and its perspectives as a therapeutic target. Gynecology and Minimally Invasive Therapy, 3(3), 67-72.

Yi, D. & Kang, Y. H. (2017) Drug-Induced Diabetes Mellitus. The Journal of Korean Diabetes, 18(3), 160-168 %@ 2233-7431.

Yi, T., Wu, X. & Li, H. (2020) Ubiquinol-cytochrome c reductase core protein 1 overexpression protects H9c2 cardiac cells against mimic ischemia/reperfusion injury through PI3K/Akt/GSK-3β pathway. Biochemical and Biophysical Research Communications, 529(4), 904-909.

Yipel, M. & İlhan, A. (2022) Potentiation of Toxicology with Proteomics: Toxicoproteomics. International Journal of Veterinary and Animal Research (IJVAR), 5(1), 36-39.

Yki-Järvinen, H. (2004) Thiazolidinediones. New England Journal of Medicine, 351(11), 1106-1118.

Yu, G., Wang, L.-G., Han, Y. & He, Q.-Y. (2012) clusterProfiler: an R package for comparing biological themes among gene clusters. Omics: a journal of integrative biology, 16(5), 284-287.

Yu, L., Li, H., Zhang, C., Zhang, Q., Guo, J., Li, J., Yuan, H., Li, L., Carmichael, P. & Peng, S. (2020) Integrating in vitro testing and physiologically-based pharmacokinetic (PBPK) modelling for chemical liver toxicity assessment—A case study of troglitazone. Environmental toxicology and pharmacology, 74, 103296.

Yu, M., Dolios, G. & Petrick, L. (2022) Reproducible untargeted metabolomics workflow for exhaustive MS2 data acquisition of MS1 features. Journal of Cheminformatics, 14(1), 6.

Yuan, H., Li, X., Zhang, X., Kang, R. & Tang, D. (2016) CISD1 inhibits ferroptosis by protection against mitochondrial lipid peroxidation. Biochemical and biophysical research communications, 478(2), 838-844.

Yue, J. & López, J. M. (2020) Understanding MAPK signaling pathways in apoptosis. International journal of molecular sciences, 21(7), 2346.

Yue, Z., Zhang, Y., Xie, J., Jiang, J. & Yue, L. (2013) Transient receptor potential (TRP) channels and cardiac fibrosis. Current topics in medicinal chemistry, 13(3), 270-282.

Zaitsu, K., Hayashi, Y., Kusano, M., Tsuchihashi, H. & Ishii, A. (2016) Application of metabolomics to toxicology of drugs of abuse: A mini review of metabolomics approach to acute and chronic toxicity studies. Drug metabolism and pharmacokinetics, 31(1), 21-26.

Zelniker, T. A., Wiviott, S. D., Raz, I., Im, K., Goodrich, E. L., Bonaca, M. P., Mosenzon, O., Kato, E. T. & Cahn, A. (2019) Articles SGLT2 inhibitors for primary and secondary prevention of cardiovascular and renal outcomes in type 2 diabetes: a systematic review and meta-analysis of cardiovascular outcome trials.

Zhang, K. & Zhao, Y. (2018) Reduced zebrafish transcriptome atlas toward understanding environmental neurotoxicants. Environmental science & technology, 52(12), 7120-7130.

Zhang, Q., Ma, C., Gearing, M., Wang, P. G., Chin, L.-S. & Li, L. (2018) Integrated proteomics and network analysis identifies protein hubs and network alterations in Alzheimer's disease. Acta neuropathologica communications, 6, 1-19.

Zhang, T., Zhang, Y., Cui, M., Jin, L., Wang, Y., Lv, F., Liu, Y., Zheng, W., Shang, H. & Zhang, J. (2016) CaMKII is a RIP3 substrate mediating ischemia-and oxidative stress–induced myocardial necroptosis. Nature medicine, 22(2), 175-182.

Zhang, X., Xia, P., Wang, P., Yang, J. & Baird, D. J. (2018) Omics advances in ecotoxicology. ACS Publications.

Zhao, L., Cong, X., Zhai, L., Hu, H., Xu, J.-Y., Zhao, W., Zhu, M., Tan, M. & Ye, B.-C. (2020) Comparative evaluation of label-free quantification strategies. Journal of proteomics, 215, 103669.

Zhao, R., Cai, K., Yang, J.-J., Zhou, Q., Cao, W., Xiang, J., Shen, Y.-H., Cheng, L.-L., Zang, W.-D. & Lin, Y. (2023) Nuclear ATR lysine-tyrosylation protects against heart failure by activating DNA damage response. Cell Reports, 42(4).

Zhong, W., Jin, W., Xu, S., Wu, Y., Luo, S., Liang, M. & Chen, L. (2018) Pioglitazone induces cardiomyocyte apoptosis and inhibits cardiomyocyte hypertrophy via VEGFR-2 signaling pathway. Arquivos Brasileiros de Cardiologia, 111, 162-169.

Zhou, T., Xu, X., Du, M., Zhao, T. & Wang, J. (2018) A preclinical overview of metformin for the treatment of type 2 diabetes. Biomedicine & Pharmacotherapy, 106, 1227-1235.

Zhou, Y.-T., Grayburn, P., Karim, A., Shimabukuro, M., Higa, M., Baetens, D., Orci, L. & Unger, R. H. (2000) Lipotoxic heart disease in obese rats: implications for human obesity. Proceedings of the National Academy of Sciences, 97(4), 1784-1789.

Zhou, Y., Huang, Y., Ji, X., Wang, X., Shen, L. & Wang, Y. (2020) Pioglitazone for the primary and secondary prevention of cardiovascular and renal outcomes in patients with or at high risk of type 2 diabetes mellitus: a meta-analysis. The Journal of Clinical Endocrinology & Metabolism, 105(5), 1670-1681.

Zinman, B., Lachin, J. M. & Inzucchi, S. E. (2016) Empagliflozin, cardiovascular outcomes, and mortality in type 2 diabetes. The New England journal of medicine, 374(11), 1094.

Zorova, L. D., Popkov, V. A., Plotnikov, E. Y., Silachev, D. N., Pevzner, I. B., Jankauskas, S. S., Babenko, V. A., Zorov, S. D., Balakireva, A. V. & Juhaszova, M. (2018) Mitochondrial membrane potential. Analytical biochemistry, 552, 50-59.

Zubarev, R. A. & Makarov, A. (2013) Orbitrap mass spectrometry. ACS Publications.